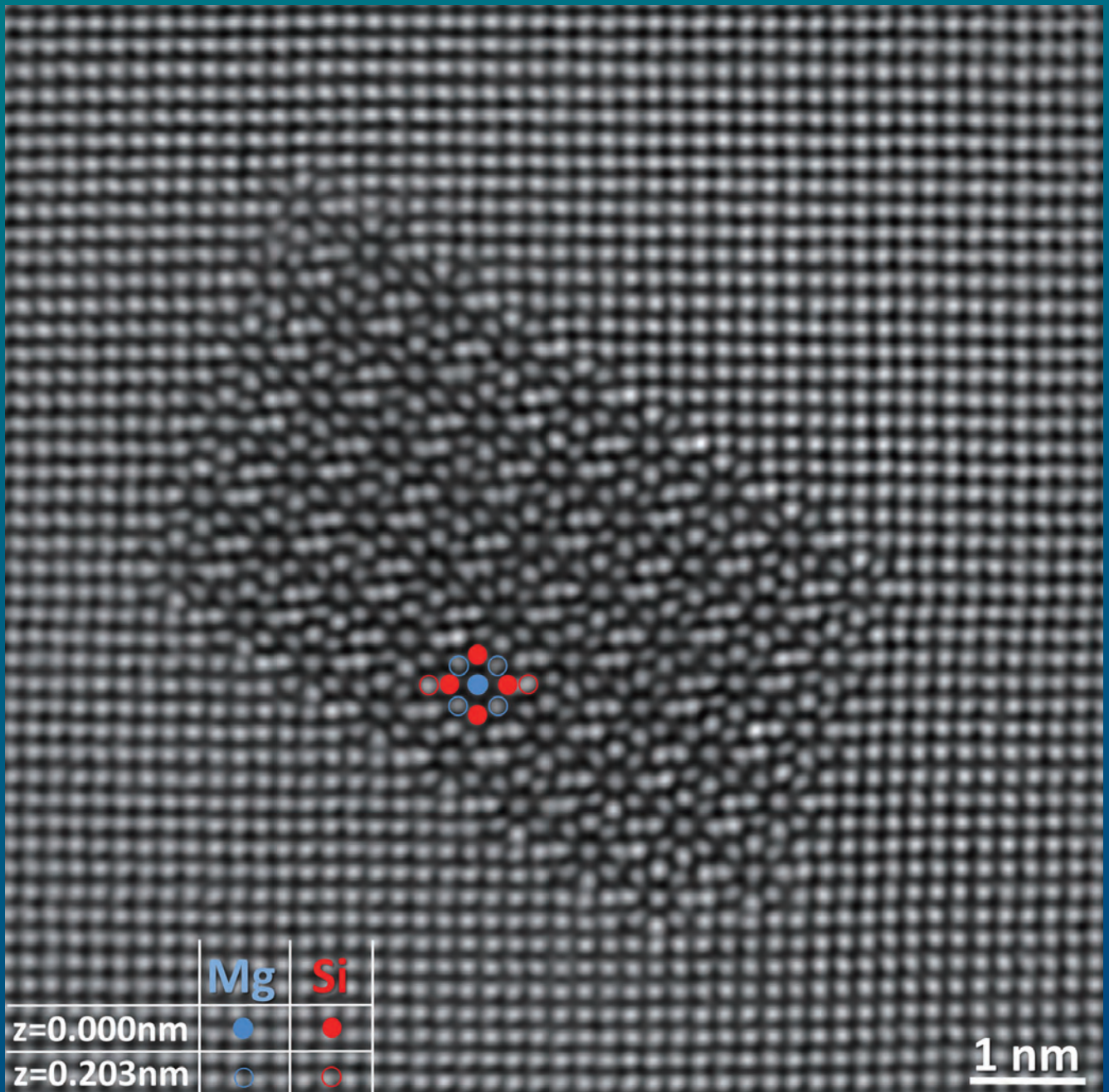
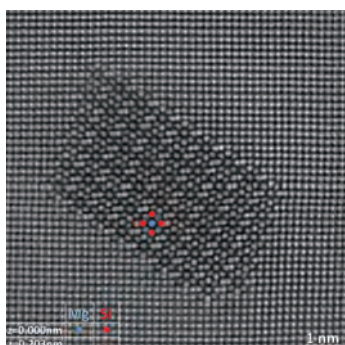


# JEOL NEWS

July 2017  
Vol.52  
No.1



- Revealing the Atomic Structure of Two Dimensional and Three Dimensional Defects by Aberration Corrected Scanning Transmission Electron Microscopy.....2  
Williams Lefebvre, Alfiia Akhatova, Lorenzo Mancini, Auriane Etienne, Bertrand Radiguet, Lorenzo Riguti, Xavier Sauvage, Celia Castro, Simona Moldovan, Philippe Pareige
- Quantitative STEM-EELS Characterizations of Oxide Superlattices and Atomic-Scale Electron Spectroscopy at 100 K at National Taiwan University.....11  
Pei-Wei Lee, Ming-Hao Lee, Shih-Chi Lee, Chin-Ping Chang, Yi-Chen Lai, Guang-Yu Guo, Ying-Hao Chu, Wei-Li Lee, Cheng Hsuan Chen, and Ming-Wen Chu
- High Spatial Resolution Scanning Electron Microscope: Evaluation and Structural Analysis of Nanostructured Materials.....17  
Osamu Terasaki, Shunsuke Asahina, Yuusuke Sakuda, Hideyuki Takahashi, Kenichi Tsutsumi, Masato Kudo, Robert W. Corkery, Yanhang Ma
- A Top-Down Drawing of the World's Smallest National Flag by JBX-6300FS Electron Beam Lithography System .....29  
Nathan Nelson-Fitzpatrick
- High Temporal Resolution Analysis of Materials Nanoprocess by Materials- and Bio-Science Ultra-High Voltage Electron Microscope at Osaka University .....33  
Hidehiro Yasuda
- A Quantitative Analytical Method "Effective Magnetic Moment Method" Based on Both Curie-Weiss Law and ESR Fundamental Equation.....40  
Nobuhiro Matsumoto
- Introduction of a Next-Generation 200 kV Cryo TEM.....49  
Naoki Hosogi
- Development of Pixelated STEM Detector "4DCanvas" .....53  
Ryusuke Sagawa
- Development of a New Field Emission Electron Probe Microanalyzer JXA-8530FPlus.....58  
Satoshi Notoya
- JMS-MT3010HRGA INFITOF, a High Resolution Time-of-Flight Mass Spectrometer (TOF-MS) for Gas Monitoring Analysis.....61  
Yukinori Yahata
- The Development of the ROYAL HFX Probe.....65  
A. Zens, T. T. Miyamoto, R. Crouch, T. Bergeron, M. Frey, A. Nomura, Y. Horino, T. Nishida
- Latest Technologies of Electron-Beam Vacuum Deposition Used for Film Formation.....70  
Masanori Kamioka, Akira Taniguchi, Toru Takashima
- New-Generation Analyzer BioMajesty™ Zero Series, JCA-ZS050, and Its Contribution to Clinical Analysis.....77  
Kazushige Kojima
- Introduction of New Products .....82



## Cover micrograph

Aberration-corrected HAADF-STEM image of a  $\beta''$  precipitate observed along the  $[001]_{Al}$  zone axis, taken with a JEM-ARM200F. (See Fig. 1 in page 4)

# Revealing the Atomic Structure of Two Dimensional and Three Dimensional Defects by Aberration Corrected Scanning Transmission Electron Microscopy

Williams Lefebvre, Alfiya Akhatova, Lorenzo Mancini, Auriane Etienne, Bertrand Radiguet, Lorenzo Riguti, Xavier Sauvage, Celia Castro, Simona Moldovan, Philippe Pareige

Normandie Univ., GPM, UNIROUEN, INSA Rouen, CNRS

This paper highlights some of the possibilities offered to materials scientists for the study of defects structure, thanks to the availability of aberration corrected Scanning Transmission Electron Microscopes. First, illustrations are shown for the topic of precipitation hardening in high strength aluminium alloys. In these materials, very detailed analyses of precipitates architecture and of their interface with the matrix are accessible and offer new perspectives for the studies of defect interactions in these systems. Moreover, it is shown here that the morphological evolution of precipitates during in situ ageing treatments is also accessible in Z-contrast imaging mode at high resolutions, enabling the time resolved analysis of these defects. In a second part of this paper, two examples are given that illustrates the relevance of correlative investigations performed by coupling of Scanning Transmission Electron Microscopy with Atom Probe Tomography.

## Introduction

The application of high resolution transmission electron microscopy (TEM) and scanning transmission electron microscopy (STEM) has obviously spread to most fields of materials sciences nowadays. Moreover, such instrumental methods have supported the conception and emergence of new materials (e.g. graphene, nano-wires). Meanwhile, their use has also allowed elucidating complex phenomena (e.g. phase transformation, structure of defects) in various other classes of materials. Such advances would not have been possible without fulfilling the following requirements: i) improving performances of microscopes in terms of resolution and sensitivity; ii) improving the stability of instruments; iii) improving their ease of use.

The standard performances of TEM/STEM were drastically overpassed with the implementation of spherical aberration correctors [1]. Referring to the deep review by P.W. Hawkes [2] of the historical development of Cs-correctors would allow the reader getting a complete view of the implications of this technique in the field of electron microscopy. Thanks to this hardware development, the horizon of spatial resolution has routinely gone beyond the old 0.17-0.20 nm limit, offering

the possibility to access much more detailed images of fine structures. In addition, Cs-correction has eluded the necessary compromise between tilt-angle amplitude and spatial resolution, which existed when the design of pole pieces was governing the ultimate resolution of instruments. In a sense, Cs-correction has offered a larger flexibility for material preparation. Meanwhile, accessing larger magnifications came along with revealing the importance of instrument stability. Small imperfections that could be neglected in the past henceforth needed to be considered carefully and one must admit that microscope designers and engineers have spent a lot of efforts to identify and correct many aspects including: voltage stability, mechanical stability of the column, magnetic noise cancelation, specimen stage stability and manipulation. Such improvements now allow performing demonstrations of STEM-EDS atomic resolution while 4 people are talking in front of the microscope. There is no doubt that such an experience would have been difficult to believe for any electron microscopist 15-20 years ago. The last necessary requirement was to improve (or, at least, not to reduce) the ease of use of the latest instruments. This necessary condition has mainly required hiding the complexity of instruments behind smart design, software development and integration. The interactive Cs-corrector alignment procedure

with the Zemlin table [3] was a very big step [2].

Nowadays, these above mentioned necessary requirements have all been fulfilled and materials scientists can foresee new ways to investigate materials at the nano and sub-nano scale. In the present paper, three themes will be discussed. First, an illustration of the relevance of Cs-corrected STEM will be given for the precipitation hardening phenomenon in one of the hardest Aluminium based alloy. In this material, the structure of main hardening precipitates has been solved thanks to a JEOL JEM-ARM200F used in HAADF-STEM mode, in combination to first principle calculations [4]. The illustrations provided here will emphasize how HAADF and annular bright (ABF) in STEM can help solving the structure and follow complex evolution of precipitates during ageing treatments, including *in situ* heating in the microscope.

In alloys, once microstructures have been designed so as to achieve desired properties, conditions of use (e.g. stress, thermal cycling, irradiation) may induce subtle changes in the distribution of elements and other microstructural entities, which may degrade the materials reliability. Once again, the drastic developments in the field of TEM/STEM and related techniques allow to unravel defects coupling in alloys under operating conditions. An example will be given in a second section, which will highlight the phosphorous segregation along grain boundaries in a model steel.

Another tool has for a while demonstrated its relevance for the investigation of materials in 3 dimensions at the sub-nanoscale: Atom probe Tomography (APT) [5–8]. Though a relatively new technique compared to TEM and STEM, APT has rapidly spread over the world and is now often used as an excellent complement to electron microscopes for materials characterization. Atom Probe Tomography, which is intrinsically a 3D technique, has received increased attention owing to drastic developments during the last decade. The “GPM-Groupe de Physique des Matériaux” (i.e. materials physics group), among others (see historical development of the technique in the following references [6–9]), has strongly contributed to the development of this technique and still pursue strong activities in the field of instrumentation related to this instrument. This tool enables reconstructing volumes of matter by determining atom positions in 3D, which nature is determined by time of flight mass spectrometry. Thanks to the improvement of specimen preparation protocols, APT can be applied to much broader areas of materials science (semi-conductors, bio-materials, geo-materials, soft mater and even liquids) as compared to the early days, when it was confined to physical metallurgy. Strong advantages of APT rely in its possibility to detect all types of atoms, independently of their atomic number, in its excellent detection limit (few ppm in favorable cases but rarely more than 100 ppm), and in its intrinsic 3D nature. Nevertheless, inherent limitations of this tool reside in its limited detection efficiency (roughly 50% of atoms are detected) and in its anisotropic spatial resolution (though sub-Angström resolution is currently accessible along the direction of analysis, sub-nanometer resolution is achieved along transverse directions). As a consequence, performing serial characterization TEM/STEM and APT is a unique way to access a more complete characterization of defects and structures at the nano-scale. Much efforts have been provided recently in various field of materials sciences to correlate data obtained separately by APT and TEM/STEM (see for instance [10–14]). An illustration of correlative microscopy by APT and STEM will be presented in a third part.

## Relevance of high angle annular dark field scanning transmission electron microscopy for the study of precipitation hardening in aluminium based alloys

More than a century ago, the development of the first high strength aluminium based alloys was achieved by mixing small fractions of Cu and Mg to Al [15] but this was long time before the description by X-ray scattering of Guinier-Preston zones [16,17]. It took even more time to reveal at the atomic scale the structure and chemistry of these nano-objects by high resolution transmission electron microscopy (HRTEM) [18]. Though the topic of precipitation hardening might sound ancient when it is put into perspective with emerging fields of materials science, it remains an up-to-date field of investigation for materials scientist and engineers. The reason for this is probably its complexity inherited from the interactions between defects (solute, vacancies, dislocations, interfaces) and the overlapping of thermally activated phenomena (diffusion, softening, recrystallization, growth, coarsening, phase transformations). All of this might be considered to describe and/or conceive a microstructural state which may lead to a given combination of properties, including electrical conductivity, corrosion resistance, mechanical strength, fatigue resistance or resistance to irradiation.

In Al-based alloys, the strength increment with respect to pure Al (from 30-35 MPa to about 700 MPa) is mainly derived from the very fine scale precipitation of one or several hardening phases. Being able to model the mechanical properties and their evolution requires determining with a maximum of accuracy the structural entities composing the material. Before the availability of Cs-corrected HAADF-STEM, the determination of precipitate structure and chemistry was hardly achievable in TEM. A main reason for this is that precipitates are embedded in an Al-matrix and have a nanometer size. The crystalline structure could be approached by a combination of nano-beam electron diffraction and HRTEM. Experimental results had to be supported by image simulations accounting for the strong dynamic interactions. The determination of compositions could be tried in electron dispersive X-ray spectroscopy (EDS) and electron energy loss spectroscopy (EELS). Nevertheless, the small size of precipitates made it hard to avoid the contribution of matrix signal and to avoid the dissolution of precipitates under beam irradiation (because of long integration times with previous detection systems). In addition, precipitates are often composed of a mixture of light and heavy elements (e.g. Cu with Li), which is not favorable for the determination of composition with a single technique.

Nowadays, HAADF-STEM allows revealing the projected structure of precipitates and to eventually combine projections in the direct space to build their atomic architecture thanks to single atom sensitivity [19]. It is hence possible with a single imaging mode to retrieve both structural and (partial) chemical information. Other significant improvements of state-of-the-art TEM/STEM such as JEOL JEM-ARM have opened new perspectives for the investigation of precipitation hardening: specimen stage stability, EDS detectors, higher probe current. Numerous questions related to precipitation hardening can therefore be addressed. The first is the question of precipitate structure and chemistry [20][21][22][4]. Second, the interaction of precipitates with defects such as dislocations or interfaces can be investigated by coupling annular dark field (ADF) imaging (signal dominated by diffraction contrast) and HAADF [23].

The fine precipitate structure evolution after shear can also be resolved so as to retrieve the sequence of shear [24]. Another important question related to the application of precipitation hardened light alloys such as aluminium is their thermal stability. Because of a low melting point, Al-based alloys may involve significant softening at moderate temperatures (i.e. 150-300°C) compared to steels and titanium for instance. Part of this softening comes from the destabilization of the structure of precipitation. Insofar as sequences of metastability are often involved either for isothermal ageing or during heating ramps applied to an aluminium supersaturated solid solution, both the nature of phases and their morphology and/or distribution are susceptible to rapidly evolve. Once again, recent improvements of TEM/STEM instruments allow investigating these aspects. For instance, the transformations can be followed during in situ heat treatments, while maintaining good imaging capabilities, as will be shown later in this paper.

A first illustration is given here for an Al alloy of the 6xxx series (Fig. 1), which composition in at.% is Al-0.52Mg-0.38Si. This alloy was solution heat treated at 545°C for 5 min, kept for 30 min at room temperature and isothermally heat treated at 190°C for 300 min, which allows reaching the peak hardening [25]. In the 6xxx alloys (i.e. Al-alloys with Mg and Si additions mainly), the peak ageing condition involves the precipitation of the  $\beta''$  structure, which forms needles growing along  $\langle 001 \rangle$  cubic axes of the aluminium matrix. Though the crystal structure was solved some time ago [26], the initial composition of the model was  $\text{Mg}_5\text{Si}_6$ , whereas APT analyses often revealed significant amounts of substitutional Al inside the precipitates [27,28]. Thanks to detailed APT investigations, which were confronted to *ab initio* calculations of the formation enthalpy of the precipitates structures [29], possible incorporation of Al inside  $\beta''$  structure could be established. However, the reasons for this incorporation as well as the actual location of Al atoms inside  $\beta''$  could only be determined recently with the help of detailed HAADF-STEM analysis [21]. For this purpose, a

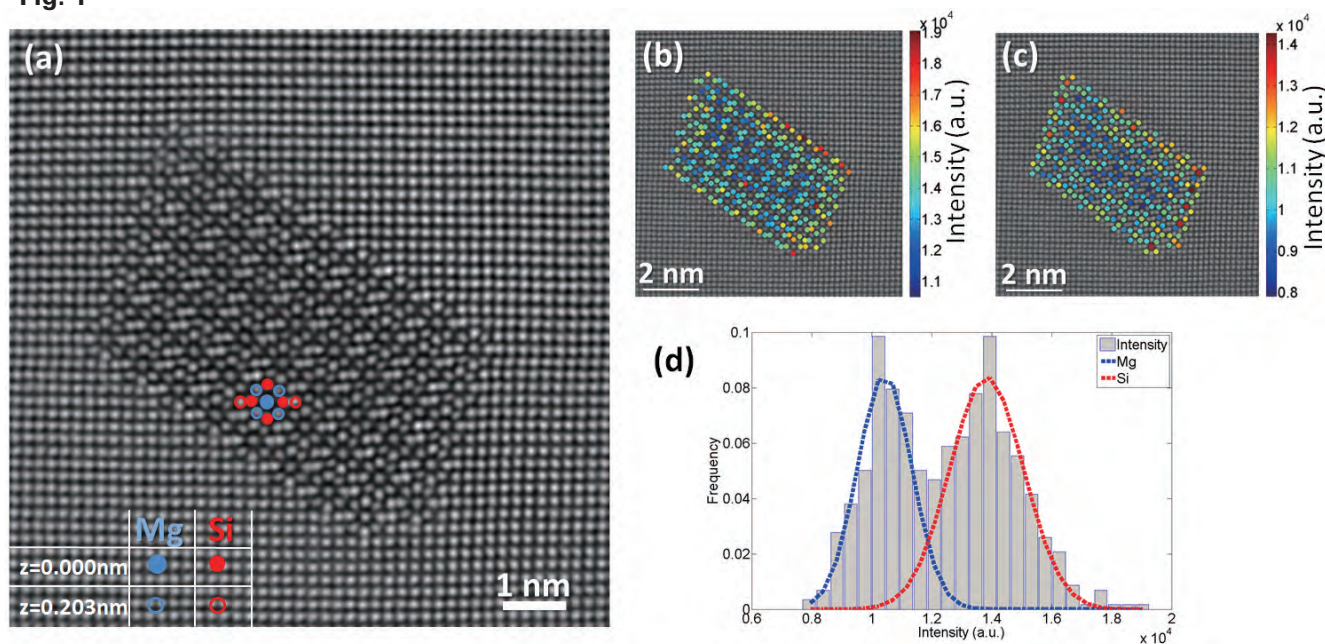
simple methodology was applied, which consists in integrating the measured HAADF-STEM intensity over each projected column position in the image. This methodology is illustrated in Fig. 1.

Here, the precipitate atomic structure was investigated using a spherical aberration (Cs) probe corrected JEM-ARM200F STEM operated at 200 kV. The following parameters were used: probe diameter of 0.1 nm, an objective aperture semi-angle of 22.5 mrad, detector half-collection angle between 40 and 150 mrad. For the quantitative analysis, Gaussian smoothing over 4 pixels and Wiener deblurring over 3x3 pixels were performed using the MatLab© image processing toolbox. In the example of Fig. 1, we observe a  $\beta''$  with its long axis pointed perpendicular to the image plane. The precipitate interface with the matrix is clearly revealed. The inner precipitate structure can be described by the periodic repetition of a pattern, which is overlapped to Fig. 1(a), in agreement with reference [26]. For the  $\beta''$ , Mg and Si sites are defined [26] and the intensities of Mg-type and Si-type columns along [001] can hence be measured separately (see Fig. 1 (b-d)). By means of HAADF-STEM image simulations, it has been shown that for the above mentioned conditions of observations, Z contrast can allow distinguishing the intensities of pure Mg (Z=12), Al (Z=13) and Si (Z=14) columns [21]. Plotting the intensities for the  $\beta''$  precipitate of Fig. 1 allows observing only two distinct contributions, indicating that for this precipitate, no significant amount of Al is detected with this methodology.

Such an observation clearly indicates that the amount of Al participating to the formation of  $\beta''$  may depend on the alloy composition but also and mainly on the precipitates size. This is what was suggested by the observations reported in [21], where detailed *ab initio* calculations demonstrated that the precipitates undergo elastic strain regions either in tension or in contraction, close to the interface, where significant substitution of Al in Mg and Si sites could be revealed by HAADF STEM.

In another Al-based system (Al-Li-Cu), the fine precipitation

Fig. 1



HAADF-STEM image of a  $\beta''$  precipitate observed along the  $[001]_m$  zone axis on a JEOL JEM-ARM200F with a Schottky field emission gun performing at 200 kV. An atomic overlay based on the original model [26] is shown and the atomic sites are defined. The HAADF-STEM intensities of atomic sites, either Si or Mg, were measured and overlapped on the original image in (b) and (c) respectively. (d) HAADF-STEM intensity histogram of Mg and Si sites. Similar methodologies were applied in [21,25].

of the  $T_1$  phase along  $\{111\}_{Al}$  planes is promoted by concomitant additions of Mg and Ag and by the presence of dislocations. A detailed literature review for this class of alloys is available in the following references [20,22,30]. The dislocations actually favor the formation of stacking faults necessary for precipitation of  $T_1$ , according to a Schockley mechanism. Thanks to the presence of a significant amount of Li and to the high strength provided by  $T_1$  precipitation, these alloys are particularly suited to aerospace and other lightweight transport applications. The structure of  $T_1$  precipitates has only been solved recently by Dwyer et al. [20]. Here, we present high resolution observations performed on a JEM-ARM200F which are comparable to the results reported by these authors.

A striking feature of  $T_1$  precipitates is their very large aspect ratio. Indeed, the thickness of these plate-shape precipitates does not exceed 1.3 nm, whereas their length can be about 100 nm, as seen in Fig. 2(a). This feature is explained by two facts. First, the nucleation of  $T_1$  requires a stacking fault in the Al matrix. The thickening of  $T_1$  (which is possible for longer ageing times) requires the nucleation of a ledge coinciding with the creation of a new stacking fault at the interface with the matrix. Second, the Al-matrix/ $T_1$  interface is perfectly coherent, which implies of low energy. It is hence more energetically favorable for  $T_1$  to propagate along  $\{111\}_{Al}$  rather than thickening along a perpendicular direction.

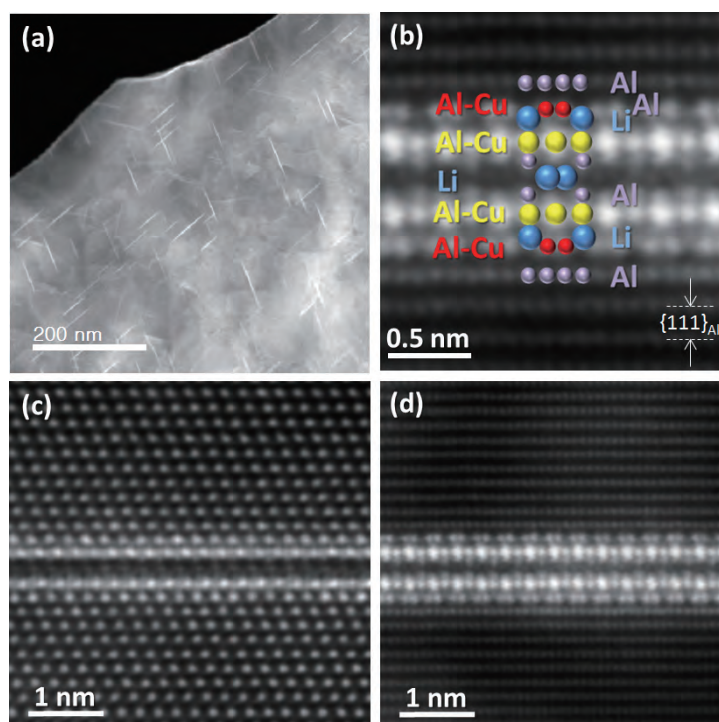
The high coherency of precipitate/matrix interface is a recurrent observation for peak age conditions in Al-based alloys, though in the previously mentioned 6xxx alloys, misfit dislocations may be observed, that can be suppressed by addition of Cu [25]. Observing such low energy interfaces is consistent with the mechanism of precipitation hardening. Indeed, sufficient hardening is only reached for large enough number densities of nanometer scale precipitates [31]. This can only be reached by “moderate temperature” decomposition of a supersaturated solution, in order to limit the effect of diffusivity and to promote the homogeneous nucleation of precipitates for

phases with a low energy nucleation barrier. Consequently, the formation of precipitates with coherent interfaces is promoted at the early stages of the precipitation sequences, whereas large incoherent precipitates are observed for either higher temperatures or longer ageing times.

The complete description of hardening precipitates structure in the peak age condition of the studied alloy has been provided in the paper by Marioara et al. [4], for which HAADF-STEM observations were performed on the JEM-ARM200F installed at the University of Rouen in 2009. In the present study, the similar material (7449 Al-Zn-Mg alloy in the overaged condition T7) has been further investigated in order to follow the evolution of precipitates upon in situ thermal ageing. Figure 3 shows a typical precipitate observed for this condition. The inner part of the precipitate incorporates layers of a rhombic units with corners defined by the high Z contrast atomic columns of Zn, similar to the rhombohedral (R) Zn units in  $\eta$ -MgZn<sub>2</sub> [32]. These units are highlighted by grey patterns R and R<sup>-1</sup> in Fig. 3(d). The presence of two Mg atoms in the rhombohedral units has previously been evidenced by summing HAADF intensity profiles across the units. Here, another methodology was adopted. Annular bright field (ABF) STEM signal has been acquired simultaneously with the HAADF STEM signal. It was hence possible to simply observe the variations of contrast in both images, shown in Figs 3(b,c). It is clear that the signal of Zn columns is almost opposite in ABF and HAADF, rhombohedral Zn units appearing as dark skeletons in the ABF image. On the contrary, Mg atom positions, which are hardly distinguished in HAADF images, appear as small dark points in the ABF image (as pointed by red arrows in Fig. 3(b)). ABF is hence helpful for the determination of complex atomic structure and proves its relevance beyond the simple study of very light atoms (i.e. oxygen and lighter elements).

In Fig. 3(a), a portion of the interface between the MgZn<sub>2</sub>-type 2 precipitate and the matrix is highlighted with a white rectangle. This portion of interface is parallel to a  $\{111\}_{Al}$  plane. It is

Fig. 2



HAADF-STEM images of an Al-Li-Cu alloy (AA 2050) peak aged at 155°C. The images were performed on a JEM-ARM200F equipped with a Schottky field emission gun. The detector ranges were set to 54-220 mrad. Spot size 8C was used with a half convergence angle of 30 mrad. Gaussian smoothing over 4 pixels and Wiener deblurring over 3x3 pixels were performed using the MatLab® image processing toolbox. (a) View along  $\langle 110 \rangle_{Al}$  zone axis, showing various  $T_1$  precipitates lying along different set of  $\{111\}_{Al}$  planes. (b) Enlarged view of image (d) with a superimposition of the structural pattern of  $T_1$ , following the conclusions of Dwyer et al. [20]. (c,d) High resolution HAADF images of a  $T_1$  precipitate performed along  $\langle 110 \rangle_{Al}$  and  $\langle 11-2 \rangle_{Al}$  zone axes respectively. The complex structure of the precipitate/matrix interface is only accessible for the  $\langle 11-2 \rangle_{Al}$  orientation.

noticeable that the structure of this interface is perfectly identical to the one of interfaces shared by  $\text{Al}_2\text{CuLi-T}_1$  precipitates and the Al matrix. Simply, Zn and Mg are substituting to Cu and Li respectively at the interface atomic positions observed in  $T_1$  [20]. Again, the flat interface along  $\{111\}_{\text{Al}}$  is the orientation of the coherent interface in the Al-Zn-Mg system. But here the aspect ratio of precipitates is significantly less compared to  $T_1$ .  $\text{MgZn}_2$ -type 2 precipitates may grow as disks though some of them are more or less globular, offering a very large density of obstacles to the motion of dislocations. The mechanism controlling the evolution of precipitates morphology in the Al-Zn-Mg system has not yet been described although interesting features have recently been reported by Xu et al. [34]. Among Al-based alloys, for equivalent number densities of precipitates, the intrinsic characteristics of precipitates in Al-Zn-Mg alloys confer the largest mechanical strength to this system [35]. This fact can partly be attributed to the mix between coherent and fully incoherent interfaces between precipitates and matrix. In Fig. 3, one can observe the loss of coherence (indicated by "LC" in (a)) along the vertical interface. This loss of coherence, which is systematic for the thickening of  $\text{MgZn}_2$ -type 2 precipitates in this system, inevitably leads to strong anisotropic strain field in the matrix.

The high strength of Al-based alloys is hardly maintained as the temperature of application reaches a critical point, which depends on the alloy system. This is mainly due to the destabilization of the precipitation structure. Such a critical effect of temperature has been investigated here for the same Al-Zn-Mg alloy. For this purpose, the 7449 Al-Zn-Mg alloy in the T7 condition (i.e. previously aged isothermally at  $150^\circ\text{C}$ ) has been placed in a Gatan heating double tilt specimen holder (model 652 with tantalum furnace). Results are presented in Fig. 4.

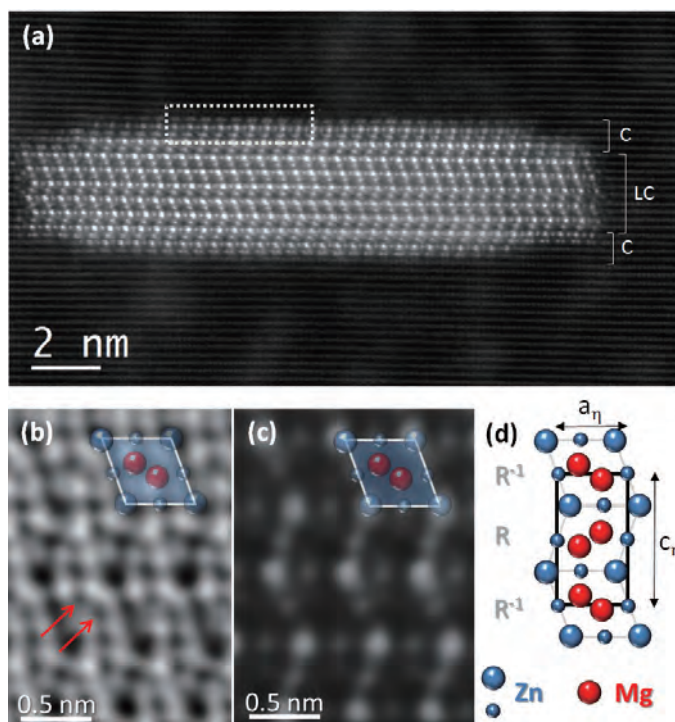
The in situ heating in HAADF STEM mode allowed confirming that the precipitate structure was stabilized by the previous isothermal ageing at  $150^\circ\text{C}$  (T7 condition). At  $170^\circ\text{C}$ , neither any evolution of the precipitate structure nor of its

morphology could be evidenced. On the contrary, short time ageing at  $185^\circ\text{C}$  induces a significant change of morphology, which is even more rapid at  $200^\circ\text{C}$ . It must be mentioned that partial dissolution of numerous of other precipitates could be imaged in the same area of the specimen. Thanks to in situ HAADF STEM, it is possible to follow the evolution of precipitate and to reveal critical phenomena while maintaining sufficient resolution. Here,  $185^\circ\text{C}$  is identified as the critical ageing temperature for which precipitate dissolution occurs. This finding is in perfect agreement with the reversion temperature usually applied to this alloy [33]. Reversion treatment may indeed be applied so as to release a significant proportion of solutes within the matrix, in order to both improve solid solution strengthening while maintaining significant precipitation hardening. Another important potentiality is to tune the corrosion resistance by adjusting the matrix composition [33].

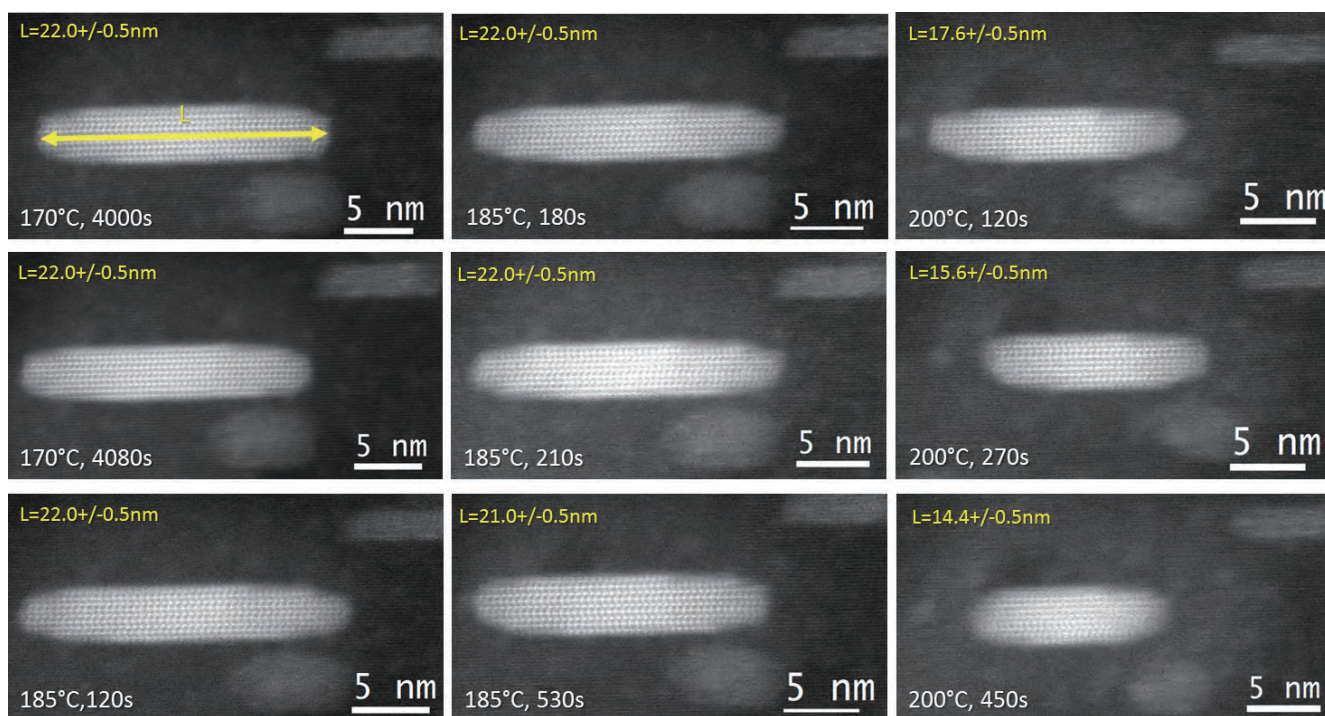
### Phosphorous intergranular segregation in steels

In the following, we are considering another illustration of the relevance of state-of-the art TEM/STEM for the study of alloys of technological interest. The following example is related to the topic of long term reliability of steels under the effect of irradiation. Phosphorous intergranular segregation in steels is known to decrease the cohesion between grains, resulting in steel embrittlement [36–38]. During thermal ageing, this phenomenon is driven by thermodynamics and is called equilibrium segregation. Under irradiation, the supersaturation of vacancies and self-interstitial atoms enhances atom diffusion and can result in enhanced segregation (same level of intergranular segregation than equilibrium one but reached faster). In addition, coupling between fluxes of point defects toward grain boundaries (GB) and solute atoms can increase the steady state level of phosphorous segregated. This kinetics driven segregation is called irradiation induced segregation.

Fig. 3



STEM images performed on a JEM-ARM200F equipped with a cold field emission gun operating at 200 kV. The Al-Zn-Mg alloy was investigated in the overaged condition (Al-Zn-Mg 7449 in the T7 temper, see ref [33] for further information). All images were obtained with a 6C spot size and a semi-convergence angle of 30 mrad, along the  $\langle 11-2 \rangle_{\text{Al}}$  zone axis. Gaussian smoothing over 4 pixels and Wiener deblurring over  $3 \times 3$  pixels were performed using the MatLab® image processing toolbox. (a) HAADF STEM image of "type 2" precipitate, following the designation introduced in [4]. The dotted rectangle highlights the interface structure. On the right, the coherent portions of the interface are pointed by the letter C, whereas the loss of coherence is indicated by LC. (b) Annular bright field image and (c) HAADF STEM image of a region in the inner part of the precipitate. (d) Projected positions of Mg and Zn atoms in the structure, as derived from the previous work reported in [4]. R and  $R^{-1}$  state for symmetric rhombohedral Zn units. The lattice parameter of the  $\eta$ - $\text{MgZn}_2$  cell are respectively  $a_\eta = 0.522$  nm and  $c_\eta = 0.857$  nm.

**Fig. 4**

Evolution of the morphology of a  $MgZn_2$ -type 2 precipitate during in situ heating of the 7449-T7 alloy, as observed in HAADF-STEM along the  $\langle 11-2 \rangle_{Al}$  zone axis. Observations were performed with the JEM-ARM200F equipped with a cold field emission gun operating at 200 kV. Low magnification HAADF STEM images were acquired with a probe size 6C, a semi-convergence angle of 30 mrad and a detector range of 54-220 mrad. The temperature has been gradually increased to 170°C, 185°C and 200°C after holding the specimen at 150°C for 1800 s. On each image, the holding temperature and the holding time are indicated. The measured largest length of the precipitate is reported on each image.

In all cases, the segregation depends of ageing conditions (temperature, irradiation dose...), material (bulk P concentration, competition with other solutes...) and of the grain boundary type (misorientation angle, rotation axis) [39–42].

The low alloyed bainitic steels used to build nuclear reactor pressure vessel (RPV) generally contain a small amount of phosphorous (in the range of 100ppm). In order to ensure the RPV reliability during operation, it is thus important to determine segregation mechanisms under irradiation (enhanced or induced segregation) and to anticipate segregation level as a function of the steel composition and the GB type. This requires developing a methodology to get accurate and representative description of GB from structural and chemical points of view. Atom probe tomography (APT) can give a 3D representation of intergranular segregation and allows to plot concentration profiles exactly through GB and measure chemical composition in well-localized nm-scale area. However, due to spatial lateral resolution and detection efficiency, GB structure cannot be reconstructed. STEM coupled with Energy Dispersive X-ray spectroscopy (EDS) provides information about GB structure and concentration profiles. However, since the information is obtained in transmission, the accuracy of the profile depends of the orientation of GB relative to electron beam. It also depends on the spatial resolution and probe size.

In this work, we are comparing the information provided by both techniques. The material is a Fe-0.02%P (0.038at.%). It was irradiated with 10 MeV  $Fe^{5+}$  ions in JANNUS facilities in Saclay (France), at a temperature of 450°C. Samples were taken from irradiated plates using focused-ion-beam (FIB) lift-out method [43], with the nuclearized Zeiss XB540 from the GENESIS platform in GPM Rouen. They were prepared at a depth of 700 nm below the surface by FIB milling. Considering the damage profile calculated with SRIM software [44], using Kinshin-

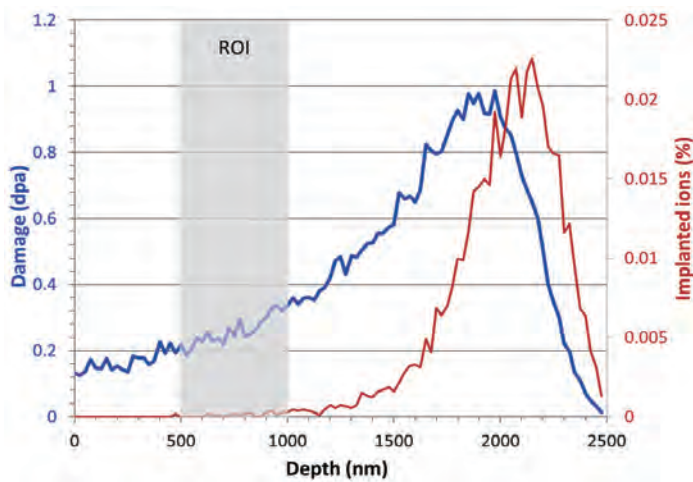
Pease approximation and a displacement threshold energy of 40eV [45], the damage dose is about 0.25 dpa (displacements per atom) in the sample (Fig. 5). It has to be noticed that before the lift-out step, Electron Backscatter Diffraction (EBSD) maps of the surface were plotted in order to localise and extract GB with desired misorientation. The samples (TEM thin foil or APT thin needle) containing desired GB were analysed using a Cameca LEAP 4000 X HR and a JEM-ARM200F (cold FEG) equipped with JEOL Centurio 100 mm<sup>2</sup> SDD EDS detector from GENESIS platform. Figure 6 shows results obtained with each technique on a high angle (41°) general GB. In the TEM image, the GB is detected thanks to crystalline structure whereas it can be distinguished in APT reconstruction thanks to P and C segregation (the model alloy contains about 50 appm of C). These two techniques provide different plus complementary views of the GB.

Concentration profiles were plotted through these GBs. Results are reported in Fig. 6. It appears that the results provided by both techniques about phosphorous level are very consistent. This demonstrates the relevance of STEM EDS when the GB is well oriented. Nevertheless, the limitation of EDS compared to APT in this system concern carbon that cannot be quantified with EDS. With this example, the ability to characterize chemically and structurally a grain boundary by combining EBSD, SEM-FIB, APT and TEM is shown. APT and TEM provide complementary information and give very consistent results.

### Correlative microscopy by Scanning Transmission Electron Microscopy and Atom Probe Tomography

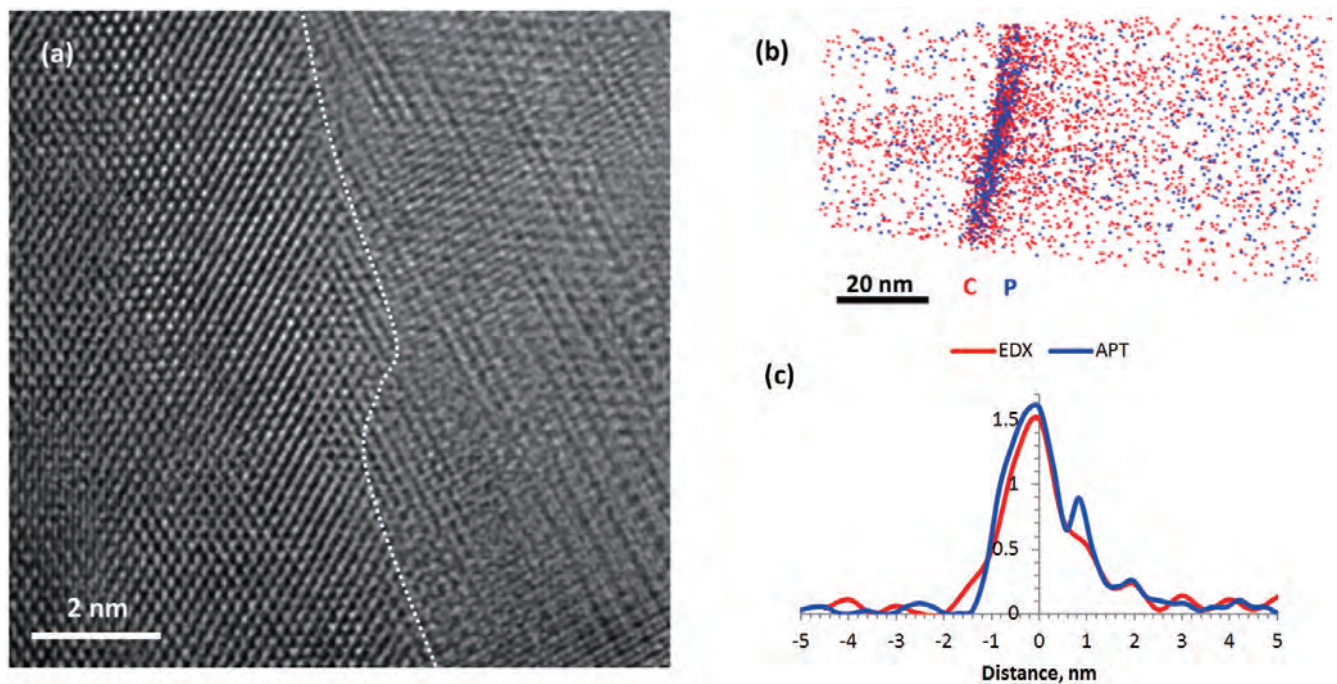
In the following, a second illustration of the particular complementarity of STEM and APT is going to be presented for

Fig. 5



Damage and implantation profiles calculated with SRIM. The region of interest (ROI) from where the samples were taken is in grey.

Fig. 6



(a) HRTEM image showing a GB (highlighted by the dotted line) and (b) APT reconstruction showing C and P atoms in a small volume of irradiated Fe-0.02P model alloy. Intergranular segregation is clearly visible. (c) Comparison of STEM-EDS and APT phosphorous concentration profiles through a high angle general grain boundary  $41^\circ[441](243)/(110)$ .

InGaN-GaN quantum wells (QWs). In the field of photonics and optoelectronics, increased attention is devoted to the problem of determining the relationship between structural and optical properties of nanostructured and nanoscale functional materials. In particular, quantum wells based on the InGaN-GaN systems show high light emission efficiency in the green-UV range [46–48] and have a technological interest as building blocks of visible light-emitting diodes (LEDs) [49–51] and laser diodes [52,53]. In a previous work [54], we have studied non-polar m-plane InGaN QWs extracted by focused ion beam annular milling (FIB) from side facets of InGaN/GaN core shell c-axis microwires through a correlative micro-photoluminescence ( $\mu$ PL), scanning transmission electron microscopy (STEM) and APT approach. APT requires samples to have a needle-like shape with an apex radius lower than  $\sim 100$  nm for the

field evaporation of surface atoms to be possible. The analyzed system was hence extracted through FIB milling from side facets of these InGaN/GaN core-shell c-axis microwires. APT tips for the correlated analysis were obtained through standard FIB annular milling [55]. A 400 nm Si capping layer was deposited on the side facets from which tips were extracted and low beam currents (1–10 pA at 30 kV or 50 pA at 2 kV, angle of incidence  $\sim 4^\circ \pm 2^\circ$ ) were used in order to limit Ga implantation at the surface and degradation of the samples optical properties [56]. We show here the correlated study of self-assembled c-oriented GaN nanowires (NWs) with lateral m-plane facets.

These NWs were grown by metal-organic vapor-phase epitaxy on c-sapphire substrates. The  $n^+$ -doped stems of the wires were grown at  $1040^\circ\text{C}$  using trimethylgallium and ammonia precursors along with silane addition for promoting

the wire geometry. The GaN wire sidewalls were then coated with 20 InGaN layers grown at 750°C using triethylgallium and trimethylindium precursors. The unintentional Si doping induced by the presence of silane during the axial growth remains under the atom probe detection limit ( $<10^{18}\text{cm}^{-3}$ ). A more detailed description of the growth conditions can be found in the literature [57,14].

Combination of carrier states in InGaN QWs leads to light emission. Whereas transition energies in stacks of InGaN QWs in a wire revealed by micro-photoluminescence consist in a continuous spectrum ranging from 2.8 to 3.3 eV, discrete transition energies can be identified when smaller volumes are investigated [14]. Thanks to a combination of micro-photoluminescence, HAADF-STEM observations and APT analysis, it has been possible to establish the relation between the structure and chemistry of InGaN QWs and the energies of radiative combination of carrier states [14]. APT being a destructive technique, observations of specimens in STEM/TEM are inevitably performed prior to APT analysis. **Figure 7** shows an APT specimen consisting of a Si cap and a stack of 9 InGaN QWs separated by GaN barriers. The typical barrier thickness is  $23 \pm 2$  nm. The QWs are brighter zones in HAADF-STEM. STEM-EDS analysis easily points out the alternation of In-rich (in QWs) and Ga-rich regions (in barriers) along the specimen axis. The enlarged view in the inset of Fig. 7(a) reveals that the quantum well interfaces are not equivalent. The interface on the core side is much more abrupt than the one on the surface side. This phenomenon could be linked to the growth technique, in which quantum wells are deposited at a lower temperature than the barriers [57].

A striking feature is the presence of bright lines, which propagate along the whole structure perpendicular to the plane of the QWs, as pointed out by red arrows in Fig. 7(a). By means of high resolution observation in HAADF-STEM mode (Fig. 7(b)), these lines could be identified as stacking faults (SFs) along the a-zone axis of the wurtzite (WZ), which behave as cubic insertions in the hexagonal WZ matrix. The origin of such defects was attributed to strain accumulation and consequent plastic relaxation during the growth process. The continuity of

stacking faults along the wire axis implies that they cross the QWs. It is hence relevant to account for the influence of these defects on the radiative combination energies in QWs. Similar QWs have been analyzed by APT. Figure 7(c) shows a typical 2D-map of In fraction in the plane of QW revealed by APT analysis. Considering both results from APT and STEM allows revealing that In enrichment is observed along the direction of stacking faults, crossing the QWs. Without the correlative investigation by STEM and APT, it would have been impossible to draw such a conclusion. Thanks to this information, calculation of transition energies could be performed [54], which revealed that stacking faults are responsible for a lowering of the recombination energies of the order of 0.1 eV with respect to those expected for defect-free QWs.

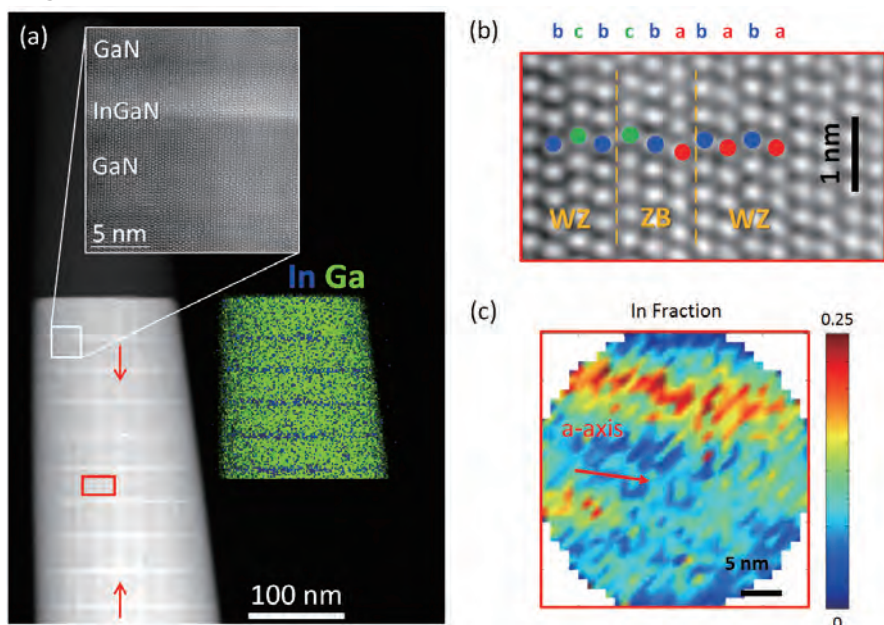
## Conclusion

Though, Atom Probe Tomography and (Scanning) Transmission Electron Microscopes are not yet combined in a single instrument, this perspective would offer new ways of investigating materials, as illustrated in the present paper. Nevertheless, the ultimate capabilities of state-of-the-art aberration corrected (Scanning) Transmission Electron Microscopes offer many perspectives to the study of defects at the sub-nanometer and nanometer scale. There is no doubt that the use of time resolved *in situ* experiments will continue giving access to complex transformation mechanisms for large classes of materials, including alloys.

## Acknowledgments

Part of this work has been funded through projects EMC3 Labex ASAP, ANR-13-JS10-0001-01 Tapoter and ANR JCJC TIPSTEM. GENESIS is supported by the Région Normandie, the Métropole Rouen Normandie, the CNRS via LABEX EMC3 and the French National Research Agency as a part of the program "Investissements d'avenir" with the reference ANR-11-EQPX-0020.

**Fig. 7**



(a) High angle annular dark field (HAADF) STEM image of a set of InGaN/GaN quantum wells in an Atom Probe Tomography specimen. The observations were performed under a JEM-ARM200F microscope equipped with a Schottky field emitter operating at 200 kV. A probe diameter of 0.13 nm was used for HAADF images, with collection angles in the range 70-250 mrad. InGaN QWs are easily identified as brighter contrast sections. STEM EDS analysis on the right shows the alternation of In- or Ga-rich regions in the specimen. Red arrows are pointing lines of brighter contrast along the specimen. (b) Enlarged view of the region indicated by the red rectangle in (a). The higher magnification allows identifying a stacking fault of the wurtzite structure, which coincides with a bright line as pointed by red arrows in (a). Letters a, b and c refer to the stacking sequence of compact planes. WZ and ZB state for wurtzite and zinc blend structures respectively. (c) Fraction of In in a single quantum well, as determined by APT. The In enrichment in the QW is found to follow the orientation of the stacking faults revealed by HAADF-STEM observations.

## References

- [1] M. Haider, H. Rose, S. Uhlemann, E. Schwan, B. Kabius, K. Urban, *Ultramicroscopy* **75** (1998) 53–60.
- [2] P.W. Hawkes, *Ultramicroscopy* **156** (2015) A1–A64.
- [3] F. Zemlin, K. Weiss, P. Schiske, W. Kunath, K.-H. Herrmann, *Ultramicroscopy* **3** (1978) 49–60.
- [4] C.D. Marioara, W. Lefebvre, S.J. Andersen, J. Friis, *J. Mater. Sci.* **48** (2013) 3638–3651.
- [5] M.K. Miller, E.A. Kenik, *Microsc. Microanal.* **10** (2004) 336–41.
- [6] B. Gault, M.P. Moody, J.M. Cairney, S.P. Ringer, Springer *Ser. Mater. Sci.* (2012) 396.
- [7] W. Lefebvre-Ulrikson, F. Vurpillot, X. Sauvage, Atom Probe Tomography Put Theory into Practice, Academic Press, 2016.
- [8] D. Larson, T. Prosa, R. Ulfig, B. Geiser, T. Kelly, Local Electrode Atom Probe Tomography, 2013.
- [9] M.K. Miller and R.G. Forbes, Atom-Probe Tomography - The Local Electrode Atom Probe, 2014.
- [10] I. Arslan, E.A. Marquis, M. Homer, M.A. Hekmaty, N.C. Bartelt, *Ultramicroscopy* **108** (2008) 1579–1585.
- [11] M. Herbig, D. Raabe, Y.J. Li, P. Choi, S. Zaefferer, S. Goto, *Phys. Rev. Lett.* **112** (2013) 1–5.
- [12] M. Kuzmina, M. Herbig, D. Ponge, S. Sandlobes, D. Raabe, *Science* (80-. ) **349** (2015) 1080–1083.
- [13] W. Lefebvre, D. Hernandez-Maldonado, F. Moyon, F. Cuvilly, C. Vaudolon, D. Shinde, F. Vurpillot, *Ultramicroscopy* **159** (2015) 403–412.
- [14] L. Rigutti, I. Blum, D. Hernández-Maldonado, W. Lefebvre, J. Houard, F. Vurpillot, A. Vella, M. Tchernycheva, C. Durand, J. Eymery, B. Deconihout, *Nano Lett.* **14** (2014) 107–114.
- [15] A. Wilm, *Metall. Zeitschrift Für Gesamte Hüttenkd.* **8** (1911) 225–227.
- [16] A. Guinier, *Nature* **142** (1938) 569–570.
- [17] G.D. Preston, *Nature* **142** (1938) 570.
- [18] M. Karlík, B. Jouffrey, S. Belliot, *Acta Mater.* **46** (1998) 1817–1825.
- [19] W. Lefebvre, V. Kopp, C. Pareige, *Appl. Phys. Lett.* **100** (2012) 141906.
- [20] C. Dwyer, M. Weyland, L.Y. Chang, B.C. Muddle, *Appl. Phys. Lett.* **98** (2011).
- [21] P.H. Ninive, A. Strandlie, S. Gulbrandsen-Dahl, W. Lefebvre, C.D. Marioara, S.J. Andersen, J. Friis, R. Holmestad, O.M. Løvvik, *Acta Mater.* **69** (2014) 126–134.
- [22] P. Donnadieu, Y. Shao, F. De Geuser, G.A. Botton, S. Lazar, M. Cheynet, M. De Boissieu, A. Deschamps, *Acta Mater.* **59** (2011) 462–472.
- [23] M. Guérin, J. Alexis, E. Andrieu, L. Laffont, W. Lefebvre, G. Odemer, C. Blanc, *Corros. Sci.* **102** (2016) 291–300.
- [24] W. Lefebvre, N. Masquelier, J. Houard, R. Patte, H. Zapolsky, *Scr. Mater.* **70** (2014) 43–46.
- [25] T. Saito, F.J.H. Ehlers, W. Lefebvre, D. Hernandez-Maldonado, R. Bjørge, C.D. Marioara, S.J. Andersen, E.A. Mørtsell, R. Holmestad, *Scr. Mater.* **110** (2016) 6–9.
- [26] S.J. Andersen, H.W. Zandbergen, J. Jansen, C. Trøholt, U. Tundal, O. Reiso, *Acta Mater.* **46** (1998) 3283–3298.
- [27] G. a. Edwards, K. Stiller, G.L. Dunlop, M.J. Couper, *Acta Mater.* **46** (1998) 3893–3904.
- [28] M. Murayama, K. Hono, *Acta Mater.* **47** (1999) 1537–1548.
- [29] H.S. Hasting, A.G. Frøseth, S.J. Andersen, R. Vissers, J.C. Walmsley, C.D. Marioara, F. Danoix, W. Lefebvre, R. Holmestad, *J. Appl. Phys.* **106** (2009) 123527.
- [30] E. Gumbmann, W. Lefebvre, F. De Geuser, C. Sigli, A. Deschamps, *Acta Mater.* **115** (2016) 104–114.
- [31] A. Ardell, *Metall. Trans. A* **16** (1985) 2131–2165.
- [32] Y. Komura, K. Tokunaga, IUCr, *Acta Crystallogr. Sect. B Struct. Crystallogr. Cryst. Chem.* **36** (1980) 1548–1554.
- [33] B.B. T. Marlaud, A. Deschamps, F. Bley, W. Lefebvre, *Acta Mater.* **58** (2010) 4814–4826.
- [34] X. Xu, J. Zheng, Z. Li, R. Luo, B. Chen, *Mater. Sci. Eng. A* **691** (2017) 60–70.
- [35] I.J. Polmear, Light Alloys, Elsevier, 2005.
- [36] Z. Lu, R.G. Faulkner, P.E.J. Flewitt, *Mater. Sci. Eng. A* **437** (2006) 306–312.
- [37] S.-H. Song, H. Zhuang, J. Wu, L.-Q. Weng, Z.-X. Yuan, T.-H. Xi, *Mater. Sci. Eng. A* **486** (2008) 433–438.
- [38] J. Kameda, Y. Nishiyama, *Mater. Sci. Eng. A* **528** (2011) 3705–3713.
- [39] A.J. Ardell, in: V. Ghetta, D. Gorse, D. Mazzière, V. Pontikis (Eds.), *Mater. Issues Gener. IV Syst.*, Springer Netherlands, Dordrecht, 2008, pp. 285–310.
- [40] M. Nastar, F. Soisson, in: R.J.M. Konings (Ed.), *Compr. Nucl. Mater.*, Elsevier, Oxford, 2012, pp. 471–496.
- [41] H. Erhart, H.J. Grabke, *Scr. Metall.* **15** (1981) 531–534.
- [42] P. Lejček, S. Hofmann, K. Bunshaw, *Encycl. Mater. ...* (2002) 1–7.
- [43] L.A. Giannuzzi, F.A. Stevie, eds., *Introduction to Focused Ion Beams*, Kluwer Academic Publishers, Boston, 2005.
- [44] J.F. Ziegler, J.P. Biersack, in: D.A. Bromley (Ed.), *Treatise Heavy-Ion Sci.*, Springer US, Boston, MA, 1985, pp. 93–129.
- [45] A. E521, *Astm, Annu. B. ASTM Stand.* **12.02** (2009) 1–21.
- [46] M. Kneissl, T. Kolbe, C. Chua, V. Kueller, N. Lobo, J. Stellmach, A. Knauer, H. Rodriguez, S. Einfeldt, Z. Yang, N.M. Johnson, M. Weyers, *Semicond. Sci. Technol.* **26** (2011) 14036.
- [47] M. Wölz, J. Lähnemann, O. Brandt, V.M. Kaganer, M. Ramsteiner, C. Pfüller, C. Hauswald, C.N. Huang, L. Geelhaar, H. Riechert, *Nanotechnology* **23** (2012) 455203.
- [48] M.A. Sousa, T.C. Esteves, N. Ben Sedrine, J. Rodrigues, M.B. Lourenço, A. Redondo-Cubero, E. Alves, K.P. O'Donnell, M. Bockowski, C. Wetzel, M.R. Correia, K. Lorenz, T. Monteiro, *Sci. Rep.* **5** (2015).
- [49] W.S. Wong, T. Sands, N.W. Cheung, M. Kneissl, D.P. Bour, P. Mei, L.T. Romano, N.M. Johnson, *Appl. Phys. Lett.* **75** (1999) 1360.
- [50] M. Yamada, Y. Narukawa, T. Mukai, *Jpn. J. Appl. Phys.* **41** (2002) L246–L248.
- [51] Y.-K. Kuo, J.-Y. Chang, M.-C. Tsai, S.-H. Yen, *Appl. Phys. Lett.* **95** (2009) 11116.
- [52] S. Nakamura, M. Senoh, S. Nagahama, N. Iwasa, T. Yamada, T. Matsushita, Y. Sugimoto, H. Kiyoku, *Appl. Phys. Lett.* **69** (1996) 4056.
- [53] Y. Taniyasu, M. Kasu, T. Makimoto, *Nature* **441** (2006) 325–328.
- [54] L. Mancini, D. Hernández-Maldonado, W. Lefebvre, J. Houard, I. Blum, F. Vurpillot, J. Eymery, C. Durand, M. Tchernycheva, L. Rigutti, *Appl. Phys. Lett.* **108** (2016) 42102.
- [55] M.K. Miller, K.F. Russell, K. Thompson, R. Alvis, D.J. Larson, *Microsc. Microanal.* **13** (2007) 428–436.
- [56] L. Rigutti, A. Vella, F. Vurpillot, A. Gaillard, N. Sevelin-Radiguet, J. Houard, A. Hideur, G. Martel, G. Jacopin, A. De Luna Bugallo, B. Deconihout, *Ultramicroscopy* **132** (2013) 75–80.
- [57] R. Koester, J.-S. Hwang, D. Salomon, X. Chen, C. Bougerol, J.-P. Barnes, D.L.S. Dang, L. Rigutti, A. de Luna Bugallo, G. Jacopin, M. Tchernycheva, C. Durand, J. Eymery, *Nano Lett.* **11** (2011) 4839–4845.

# Quantitative STEM-EELS Characterizations of Oxide Superlattices and Atomic-Scale Electron Spectroscopy at 100 K at National Taiwan University

Pei-Wei Lee,<sup>1</sup> Ming-Hao Lee,<sup>1</sup> Shih-Chi Lee,<sup>1</sup> Chin-Ping Chang,<sup>1</sup> Yi-Chen Lai,<sup>1</sup>  
Guang-Yu Guo,<sup>2</sup> Ying-Hao Chu,<sup>3</sup> Wei-Li Lee,<sup>4</sup> Cheng Hsuan Chen,<sup>1</sup> and Ming-Wen Chu<sup>1</sup>

<sup>1</sup> Center for Condensed Matter Sciences, National Taiwan University, Taiwan

<sup>2</sup> Department of Physics, National Taiwan University, Taiwan

<sup>3</sup> Department of Materials Science and Engineering, National Chiao Tung University, Taiwan

<sup>4</sup> Institute of Physics, Academia Sinica, Taiwan

With the modern advance in thin-film growth techniques, oxide superlattices with superb interface quality have become available and can manifest a plethora of interfacial phenomena that do not exist in the bulk counterparts. Why there shall be the emergent two-dimensional states represents an outstanding problem in the context and demands for experimental probing across the heterointerfaces at quantitative atomic accuracy. The atomically-resolved electron energy-loss spectroscopy (EELS) in conjunction with scanning transmission electron microscopy (STEM) is an ideal tool in this regard and pushing the corresponding quantitative atomic limit has been continuously under developments. The onset of the two-dimensional ground states can also take place at low temperatures. The STEM-EELS characterization at low-temperature regimes without compromising atomic resolution is hence important, while largely unexplored. Here, we report our efforts for quantitative STEM-EELS tackling of oxide heterostructures at room temperature and preliminary results on atomic-scale chemical mapping at 100 K. The perspectives on both technological advances are briefly discussed.

## Introduction

The birth of aberration-corrected STEM optics reduces the electron-probe size down to sub-angstrom scale and, meanwhile, increases the probe current by folds of magnitude, opening up vast opportunities for the STEM-EELS spectral mapping of individual atomic columns in crystals and also single atoms [1-4]. The spectral probing at such high spatial resolution has been challenging in the past [5]. Nowadays, seeing atomic features with the simultaneous addressing of their electronic-excitation characteristics rather becomes a routine [1-4]. Understanding materials science, chemistry, and physics from unprecedented atom-by-atom aspects turns out to be possible and would be particularly essential for phenomena that occur at a finite length scale [6-9], the characterizations of which using typical bulk techniques can only deliver limited and average information. An outstanding exemplification within the framework is the tackling of emergent oxide-interfacial states [7-10].

Indeed, the interface of oxide heterostructures can display a broad spectrum of novel properties, ranging from two-dimensional electron gas (2DEG) between two insulators

[11, 12], interfacial magnetism between two non-magnetic materials [13, 14], to two-dimensional superconductivity out of the heterojunction between two insulating substances [15, 16]. Among these distinct properties, the 2DEG between insulating LaAlO<sub>3</sub> (LAO) and SrTiO<sub>3</sub> (STO) stands for the most renowned example considering that it opens the area of oxide electronics that could be complementary to the grand classics of semiconductor electronics [17, 18]. For the oxide electronics to come true, it is nonetheless crucial for capturing why there shall be the metallic LAO/STO interface, which is the model system in all oxide heterostructural engineering [7-18].

In LAO/STO, it is generally accepted that the 2DEG resides in the STO substrate with a length scale of few nanometers [11-18]. With such a finite distance from the interface, effects of chemical intermixing, misfit strain, and atomic-plane charge mismatch (so-called polar discontinuity) on the 2DEG formation shall be considered [19-21], and oxygen vacancies constitute an otherwise factor [22]. To unambiguously resolve the 2DEG origin, a simultaneous scrutiny of the chemical, structural, and electronic degrees of freedom across the interfacial unit cells (uc) at quantitative atomic accuracy is

readily indispensable [7-9]. Using the simple methodology of statistical improvements by summing up numerous STEM-EELS and high-angle annular dark-field (HAADF) imaging datasets, the current group of authors have demonstrated the atomic-precision quantification of length scale and carrier density of 2D oxide-interfacial states [7-9] and also that of structural distortions of the corresponding interfacial uc [9]. The 2DEG in LAO/STO was found to arise from the strain rejuvenation of head-to-head ferroelectric (FE)-like polarizations across the interface, with the associated depolarization fields casting the interface into an electron reservoir. The 2DEG readily appears in the STO for electrostatic screening of the divergent polarizations and the complementary holes for the 2DEG localize in the LAO [9]. The role of chemical intermixing, polar discontinuity, and oxygen vacancies were discounted [9].

Indeed, the LAO/STO represents a vivid example of the strain activation of unexpected physics [9]. Upon the subtle change of strain and electrostatic boundary conditions in the LAO/STO, it is then intriguing about what would happen to the 2DEG. Hereby, we report our first examinations of the idea using  $\text{Pb}(\text{Zr}_{0.2}\text{Ti}_{0.8})\text{O}_3/\text{LAO}/\text{STO}$  superlattices, with the ferroelectric  $\text{Pb}(\text{Zr}_{0.2}\text{Ti}_{0.8})\text{O}_3$ , PZT, overlayer intended for altering the inherent mechanical and electrostatic balances in the LAO/STO [23]. Moreover, we explored the possibility of atomically-resolved STEM-EELS chemical mapping at 100 K with encouraging preliminary results.

## Experimental

The PZT(40 nm)/LAO(6 uc)/STO superlattices were grown by pulsed-laser depositions using  $\text{TiO}_2$ -terminated substrates, with the growth detail elucidated in Ref. 23. Using scanning probe switching, the polarization (P) direction of the PZT points to the PZT surface (P+) in one superlattice and points away from the surface (P-) in the other. We investigated both the PZT(P+)/LAO/STO and PZT(P-)/LAO/STO samples in this work. The STEM-EELS probing and HAADF imaging were conducted on spherical-aberration corrected JEOL 2100FX operated at 200 keV and equipped with a Gatan Efsim EELS spectrometer, with the electron-probe size of 0.9~1 Å, the respective HAADF and STEM-EELS collection angles of 70-190 and 30 mrad, and the specimen thickness of 0.3~0.6  $\lambda$  ( $\lambda$ , inelastic mean-free path) [7-9, 24]. The JEOL liquid-nitrogen holder (EM-31660) was exploited in the low-temperature experiments. The conventional mechanical polishing and Ar-ion milling were used to prepare the specimens [7-9, 24].

## Results and Discussion

The HAADF images of the two PZT(P+)/LAO/STO and PZT(P-)/LAO/STO heterostructures are shown in Figs. 1(a) and 1(b), respectively. Fig. 1(c) exhibits the epitaxial strain scheme in the superlattices considering the cubic STO lattice parameter of  $a_{\text{STO}} = 3.905$  Å [9], quasi-cubic LAO of  $a_{\text{LAO}} = 3.79$  Å [9], and tetragonal PZT of  $a_{\text{PZT}} = 3.95$  Å and  $c_{\text{PZT}} = 4.15$  Å [25]. Upon the epitaxial clamping of *ab*-plane by the STO substrate [9, 26], the LAO (PZT) would be subject to tensile (compressive) strain as shown in Fig. 1(c).

Compared to the pristine LAO/STO, the system of PZT/LAO/STO adds on two complexities by (i) the electrostatically degenerate P+ and P- (Figs. 1(a) and 1(b)) and (ii) the sandwiched strain condition (Fig. 1(c)). We first focus on the strain effect of PZT.

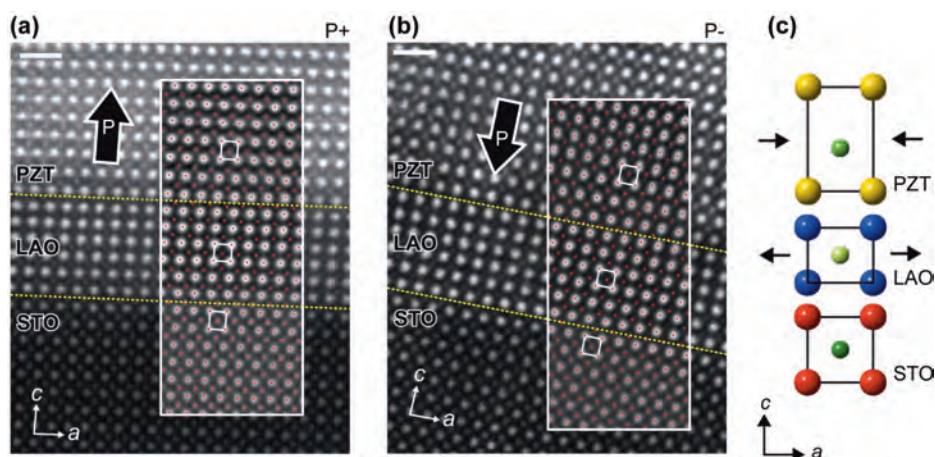
Due to the significant PZT overlayer of 40 nm, the superlattices are, in effect, subject to notable epitaxial-strain energy (linearly scaling with the PZT thickness) [9, 26] and, therefore, misfit dislocations appear in the heterostructures as a strain relaxation mechanism [27]. A careful examination of the dislocation spacing, however, indicated that the dislocations are randomly distributed [27] instead of being regularly spaced by ~34 nm in a fully strain-relaxed system [8, 26]. The PZT(P+)/LAO/STO and PZT(P-)/LAO/STO are hence not homogeneously strained owing perhaps to the significant accumulated strain energy and/or growth subtleties [8, 9, 26] and show a combination of elastically-strained regions (Figs. 1(a) and 1(b)), dislocation areas, and also azimuthally-rotated nanocrystallites [27]. Considering such structural imperfections, the elaborations below are for revealing the usefulness of quantitative characterizations with atomic precision, but not for rigorously comparing to the physics of pristine LAO/STO.

Figures 1(a) and 1(b) were acquired on two separate samples in regions far away from the misfit dislocations and misoriented crystallites (dashed yellow lines, the interfaces; black arrows, the polarization directions). The embedded white-boxed areas demonstrate the peak-pair analysis (PPA) of the images in order to capture the atomic-column coordinates therein at subpixel accuracy (red points) [9]. The nominal pixel size is 0.36 Å and the thorough statistical evaluation of the PPA results like that in Ref. 9 led to the estimated atomic-column determination precision of ~0.05 Å in this current exemplification. This noticeably improved precision enables the in-depth structural characterizations of Figs. 1(a) and 1(b) in Fig. 2.

Figure 2(a) shows the lattice-parameter characteristics of

**Fig. 1**

HAADF images of (a) PZT(P+)/LAO/STO and (b) PZT(P-)/LAO/STO, with 6 uc of LAO and 40 nm of PZT. Yellow dashed lines, the interfaces. Black arrows, the nominal polarization (P) directions. Embedded images, the PPA characterizations with the red dots for the subpixel capturing of the atomic-column positions. Scale bars, 1 nm. (c) The schematic epitaxial strains in the superlattices, with the tensile strain for LAO and the compressive strain for PZT. Oxygen, omitted for simplicity.



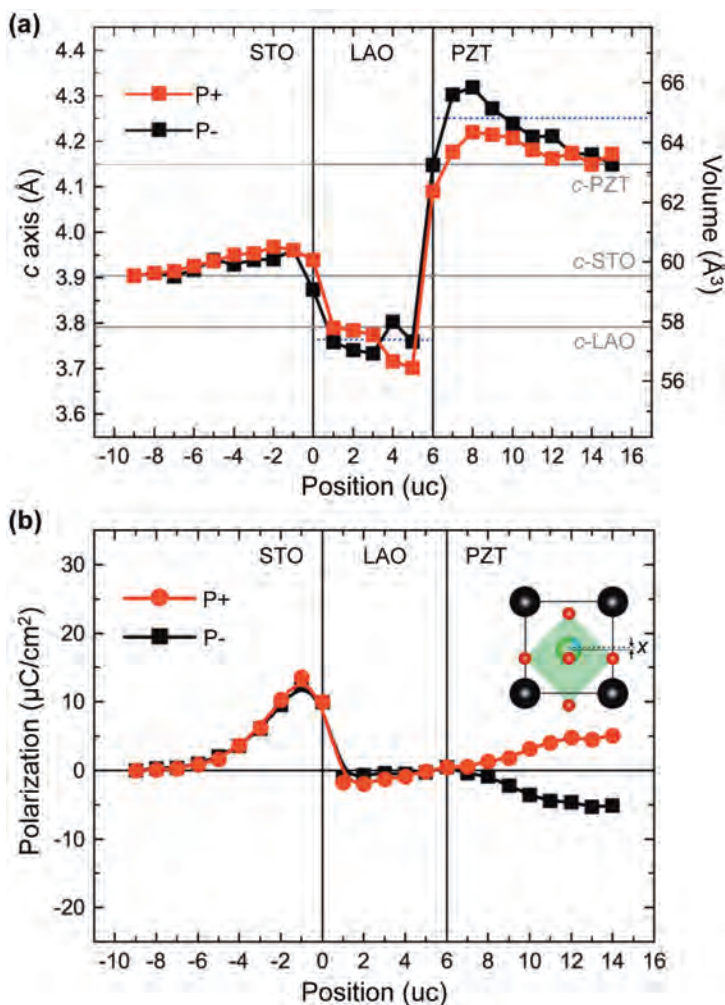
Figs. 1(a) and 1(b) along  $c$ -axis, with the  $ab$ -plane clamped to that of the STO. The gray solid lines denote the nominal  $c$ -axes of STO, LAO, and PZT and the blue dashed lines indicate the tensile- and compressive-strained  $c$ -axis parameters of LAO and PZT considering the respective Poisson's ratios of 0.24 [21] and 0.31 [28]. Several remarkable features appear in Fig. 2(a). Firstly, the interfacial STO uc are elongated along  $c$ -axis within a length scale of 8 uc, while the substrate uc are not supposed to be strained in accordance with the established wisdom on epitaxy [9]. Secondly, the  $c$ -axis of interfacial LAO uc can be noticeably shorter than the nominally tensile-strained value (blue dashed, Fig. 2(a)). Thirdly, the  $c$ -elongated PZT by the compressive strain (Fig. 1(c)) relaxes to the nominal 4.15 Å within 8~9 uc from the LAO/PZT interface.

Due to the comparable elastic constants of STO and LAO (respective Young's moduli of 330 and 306 GPa), the materials are rather equally hard (or soft) and the lattice misfit would strain both of the materials when growing one on top of the other, in stark contrast to the classical epitaxy of straining the film materials only [9, 26]. The characteristic strain-accommodation mechanism in pristine LAO/STO was found to be the simultaneous  $c$ -elongation of the STO and LAO [9]. The observed  $c$ -elongated STO in Fig. 2(a) can then be associated with the reported strain accommodation [9]. However, we did not observe the accompanied  $c$ -elongation of the interfacial LAO uc. Considering the Young's modulus of PZT (105 GPa [28]),

the material would be too soft to noticeably strain the LAO as the current observations in Fig. 2(a). The shrunk  $c$ -parameter of the LAO could thus be due to the squeezing by the heavy PZT overlayer (nearly 100 uc), representing an intriguing example barely discussed in the literature [9, 23, 26]. Moreover, the relaxation of PZT back to the nominal  $c$ -parameter within just few uc from the interface is at odds with the conventional epitaxy, which would depict  $c$ -elongation throughout the PZT uc [26]. All these structural characteristics in Fig. 2(a) point out that the classical thin-film epitaxy (Fig. 1(c)) can turn out to be far more complicated in reality and precise uc-by-uc structural characterizations like the presently demonstrated Fig. 2(a) are critical for unveiling the associated detail.

In Fig. 2(b), we further elaborated on the FE-like polarization across all interfacial uc using the off-center displacements of Sr, Ti, Al, and (Zr, Ti) columns correlated with Fig. 2(a) and the point-charge approximation of  $P = qx/V$ , where  $q$  is the nominal charge of the cation,  $V$  is the individual uc volume, and  $x$  is the cation off-center displacement along  $c$ -axis as schematized in the inset for PZT [9]. The oxygen contribution to  $P$  in the STO and LAO is ignorable due to the characteristic antiferrodistortive buckling of the octahedra [9]. For simplicity, we also omitted the oxygen contribution to  $P_{\text{PZT}}$  in Fig. 2(b), since it does not change the sign of  $P_{\text{PZT}}$ , which is the central measure hereby with the positive (negative) sign for the  $P_{\text{PZT}}$  pointing to (away from) the PZT surface. Remarkably, the nominal P+ and P-

Fig. 2



(a) The quantitative PPA-derived characterizations of the  $c$ -axis parameters in the PZT(P+)/LAO/STO and PZT(P-)/LAO/STO superlattices, with the corresponding uc volumes being denoted as well ( $ab$ -plane clamped to that of the substrate STO). Gray lines, the respective primitive  $c$ -axis parameters of STO, LAO and PZT. Blue dashed lines, the nominal tensile- and compressive-strained  $c$ -axis parameters of LAO and PZT, respectively. (b) The estimated polarizations in all interfacial uc. Inset, the schematized off-center (Zr,Ti) displacement,  $x$ , in the PZT. Red, PZT(P+)/LAO/STO; black, PZT(P-)/LAO/STO. Error bars corresponding to the  $\sim 0.05$ -Å structural-determination precision invisible in the scales of the figures, thus omitted.

directions (black arrows, Figs. 1(a) and 1(b)) are captured by our quantitative  $P_{\text{PZT}}$  estimations in Fig. 2(b), demonstrating again the physical significance of our PPA-derived characterization method at  $\sim 0.05\text{-}\text{\AA}$  precision.

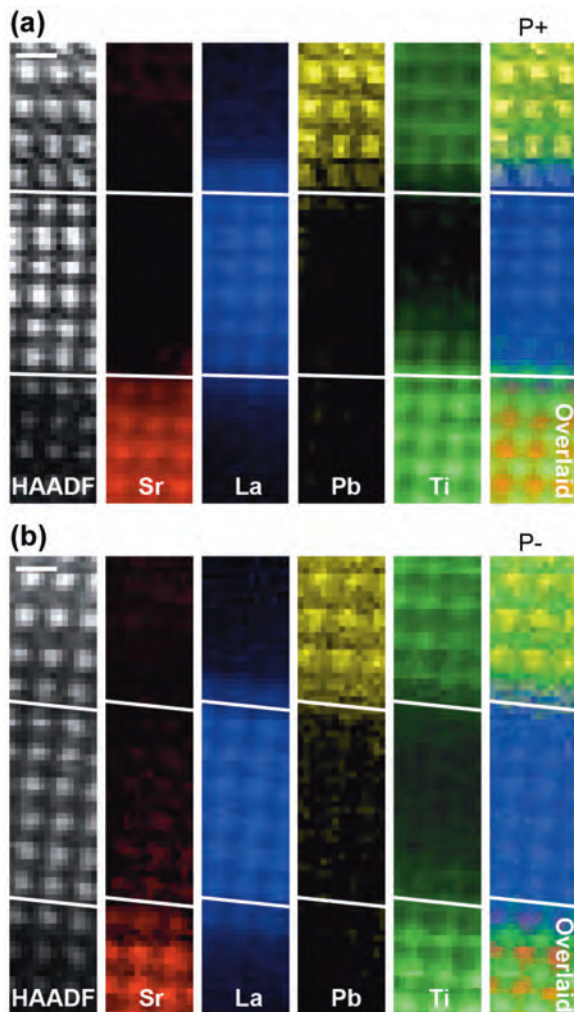
In pristine LAO/STO, the existence of head-to-head  $P_{\text{STO}}$  and  $P_{\text{LAO}}$  (i.e., both pointing to the LAO/STO interface) has been known to be the product of the characteristic strain accommodation [9]. In Fig. 2(b), we did observe the  $P_{\text{STO}}$ , while the primitively accompanied  $P_{\text{LAO}}$  is almost suppressed by the heavy PZT overlayer. In addition, the sign of  $P_{\text{PZT}}$  (P+ and P-, Fig. 2(b)) hardly affects that of the  $P_{\text{STO}}$ , altogether suggesting that in these elastically-strained areas the effect of the PZT is mainly mechanical (squeezing the LAO) and the electrostatic polarity of PZT (P+ and P-) plays an ambiguous role, instead, as discussed below.

**Figure 3** shows the STEM-EELS chemical mapping of PZT(P+)/LAO/STO in (a) and PZT(P-)/LAO/STO in (b) using the Sr- $M_3$  (269 eV), La- $M_4$  (849 eV), Pb- $N_{4,5}$  (413 eV), and Ti- $L_2$  (462 eV) edges. The mapping of the weak spectral features of Sr and Pb was subtle, but doable [7-9]. Obviously, chemical intermixing occurs across all interfaces due to the growths at elevated temperatures [9, 19]. The nominal compositions of respective STO, LAO, and PZT interfacial uc thus become (Sr,La)(Ti,Al)O<sub>3</sub>, (La,Sr,Pb)(Al,Ti,Zr)O<sub>3</sub>, and (Pb,La)(Zr,Ti,Al)O<sub>3</sub> empirically [27]. Using the summation of 5 STEM-EELS datasets with comparable quality to Fig. 3, we

have estimated the interfacial-uc compositions [7-9, 27] that were used in the uc-by-uc charge derivations in later Fig. 4(c). The estimations of Al and Zr, of which the related edges are too deep to be accessed by our conventional EELS spectrometer, have been accounted for by the formulation of (1 - Ti) taking into account our high confidence level in the Ti quantification [7-9].

The atom-by-atom probing of the Ti edge across the LAO/STO (red) and PZT/LAO (orange) interfaces in the two sets of PZT(P+)/LAO/STO and PZT(P-)/LAO/STO is exhibited in **Figs. 4(a)** and **4(b)**, respectively, with the incorporation of the Ti<sup>3+</sup> reference (Ti<sub>2</sub>O<sub>3</sub>). In PZT(P+)/LAO/STO (Fig. 4(a)), the STO interfacial uc manifest noticeable chemical shifts toward Ti<sup>3+</sup>. By contrast, the Ti<sup>3+</sup> feature in the STO counterparts in PZT(P-)/LAO/STO (Fig. 4(b)) is weaker. In the interfacial LAO and PZT uc of PZT(P+)/LAO/STO (Fig. 4(a)) and PZT(P-)/LAO/STO (Fig. 4(b)), the Ti cations are notably Ti<sup>3+</sup>-like for both. This Ti<sup>3+</sup>-like tendency in the PZT (Figs. 4(a) and 4(b)) is largely unexpected considering the FE PZT shall robustly feature Ti<sup>4+</sup>, otherwise lossy due to the associated electron doping [23]. Indeed, PZT can be prone to oxygen-vacancy formations upon growths [26] and an electron doping by the defects is plausible hereby. It is otherwise notable that the characteristic crystal-field, so-called  $t_{2g}-e_g$ , splitting of the Ti edge in the perovskites is broaden in the LAO and PZT and typically induced by strains [7, 8], electronically revealing the strained states of the materials discussed in Fig. 2. The Ti<sup>3+</sup> ratio in all interfacial uc was also

**Fig. 3**



STEM-EELS chemical maps of Sr, La, Pb, and Ti in (a) PZT(P+)/LAO/STO and (b) PZT(P-)/LAO/STO, with the simultaneous HAADF and overlaid maps being also incorporated. White lines, the LAO/STO interface (lower) and the PZT/LAO interface (higher). Scale bars, 4 Å.

evaluated using a linear least-square fitting with the  $Ti^{3+}$  and  $Ti^{4+}$  (bottom STO, Figs. 4(a) and 4(b)) references [7-9]. With these compositional (Fig. 3 [27]) and electronic ( $Ti^{3+}$ , Figs. 4(a) and 4(b)) details, the uc-by-uc charge variations can be derived and is shown in Fig. 4(c).

In Fig. 4(c), there exist 2D electron densities in the STO and PZT of both PZT(P+)/LAO/STO and PZT(P-)/LAO/STO, and the interfacial LAO uc otherwise host appreciable 2D holes. Regardless of P+ and P- (Fig. 4(c)), the PZT uc in the two superlattices are all electron doped, revealing that the 2D electron densities are anyhow irrelevant with electrostatic screening for the PZT polarizations (requiring charges with opposite signs) and, therefore, could be indeed contributed by oxygen vacancies. By contrast, the respective 2D electron and hole densities on the STO and LAO sides show an intricate dependence on P+ and P- (Fig. 4(c)). The charge densities in the STO and LAO shall, however, not be related to any electrostatic-screening essence for the P+ and P- considering the screening of P+ would require more 2D holes in the LAO, at odds with the experimental observations in Fig. 4(c). As indicated above (Fig. 2(b)), the effect of the PZT overlayer is principally mechanical, but not electrostatic, and the electronic scrutiny in Fig. 4(c) is consistent with this argument. Indeed, what led to the subtle charge variations in PZT(P+)/LAO/STO and PZT(P-)/LAO/STO is currently unclear and would demand for further atomically-precise quantitative studies of the heterojunctions with coherent interfaces free from dislocations and crystallographic misorientations, which are nonetheless separate works on their owns.

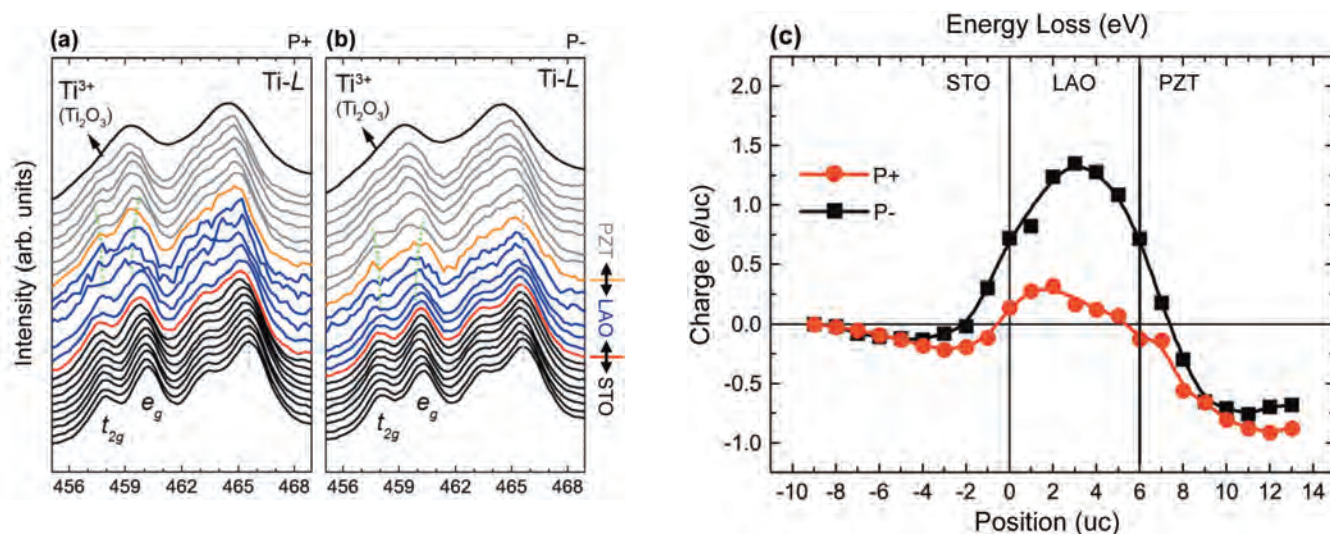
Now, we turn to STEM-EELS at liquid-nitrogen temperature. Due to thermal radiation, the minimal achievable temperature of our liquid-nitrogen holder is 100 K. In Fig. 5(a), we show the [010]-projected HAADF images of STO using the holder at room temperature (RT), with the acquisition time of 8 and 68 s (inset). Despite the stability concern due to the heavy Dewar tank, the RT imaging (Fig. 5(a)) is remarkably stable upon our further in-house mechanical reinforcements. More surprisingly, the HAADF imaging of STO at 100 K for the prolonged

acquisition condition of 68 s gave rise to recognizable lattice contrasts as shown in Fig. 5(b) (uc rotated by  $\sim 45^\circ$ , compared to Fig. 5(a)), with the corresponding fast Fourier transform in the inset indicating a resolution of  $\sim 1.38 \text{ \AA}$  (220-type reflections; otherwise  $\sim 1 \text{ \AA}$  at RT, Fig. 5(a)). A stability of this level at 100 K (Fig. 5(b)) is considerable and facilitates the further STEM-EELS exploration at the temperature [2]. Figure 5(c) shows the simultaneously acquired HAADF imaging of the STEM-EELS map of Ti in Fig. 5(d) at 100 K (pixel time, 60 ms; acquisition time plus readout,  $\sim 84 \text{ s}$ ). Within the 84 s, the STO uc remain resolvable (Fig. 5(c)) and the Ti map (Fig. 5(d)) indeed reveals atomic features as shown in the line profile (along dashed white line, Fig. 5(d)) in Fig. 5(e) with oscillating maxima characteristic of atomic probing. These first results in Fig. 5 pave the avenue to STEM-EELS characterizations of the rich electronic phase diagrams in solids at low temperatures [7, 17, 18], of which the atomic-scale study like Figs. 1-4 is unachieved in the past and represents a fertile ground to explore in the near future.

## Conclusion

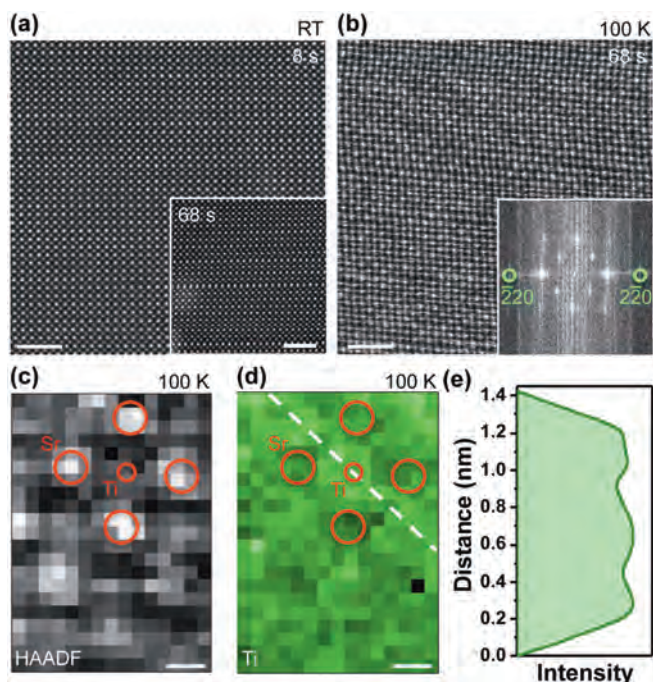
Quantitative structural and electronic characterizations at atomic accuracy are increasingly important for modern materials with reduced dimensions and emergent phenomena at buried interfaces and/or with a finite length scale. There had been concerns on how precise and how far the quantitative probing can go. In this work, we demonstrate the lifting of such concerns using quantitative STEM and EELS elaborations, which are as straightforward as acquiring high-stability datasets and then summing them up for statistics improvements. The STEM-EELS probing at low temperatures with atomic resolution is actively tested worldwide and believed to be challenging. We demonstrate the satisfactory first results on atomic-scale STEM-EELS mapping at 100 K hereby. With our ongoing stability improvements at 100 K, atomic-scale investigations of low-temperature ground states shall become achievable, possibly shedding new light on versatile unresolved outstanding problems.

Fig. 4



The Ti-L edge spectra across the interfaces in (a) PZT(P+)/LAO/STO and (b) PZT(P-)/LAO/STO. Red (orange), the spectrum at the LAO/STO (PZT/LAO) interface. Green, the broadening of the characteristic crystal-field splitting. The  $Ti^{3+}$  reference ( $Ti_2O_3$  powders) is incorporated for revealing the chemical-valence changes in the superlattices. (c) The estimated uc-by-uc charge variations across the interfaces, results integrated over 5 STEM-EELS datasets. Red, PZT(P+)/LAO/STO; black, PZT(P-)/LAO/STO. The 10% error bars have been omitted for clarity of the figure presentation.

Fig. 5



The HAADF imaging of [010]-projected STO (a) at RT with 8 and 68 s of acquisition times and (b) at 100 K (acquisition, 68 s) with the corresponding fast Fourier transform in the inset, indicating  $\sim 1.38\text{-\AA}$  resolution by the resolved 220-type reflections, using JEOL liquid-nitrogen temperature holder. Scale bars, 2 nm. The STO in (b) is rotated by  $\sim 45^\circ$  compared to (a). (c) The simultaneous HAADF of the STEM-EELS chemical mapping in (d) at 100 K (acquisition time,  $\sim 84$  s). Scale bars, 1 nm. Dashed white line in (d), the line profiling over the Ti map. (e) The thus-revealed Ti intensity profile by the dashed line in (d).

## Acknowledgments

This work was supported by Ministry of Science and Technology Taiwan, National Taiwan University, and Academia Sinica Taiwan.

## References

- [ 1 ] D. A. Muller, L. F. Kourkoutis, M. F. Murfitt, J. H. Song, H. Y. Hwang, J. Silcox, N. Dellby, O. L. Krivanek, *Science* **319**, 1073 (2008).
- [ 2 ] M.-W. Chu and C. H. Chen, *ACS Nano* **7**, 4700 (2013).
- [ 3 ] K. Suenaga and M. Koshino, *Nature* **468**, 1088 (2010).
- [ 4 ] O. L. Krivanek, M. F. Chisholm, V. Nicolosi, T. J. Pennycook, G. J. Corbin, N. Dellby, M. F. Murfitt, C. S. Own, Z. S. Szilagy, M. P. Oxley, S. T. Pantelides, S. J. Pennycook, *Nature* **464**, 571 (2010).
- [ 5 ] K. Kimoto, T. Asaka, T. Nagai, M. Saito, Y. Matsui, K. Ishizuka, *Nature* **450**, 702 (2007).
- [ 6 ] Y.-M. Kim, J. He, M. D. Biegalski, H. Ambaye, V. Lauter, H. M. Christen, S. T. Pantelides, S. J. Pennycook, S. V. Kalinin, A. Y. Borisevich, *Nat. Mater.* **11**, 888 (2012).
- [ 7 ] C. P. Chang, J. G. Lin, H. T. Jeng, S.-L. Cheng, W. F. Pong, Y. C. Shao, Y. Y. Chin, H.-J. Lin, C. W. Chen, J.-R. Yang, C. H. Chen, and M.-W. Chu, *Phys. Rev. B* **87**, 075129 (2013).
- [ 8 ] C. P. Chang, M.-W. Chu, H. T. Jeng, S.-L. Cheng, J. G. Lin, J.-R. Yang, and C. H. Chen, *Nat. Commun.* **5**, 3522 (2014).
- [ 9 ] P. W. Lee, V. N. Singh, G. Y. Guo, H.-J. Liu, J.-C. Lin, Y.-H. Chu, C. H. Chen, and M.-W. Chu, *Nat. Commun.* **7**, 12773 (2016).
- [ 10 ] M. N. Grisolia, J. Varignon, G. Sanchez-Santolino, A. Arora, S. Valencia, M. Valera, R. Abrudan, E. Weschke, E. Schierle, J. E. Rault, J.-P. Rueff, A. Barthélemy, J. Santamaria, and M. Bibes, *Nat. Phys.* **12**, 484 (2016).
- [ 11 ] A. Ohtomo and H. Y. Hwang, *Nature* **427**, 423 (2004).
- [ 12 ] S. Thiel, G. Hammerl, A. Schmehl, C. W. Schneider, and J. Mannhart, *Science* **313**, 1942 (2006).
- [ 13 ] L. Li, C. Richter, J. Mannhart, and R.C. Ashoori, *Nat. Phys.* **7**, 762 (2011).
- [ 14 ] J. A. Bert, B. Kalisky, C. Bell, M. Kim, Y. Hikita, H. Y. Hwang, and K. A. Moler, *Nat. Phys.* **7**, 767 (2011).
- [ 15 ] N. Reyren, S. Thiel, A. D. Caviglia, L. F. Kourkoutis, G. Hammerl, C. Richter, C. W. Schneider, T. Kopp, A.-S. Rüetschi, D. Jaccard, M. Gabay, D. A. Muller, J.-M. Triscone, and J. Mannhart, *Science* **317**, 1196 (2007).
- [ 16 ] B. Kalisky, J. A. Bert, B. B. Klopfer, C. Bell, H. K. Sato, M. Hosoda, Y. Hikita, H. Y. Hwang, and K. A. Moler, *Nat. Commun.* **3**, 922 (2012).
- [ 17 ] H. Y. Hwang, Y. Iwasa, M. Kawasaki, B. Keimer, N. Nagaosa, and Y. Tokura, *Nat. Mater.* **11**, 103 (2012).
- [ 18 ] J. Chakhalian, J. W. Freeland, A. J. Millis, C. Panagopoulos, and J. M. Rondinelli, *Rev. Mod. Phys.* **86**, 1189 (2014).
- [ 19 ] P. R. Willmott, S. A. Pauli, R. Herger, C. M. Schlepütz, D. Martoccia, B. D. Patterson, B. Delley, R. Clarke, D. Kumah, C. Cionca, and Y. Yacoby, *Phys. Rev. Lett.* **99**, 155502 (2007).
- [ 20 ] R. Yamamoto, C. Bell, Y. Hikita, H. Y. Hwang, H. Nakamura, T. Kimura, and Y. Wakabayashi, *Phys. Rev. Lett.* **106**, 036104 (2011).
- [ 21 ] S. A. Pauli, S. J. Leake, B. Delley, M. Björck, C. W. Schneider, C. M. Schlepütz, D. Martoccia, S. Paetel, J. Mannhart, and P. R. Willmott, *Phys. Rev. Lett.* **106**, 036101 (2011).
- [ 22 ] K. Yoshimatsu, R. Yasuhara, H. Kumigashira, and M. Oshima, *Phys. Rev. Lett.* **101**, 026802 (2008).
- [ 23 ] V. T. Tra, J.-W. Chen, P.-C. Huang, B.-C. Huang, Y. Cao, C.-H. Yeh, H.-J. Liu, E. A. Eliseev, A. N. Morozovska, J.-Y. Lin, Y.-C. Chen, M.-W. Chu, P.-W. Chiu, Y.-P. Chiu, L.-Q. Chen, C.-L. Wu, and Y.-H. Chu, *Adv. Mater.* **25**, 3357 (2013).
- [ 24 ] M.-W. Chu, S.C. Liou, C. P. Chang, F.-S. Choa, and C. H. Chen, *Phys. Rev. Lett.* **104**, 196101 (2010).
- [ 25 ] P.-E. Janolin, B. Fraisse, B. Dkhil, F. le Marrec, and E. Ringgaard, *Appl. Phys. Lett.* **90**, 162906 (2007).
- [ 26 ] M.-W. Chu, I. Szafraniak, R. Scholz, C. Harnagea, D. Hesse, M. Alexe, and U. Gösele, *Nat. Mater.* **3**, 87 (2004).
- [ 27 ] P. W. Lee, Ph. D. thesis, National Taiwan University (2016).
- [ 28 ] H. Nazeer, M. D. Nguyen, O. S. Sukas, G. Rijnders, L. Abelmann, and M. C. Elwenspoeck, *J. Microelectromech. Syst.* **24**, 166 (2015).

# High Spatial Resolution Scanning Electron Microscope: Evaluation and Structural Analysis of Nanostructured Materials

Osamu Terasaki<sup>1</sup>, Shunsuke Asahina<sup>2</sup>, Yuusuke Sakuda<sup>2</sup>, Hideyuki Takahashi<sup>3</sup>, Kenichi Tsutsumi<sup>3</sup>, Masato Kudo<sup>4</sup>, Robert W. Corkery<sup>5,6</sup>, Yanhang Ma<sup>1</sup>

<sup>1</sup> SPST, ShanghaiTech University, China

<sup>4</sup> JEOL TECHNICS LTD.

<sup>2</sup> SM Business Unit, JEOL Ltd.

<sup>5</sup> Department of Chemistry, KTH (Royal Institute of Technology), Sweden

<sup>3</sup> SA Business Unit, JEOL Ltd.

<sup>6</sup> Applied Mathematics Department, Australian National University, Australia

In scanning electron microscopy (SEM) an electron beam is produced from an emitter, and the beam is demagnified into a finely focused electron probe that irradiates and scans across the surface of a sample in raster fashion. Signals are generated in the form of secondary and backscattered electrons (SEs and BSEs), and characteristic X-rays. These signals contain information about the surface topography, composition, crystal structure and chemical bonding of the sample, and with nano-scale spatial resolution [1, 2]. By lowering the energy of the incident electrons, irradiation damage by the beam and adverse effects on the image of an insulating sample can be suppressed, and at the same time information from the surface can be selectively obtained [3].

Recent advances in electron optical technology have enabled imaging at or below a spatial resolution of 1.0 nm, even for relatively low energy incident electrons on the order of 1 keV. Together with the development of electron beam and characteristic X-ray spectroscopic techniques, these advances now enable contrast based on morphology/topography and atomic number ( $Z$ ) to be obtained separately, and with nano-scale spatial resolution. This is achieved by selecting specific types of emitted electrons, known as SEs (< 50 eV) and BSEs (> 50 eV), respectively.

In this review we give examples of surface structures imaged with the latest Low-Voltage, High Resolution SEM (LVHRSEM) using a through-the-lens (TTL) system incorporating an energy filtering capability. We also discuss the contribution of BSEs and SEs to the contrast of the image, and the composition and chemical bonding information using Auger Electron Spectroscopy (AES) and X-ray spectroscopy (for characteristic X-rays including soft X-rays), respectively. Furthermore the advantage of using SEM with a large depth of field (DOF) is exemplified by imaging the wings of a butterfly.

## Electron optics of low accelerating voltage SEM

First, since the resolution of the SEM is determined primarily by the size of the electron-probe diameter on a specimen surface, we start with a review of what are the dominating factors for the resolution [4].

One of the main elements is the performance and function of "electron source and irradiation system". The system is composed of an electron gun, several electron lenses, aperture stops, deflectors and additional optical elements. The part of an electron microscope where electrons are extracted from an emitter as an electron beam with a certain directionality is called an electron gun. Ideally an electron gun would act as a single point source,

however, this is not the case. Therefore much effort is made in reducing the area of the disk-shaped source by controlling the shape of the emitter and electrodes, the voltage applied to them, and optimizing the distribution of the electric field. This disk is called a virtual electron or virtual light source. Subsequent electromagnetic lenses converge the electrons emitted from points of the virtual light source so their area is as small as possible, and in doing so, forming an image of the virtual electron source as an electron probe on the sample surface.

In order to maximally concentrate the electron distribution in the probe along the electron optical axis, an aperture stop is installed in the electron irradiation system eliminating the peripheral off axis part of the beam. The semi-apex angle of a cone that includes all the electrons emitted from the electron gun

and passing through the aperture stop (the total electron current is taken as the probe current amount  $i_p$ ) is defined as the semi-aperture angle of rays in the object space  $\alpha_o$ . By changing the strength of the condenser lens, we can change  $\alpha_o$  and eventually  $i_p$ .

When an electron beam is focused conically on the specimen surface, the half apex angle of the cone is an important parameter for discussing spatial resolution and is defined as the semi-aperture angle of rays in the image space and expressed by  $\alpha_i$ . As will be described later, there is an optimum value of  $\alpha_i$  for minimizing the probe diameter depending on the probe current. Therefore, the opening angle control lens and the objective lens are adjusted through their strengths to fulfill the optimum condition for  $\alpha_i$ .

The magnetic field generated by the coil of the electromagnetic lens always acts as a central force, rotating its orbit and bending toward the optical axis, so the axial electron lens is always a convex lens (Fig. 1(a)). The values of  $\alpha_o$  and  $\alpha_i$  are so small in the order of milliradians that this figure is enlarged in the direction perpendicular to the optical axis.

Although not shown in the figure, two deflectors are placed above or below the objective lens - one for scanning the electron probe on the specimen surface and another for correcting a deviation from the optical axis in the traveling direction of the electron beam.

The diameter of the electron probe on the specimen surface cannot be made infinitely small. Instead the diameter is finite due to the limitations of various optical aberrations, including the luminance limitation described below and imperfections of the electron lens. This is in addition to the wave nature of the electron. These limitations and restrictions are described below.

(1) Luminance limitation

Electrons are not emitted from the gun from a single point but from an area of a certain finite size. The luminance  $B$  of the electron gun is the electron current per unit solid angle and unit area. Since luminance is unchanged regardless of the cross section of the electron beam (luminance invariant law),  $B$  defined on the object side (electron gun side) should be equal to that on the image plane side (specimen side). This leads to the following equation;

$$B = \frac{i_p}{\pi \alpha_o^2 \cdot \pi (d_o/2)^2} = \frac{i_p}{\pi \alpha_i^2 \cdot \pi (d_g/2)^2} \tag{1}$$

Here,  $d_o$  is the diameter of the virtual electrons source, and  $d_g$  is the probe diameter on the specimen surface due to luminance limitation. From equation (1) we can obtain

$$d_g = \frac{2}{\pi} \sqrt{\frac{i_p}{B}} \frac{1}{\alpha_i} \tag{2}$$

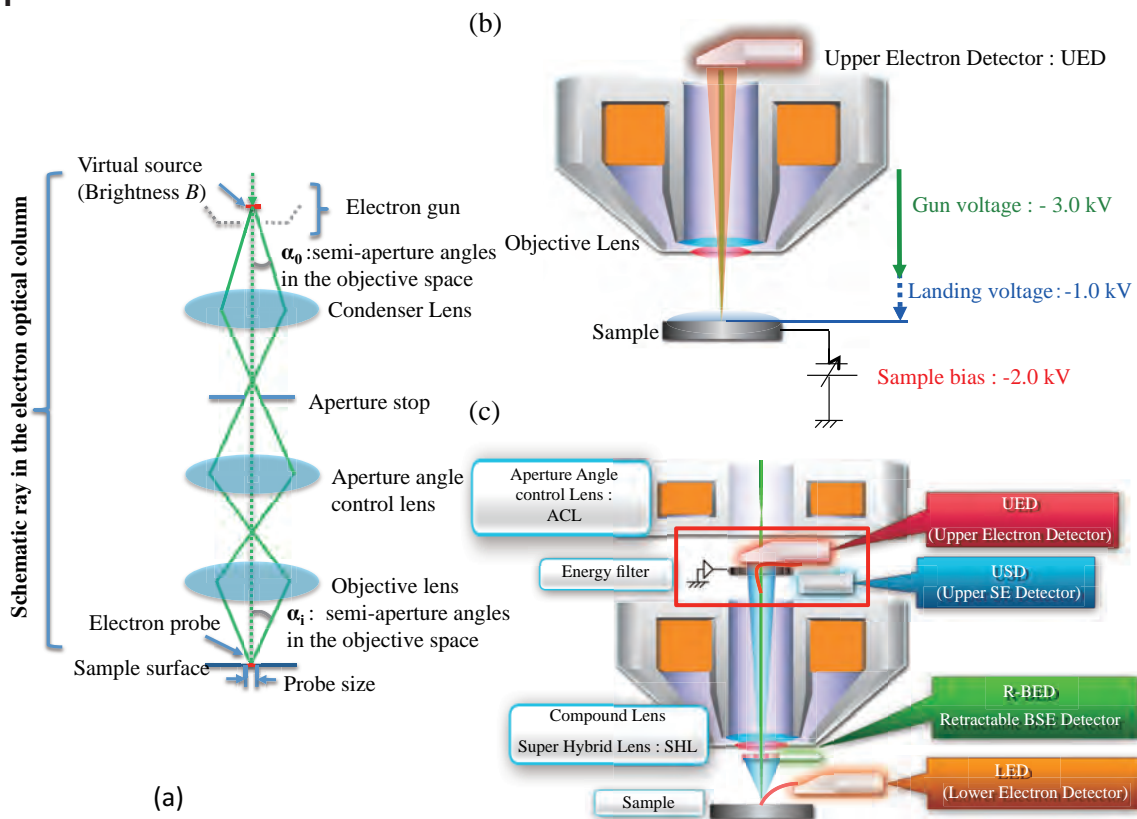
The value of the luminance  $B$  decreases as the accelerating voltage decreases.

(2) Spherical aberration restriction

Since  $\alpha_i$  is small, the spread  $d_s$  due to spherical aberration of the electron lens can be approximated by the following equation;

$$d_s = \frac{1}{2} C_s \alpha_i^2 \tan \alpha_i \cong \frac{1}{2} C_s \alpha_i^3 \tag{3}$$

Fig. 1



Schematic illustrations of electron optics (a), principles of gentle beam (GB) in TTL (b) and arrangements of aperture angle control lens (ACL), energy filter, and detectors of UED/USD above/below the energy filter in TTL/SHL system (c).

where  $C_s$  is a spherical aberration coefficient (defined on the image plane side) of the objective lens.

The spherical aberration is a spread of the probe caused by bending the electron trajectory to a greater extent from the optical axis and traversing the optical axis in shorter distance than electrons in the trajectory near the axis.

$C_s$  depends on the operating conditions of the lens even if it is the same lens, generally speaking, the longer the focal length of the electron lens the larger the spherical aberration coefficient  $C_s$ .

### (3) Chromatic aberration limit

The energy of emitted electrons is subjected to thermal fluctuation/energy-spread corresponding to the temperature of the emitter. The spread of the probe diameter caused by this fluctuation is called the spread  $d_c$  due to chromatic aberration:

$$d_c = C_c \left( \frac{\delta V}{V} \right) \alpha_i \quad (4)$$

Here,  $V$  is the accelerating voltage of electrons,  $\delta V$  is the energy spread when electrons pass through the objective lens (energy width when emitted from the electron gun),  $C_c$  is the chromatic aberration-coefficient of the objective lens (defined on the image plane side).

Chromatic aberration occurs because of the fact that electrons become more difficult to bend as the electron energy increases and the focal length of the lens becomes longer. Like the spherical aberration coefficient,  $C_c$  is dependent on operating conditions of the lens, and the longer the focal length is the larger the chromatic aberration coefficient  $C_c$  becomes. Also, since  $\delta V$  does not depend on the accelerating voltage, spreading due to chromatic aberration becomes more serious through  $\delta V/V$  when the accelerating voltage is low.

### (4) Diffraction aberration limit

Since the electron beam is a matter wave having a mass (de Broglie), a diffraction phenomenon occurs. Since the outside of the electron probe is blocked off by an aperture stop, where a diffraction phenomenon occurs and the probe diameter expands. For an electron beam with wavelength  $\lambda$ , the diameter of the spread  $d_d$  is given by:

$$d_d = 1.22\lambda \frac{1}{\alpha_i} \quad (5)$$

Since the wavelength of the electron beam becomes longer as the accelerating voltage becomes lower, the diffraction aberration becomes larger.

$$(\lambda(nm)) = \frac{1.227}{\sqrt{V(volts)}} \quad (6)$$

These limit terms are superposed for the final probe diameter  $d_p$ . Since each is an independent event that can be approximated by a Gaussian function, therefore it is simply expressed as their convolution (Gaussian convolution) as a whole. Therefore,  $d_p$  can be approximately expressed as the square root of the sum of squares of the probe diameters as follows.

$$d_p = \left[ \frac{4i_b}{\pi^2 B} \frac{1}{\alpha_i^2} + C_c^2 \left( \frac{\delta V}{V} \right)^2 \alpha_i^2 + \frac{1}{4} C_s^2 \alpha_i^6 + (1.22\lambda)^2 \frac{1}{\alpha_i^2} \right]^{1/2} \quad (7)$$

Although this equation is obtained semi-empirically, it fits the actual situation well. Since  $\alpha_i^{-2}$  and  $\alpha_i^2$  and  $\alpha_i^6$  are terms existing

on the right side of this equation, there exists a value of  $\alpha_i$  that minimizes  $d_p$ . The value and the value  $\alpha_i$  giving the minimum value for  $d_p$  is called the optimum opening angle.

It is particularly important in high resolution SEM that the electron optical lens system and aperture diameter should be controlled so as to obtain the optimum divergence angle, so at least two lenses are required behind the aperture stop (two degrees of freedom are required). Therefore, an "angle-of-aperture control lens" is provided so that both the intensity of this and the intensity of the objective lens are adjusted so as to obtain an optimum  $\alpha_i$ . However, in the case of inexpensive SEMs, this lens is often not incorporated. Instead, it is possible to be close to the optimum aperture angle in a wide range of probe current values by switching between several apertures of different diameters.

When the incident voltage is lowered, the diffraction aberration increases due to the increase of  $\lambda$ . Also, since the luminance also decreases, the luminance limit term increases and the optimum divergence angle also increases. For this reason, the aberration terms given by equations (3) and (4) increase, so that the probe diameter is generally large (resolution is poor). Which of these terms will be dominant cannot be unconditionally determined and depends on the type of the electron gun and the amount of the probe current.

Although the luminance limiting term does not have much influence in the field emission type electron gun, in the thermionic electron gun, although it depends on the magnitude of the aberration coefficient of the objective lens, it is dominant over the entire range of the probe current.

Although the angular current density is large in the case of the field emission type, if an attempt to increase the probe current to the order of  $\mu A$  is made, the object side opening angle,  $\alpha_o$ , becomes large, and significant spherical aberration of the condenser lens occurs, with a consequent sharp increase in the probe diameter.

As a method of keeping the beam diameter small at low accelerating voltage, a deceleration method (Gentle Beam: GB) is conceivable, and its principle is illustrated in Fig. 1(b). It becomes a compound lens of a magnetic field and an electric field that allows electrons to pass through the objective lens at a high accelerating voltage and decelerate at the electrostatic field generated on the sample surface, thereby reducing the spherical aberration coefficient  $C_s$  and the chromatic aberration coefficient  $C_c$  [2, 5]. For example, the accelerating voltage is set to -3 kV (-3 kV is applied to Gun) and the sample bias is set to -2 kV, then the energy of electrons reaching the sample is 1 keV [Footnote]. Furthermore, a JEOL JSM-7800FPRIME has an electron optical system combined with an intermediate acceleration method. This is also called super hybrid lens (SHL) method. In the intermediate acceleration method, the relative potential difference between the electron gun and the sample is determined as the incident voltage value, and then the voltage of electrons passing through the interior of the electron irradiation system is temporarily increased, and the electron optics. Various aberrations in the convergent action are kept as small as possible and the diameter of the electron probe finally irradiated to the sample surface is made as small as possible. In principle, the objective lens becomes an electromagnetic superposition type [6].

Figure 1(c) shows the schematic diagram and each detector arrangement together with an energy filter. This objective lens is also called a super hybrid lens (SHL).

--Note--

In this review, we use the actual value of electric potential, in order to discuss deceleration method properly. Although it is

normally stated SEM was operated at accelerating voltage of 10 kV, in this review we state for this case the accelerating voltage (emitter's voltage) was -10 kV and anode was ground voltage (0 V), and electron with a negative charge “-e” will be accelerated from emitter to anode and gain kinetic energy 10 keV.

### Distinction between secondary electrons and back-scattered electrons

In the FE-SEM, a grid (energy filter) and appropriate detectors, UED and USD, are installed in the column directly above the objective lens, so SEs are detected by the USD and BSEs are detectable by the UED by applying a specified voltage. When this UED is used, a BSE image can be acquired with a good S/N ratio even at low accelerating voltage. **Figure 2** shows the BSE image of Ru and Pt clusters in carbon. In the positions marked by red arrows, the cluster is visible as bright contrast at -3 kV but not visible at -1 kV. This indicates that the escape depth varies depending on the energy of the BSE. Assuming that the escape depths of BSE with energies of 1 keV and 3 keV are  $t_1$  and  $t_3$ , respectively, the depth  $t$  of the metal cluster is given by  $t_1 < t < t_3$ . As described above, it is useful to obtain the depth information of the particles while changing the incident voltage.

### Sample preparation for SEM observation at low acceleration incident voltage

In order to enhance the effective electrical conductivity from the surface of a particle to the sample stand when observing a nanostructured material by SEM, particularly when imaging particles amongst electrically insulating powder samples. Here, a simple and useful method for observing at high resolution and low incidence voltage is described, taking as an example electrically insulating nanoparticles of zeolite FAU.

High purity carbon rod is used as a base for holding the sample. The carbon rod is polished with abrasive paper and then polished with filter paper to such an extent that a gloss surface is visibly induced. Next, the powdered sample is dispersed in ethanol, sufficiently stirred by an ultrasonic bath, dropped on a carbon stub, and heated at 150 °C for about 20 minutes. The importance of removing the organic dispersant by this heat treatment is shown in **Fig. 3**, by comparing the two SE images with "with heating" and "without heating". The carbon table is cleaned "with heating" so that irregularities of its surface are clearly observed, and at the same time, movement of the contamination component to the specimen surface from the carbon table and the inside of the sample is very much suppressed, and sharper images of surfaces in both carbon and FAU are obtained.

### Selection of observation condition

For SEM observations at low accelerating voltage, the selection of a particular acceleration (electron gun) and impact voltage to a specimen is a particularly important point and is assisted by checking the optimum sample depth in order to grasp the target structural information. For example, the lower part of **Fig. 4(a)** shows some of images corresponding to the same field of view of a microporous titanosilicate ( $\text{Ti}_{16}\text{Si}_{80}\text{O}_{208}$  (Na, K)<sub>n</sub>, ETS-10) sample at impact voltages of -0.4 kV, -0.8 kV and -1.6 kV. Monte Carlo simulations under the same conditions are shown in b) [8]. Surface steps are clearly confirmed at low impact voltage of 0.4 kV. Changing the impact voltage to -0.8

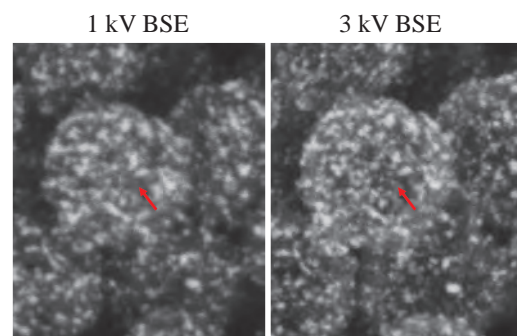
kV increases the edge effect, and it seems that a very fine uneven structure is emphasized. At -1.6 kV, a crystal contrast coming from the internal structure covered information from the surface. The images clearly show importance of setting the observation conditions, both accelerating and impact voltages, for analysis of nanostructured materials.

### Low accelerating voltage SEM by Auger Electron Microscopy (AES) method

During AES, electron spectroscopy is conducted using an electrostatic hemispherical detector [9]. Electrons are introduced into a hemispherical energy analyzer to which a voltage is applied and an electron spectrum with high-energy resolution is obtained. Here we discuss the dependence of contrast on the landing energy of electrons, and on the magnitude of the SE3 component in SE image formation in the low voltage high resolution SEM (LVHRSEM) under deceleration from the electron energy spectrum obtained by AES.

**Figure 5** shows an FE-SEM image of a sample half sputtered with gold and half with carbon and the corresponding intensity profiles obtained from the regions bounded by parallel dotted

**Fig. 2**

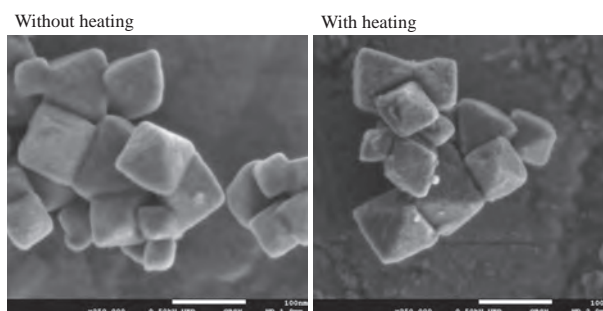


Sample : Ru and Pt at Carbon  
Prof Ferdi Schüth  
Detector : UED Filter bias : -500V

100 nm

Filtered BSE images of carbon containing Ru and Pt nano-particles. Taken at the impact electron-energy of 1 keV (a) and 3 keV (b), respectively, with UED. -500 V was applied to the energy filter so as to cut off electrons with energy smaller than 500 eV, of which major part is SEs.

**Fig. 3**



Sample : Zeolite FAU, Heating condition: 150°C for 20 min

SEM images taken with electron impact energy of 500 eV (Acc = 5.5 kV, sample bias = -5.0 kV) with BED, before heating (a) and after heating at 150 °C for 20 min (b).

lines. Carbon is darker than gold at a landing voltage of -500 V, while brighter than gold at 220 V. The main component of BSEs is elastically scattered electrons which do not lose energy during the scattering process inside the sample. In contrast, SEs are inelastically scattered electrons that can escape from the vicinity of the surface while losing energy, and in many cases has a peak at ~ 20 eV or less.

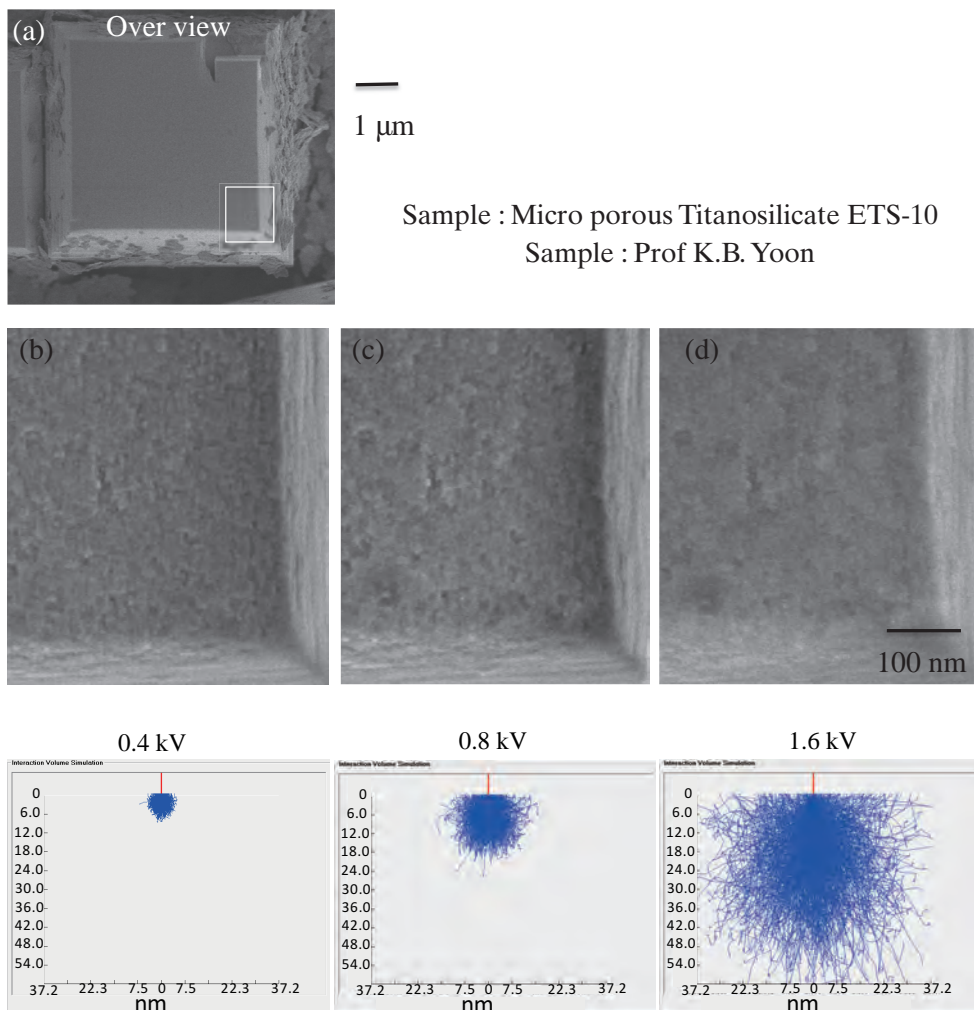
**Figure 6** shows AES spectra obtained under the same accelerating voltage condition of -500 V. Impact/landing voltages are -500 V when conducted without sample bias, and 220 V when conducted with a bias of -280 V). Here, the electric field created by the specimen bias acts as a deceleration field for incident electrons until they contact the specimen, and as an acceleration field after the electrons exit the specimen. When using a specimen bias of -280 V, the energy of incident electrons accelerated with -500 V at the gun becomes 220 eV (500 - 280) at the specimen surface by this field. SEs are decomposed into two parts, ~20 eV (SE3) and ~300 eV (SE1 and SE2) in **Fig. 7** below. The energy of the BSEs emitted from the interaction volume is 220 eV directly under the sample surface but after exiting the surface the energy changes to 500 eV (220 + 280), which takes the same value with or without bias, as BSEs are accelerated with the field produced by bias. On the other hand, the secondary electrons (SE1 + SE2) emitted from the sample surface are accelerated by the bias and the energy reaches ~300 eV (~20 + 280). Secondary electrons (SE3) have a peak at ~20 eV and are generated when accelerated

secondary electrons and back-scattered electrons hit some parts in the microscope. In order to improve the point resolution of SEs images, and taking the previous points into consideration, it is important to pick up selectively the component of SE1 from the mixture of (SE1 + SE2) and to reduce the component of SE3. For collecting surface structure in an SE image at highest resolution, it would be best to reduce the size of the interaction volume through lowering electron impact energy while balancing the increase in the size of electron probe. In Fig. 6(a), both the secondary electrons (SEs) and the back-scattered electrons (BSEs) show higher counts in gold at an incident voltage of -500 V. On the other hand, in the case of an incident voltage of -220 V (deceleration field -280 V) in Fig. 6(b), carbon shows brighter contrast than Au both in SE and BSE. In particular, carbon showed about twice the contrast of gold in BSE. This spectrum was acquired with the sample inclined at 30° and is not exactly the same system as FE-SEM, but the image contrast observed by FE-SEM matches well with the spectrum obtained with AES under the same conditions. In the future we will conduct a detailed analysis to better understand SEM image contrast at low impact electron energy.

### Large Depth of Field (LDF)

It is well known that the SEM has a larger depth of focus than other optical instruments, and the main factor determining

**Fig. 4**



(a) SEM observations of Micro porous Titanosilicate ETS-10 taken with LED. Over view image was taken at Acc voltages: 5.4 kV, Specimen bias voltage: -5.0 kV (a). The images of surface fine structure with higher magnification were taken at the conditions, at the Acceleration voltages of 5.4 (b) 5.8 (c) & 6.6 kV (d) by keeping Specimen bias voltage at -5.0 kV and Probe current 7.0 pA.

(b) Monte Carlo simulations corresponding to Fig. 4(a)

the depth of focus is the image side aperture angle ( $\alpha_i$ ) onto the sample. In the conventional SEM, the objective lens is used to converge the electron beam onto the specimen. However, when an Aperture-angle Control Lens (ACL) is placed immediately above the objective lens, it can be used for focusing electrons on a sample instead of the objective lens. This is called the Large Depth of Field or LDF mode. The semi-aperture angles in the objective space,  $\alpha_o$ , (see Fig. 1(a)) can be made very small. This situation is shown schematically in the optical path diagram of the electron beam (Fig. 8). As a result, when LDF mode is used, images are obtained with an extremely high depth of field. Note that a higher spatial resolution can be obtained by the usual observation method although the depth of focus is shallow compared with LDF. Figure 9 shows the images of butterfly wing scales obtained in both normal and LDF modes. The sample was imaged after osmium coating. In both the side and top view images at low magnification, the LDF mode enabled observation at a long focal length without significant loss of focus. In particular, the difference indicated by arrow (1) is remarkable. In normal mode, some distortion is observed in the image indicated by arrow (2), but distortion is hardly seen in LDF mode.

### Observation of butterfly wing scales

Everyone has childhood memories of chasing a butterfly. The mysterious colors and patterns are different for each species. When you caught one, the color of the wings faded away leaving powdered (scales) on the fingers. At the same time, the super-hydrophobic (water repellent) wing turns into a form that gets wet by rain.

When observing wings from the Green Hairstreak butterfly *Callophrys rubi* (*C. rubi*) in LDF mode, the powder (wing scales) are seen covering the wing surface like overlapping roof tiles and in large numbers. Each wing scale is a specialized, flattened form of a hair (bristle) cell, composed of the

biopolymer chitin which is also the same material used by crabs to make their shells. There are two types of flattened scales in *C. rubi* and many other butterflies, cover and ground scales. Colored cover scales overlay the ground scales. The area density of cover scales on a wing is approximately 50,000 cm<sup>2</sup> [7].

It is obvious from the top and side views in Fig. 9 that the depth of focus becomes very deep in the LDF mode and the amount of distortion in the peripheral area is reduced compared to the image taken using the normal mode. When the wing scales (~20 μm × ~160 μm) and hairs are enlarged, a similarity is found in the internal structure, and both are connected via a socket shape docking structure to the wing membrane surface in the same manner (Fig. 10). During growth, the viable cell that later forms the cover and ground scales grows out through the socket cell. Long actin filaments form bundles that elongate the scale longitudinally. Chitin is later deposited between the actin bundles forming the ribs. Actin is then depolymerized, with cross ribs and finally the luminal structure that forms the photonic crystals formed late. Upper and lower plates of chitin bound the cell. As the cell dies it retracts back through the docking cell into the wing, and rectangular windows open in the upper plate in the space between the ribs and cross ribs.

The wing scale is like the bottom of a small wooden boat, with a raised central rib and many parallel ribs running the length of the scale, and a number of thin rails (cross ribs) orthogonal to these, reinforcing the ribs while maintaining their distance.

The lower (ventral) surfaces of wings of *C. rubi* reflect almost the same green color as the leaves of plants for the purpose of camouflage. The green color arises from photonic crystal structures on the inside of the cover scales. Each cover scale contains 200-300 single gyroid photonic crystals in various orientations. Such structural color is seen when substances with different refractive indexes are arranged periodically, like in opal, where the reflected color is strongly direction dependent.

Single-gyroid photonic crystals are seen in the luminal space between the lower base plate and the top surface defined by

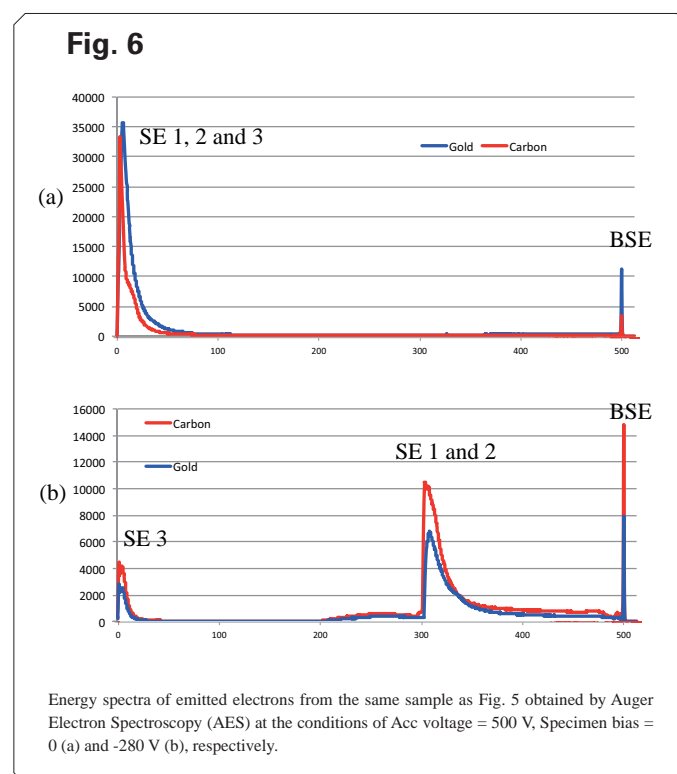
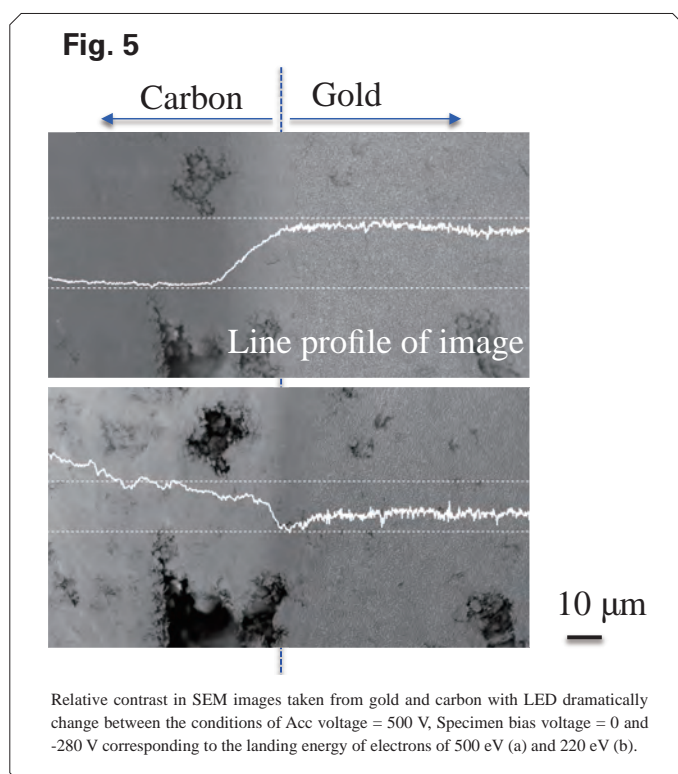
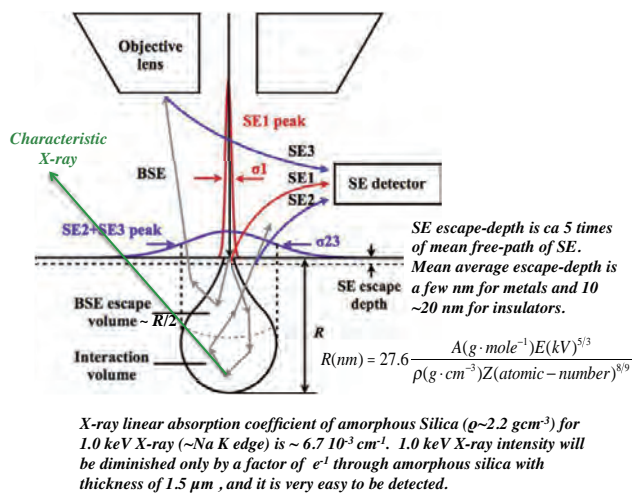
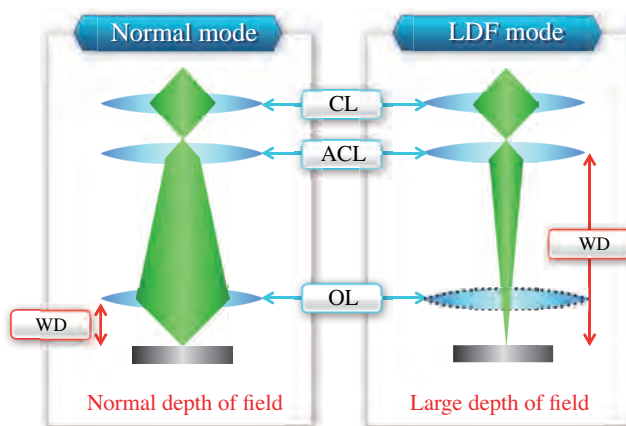


**Fig. 7**



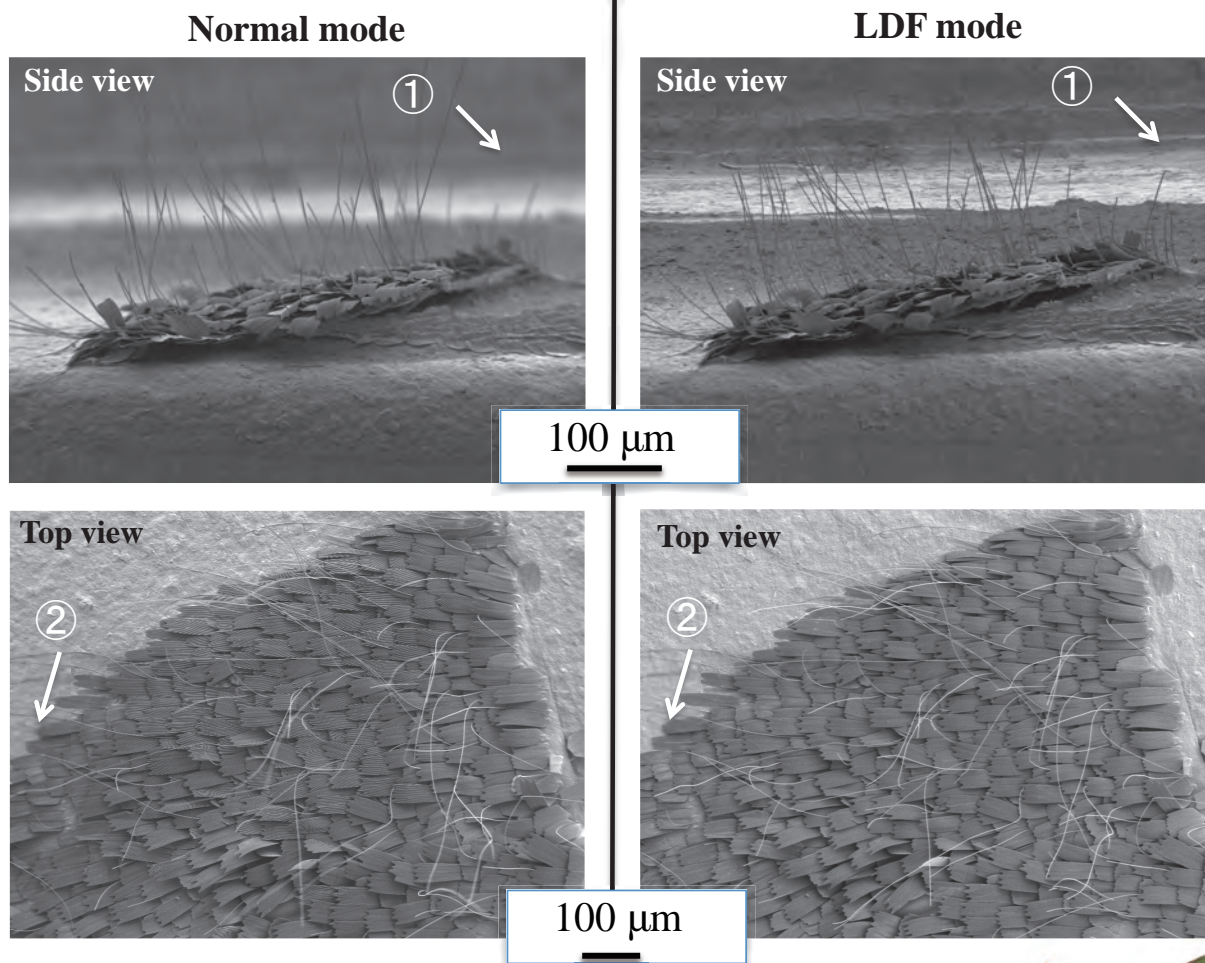
Schematic drawing where BSE/SEs and characteristic X-ray are produced inside and outside of a sample.

**Fig. 8**



Schematic illustrations of electron ray diagram for normal-mode and large depth of field (LDF)-mode.

**Fig. 9**



Comparison of SEM images of *callophrys rubi* (c. rubi) taken with LED from normal-mode (left column) and LDF-mode (right column). Following conditions were applied: Acc voltage: 500 eV, Working distance (WD): 10 mm, Magnifications: Side view  $\times 100$ , Top view  $\times 70$ . OL: ON for normal mode, OFF for LDF-mode.



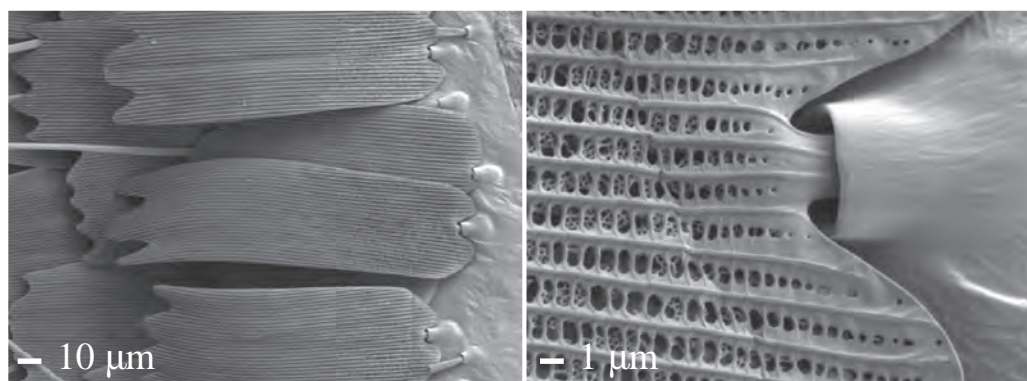
the ribs and cross ribs in **Fig. 11**. They only form in the apical (distal) and of the wing scales where the luminal space is thicker. The single gyroid crystals are formed via expression and deposition of chitin on only one side of a biological membrane complex. The formation of the membrane complex is thought to proceed via an in-folding of the plasma membrane with the endoplasmic reticulum membrane, with the resulting interface closely resembling the double gyroid minimal surface. As the development proceeds, the space on one side of the minimal surface is filled with chitin. As the cell dies, the space on the other side becomes filled with air.

Despite the directionality of the reflected color, the butterfly uses millions of crystals to suppress the iridescence of the individual crystals achieving an average green color overall. The single gyroid photonic crystals in *C. rubi* are chiral and both left and right handed crystals coexist in a single wing scale. The average unit cell size is ~340 nm. The volume fraction of chitin is approximately 20-30%. The single gyroid structure is well resolved in the sectioned sample [7].

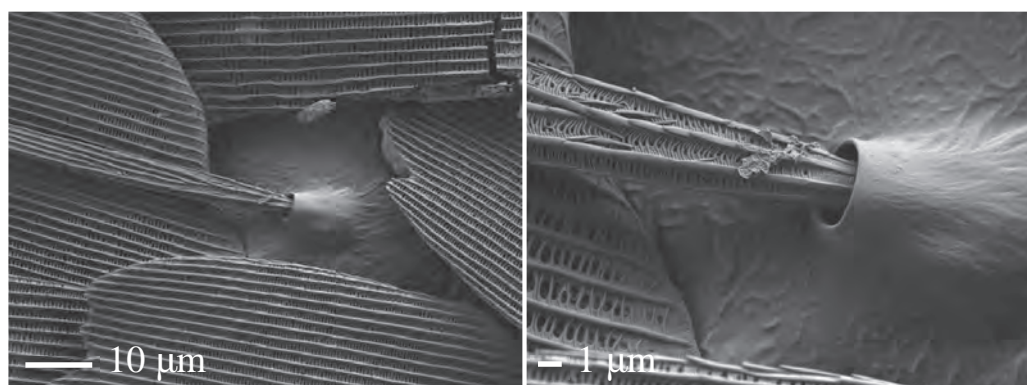
### Chemical analysis of nanostructures using an EDS detector with high solid angle and WDS detector with high sensitivity for soft X-ray

A silicon drift detector (SDD) with a short counter dead time was developed to improve on existing SSD technology. It then became possible to detect X-rays with a large dynamic range (high count rate) without liquid N<sub>2</sub> cooling. In addition, the degree of freedom in choosing the size and shape of the detection element has expanded, which makes it possible to design SDDs with a higher solid angle. Currently, the maximum receiving area for X-rays reaches 150 cm<sup>2</sup>. In addition, detectors have been developed that suppress the influence of shadowing and eclipsing by other parts on the detector as well as improving detection speed by combining multiple detectors. Also, with the advent of windowless detectors (i.e. without a Be window for protecting the detector), low atomic number atoms like Li (Z=3), which have so far remained undetectable, can also be detected and quantified.

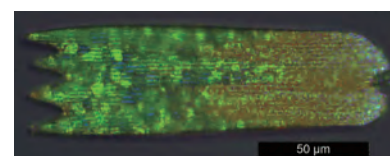
**Fig. 10 Details of Butterfly with topographical contrast by LED**

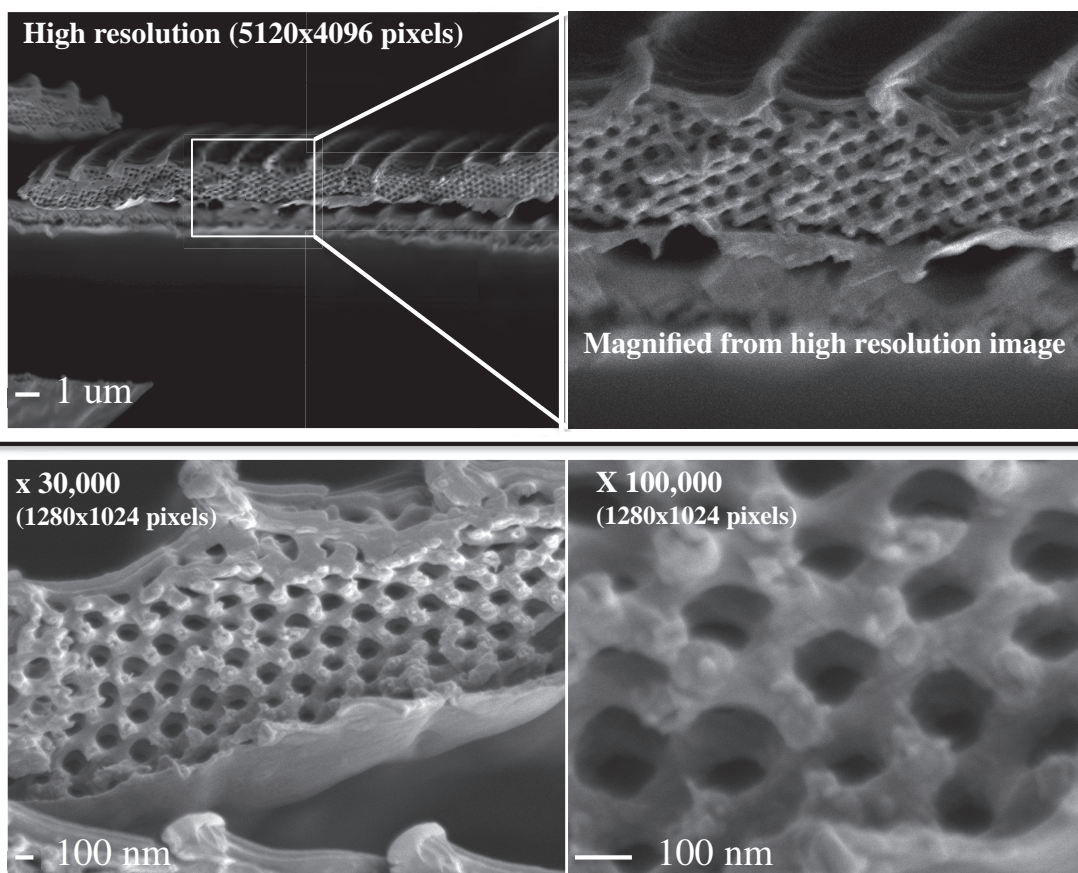


Landing voltage : 0.5 kV, Detector : LED, WD : 8 mm (For larger depth of field)



Landing voltage : 0.5 kV, Detector : LED, WD : 4 mm (For higher spatial resolution)



**Fig. 11**

Fine details in SEM images of Butterfly (*c. rubi*) scales with topological contrast take by LED at Acc voltage: 3.5 kV, Landing energy: 500 eV, WD : 8 mm (For larger depth of field, Left column) and 4 mm (For higher spatial resolution, Right column).

Here is an example of Co - ZIF - 8 @ Zn - ZIF - 67 (Zeolitic Imidazolate Framework: ZIF). Co - ZIF - 8 and Zn - ZIF - 67 have the same crystal morphology (rhombic dodecahedron), crystal structure (space group) and similar lattice constants but differ by metal cluster type (Co versus Zn). It is impossible to distinguish one from the other using powder X-ray diffraction experiments. **Figure 12** shows the backscattered electron image and elemental map obtained by processing the crystal by Ar ion milling. A JEOL IB-19520CCP was used for cross section fabrication. The sample was processed with Ar ions (accelerating voltage: 4 kV processing time: 4 hours) while cooling at -120 °C or lower. From this image, the ZIF-8 @ ZIF-67 crystal is observed to have a strong Co signal on the surface, Zn clusters on the inside, and the Co-ZIF-8 epitaxially grown over the Zn-ZIF-67. It was first revealed in this experiment that a core-shell structure was formed. Also, it can be seen that the Co oxide on the surface has a thin portion indicated by arrow ① and a uniform layer of about 100 nm shown by arrow ②.

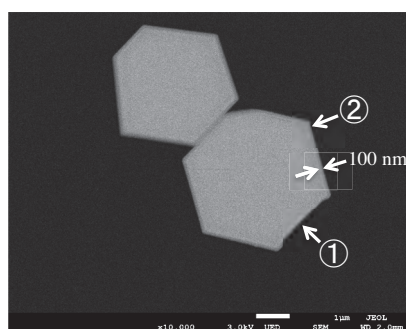
Next, element mapping with high spatial resolution was tried using an EDS detector with a high solid angle (about 0.2 sr). The sample is polymer carrying Ru and Pt nanoclusters (**Fig. 13**). Here, three Oxford X-Max 150 mm<sup>2</sup> (total effective area 450 mm<sup>2</sup>) were used. The incident voltage was 30 kV to obtain high spatial resolution. Mapping was performed for 30 minutes by using an EDS detector with a high solid angle (about 0.2 sr), and as a result, mapping of Pt particles of about 5 nm was successful [10]. It shows that element mapping has become possible with nanostructures of several nm which had been difficult in SEM so far.

## Pt-Ni nano-framework

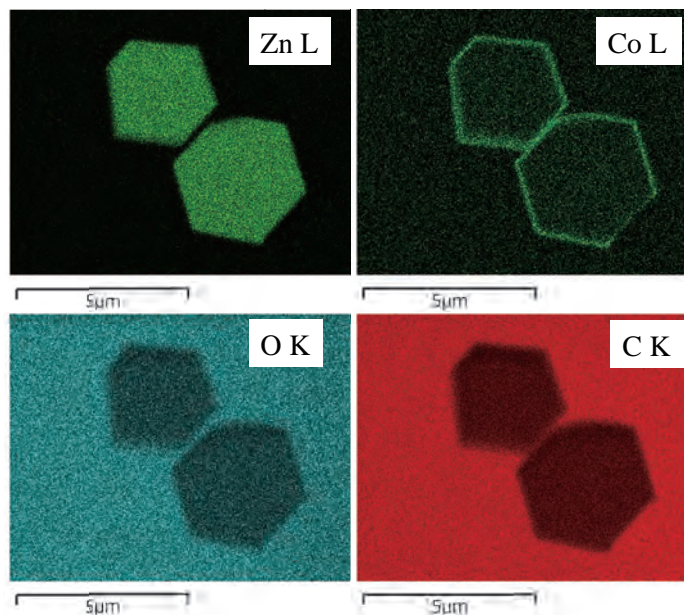
This was stimulated by a paper [11] in which Prof. Peidong Yang (UC Berkeley) group produced a porous Pt<sub>3</sub>Ni nano-framework starting from Ni<sub>3</sub>Pt nano-crystals. This Pt<sub>3</sub>Ni material shows an activity of two orders of magnitude in the oxygen reduction reaction (ORR). **Figure 14** shows the advantages of using SEM to study these materials. Uniform size nano-crystals of Ni<sub>3</sub>Pt nano-crystal were prepared by capping them with oleylamine (Sample A). When these nanocrystals are left in a nonpolar liquid (hexane or chloroform), Pt<sub>3</sub>Ni nano-framework (sample C) nanocrystals were formed. The starting sample A has the Al structure (disordered *fcc* structure) and a composition of Ni<sub>3</sub>Pt. Its morphology looks like the Wigner-Seitz Cell of *fcc* as schematically shown in Fig. 14. On the other hand, in sample C (composition analysis indicates ~Pt<sub>3</sub>Ni), a porous Pt<sub>3</sub>Ni nano-framework, Pt preferentially occupied the edge of the cell indicated by green lines in Fig. 14. This result shows that if we select the observation conditions of SEM appropriately, useful information corresponding to the structure evaluation section described in the paper [11] can be obtained by a much simpler method. In particular the three-dimensional geometrical information is more clearly elucidated.

Analysis by soft X-ray spectroscopy technology is also progressing. A new analytical method using a soft X-ray spectrometer (SXES) has been introduced into FE-SEM [12, 13]. This SXES has high energy-resolution of 0.3 eV, and information concerning the transition state of electrons in the valence band

**Fig. 12**



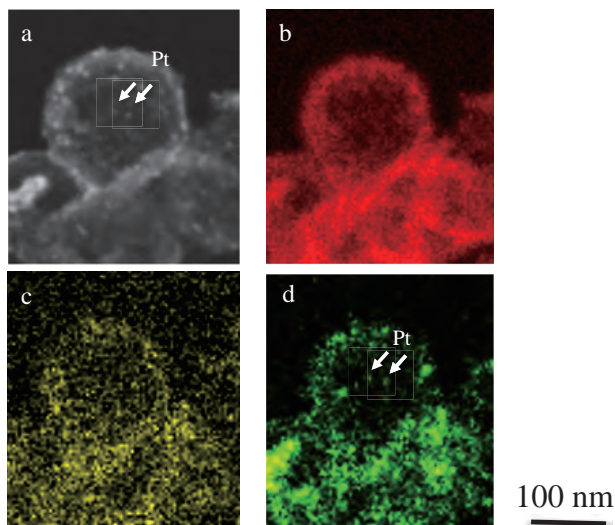
3kV BSE image by UED  
 UED filter -1000V  
 Sample : Co-ZIF-8@Zn-ZIF-67  
 Prof Yusuke Yamauchi  
 Cross sectioned with Cooling CP



Landing voltage : 3 kV, Probe current : 100 pA,  
 Acquisition time : 30 min, Detector : Oxford 150 mm<sup>2</sup>

BSE image and elemental maps of Zn, Co, O and C through EDS analysis from cross sectioned sample of Co-ZIF-8@Zn-ZIF-67

**Fig. 13**



Samples: Prof. Ferdi Schüth

SE image of Pt/Ru@Polymer (a) and high spatial resolution EDS maps of C (K-line) in Red (b), Ru (L-line) in Yellow (c) and Pt (M-line) in Green (d), taken at acc. voltage: 30 kV for 8 min using SDD with 3 units of 150 mm<sup>2</sup>. Scale bars: 100 nm.

damage. For measurement at room temperature, an attenuation of the shoulder peak was observed at around 0.175 keV, suggesting that the crystal structure is damaged by the beam [12]. By combining the cooling mechanism with the low accelerating voltage, it is possible to analyze the chemical state of electron beam sensitive materials such as zeolites, through the various developments of chemical state analysis in FE-SEM.

### Summary

SEM is currently used for product inspection in factories, in universities for advanced basic research, and even in some elementary schools for science classes. The demand for using SEM is increasing more and more. On the other hand, the authors believe that SEM still has significant potential for further development.

In this article we have introduced the fundamentals of electron optics, for SEM in particular. Examples given and discussed include the concepts of low accelerating voltage SEM, observations of surface related structures, the origin of image contrast under low accelerating voltage conditions in Auger Electron microscopy (AES), and acquisition of composition and chemical bonding information using characteristic x-ray spectrometers (EDS and soft x-ray spectrometers) etc. To highlight these concepts, methods and techniques, we have given specific examples applied to the understanding of the characteristics of nanostructured materials. We hope that this initiative will lead to future development of SEM technology and expansion of its use.

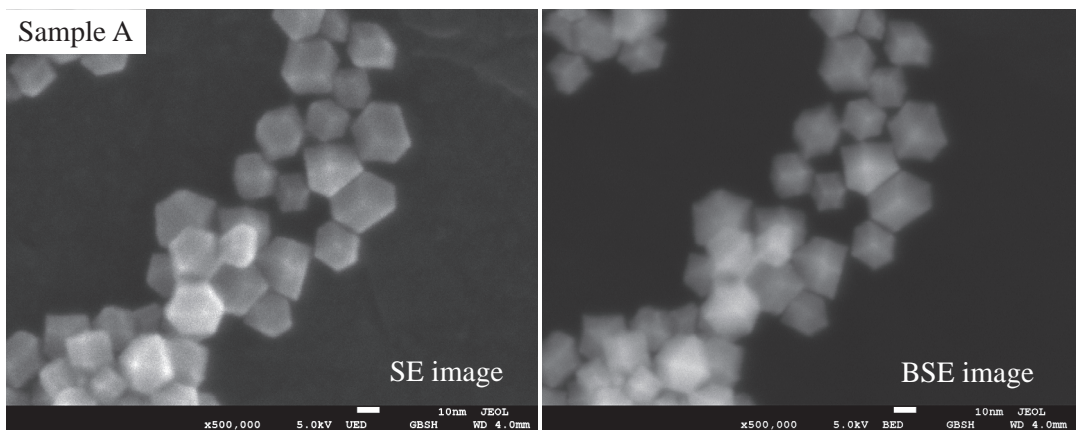
### Acknowledgments

This paper was promoted as a collaborative research between ShanghaiTech and JEOL Ltd. We would like to thank both for their strong support and at the same time for strongly encouraging our efforts to link the development of SEM technology and advances in basic science.

can be obtained, so chemical state analysis can be performed. The principle of measurement is illustrated in Fig. 15.

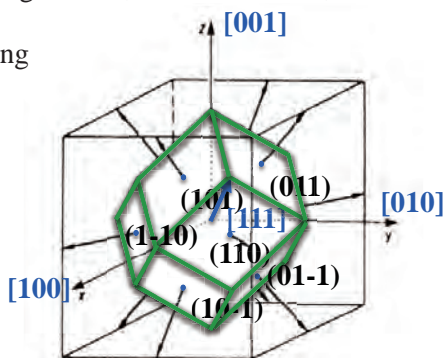
The principle is as follows; Characteristic soft x-rays emitted from a sample induced by the electron beam are guided by a collector mirror to a diffraction grating. Grooves of unequal spacing formed in this grating make it possible to simultaneously characterize X-rays of differing energies. Figure 16 shows the spectrum obtained from an SXES measurement on zeolite LTA. The third order oxygen K $\alpha$  line of the zeolite is detected. The measurement was made at low temperature (-50 °C) and low accelerating voltage in order to reduce electron irradiation

**Fig. 14**

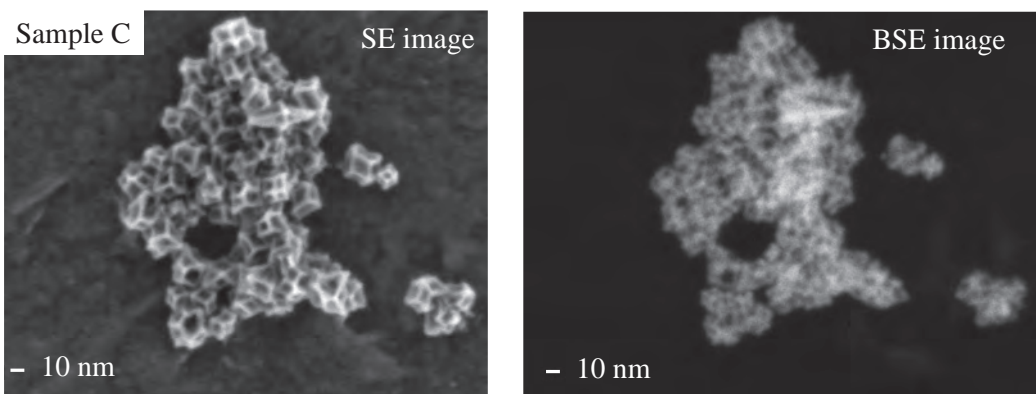


SE image (Landing voltage : 5 kV, Sample bias : -5 kV, Detector : UED, WD 4 mm)  
 BSE image (Landing voltage : 5 kV, Detector : UED, Filter bias : -1.2 kV, WD 4 mm)

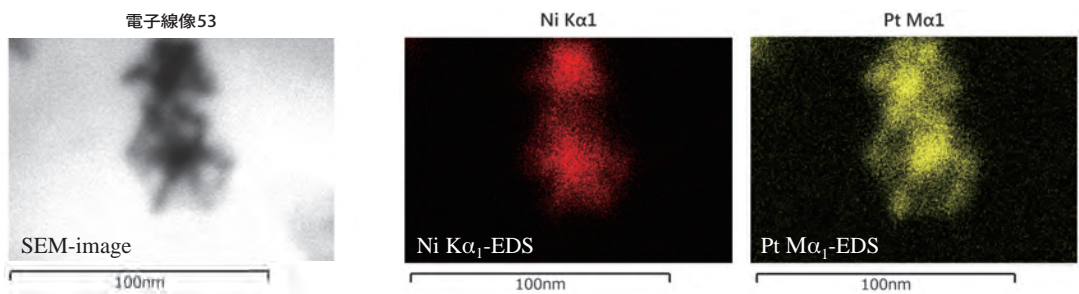
Samples: Prof. Peidong Yang



SE and BSE images (top) from nano frameworks of Ni-Pt alloy (Sample A) and schematic drawing for the shape of the crystal (right).

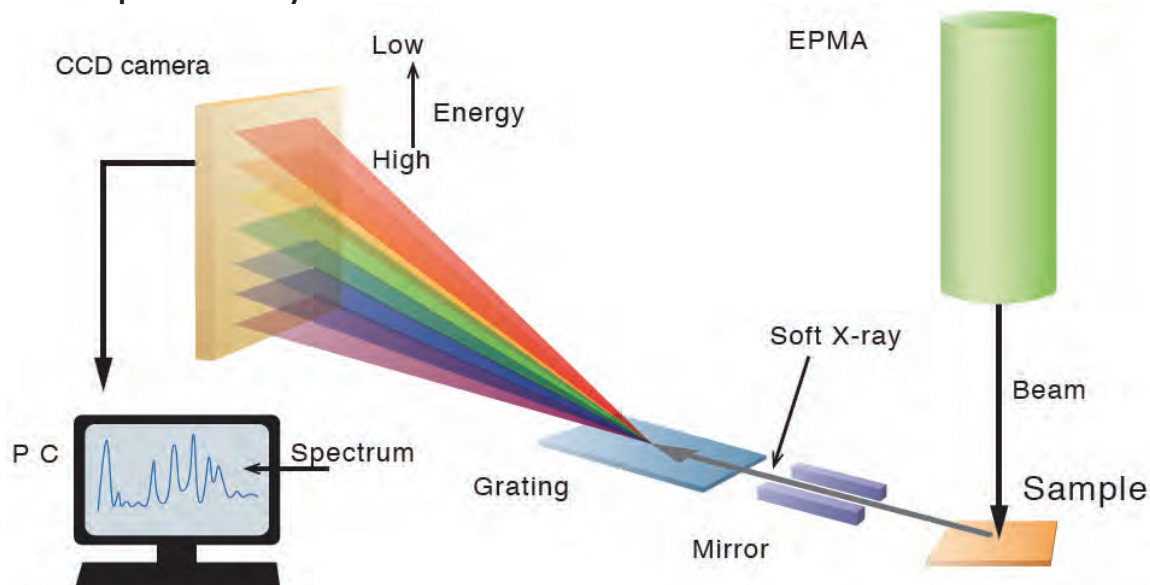
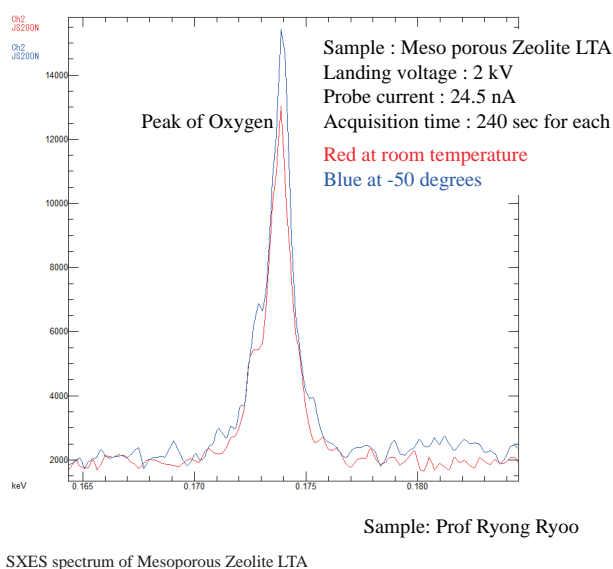


SE image (Landing voltage : 0.5 kV, Sample bias : -5 kV, Detector : UED, WD 2 mm)  
 BSE image (Landing voltage : 5 kV, Detector : UED, Filter bias : -1.2 kV, WD 2 mm)



Landing voltage : 30 kV, Magnification : X1,000,000, EDS : Oxford EDS 150 mm<sup>2</sup>×2+50 mm<sup>2</sup>  
 Samples : Prof. Peidong Yang

SE and BSE images (Top) from nano frameworks of Ni-Pt alloy (Sample C) and elemental mappings of Ni and Pt from the framework (Bottom)

**Fig. 15 Principle of SXES system**

**Fig. 16 SXES spectrum of Mesoporous Zeolite LTA**


## References

- [ 1 ] Z. Liu, N. Fujita, K. Miyasaka, L. Han, S. M. Stevens, M. Suga, S. Asahina, B. Slater, C. Xiao, Y. Sakamoto, M. W. Anderson, R. Ryoo and O. Terasaki: A review of fine structures of nanoporous materials as evidenced by microscopic methods, *Microscopy*, **62** (1): 109-146 (2013).
- [ 2 ] L. Reimer: Image Formation in Low-Voltage Scanning Electron Microscopy, SPIE Press, (1993).
- [ 3 ] M. Kobayashi, K. Susuki, H. Otsuji, Y. Sakuda, S. Asahina, N. Kikuchi, T. Kanazawa, Y. Kuroda, H. Wada, A. Shimojima, K. Kuroda: Direct Observation of the Outermost Surfaces of Mesoporous Silica Thin Films by High Resolution Ultra-Low Voltage Scanning Electron Microscopy, *Langmuir*, **33** (9), pp 2148–2156, (2017).
- [ 4 ] 製品中に含まれる(超)微量成分・不純物の同定・定量ノウハウ - 試料前処理からデータ解釈まで - 第9章 極微小領域の構造観察 第10節 高分解能SEMによるナノ多孔質材の構造観察、技術情報協会(2014) (in Japanese).
- [ 5 ] R. F. Pease; Proc. Of the 9th Symp. On Electron, Ion and Laser beam Technology, p. 176, (San Francisco Press, San Francisco, 1967).
- [ 6 ] J. Frosien, E. Plies and K. Anger: Compound magnetic and electrostatic lenses for low-voltage applications, *J. Vac. Sci. Technol.* **B 7** (6) (1989).
- [ 7 ] C. Mille, E.C. Tyrode and R.W. Corkery: Inorganic chiral 3-D photonic crystals with bicontinuous gyroid structure replicated from butterfly wing scales, *Chem. Commun.*, 2011, **47**, 9873-9875. and Corkery, R. W. and Tyrode, E. C. On the colour of wing scales in butterflies: Iridescence and preferred orientation of single-gyroid photonic crystals. *Journal of the Royal Society, Interface Focus*, **7**, 20160154 (2017).
- [ 8 ] D. Briggs, M. P. Seah, eds., “ Practical Surface Analysis, vol. 1 Auger and X-ray Photoelectron Spectroscopy”, John Wiley & Sons (1990).
- [ 9 ] T. Wang, L. Shi, J. Tang, V. Malgras, S. Asahina, G. Liu, H. Zhang, X. Meng, K. Chang, J. He, O. Terasaki, Y. Yamauchi, J. Ye: Co<sub>3</sub>O<sub>4</sub>-embedded porous ZnO rhombic dodecahedron prepared by the use of zeolitic imidazolate frameworks as precursors for CO<sub>2</sub> photoreduction, *Nanoscale* **8** (12) (2016).
- [ 10 ] S. Asahina, M. Suga, H. Takahashi, H. Y. Jeong, C. Galeano, F. Schuth, and O. Terasaki: Direct observation and analysis of yolk-shell materials using low-voltage high-resolution scanning electron microscopy: Nanometal-particles encapsulated in metal-oxide, carbon, and polymer, *APL Materials* **2**, 113317 (2014).
- [ 11 ] C. Chen, Y. Kang, Z. Huo, Z. Zhu, W. Huang, H. L. Xin, J. D. Snyder, D. Li, Jeffrey A. Herron, M. Mavrikakis, M. Chi, K. L. More, Y. Li, N. M. Markovic, G. A. Somorjai, P. Yang, V. R. Stamenkovic: Highly Crystalline Multimetallic Nanoframes with Three-Dimensional Electrocatalytic Surfaces, *Science*, **343**, 1339-1343, (2014).
- [ 12 ] M. Terauchi, H. Yamamoto and M. Tanaka: *Journal of Electron Microscopy*, **50**, 101, (2001).
- [ 13 ] Y. Sakuda, S. Asahina, M. Ishizaki, T. Togashi and M. Kurihara: Analysis for Nano Porous Material by Scanning Electron Microscopy, *ゼオライト*, Vol. 34, No. 1 (2017) (in Japanese).

# A Top-Down Drawing of the World's Smallest National Flag by JBX-6300FS Electron Beam Lithography System

Nathan Nelson-Fitzpatrick Quantum NanoFab, University of Waterloo

In this article, we will describe the application of electron beam lithography (EBL) to fabricate the world's smallest national flag, as certified by Guinness World Records. As part of this work we will demonstrate that EBL can straightforwardly and easily be applied to the reproduction of arbitrary bitmap images on the nanoscale. While the purpose of this work was to generate publicity for the Institute for Quantum Computing and Canada's 150th anniversary celebration, this work could be applied by novice EBL users to fabricate almost any pattern on the nanoscale.

## Introduction

Electron Beam Lithography (EBL) is a mature technology for the fabrication of submicron structures. Early applications of EBL included the patterning of resist coated chrome on glass plates to support photolithography processes [1]. Mask fabrication continues to be a popular application for EBL with companies like JEOL and IMS targeting multi-beam EBL technologies to enable mask fabrication for the 7 nm technology node [2]. A secondary application for EBL that many academic and research semiconductor fabs have pursued is the direct patterning of substrate samples, so-called Direct Write Electron Beam Lithography (DWEBL) [3].

Currently DWEBL systems take many forms, from SEM systems equipped with a pattern generator [4] all the way to dedicated turn-key systems, designed from the ground up for EBL. The University of Waterloo's Quantum NanoFab recently acquired a JEOL JBX-6300FS purpose-built DWEBL tool [5] to enable our lab members to build quantum and nano-devices on Silicon, III-V materials and other exotic substrates. A photograph of the JBX-6300FS is provided in **Fig. 1**. The JBX-6300FS features:

- 100 kV electron source minimize process blur associated with the forward scattering of electrons in E-beam resist.
- 50 MHz pattern generator for fast operation.
- 19-bit DAC for fine beam stepping within field.
- Interferometer stage and correction of deflection induced beam distortions to enable better than 20 nm stitching and overlay accuracy.

Upon commissioning our JBX-6300FS demonstrated the ability to write 8 nm lines with a 40 nm pitch in a 50 nm thick film of ZEP520A E-beam resist (**Fig. 2**). Seeing these results, we set ourselves the task of trying to pattern the world's smallest national flag via DWEBL.

## Experimental Procedure: Data Flow

The first step in electron beam lithography is to use a computer aided design (CAD) package to define the pattern files that are to be written. As we intended to write a pre-designed pattern (a Canadian flag), we obtained a 1200 by 600 pixel bitmap file of this pattern. Bitmap type files are a typical format for digital images that are commonly encountered, however microelectronics CAD packages do not store images in this manner. To apply our bitmap file, we needed to translate it into a series of polygons which could then be written by the EBL system. Using the LayoutEditor [6] software package, we imported our pattern bitmap file at a resolution of 1 nm/pixel then applied a "merge" function to join smaller boxes and polygons together and reduce polygon count and file size. A top-level design cell was then generated, containing the "merged" image at a number of different magnifications (1x, 2x, 3x, 4x, 5x and 10x). This top-level design was saved in the GDS-II format which is a common format readable by most microelectronics CAD packages.

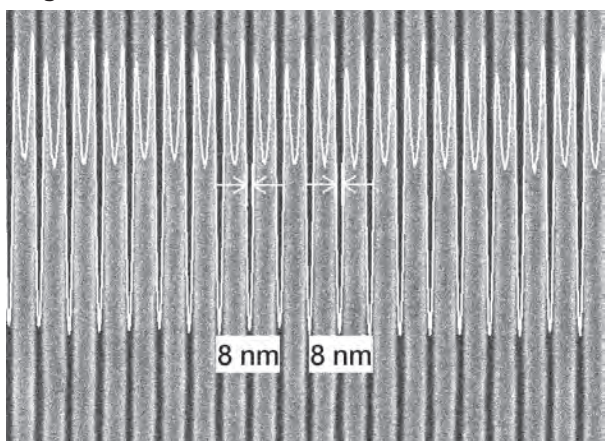
To prepare the GDS-II file for exposure, we then needed to translate it to the machine specific format that can be exposed by our EBL system. The GDS-II file was imported into the BEAMER software package [7]. Within BEAMER, a 2D

**Fig. 1**



JEOL JBX-6300FS Electron Beam Lithography system, as installed at University of Waterloo Quantum NanoFab. Photo credit: University of Waterloo

**Fig. 2**



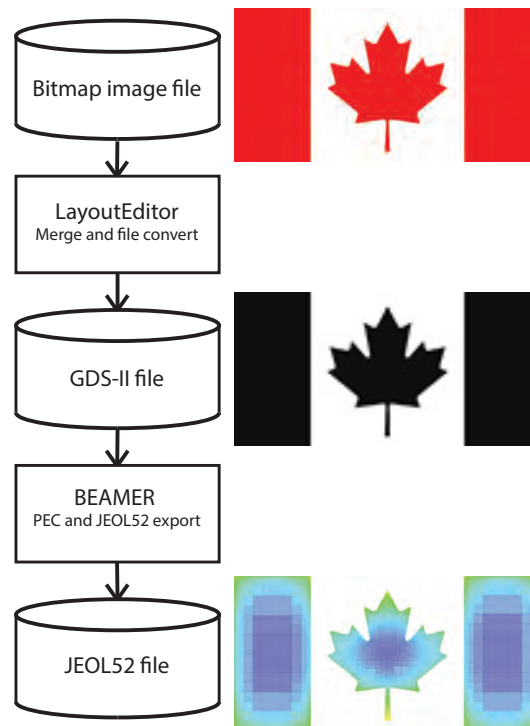
Scanning Electron Micrograph of 8 nm wide lines patterned in a 50 nm thick film of ZEP-520A electron beam resist. Credit: JEOL

proximity effect correction (PEC) was applied to the pattern. Larger instances of the flag pattern did receive dose modulation by the PEC function in order to achieve a uniform exposure. Smaller instances of the flag pattern required no modulation as backscattered electron contribution to dose was nearly uniform over the small pattern area. The pattern and dose modulation table were then exported into the “JEOL52” and “jdi” formats respectively and prepared for writing using the JBX-6300FS’ fifth lens (nanolithography) mode. A schematic summary of the data flow for this project is illustrated in Fig. 3.

### Experimental Procedure: Fabrication Process

The substrate we chose for this experiment was a 100 mm p-type prime Si wafer. Wafers used in this report contained a pre-existing pattern of thermally grown SiO<sub>2</sub> in the shape of the Canada150 logo. A photograph of one of these wafers, loaded onto a JBX-6300FS cassette is provided in Fig. 4. The logo pattern on this wafer was achieved by first taking a clean Si wafer and growing a thermal SiO<sub>2</sub> film on it through a wet thermal oxidation process. The oxidized wafer was

**Fig. 3**



A schematic flow of pattern data, starting with input of a bitmap image and concluding with a machine usable JEOL52 pattern exposure file.

then patterned with a contact mask aligner using a typical UV photolithography process. Reactive ion etching was used to etch the photoresist pattern into the SiO<sub>2</sub> layer. Lastly, photoresist was removed by immersion in acetone and isopropyl alcohol (IPA) followed by O<sub>2</sub> plasma ashing. After this process, the wafers were ready for the E-beam lithography process.

The cleaned wafer was baked on a hotplate for 5 minutes at 120 °C to promote desorption of water vapor. Hydrogen Silsesquioxane also known as HSQ resist [8] was then applied to the wafer by spin casting and was baked on a hotplate for 4 minutes at 80 °C. HSQ is an inorganic, negative tone resist that

becomes an SiO<sub>2</sub>-like film after it is exposed to the electron beam and developed in a basic solution [9]. The resulting resist film was approximately 32 nm in thickness as verified by spectroscopic ellipsometry.

The resist coated wafer was then mounted in the JBX-6300FS electron beam lithography system. A manual global alignment was carried out to align our nanoscale flag pattern with pre-existing alignment marks that were left in the SiO<sub>2</sub> layer. Once aligned to the previous pattern, the nanoscale flag pattern was exposed with a base dose of 2800 μC/cm<sup>2</sup> using the 5th lens. The exposed wafers were then removed from the EBL system and developed in a bath of 25% Tetramethyl ammonium hydroxide (TMAH) for 4 minutes, rinsed under running deionized (DI) water for one minute and then dried in N<sub>2</sub>.

## Fabrication Results and Discussion

The first set of exposures was inspected in a scanning electron microscope (SEM). This initial batch of devices yielded complete nano-scale Canadian flags that had a whole pattern width of 2.4 μm, this represents a 2x magnification of the baseline pattern. The smaller 1x magnification patterns all suffered from breakages in the “stem” of the maple leaf portion of the flag (Fig. 5). The “stem” feature in the CAD file is a gently tapering line that varies in width from 11 nm at the top to 18 nm at the tip of the stem. From the electron micrograph inspection, it was hypothesized that the high aspect ratio of the resist profile in the “stem” (between 2.9:1 and 1.8:1), combined with rinsing in DI water was contributing to this part of the pattern collapsing from capillary forces during the development process. The collapsed “stem” was then likely carried away from the bulk of the flag when the wafer was dried with N<sub>2</sub>.

To solve the pattern collapse, a new version of the maple leaf CAD pattern was developed, manually increasing the width of

the “stem” (a process we will call “shape biasing”). The revised “stem” width now varied between 14 nm and 25 nm. HSQ resist was prepared identically to the first attempt and was exposed on the JBX-6300FS system using identical parameters to the first run. The second set of exposures was developed in the same manner, but after the rinse in DI water the samples were then rinsed in IPA prior to drying. It was hypothesized that the lower surface tension of the IPA would help avoid pattern collapse during the N<sub>2</sub> dry. An electron micrograph of the resulting revised flag pattern is also provided in Fig. 5. A complete listing of this final set of process parameters is provided in Table 1.

The wafer containing the nanoscale Canadian flag (Fig. 6) was then taken to an independent lab for dimensional measurement with SEM. The independent lab determined the size of the whole pattern to be 1.178 μm wide by 591.7 nm tall. An electron micrograph of the independent measurement is provided in Fig. 7. The width of the “stem” (the finest feature on the pattern) was also measured and determined to be approximately 20 nm. This electron micrograph measurement was subsequently submitted to Guinness World Records and recognized as the smallest national flag, with an area of 0.697 μm<sup>2</sup> [10].

## Summary

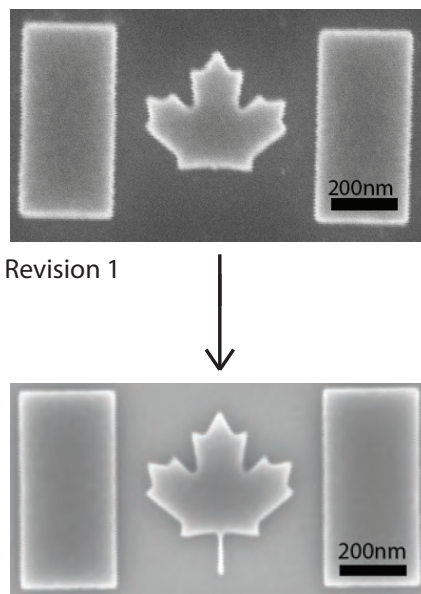
In summary, we were able to apply our JBX-6300FS direct write electron beam lithography system to fabricate the world’s smallest national flag. The flag image was generated by taking a bitmap file of a Canadian flag and converting this for writing in our EBL system. The flag was drawn in a 32 nm thick film of HSQ electron beam resist that was spin cast on a patterned Silicon wafer. The total area of the flag was 0.697 μm<sup>2</sup> and the smallest individual feature (the stem of the maple leaf) was found to be approximately 20 nm wide. The process used in this article could be applied generally to any bitmapped image.

Fig. 4



Photograph of HSQ coated 100 mm wafer with Canada150 logo. Wafer is mounted in cassette prior to exposure in JBX-6300FS. Photo credit: University of Waterloo

Fig. 5



Revision 1

Revision 2

Scanning electron micrographs showing resulting flag patterns after development. First version was rinsed in DI water after development. Second revision was patterned with "shape biased" stem and underwent post-development rinsing in DI water and IPA. Credit: University of Waterloo

**Table 1 Table of electron lithography parameters used in this article**

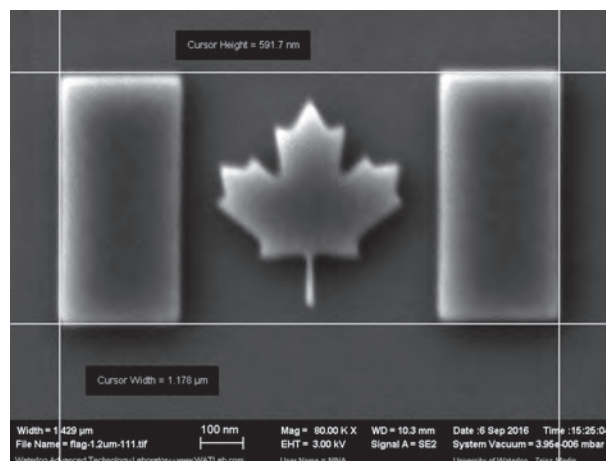
Resist Application	Resist	2 part MIBK: 1 part XR-1541-006
	Prebake step	120 °C for 5 minutes
	Spin step	Spin 5000 RPM for 45 seconds (Ramp 2000 RPM/s)
	Softbake step	80 °C for 4 minutes
Exposure	Base dose	2800 $\mu\text{C}/\text{cm}^2$ at 100 kV
Development	Develop step	TMAH 25% for 4 minutes
	Rinse 1	Flowing DI water, 1 minute
	Rinse 2	IPA, 15 seconds
	Dry step	$\text{N}_2$

**Fig. 6**



Photograph of completed wafer with electron micrograph of nanoscale Canadian flag inset. Photo credit: University of Waterloo

**Fig. 7**



Scanning Electron Micrograph of nanoscale Canadian flag used to certify Guinness World Record. Credit: University of Waterloo

## Acknowledgments

The author would like to acknowledge Natalie Pinchin for design of the UV photomask and for her assistance in preparing wafers prior to Electron Beam processing. The University of Waterloo's Quantum NanoFab was used for this work. This infrastructure would not be possible without the significant contributions of the Canada Foundation for Innovation, Innovation Science and Economic Development Canada, Mike & Ophelia Lazaridis, and the Ontario Ministry of Research & Innovation. Their support is gratefully acknowledged. Funding for this work was also provided by Canadian Heritage.

## References

- [ 1 ] D.R. Herriott, R.J. Collier, D.S. Alles, and J.W. Stafford, IEEE Transactions on Electron Devices, ED-22, 7, (1975).
- [ 2 ] URL : <http://www.businesswire.com/news/home/20170215005023/en/IMS-JEOL-Partner-Provide-World's-Production-Multi-Beam>.
- [ 3 ] M.G. Rosenfield, M.G.R. Thomson, P.J. Coane, K.T. Kwietniak, J. Keller, D.P. Klaus, R.P. Volant, C.R. Blair, K.S. Tremaine, T.H. Newman, and F.J. Hohn, Journal of Vacuum Science and Technology B, 11, 6, (1993).
- [ 4 ] URL: [www.jcnabity.com](http://www.jcnabity.com)
- [ 5 ] URL: <http://www.jeolusa.com/NEWS-EVENTS/Press-Releases/ID/339/New-JEOL-E-Beam-Lithography-System-to-Enhance-Quantum-NanoFab-Capabilities>.
- [ 6 ] Juspertor UG, URL: <https://www.juspertor.com>
- [ 7 ] GenIsys GMBH, URL: <https://www.genisys-gmbh.com/web/>
- [ 8 ] Dow Corning, URL: <http://www.dowcorning.com/applications/search/products/details.aspx?prod=04058447>
- [ 9 ] A E Grigorescu and C W Hagen, *Nanotechnology*, **20**, 292001, (2009).
- [10] URL:<http://www.guinnessworldrecords.com/news/2016/9/canada-shows-exhibits-national-pride-with-a-new-tiny-record-445252>.

# High Temporal Resolution Analysis of Materials Nanoprocess by Materials- and Bio-Science Ultra-High Voltage Electron Microscope at Osaka University

Hidehiro Yasuda    Research Center for Ultra-High Voltage Electron Microscopy, Osaka University

“Materials-and Bio-Science Ultra-High Voltage Electron Microscope” at Osaka University displays its power in investigations of materials science which require high temporal and spatial resolutions, such as observations of specimens with a few micrometer thickness, three dimensional structural analysis in nanometer or picometer spatial scale, in situ observations of materials nanoprocess by microsecond temporal resolution and so on. In the present review, performances of the Materials- and Bio-Science Ultra-High Voltage Electron Microscope will be introduced. As one of the applications, electron-irradiation-induced crystallization in amorphous antimony nanoparticles has been studied by fast in situ UHVEM observations. Both of timescale of the crystallization and its mechanisms will be discussed in detail.

## Introduction

In 2016, the forefront ultra-high voltage electron microscope was newly developed at Research Center for Ultra-High Voltage Electron Microscopy, Osaka University in cooperation with JEOL Ltd. The name is “Materials- and Bio-Science Ultra-High Voltage Electron Microscope”. This ultra-high voltage electron microscope (UHVEM) has two functions of TEM and STEM mode. The great advantage of the UHVEM is to be able to observe specimens with a few micrometer thickness due to deep penetration of high energy electrons. The UHVEM displays its power in microstructural analysis of various electronic devices and biological cells, especially their three dimensional structural analysis in nanometer or picometer scale. This UHVEM is equipped with a high speed direct electron detection camera, and has an advantage to do in situ observations of materials nanoprocess by microsecond temporal and picometer spatial resolution. Additionally, extremely stable cryo-stage is equipped. Biological specimens such as cells or proteins can be observed under a natural condition suppressed from electron irradiation damages, when this stage is effectively combined with the high speed camera.

In the present review, performances of the Materials- and Bio-Science Ultra-High Voltage Electron Microscope will be introduced and results on investigations of nanomaterials process by high temporal and spatial resolutions will be shown as one of the applications.

## What is the Materials-and bio-science ultra-high voltage electron microscope?

The Materials- and Bio-Science Ultra-High Voltage Electron Microscope (JEM-1000EES) is 14 m in height and 330 tons in total weight including the anti-vibrating device, as shown by an overview in **Fig. 1**. The high voltage generator is located on the 2nd floor, the TEM column on the 1st floor and the anti-vibrating device in the underground. **Fig. 2** shows the cross-sectional view. The high voltage generator consists of two tanks, and the tank for housing of the accelerating tube is independent of that of Cockcroft-Walton circuit. The lenses consist of three condenser lenses, a condenser mini-lens, an objective lens, an objective mini-lens, three intermediate lenses and a projective lens. As indicated by a bird's-eye view in **Fig. 3**, the UHVEM is set on the anti-vibrating device consisting of a heavy concrete block about 300 tons in weight. Vibrations from the outside are removed almost, since the UHVEM is floating through air dumpers as shown in **Fig. 4**. Specifications of the UHVEM are shown in **Fig. 5**. The maximum accelerating voltage is 1 MV. The spatial resolution in TEM and STEM mode are 0.16 nm and 1.0 nm, respectively. The image recording systems consist of four digital cameras; a camera for monitoring scintillator, a 1k×1k CCD camera, a 2k×2k CCD camera and a 4k×4k (or an 8k×8k) direct electron detection CMOS camera.

**Fig. 6** shows an example of high resolution images of a

crystalline silicon film. In the lattice image from [110] zone axis, silicon atoms with black contrast are clearly separated by 0.136 nm spacing as referred in the crystalline model. It was confirmed that in the lattice image from [11 $\bar{2}$ 0] zone axis of 6H-SiC, silicon and carbon atoms are separated by 0.11 nm spacing.

One of the specific performances of the UHVEM is that microsecond-scale temporal resolution image recording system is installed. A digital image by 3840×3840 pixels at frame rate from 400 to 1600 per second is able to be recorded by this high sensitive direct electron detection camera. As shown in Fig. 7, Prof. A. Zewail, California Institute of Technology, USA shows achievements of in situ TEM imaging techniques as functions of spatial and temporal resolution in his textbook “4D Electron Microscopy”. In the literature, it is shown that high spatial resolution imaging will advance from video rate imaging to ultrafast imaging [1]. This UHVEM which has the temporal resolution of 625  $\mu$ s / frame is possible to do in situ observation by

**Fig. 1 An overview of the Materials- and Bio-Science Ultra-High Voltage Electron Microscope.**



**Fig. 2 A cross-sectional view of the UHVEM.**

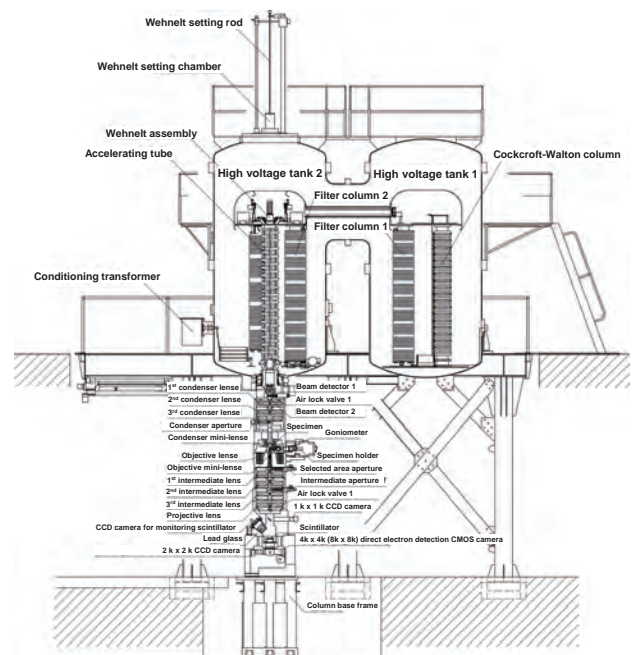


**Fig. 3 A bird's-eye view of the UHVEM.**

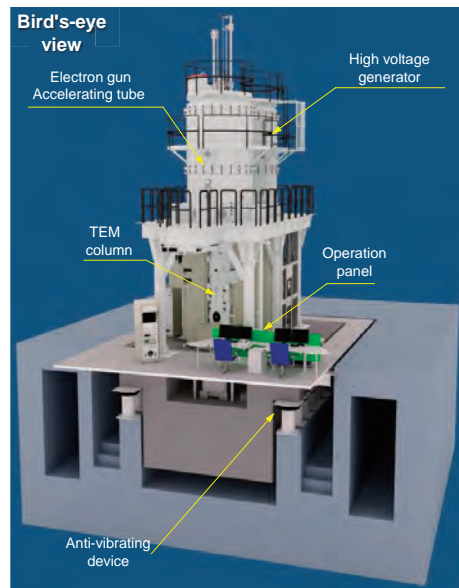


**Fig. 4 Air dumpers of the anti-vibrating device.**



ultrafast imaging region as indicated by the red star in the figure.

Another is that the cryo-stage combined with objective lens is exchangeable as shown in **Fig. 8**. Using the cryo-stage, specimens can be kept at temperature below 100 K and loaded automatically up to maximum 12 specimens on standby at low temperature. This stage is available to electron tomography or single particle analysis.

## Materials research by fast in situ observations

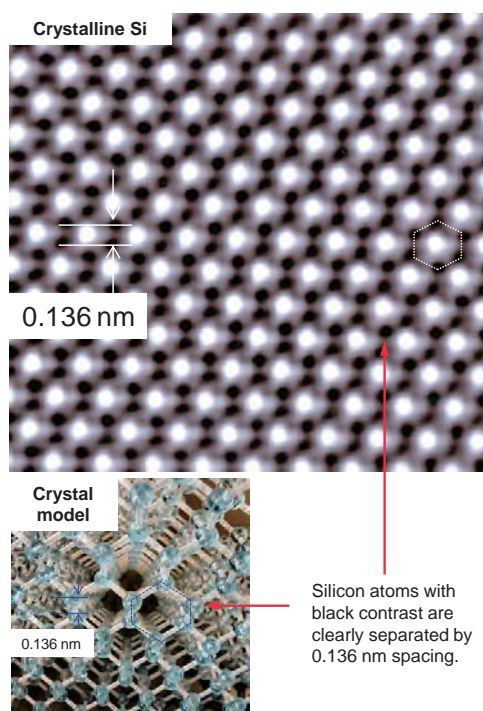
Fast in situ observation by transmission electron microscope is one of useful techniques in researches on phase transformations in materials. This technique plays an important role not only in

basic scientific researches but also in developments of recording materials utilizing phase transformations. In the previous in situ observation techniques, video rate imaging of 30 frames per second is popular [2]. However, developments of transmission electron microscopy with high temporal resolution have been made recently. Electron microscopy with high temporal resolution has already found numerous applications of materials science, in the study of dynamic phenomena such as faster phase transformations, transient states, or chemical reactions [1]. For example, pulsed electron beams make the timescale from nanoseconds to femtoseconds accessible to microscopy with nanometer spatial resolution. At Lawrence Livermore National Laboratory, this technique has been applied the observations of dynamic events with snapshot diffraction and imaging at

**Fig. 5 Specifications of the UHVEM.**

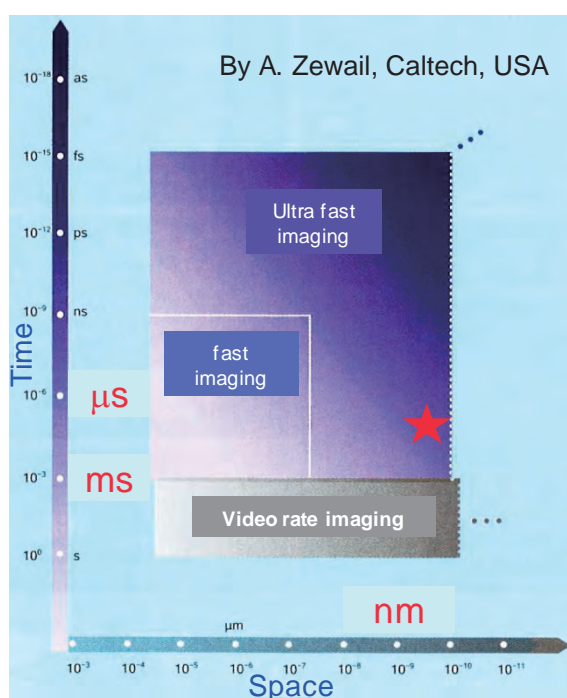
Specifications			
High voltage tank	2 tanks (C-W circuit and electron accelerator )	Objective lens current stability	Less than $5 \times 10^{-7}/\text{min}$
Accelerating voltages(kV)	1000, 800	Magnification (steps in image/diffraction)	
Step of acc. voltage	1 kV step	Low magnification mode	$\times 200 \sim 1,500$ (9)
Emitter	LaB <sub>6</sub>	Magnification mode	$\times 2,000 \sim 1,200$ k (30)
Energy shift	Maximum 3000 V(0.2 V step)	Selected area magnification mode	$\times 20$ k $\sim$ 600 k (10)
Stability of acc. voltage	Less than $8 \times 10^{-7}/\text{min}$ at 1000 kV	Selected area diffraction mode	$\leq 10.0$ nm $\cdot$ mm (10)
Ripple voltage	Less than $4 \times 10^{-7}$ at 1000 kV	Diffraction	$\lambda \cdot L$ (nm $\cdot$ mm)
Maximum beam current	10 $\mu\text{A}$ at 1000 kV	Imaging system (digital camera)	
High voltage insulator gas	SF <sub>6</sub> 0.4 MPa by gauge pressure	Camera for monitoring scintillator	
TEM resolution	Point resolution: 0.16 nm at 1000 kV	1k x 1k CCD camera	
at room temperature	at room temperature	2k x 2k CCD camera	
STEM resolution	1.0 nm at 1000 kV (by edge to edge)	4k x 4k (or 8k x 8k) direct electron detection CMOS camera	
at room temperature			

**Fig. 6 An example of high resolution images of a crystalline silicon film and the crystalline model.**

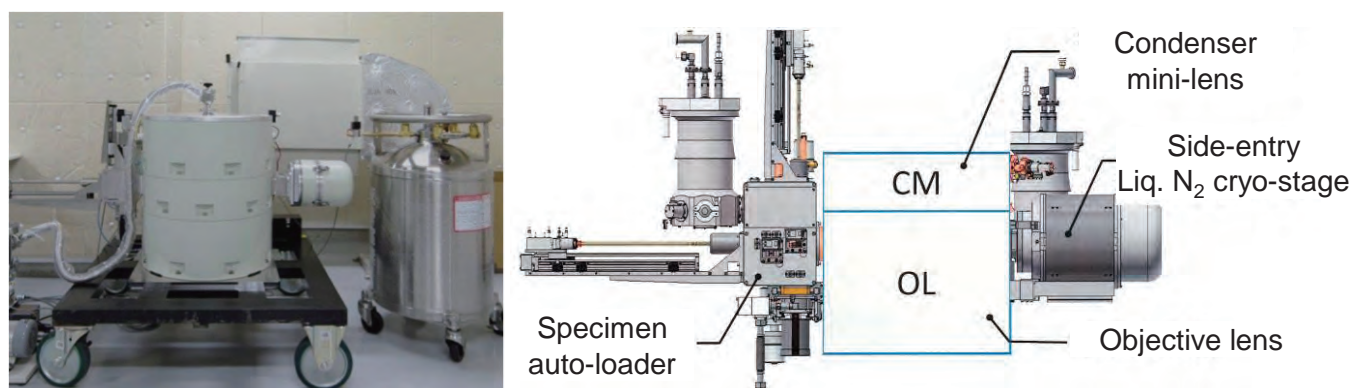


Silicon atoms with black contrast are clearly separated by 0.136 nm spacing.

**Fig. 7 In situ TEM imaging techniques as functions of spatial and temporal resolution [1].**



By A. Zewail, Caltech, USA

**Fig. 8 The cryo-stage combined with objective lens.**

nanosecond temporal resolution, such as crystallization of amorphous germanium film or metallic glass [3, 4], the  $\alpha - \beta$  phase transformation in nanocrystalline Ti [5], solidification in Al thin film [6], mixing in reactive multilayer foil composed of five bilayers of Al/Ni<sub>0.91</sub>V<sub>0.09</sub> [7], and so on. On the other hand, using a continuous electron beam, the microsecond-scale temporal resolution has been reached at atomic resolution by using direct electron detection systems. These recording systems are consisting of both supersensitive imaging system by counting electrons utilizing a position-sensitive electron detector and high speed recording system by processing data utilizing mass storages and servers. Using one of the systems developed, image recording of 1,600 frames per second is possible.

### Analysis of crystallization mechanisms in amorphous antimony nanoparticles

The UHVEM has been applied to observe a crystallization process of an amorphous material. A semi-metallic antimony material, which is utilized as a component of recording materials for optical disk and so on, has been focused here. On the assumption that the recording region is nanometer-sized region of antimony materials, nanoparticles were adopted as an analytic sample.

#### In situ observation of crystallization process

As the background, it was previously evident by our research group that amorphous antimony nanoparticles can be crystallized with ease not only by annealing but also by stimulation from the outside. For example, it was revealed that when a crystalline nucleus consisting of lead atoms which are not reactive with antimony atoms is attached on the surface of an amorphous antimony nanoparticle, crystallization of the amorphous nanoparticles is abruptly induced [8, 9]. On the other hand, researches on phase transformations using knock-on displacements by high energy electrons have also been carried out. In this technique, crystalline-to-amorphous or its reverse phase transformations can be controlled by electron irradiation [10, 11]. Knock-on displacements also become one of the stimulations for the crystallization of the amorphous nanoparticles. In amorphous antimony materials, knock-on displacements of atoms by 1 MeV electrons occur with ease, and crystallization can be induced via atomic displacements [12].

From the above overview, in the present study, electron-irradiation-induced crystallization in amorphous antimony nanoparticles has been studied by fast in situ UHVEM observations. Both of timescale of the crystallization and its mechanisms will be discussed in detail.

Preparation of size-controlled amorphous antimony nanoparticles was carried out using an evaporator installed in a specimen chamber of a conventional TEM. The evaporator consists of a spiral-shaped tungsten filament. An amorphous carbon film mounted on a copper grid was used as a supporting film. Using this evaporator, antimony was evaporated from the filament to produce nm-sized antimony nanoparticles on the supporting film. Electron irradiation experiments and the simultaneous in situ observations were carried out by JEM-1000EES UHVEM operating at an accelerating voltage of 1 MV, and the electron flux of the order of approximately  $10^{24} \text{ e} \cdot \text{m}^{-2} \text{ s}^{-1}$ , which was equipped with Gatan K2-IS direct electron detection CMOS camera. The time for one frame was 625  $\mu\text{s}$ . The base pressure in the specimen chamber was below  $1 \times 10^{-5} \text{ Pa}$ , and is enough low to keep oxidation in the specimens negligibly slow.

Atomic scale observations by high resolution electron microscopy were carried out. **Fig. 9** shows several snapshots during crystallization in an about 20 nm sized nanoparticle. A bandpass Fourier transform filtering of snapshots were done in order to remove the noise and enhance the contrast of a nanoparticle. In Fig. 9(a), an amorphous antimony nanoparticle before crystallization shows a salt and pepper contrast. The difference in the contrast between an amorphous antimony nanoparticle and an amorphous carbon substrate is small because of small number of electrons to capture an image. In the fast Fourier transformation (FFT) pattern from the particle, a halo ring which indicates an amorphous structure is recognized. The particle in Fig. 9(b) indicates the same one after 8125  $\mu\text{s}$  under electron irradiation. As indicated by a red arrow, an approximately 2 nm-sized crystalline nucleus appears in a part of the particle, and in the corresponding FFT pattern, two weak spots as indicated by yellow arrows appear superimposed on the halo ring. From Fig. 9(c) to (e), the nucleus in the particle repeats to disappear and appear at irregular time intervals. Weak two or four spots are sometimes recognized as indicated yellow arrows in the individual FFT patterns, and correspond to a nucleation of the small crystal. In Fig. 9(f), the nucleus grows up to approximately 5 nm in diameter, and after that, the amorphous nanoparticle crystallizes in the whole nanoparticle as indicated in Fig. 9(g) and (h). In the FFT patterns, the weak four spots change to an obvious net pattern. It is indexed as the  $[2\bar{2}1]$  zone axis pattern of an antimony crystal which has a hexagonal structure with the lattice constants of  $a_0=0.43 \text{ nm}$  and  $c_0=1.13 \text{ nm}$ . From the results of Fig. 9(f) to (h), in the 20 nm-sized particle, the velocity of crystalline-amorphous interface migration after the formation of an approximately 5 nm-sized nucleus is estimated to be approximately  $20 \mu\text{m s}^{-1}$ . The schematic illustration of the crystallization process is attached in

**Fig. 9** Several snapshots of atomic scale observations during crystallization in an approximately 20 nm-sized amorphous antimony nanoparticle. A schematic illustration of the crystallization process is attached.

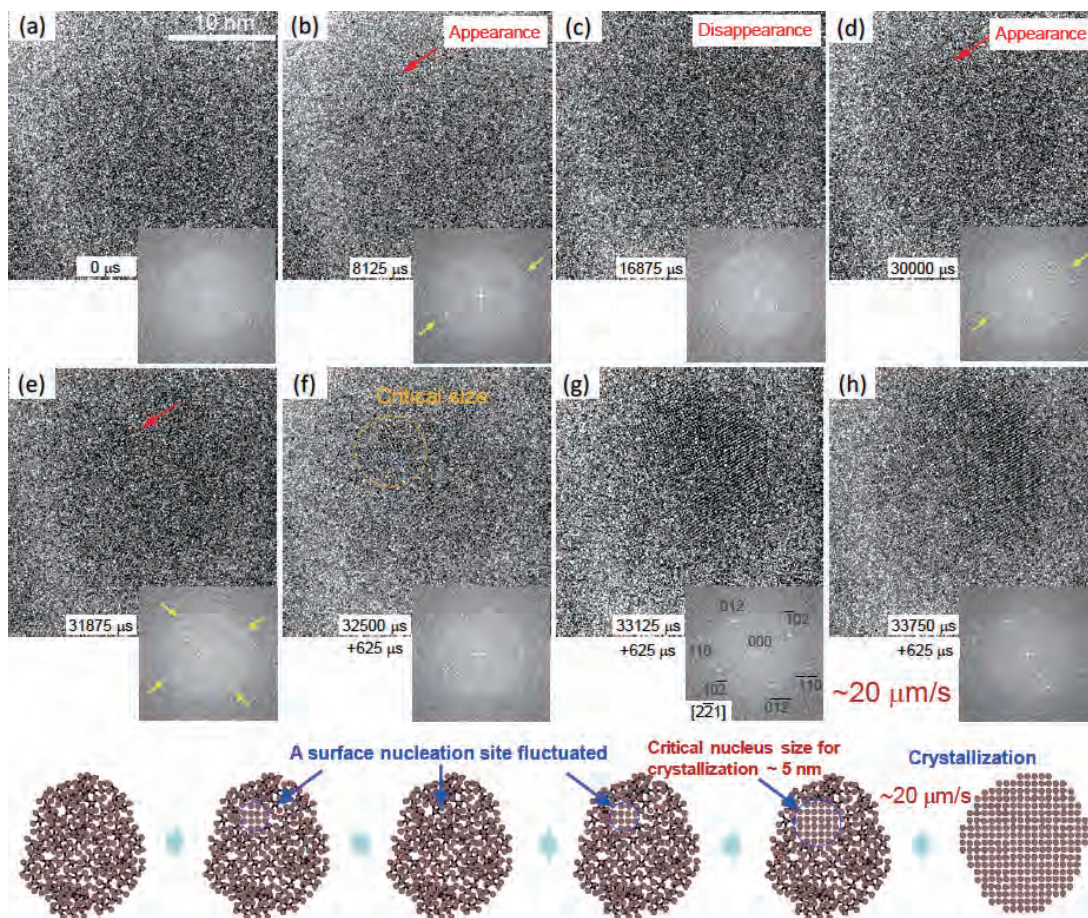


**Fig. 10** A series of snapshots of bright field images during migration of interface between an amorphous and crystalline phase in an approximately 60 nm-sized nanoparticle. A schematic illustration of interface migration during crystallization of the amorphous antimony nanoparticle is attached.

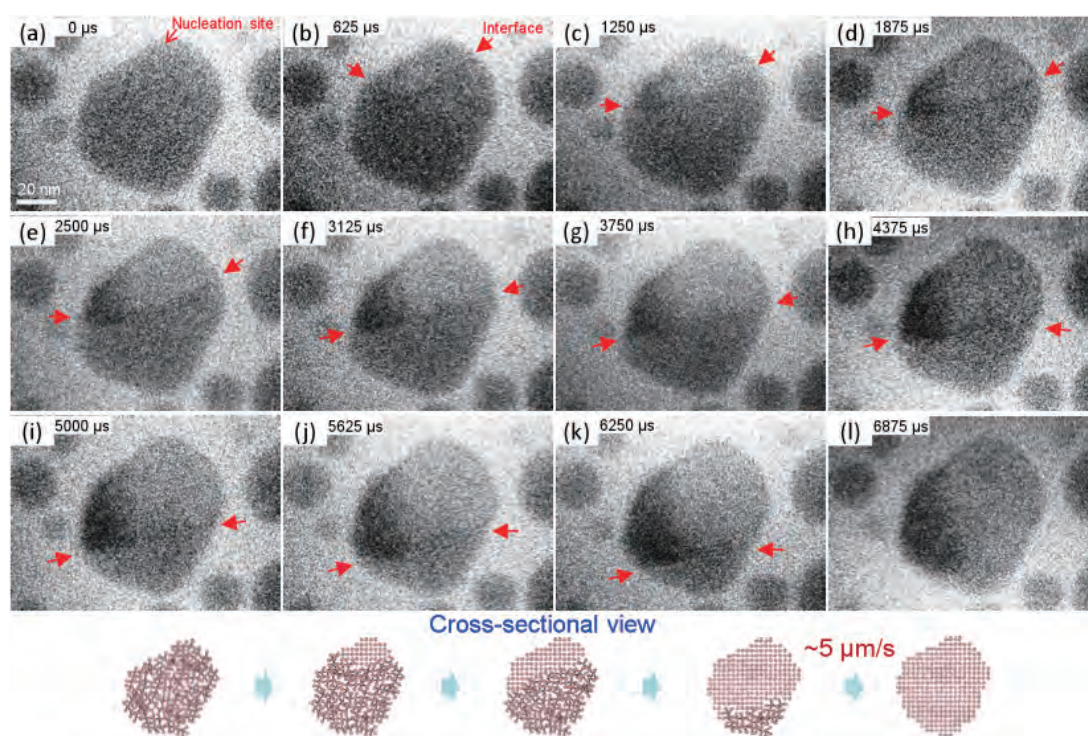


Fig. 9. At the early stage of the crystallization, a small nucleus on the particle surface fluctuates between an appearance and a disappearance. When the nucleus size becomes more than the critical size of approximately 5 nm in diameter, the crystallization quickly takes place in the amorphous particle over all.

#### Atomic diffusivity during crystal growth

The Fig. 10 shows a typical example of bright field images during migration of an interface between an amorphous and crystalline phase in an approximately 60 nm-sized particle. The time interval of the individual snapshots is 625  $\mu\text{s}$ . From a comparison of Fig. 10(a) with (b), a crystalline nucleation site is located on the particle surface. In Fig. 10(b) ~ (k), the two red arrows indicate the across lines of surface with the interface between the amorphous and crystalline phase. At the early stage of the crystallization, the interface has a small curvature as shown in (b) ~ (f), but from the steady state to final stage of (g) ~ (l), the interface becomes flat. The velocity of the interface migration during the steady state is estimated to be approximately 5  $\mu\text{m s}^{-1}$ . The schematic illustration of interface migration during crystallization of the amorphous antimony nanoparticle is attached in Fig. 10. From the result, it is evident that the crystallization gradually proceeds from a surface nucleation site. As compared with the result in Fig. 9, the velocity of the interface migration depends on the particle size, and it was confirmed that the smaller the particle size is, the faster the velocity is.

After a formation of a crystalline nucleus with a critical size, an interface between the crystalline and amorphous phase migrates toward the amorphous phase. Fig. 11 shows distance from the crystalline nucleation site to the interface as a function of time. In amorphous materials, a crystalline nucleus diameter  $d$  is indicated by the equation of  $d = \sqrt{Dt}$ , where  $D$  is diffusion coefficient and  $t$  is time. A value of  $D$  is estimated to be  $5.2 \times 10^{-13} [\text{m}^2 \text{s}^{-1}]$  by fitting data at the early stage of crystallization in Fig. 11 using the equation. On the other hand, self-diffusion coefficient of bulk antimony is estimated by  $D_{\text{bulk}} = 2.21 \times 10^{-3} \exp(-2.37 \times 10^4 / T)$ , where  $T$  is temperature [13]. Extrapolation of this relationship to 300 K gives a value of  $1.08 \times 10^{-37} [\text{m}^2 \text{s}^{-1}]$ . It can be revealed that the antimony self-diffusivity in nanoparticles observed here is at least  $10^{24}$  larger than that in bulk antimony. This fact on the fast diffusivity suggests that crystallization in pure elemental amorphous nanoparticles such as amorphous antimony nanoparticles takes place not by long range atomic diffusion but

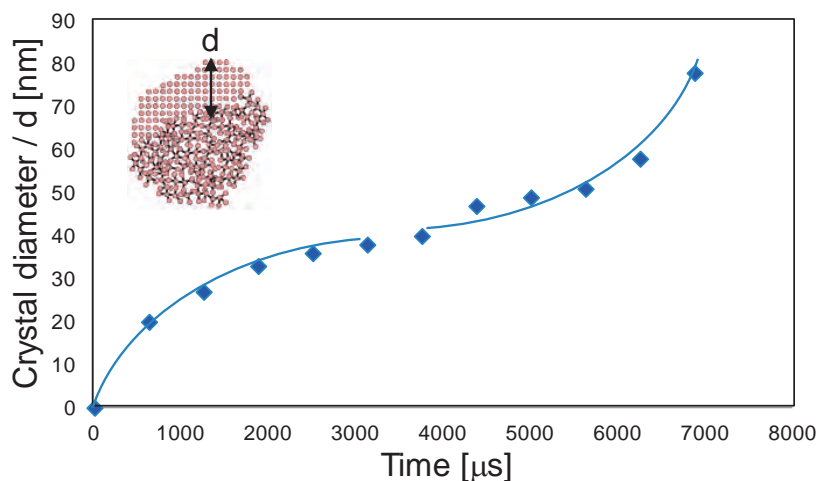
by short range atomic displacements.

#### Crystalline nucleation and growth mechanisms

In the present experiments, microsecond temporal and picometer spacial scale in situ observations have been achieved firstly by the ultra-high voltage electron microscope equipped with direct electron detection camera. The candidate mechanisms of crystallization in amorphous antimony nanoparticles are proposed based on the fast timescale observations. Crystallization of amorphous materials proceeds by the processes of crystalline nucleation and growth. The free energy difference in a crystalline nucleation of a bulk amorphous system  $\Delta G$  is indicated by the following equation  $\Delta G = (4\pi r^3/3) \Delta G_v + 4\pi r^2 \sigma$ , based on the classical homogeneous nucleation theory, where  $r$  is radius of a crystalline nucleus,  $\Delta G_v$  free energy reduction per unit volume by the nucleation,  $\sigma$  interfacial energy per unit area between the crystalline nucleus and amorphous matrix. In this theory, when the crystalline nucleus size is smaller than a critical size, the free energy difference in the crystalline nucleation becomes positive value. Consequently, the nucleus is not stable and repeats between appearance and disappearance. In the case that a size of a crystalline nucleus becomes larger than a critical size, the nucleus will survive and grow stably [14].

At first view, an appearance and disappearance of a crystalline nucleus explained by classical homogeneous nucleation theory appear to be observed in the present study. However, free energy changes in nanometer-sized system are remarkably sensitive to the local structural changes such as a crystalline nucleation. An amorphous matrix near the interface of a crystalline nucleus with the amorphous phase in the nanoparticle is going to grow epitaxially with the crystalline interface, and consequently elastic strain is induced in the amorphous matrix. Such an elastic interaction is long range interaction over all a nanoparticle and leads to decrease the interfacial energy. An absolute critical crystalline nucleus size described by the free energy changes originated from local formation of steep interface based on the classical homogeneous nucleation theory may not be defined under such a nanoscale condition. The critical crystalline nucleus size changes depending on the system size. From the effect of the long range interaction, the crystallization in amorphous nanoparticles is not controlled by the two-step mechanism, in which a crystalline nucleation and the consequent growth take place by trade-off between the free energy and interfacial energy of the nucleus with a critical size. It is suggested that a

Fig. 11 Distance from the crystalline nucleation site to the interface as a function of time.



cooperative phenomenon by the long range elastic interaction becomes the driving force of the crystal growth induced almost simultaneously with a crystalline nucleation.

Generally in amorphous materials, activation energy during incubation at an early nucleation stage of crystallization  $\Delta E$  is equivalent to that during the consequent crystal growth, and accordingly the atomic diffusion during incubation and growth are controlled by the same mechanism [15]. Especially, in pure elemental amorphous materials the atomic diffusion is controlled by short range atomic displacements mentioned above, and the nucleation and growth will proceed simultaneously.

**Fig. 12** shows a schematic illustration of the crystalline nucleation and growth processes as functions of free energy and reaction coordinate. The free energy in an amorphous phase  $E_{Am}$  is higher than that in a crystalline phase  $E_{Cry}$ . A driving force to overcome the activation energy for crystallization  $\Delta E$  is supplied by the free energy increasing by the long range elastic interaction near the amorphous-crystalline interface in the nanoparticle  $\Delta E_e$ . As indicated by the figure, when the size of the crystalline nucleus is smaller than a critical size for crystallization, the elastic interaction is localized around the nucleus, but with increasing the nucleus size, the elastic interaction affects all over the nanoparticle. As soon as the elastic interaction energy  $\Delta E_e$  is larger than the activation energy  $\Delta E$ , crystallization takes place epitaxially from the crystalline nucleus with a critical size by short range atomic displacements like a domino toppling.

## Summary

The Materials-and Bio-Science Ultra-High Voltage Electron Microscope has enabled us to investigate materials science at high temporal and spatial resolutions. In biological science, specimens such as cells can be observed under a natural condition using extremely stable cryo-stage. In future, the specific performances will be applied to the advanced researches.

## Acknowledgments

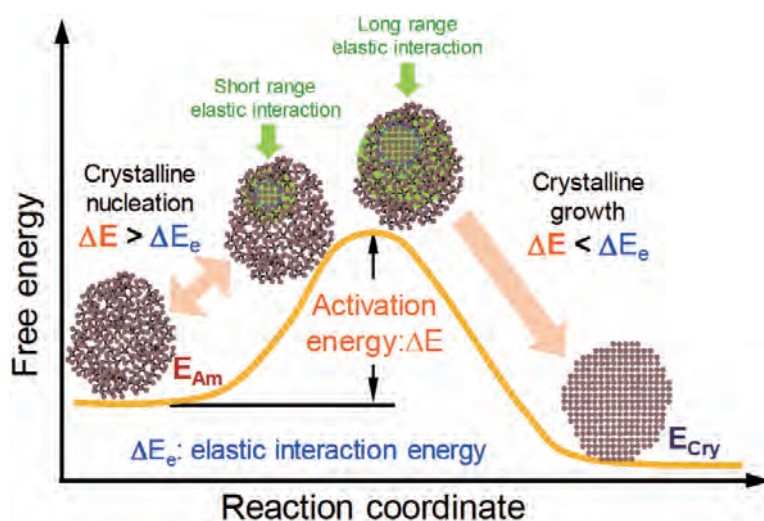
The author is grateful to kind support to construct the Materials- and Bio-Science Ultra-High Voltage Electron

Microscope by Shigemasa Ohta, Akihiro Ohsaki, Yusuke Agatsuma, Sadayuki Takakuwa, Mitsuaki Ohsaki and the JEM-1000EES UHVEM project members at JEOL Ltd.

## References

- [ 1 ] A. Zewail and J. Thomas, "4D Electron Microscopy", Imperial College Press, (2010).
- [ 2 ] D. Jacobsson, F. Panciera, J. Tersoff, M. C. Reuter, S. Lehmann, S. Hofmann, K. A. Dick and F. M. Ross, *Nature*, **531** (2016) 317.
- [ 3 ] L. Nikolova, T. LaGrange, B. W. Reed, M. J. Stern, N. D. Browning, G. H. Campbell, J.-C. Kieffer, J. Siwick and F. Roseil, *Appl. Phys. Lett.*, **97** (2010) 203102.
- [ 4 ] T. LaGrange, D. S. Grummon, B. W. Reed, N. D. Browning, W. E. King, and G. H. Campbell, *Appl. Phys. Lett.*, **94** (2009) 184101.
- [ 5 ] T. LaGrange, M. R. Armstrong, K. Boyden, C. G. Brown, G. H. Campbell, J. D. Colvin, W. J. DeHope, A. M. Frank, D. J. Gibson, F. V. Hartemann, J. S. Kim, W. E. King, B. J. Pyke, B. W. Reed, M. D. Shirk, R. M. Shuttlesworth, B. C. Stuart, B. R. Torralva, and N. D. Browning, *Appl. Phys. Lett.*, **89** (2006) 044105.
- [ 6 ] A. Kulovits, J. M. K. Wiezorek, T. LaGrange, B. W. Reed and G. H. Campbell, *Philos. Mag. Lett.*, **91** (2011) 287.
- [ 7 ] J. S. Kim, T. LaGrange, B. W. Reed, M. L. Taheri, M. R. Armstrong, W. E. King, N. D. Browning and G. H. Campbell, *Science*, **321** (2008) 1472.
- [ 8 ] H. Yasuda and H. Mori, *Phys. Rev. Lett.*, **69** (1992) 3747.
- [ 9 ] H. Yasuda and H. Mori, *Thin Solid Films*, **298** (1997) 143.
- [ 10 ] G. Thomas, H. Mori, H. Fujita and R. Sinclair, *Scripta Met.*, **16** (1982) 589.
- [ 11 ] S. Anada, T. Nagase, K. Kobayashi, H. Yasuda, H. Mori, *Acta Mater.*, **71** (2014) 195.
- [ 12 ] H. Yasuda and K. Furuya, *Philos. Mag. A*, **80** (2000) 2355.
- [ 13 ] L. A. Gilifalco, "Atomic Migration in Crystals", Blaisdell, Waltham, MA, (1964).
- [ 14 ] F. F. Abraham, "Homogeneous nucleation theory", Academic Press, NY, (1974).
- [ 15 ] A. K. Varshneya, "Fundamentals of Inorganic Glasses", Academic Press, (1994).

**Fig. 12 A schematic illustration of the nucleation and growth processes in an amorphous antimony nanoparticle by free energy and reaction coordinate diagram.**



# A Quantitative Analytical Method “Effective Magnetic Moment Method” Based on Both Curie- Weiss Law and ESR Fundamental Equation

Nobuhiro Matsumoto

National Metrology Institute of Japan (NMIJ), National Institute of Advanced Industrial Science and Technology (AIST)

“Primary direct method for amount of substances” is a quantitative analytical method which purity or concentration of chemicals can be obtained from physical quantities measured by experiments and physical constants. Three potential primary direct methods - gravimetry, coulometry, and, freezing point depression method - play an important role in both analytical chemistry and metrology-in-chemistry. In this study, a quantitative analytical method “effective magnetic moment method” has been proposed for future 4th primary direct method. The principle of this method uses difference of temperature dependences of magnetic moments between unpaired electrons and “closed-shell electrons”. The unpaired electrons show the magnetic moment obeying Curie-Weiss law. Effective magnetic moment, which is magnitude of “mini magnet” due to the unpaired electrons, is obtained using g-value from ESR fundamental equation. Combination of both the scientific laws gives number of quantum free spins (atoms with unpaired electrons, or, free radicals) existing among atoms with only the closed-shell electrons. This review will firstly introduce quantification of gadolinium (III) ions in diamagnetic materials for experimental validation on the principle of the “effective magnetic moment method”. After that, purity analyses as free radicals will be tried for three stable high-purity organic compounds with a nitroxyl radical moiety by the “effective magnetic moment method”. This method has a possibility to develop reference materials with certified values traceable to the International System of Units (SI), for quantitative analysis using ESR spectrometers, or, other analytical instruments.

## Introduction

*Analytical chemistry and Potential primary direct methods for amount of substance*

‘Analytical chemistry’ is a measurement science consisting of a set of powerful ideas and methods that are useful in all fields of science and medicine [1]. ‘Quantitative analysis’ determines the relative amounts of species in a sample, or, analytes, in numerical terms. ‘Potential primary methods of measurement for the amount of substance’ are fundamental quantitative analytical methods and play an important role in both analytical chemistry and metrology-in-chemistry [2]. The ‘metrology-in-chemistry’ means a measurement science related to mole (mol), which is one of the SI base units. In the field of analytical chemistry, the term “absolute method” is used to describe a technique similar to the potential primary method in metrology-in-chemistry,

a method of chemical analysis that bases characterization completely on standards defined in terms of physical properties [3]. These potential primary methods can produce many certified reference materials (CRMs) that are traceable to the International System of Units (SI).

There are two types of potential primary method [2, 4]. One is a potential primary direct method, which can measure an unknown concentration without reference to a standard of the same quantity. The gravimetry, coulometry, and, freezing point depression method listed in table 1(a) are potential primary direct methods for amount of substance that are approved by the Consultative Committee for Amount of Substance (CCQM) under the Comité International des Poids et Mesures (CIPM) [2, 4]. **Table 1(a)** summarizes the features of each potential primary direct method [4, 5]. Faraday’s law and the van’t Hoff equation provide the bases for the coulometry and the freezing point depression methods, respectively. Applicable main

target substances are different for each primary direct method. Each potential primary method is described by a measurement equation. For example, in the equation of coulometry, the amount of substance of metal ions can be obtained from the number of coulombs, the Faraday's constant and the valency number of an ion.

The other type of potential primary method is 'primary ratio methods', such as titrimetry and isotope dilution mass spectroscopy. These primary ratio methods need CRMs assigned by the potential primary direct methods described above, in order to link them to the SI. Quantitative NMR spectroscopy [5] and neutron activation analysis [6] also need such CRMs.

#### Idea of "effective magnetic moment method"

All potential primary direct methods in table 1(a) are applicable to a sample with large numbers of atoms more than the Avogadro's number and are based on well-established and reliable scientific laws, nowadays. An adiabatic calorimeter [7-8] used for the freezing point depression method is also well-used high accuracy calorimeter in a field of solid-state physics, which part of it was my previous research field. The analytical chemistry and the solid-state physics are quite different research areas. However, there seems to be a kind of connection between the two research areas. In an experimental procedure of my previous research, transition-metal compounds were synthesized and then their electronic conductivity and magnetic susceptibility were measured [9-14]. In addition, as appropriate, thermodynamic properties such as specific heat were measured by research collaborators. These physical quantities are representative macroscopic physical properties.

Let's go back to table 1(a). There was a question 'While there are the primary direct method using electric property and the primary direct method using thermodynamic property, why is

there no primary direct method using any magnetic property?' This study has proposed a magnetic quantitative analytical method, "effective magnetic moment method", described in table 1(b), as a future potential primary direct method candidate [15-16]. This method is based on Curie-Weiss law (Curie law), which is a well-known and well-established law in the field of electronic paramagnetism [17-18]. There are three representative types of electronic paramagnetic properties: Langevin paramagnetism (for free quantum spin), Pauli paramagnetism (due to electron conduction in metal), and Van Vleck paramagnetism. While both the Pauli paramagnetism and Van Vleck paramagnetism show temperature-independent positive magnetic susceptibility, Langevin paramagnetism exhibits a temperature dependence of magnetic susceptibility that obeys Curie-Weiss law. Examples of compounds with Langevin paramagnetism include rare earth ions, transition metal ions, and organic free radicals. In contrast, many materials have only diamagnetism, such as ionic salts and organic compounds with no free radicals. Such materials show temperature-independent magnetic susceptibilities due to "closed-shell electrons", which is originated from Langevin diamagnetism equation [17]. The "effective magnetic moment method" proposed in this study utilizes the difference in temperature-dependence between the Langevin paramagnetism and the diamagnetism.

#### Principle of "effective magnetic moment method"

Principle of the effective magnetic moment is abstractly illustrated in figure 1. Let a constant magnetic field of strength  $H$  ( $A \cdot m^{-1}$ ) be applied to a sample (atoms). The sample consists of atom A with both unpaired electron and "closed-shell electrons", and atom B with only the closed-shell electrons, as shown in figure 1(a). Let  $W$  (g) and  $T$  (K) be the total mass and

**Table 1**

Name of method	(a) Potential primary direct method approved by CCQM [2, 4-5]			(b) "effective magnetic moment method"
	Gravimetry	Coulometry	Freezing point depression method	
Field	Inorganic chemistry	Electrochemistry	Thermodynamics	Solid state physics (Magnetism)
Outline of analytical method	setting quantity of specified substances in solution is measured.	amount of electricity used in electrolysis of specified substances is measured.	relationship between fraction melted and temperature around the melting point is measured.	relationship between magnetic moment and temperature around thermal energy much higher than magnetic energy is measured.
Law	-	Faraday's law	Van't Hoff's equation	Curie-Weiss's law ESR fundamental equation
Analyte	inorganic salts	metallic elements	high purity organic liquids	rare earth ions, transition metal ions, organic free radicals
Measurement equation	$n_g = w M_w^{-1}$ <sup>a</sup>	$n_q = Q (zF)^{-1}$ <sup>b</sup>	$x_p = 1 - \frac{\Delta_{fus} H \Delta T}{RT_0^2}$ <sup>c</sup>	$n = 3k_B c_{Curie} (\mu_B \mu_{eff}^2 H)^{-1}$ <sup>d</sup>
Main equipment	balance	titration system	adiabatic calorimeter	Magnetometer ESR spectrometer

<sup>a</sup>  $n_g$  is amount of substance.  $w$  is mass.  $M_w$  is molar mass.

<sup>b</sup>  $n_q$  is amount of substance.  $Q$  is number of coulombs.  $z$  is the valency number of an ion.  $F$  is Faraday's constant.

<sup>c</sup>  $x_p$  is purity.  $\Delta_{fus} H$  is molar enthalpy of fusion.  $\Delta T$  is the melting-point depression.  $R$  is the gas constant.  $T_0$  is the melting point of the pure main component.

<sup>d</sup>  $n$ ,  $k_B$ ,  $c_{Curie}$ ,  $\mu_B$ ,  $\mu_{eff}$ , and  $H$  are described in principle section of this paper

Features of potential primary direct methods for amount of substances.

(a) Three potential primary direct method approved by CCQM. (b) "Effective magnetic moment method" proposed in this study.

temperature, respectively.

The magnetic moment of the mixture,  $m$ , is measured with a magnetometer. It is assumed that  $m$  is proportional to  $H$ , if  $H$  varies and other environmental parameter such as temperature is constant.  $m$  ( $A \cdot m^2$ ) is expressed by the following equation:

$$m = m_{T,A} + m_{0,A} + m_{0,B} + m_{0,bg}, \dots\dots\dots(1)$$

where  $m_{T,A}$  is the temperature-dependent magnetic moment due to the Langevin paramagnetism of unpaired electrons, and  $m_{0,A}$ ,  $m_{0,B}$ , and  $m_{0,bg}$  are the temperature-independent magnetic moments due to the diamagnetism of the closed-shell electrons of atom A, atom B and background, respectively. In the right-hand side of this equation, the terms were independently summed under an assumption that there is no interaction between the terms.

The atom A has free quantum spins originated from unpaired electrons, which cause Langevin paramagnetism in agreement with the Curie-Weiss law. According to this law, the magnetic susceptibility is proportional to the inverse of  $(T-\Theta)$ , where  $\Theta$  is the Weiss temperature. When  $T$  is much greater than  $\mu_B B/k_B$  (where  $\mu_B$  and  $k_B$  are Bohr magneton and Boltzmann's constant, respectively.  $B$  is magnetic flux density and equals to  $\mu_0 H$ .  $\mu_0$  is the magnetic permeability of free space.), the Curie-Weiss law is applicable:

$$M_{T,A} \cdot H^{-1} = C_{Curie} \cdot (T-\Theta)^{-1}, \dots\dots\dots(2)$$

where the volume magnetization,  $M_{T,A}$ , is  $m_{T,A}$  divided by the sample volume and  $C_{Curie}$  is the Curie constant per unit volume.  $C_{Curie}$  is  $N_v \mu_0 \mu_{eff}^2 / (3k_B)$ , where  $N_v$  is the number of atoms (or ions, each possessing an effective magnetic moment of  $\mu_{eff}$  in  $\mu_B$  per formula unit) with free quantum spins per volume. The effective magnetic moment  $\mu_{eff}$  is theoretically given by

$$\mu_{eff} = g_J [L(J+1)]^{1/2} \mu_B \equiv p \mu_B, \dots\dots\dots(3)$$

where  $g_J$  is the Landé g-value,  $J$  is the total angular momentum quantum number, and  $p$  is the theoretical effective magnetic moment in units of  $\mu_B$  (effective magneton number). Both  $g_J$  and  $J$  are calculated on the basis of the electron configuration by using both the Pauli exclusion principle and Hund's rule. Equation 2 is rewritten as

$$m_{T,A} H^{-1} = n \mu_0 \mu_{eff}^2 [3k_B (T-\Theta)]^{-1}, \dots\dots\dots(4)$$

where  $n$  is the number of atoms (or ions, each possessing an effective magnetic moment of  $\mu_{eff}$  in  $\mu_B$  per formula unit) with free quantum spins in sample.

By using equation 4, equation 1 is expressed as

$$m = n \mu_0 \mu_{eff}^2 H [3k_B (T-\Theta)]^{-1} + m_{0,A} + m_{0,B} + m_{0,bg}, \\ = c_{Curie} (T-\Theta)^{-1} + m_0, \dots\dots\dots(5)$$

where  $c_{Curie} = n \mu_0 \mu_{eff}^2 H / (3k_B)$  and  $m_0 = (m_{0,A} + m_{0,B} + m_{0,bg})$ .  $c_{Curie}$  is  $C_{Curie}$  multiplied by both magnetic field and volume. The experimental values of  $c_{Curie}$ ,  $\Theta$ , and  $m_0$  are obtained by nonlinear regression analysis [19-21] of the  $m$  vs.  $T^{-1}$  plot. This regression analysis can separate contribution due to unpaired electrons and contribution due to the closed-shell electrons, as shown in Figure 1 (b). In the figure 1(b), an  $m$  vs  $(T-\Theta)^{-1}$  plot is shown for understandability. The measurement equation for this "effective magnetic moment method" is

$$n = 3k_B c_{Curie} (\mu_0 \mu_{eff}^2 H)^{-1}, \dots\dots\dots(6)$$

The analytical mass fraction of  $Gd_2O_3$  in the sample,  $x_{anal}$ , is given by

$$x_{anal} = n M_{analyte} (n_{molecule} N_A)^{-1} W^{-1}, \dots\dots\dots(7)$$

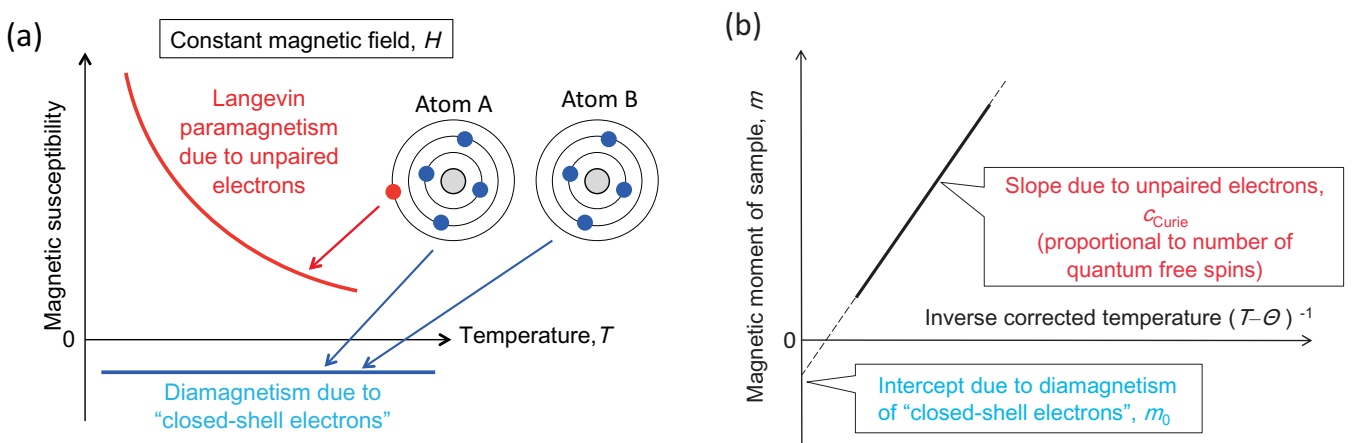
where  $M_{analyte}$  is the molar mass of the analyte A,  $n_{molecule}$  is the number of atoms (each possessing  $\mu_{eff}$ ) in a molecule of the analyte, and  $N_A$  is Avogadro's constant.

In general, Curie-Weiss law has been used to estimate the experimental value of the effective magnetic moment,  $\mu_{eff}$ , for high-purity materials in solid-state physics research. In most cases, the purity of the high-purity material was treated as a known value (for example, 100 percent purity). Regression analysis of the magnetic susceptibility and temperature data can give an experimental value of  $\mu_{eff}$ . Differences between experimental values of  $\mu_{eff}$  and the theoretical values obtained from equation 3 have been well reported and discussed. In the effective magnetic moment, the Curie-Weiss law is used in an opposite manner to such usage in the solid-state physics.

### Experimental validation on the principle – quantification of $Gd^{3+}$ ion –

Procedure of  $Gd^{3+}$  ion and outline of principle of magnetometer

Fig. 1



Principle of the effective magnetic moment method based on Curie-Weiss law.

- (a) Difference of temperature dependence of magnetic susceptibilities between unpaired electron and "closed-shell electrons"
- (b) Plot of magnetic moment of sample versus inverse temperature gives number of quantum free spins due to unpaired electrons.

For the purpose of an experimental validation on the principle, quantification of a rare earth ion, gadolinium ion ( $Gd^{3+}$ ), was tried for powder sample mixtures of gadolinium oxide ( $Gd_2O_3$ ) and silicon oxide ( $SiO_2$ ). This procedure is shown in **figure 2**. The purpose of this validation is;

- Is an analyte able to be actually quantified on the basis of the principle?

- How is minimum detectable concentration, accuracy and precision?

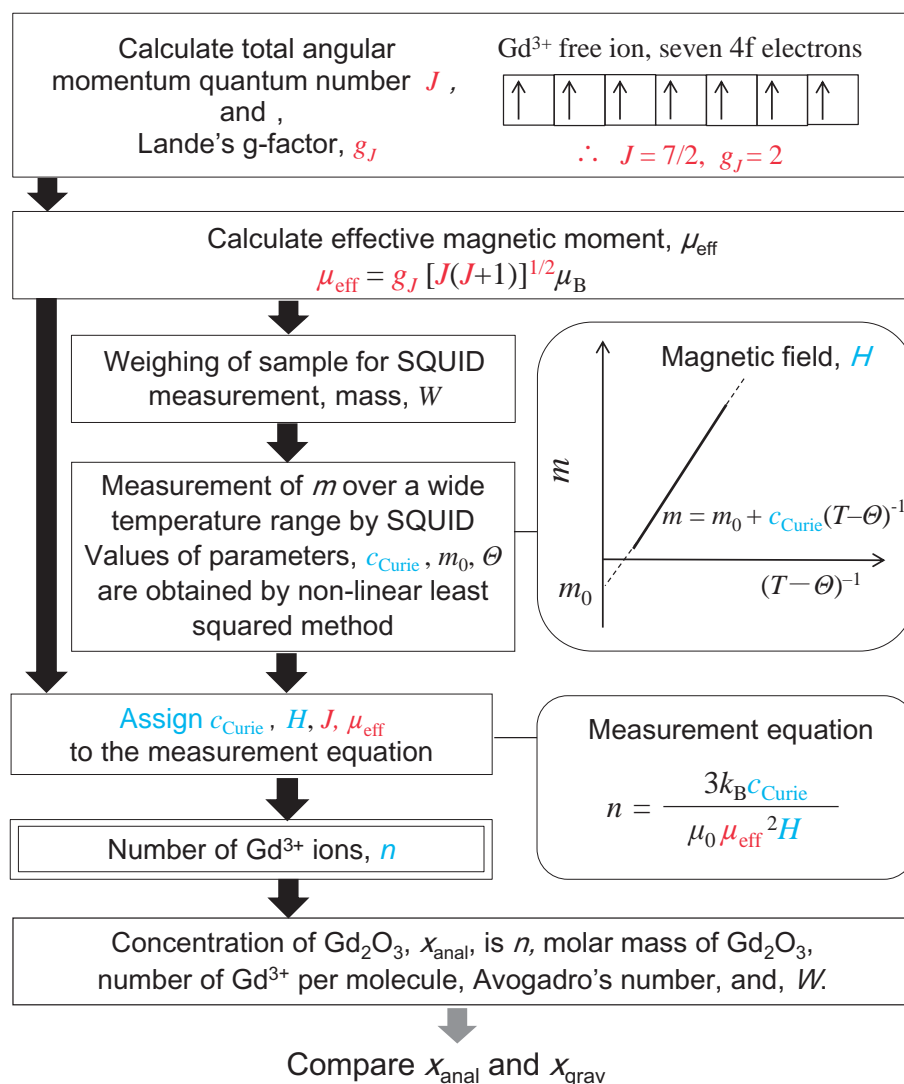
$Gd_2O_3$  was selected because 4f electrons of  $Gd^{3+}$  ion is in inner side of 5s electron orbitals and it is likely for the 4f electrons to be free ions. The shape of 4f electron orbital is not anisotropic and ideal sphere. The  $Gd^{3+}$  free ion has an  $^8S_{7/2}$  ground term, i.e. orbital angular momentum number,  $L=0$ , and, spin quantum number,  $S=7/2$ . Its theoretical effective magneton number is  $p = 7.937$ , calculated using  $g_J = [3/2 + \{S(S+1) - L(L+1)\} / \{2J(J+1)\}] = 2$  and  $J=S=7/2$ .

Both powders of  $Gd_2O_3$  and  $SiO_2$  are chemically stable and commercial good high-purity materials are easily available. The powder mixtures were prepared by a gravimetric blending method. ( $Gd_2O_3$ ) and ( $SiO_2$ ) were analyte and major component, respectively. Gravimetric concentration (mass fraction) of the

analyte  $Gd_2O_3$  in the mixture,  $x_{grav}$ , was calculated from values of mass of each component and purity of each high-purity materials. The mass of each powder was weighed using an electronic analytical balance, with a maximum capacity of 200 g/41 g and a minimum readability of 0.1 mg/0.01 mg. After weighing, both starting materials were manually mixed using a mortar for approximately 1 h. The purity of each high-purity material was assumed to be 1 kg/kg in the calculation of  $x_{grav}$ .

Next, a superconducting quantum interference device (SQUID) magnetometer [22] was used as the magnetometer for measuring the temperature dependence of magnetic moment,  $m$ , under the constant magnetic field,  $H$ , generated by a superconducting magnet. The simple schematic illustration of the SQUID magnetometer is shown in **figure 3**. In this study, the sample powder was packed in a cellulose capsule with a diameter of 5 mm and a length of 12 mm, into which approximately 20 mg of cotton was also stuffed to prevent the powder from moving. Both cellulose and cotton are weak diamagnetic materials. The mass of the powder,  $W$ , was precisely weighed with the above electronic analytical balance. The capsule was set on a drinking straw as a sample holder. The end of holder is attached to a sample rod and the sample is able to move inside

**Fig. 2**



Procedure of quantification of  $Gd^{3+}$  ions in a powder sample of  $Gd_2O_3$ - $SiO_2$  mixture, for experimental validation on the principle of effective magnetic moment method.

a superconducting detection coil, upward and downward. In a sample space of the SQUID magnetometer, there is helium gas with low pressure less than atmosphere. A SQUID is connected to the detection coil and plays a role as amplifier. When the sample moves through the coil, the voltage is dependent on the position inside the coil the graph in figure 3. The value of magnetic moment is obtained by comparison the position dependences of voltage between due to the sample and due to a standard sample of magnetic moment. In this study, a NMR magnetometer with a custom-made probe, a platinum resistance thermometer, and, a standard reference material of yttrium iron garnet with certified value of magnetic moment by the National Institute of Standards and Technology (NIST) were used for calibrations of magnetic field and temperature in the sample space and magnetic moment detected by the coil. These magnetometer, thermometer, and, standard reference material have metrological traceability.

For the fitting the data set of  $m$  and  $T$  to the equation 5, non-linear regression analysis was performed using a home-made program [16]. The regression analysis gave simultaneously the values and their uncertainties of  $c_{\text{Curie}}$ ,  $m_0$ , and,  $\Theta$ .

Next, the experimental values of  $c_{\text{Curie}}$  and  $H$  and theoretical effective magnetic moment  $\mu_{\text{eff}}$  are assigned to the measurement equation 6. Then, the number of  $\text{Gd}^{3+}$  ions,  $n$ , is obtained. Analytical concentration of  $\text{Gd}_2\text{O}_3$  in  $\text{SiO}_2$ ,  $x_{\text{anal}}$ , as mass fraction was obtained from molar mass of  $\text{Gd}_2\text{O}_3$ , number of  $\text{Gd}^{3+}$  ions per molecule, Avogadro's number, and,  $W$ .

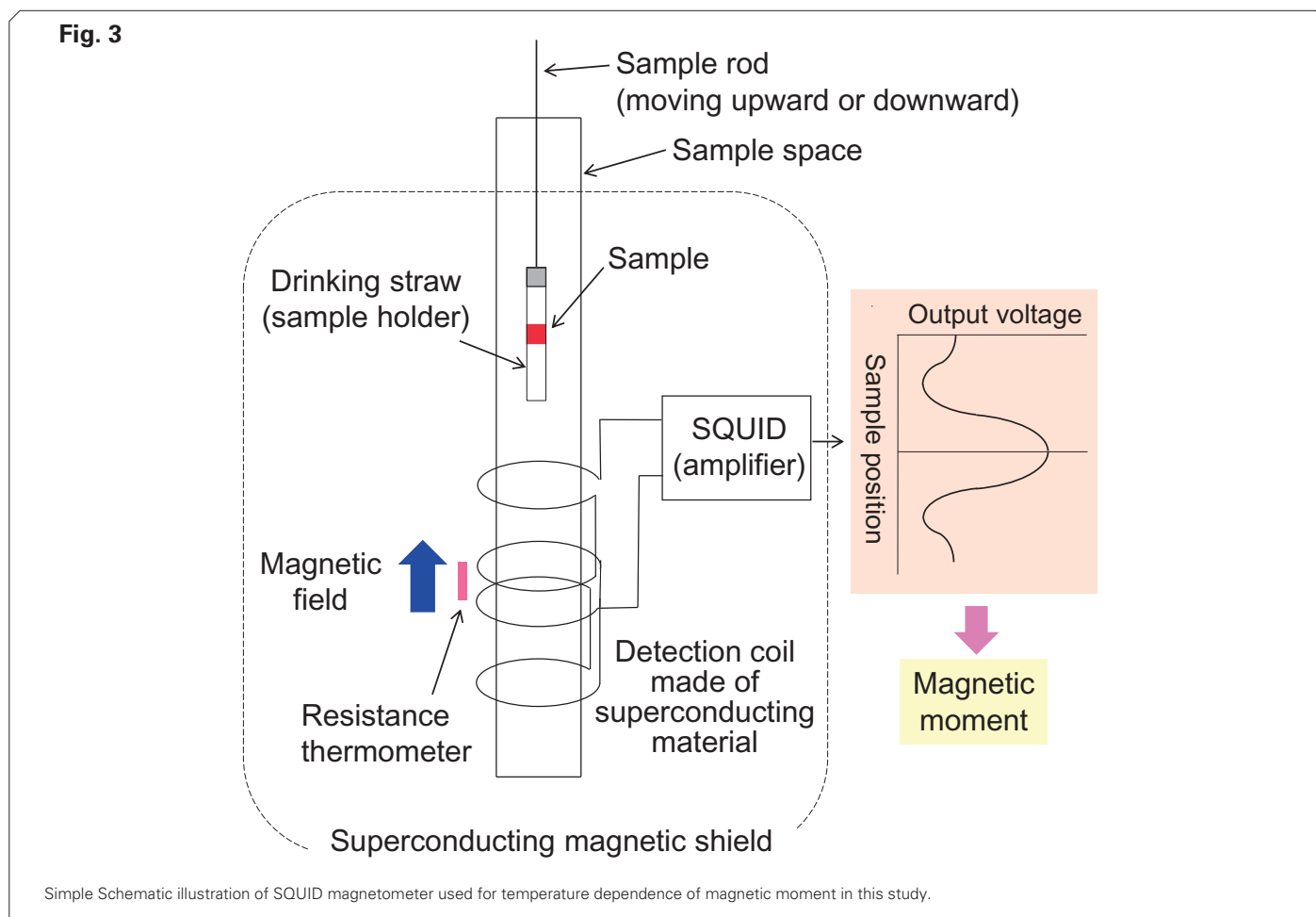
Finally, the  $x_{\text{anal}}$  and  $x_{\text{grav}}$  is compared with each other, to confirm whether both values are consistent within their uncertainties.

#### Experimental results on quantification of $\text{Gd}^{3+}$ ion

Four samples of  $\text{Gd}_2\text{O}_3\text{-SiO}_2$  mixtures were prepared by the gravimetric blending method. The gravimetric concentrations,  $x_{\text{grav}}$ , are,  $0.237100 \pm 0.000034 \text{ kg kg}^{-1}$ ,  $0.103625 \pm 0.000035 \text{ kg kg}^{-1}$ ,  $0.048566 \pm 0.000025 \text{ kg kg}^{-1}$ , and,  $0.0080500 \pm 0.0000041 \text{ kg kg}^{-1}$ .

The magnetic moments for samples of four  $\text{Gd}_2\text{O}_3\text{-SiO}_2$  mixtures were measured at temperatures ranging from 80 to 340 K as shown in figure 4. The magnetic field was set at  $795.775 \text{ kA m}^{-1}$  (in cgs unit,  $10.0000 \text{ kOe}$ ), which was corresponding to 1 tesla. The sample mass,  $W$ , ranged from 21 to 50 mg and each sample mass has standard uncertainty of 0.03 mg. In the case of mixture no. 4, with  $x_{\text{grav}} = 0.008058 \text{ kg kg}^{-1}$ , the temperature dependence of the diamagnetic magnetic moment due to the capsule and cotton alone,  $m_{0,\text{bg}}$ , was previously measured.  $m_{0,\text{bg}}$  was then subtracted from the raw magnetic moments because it showed a degree of significant temperature dependence (from 1.3 to  $-0.4 \text{ nA}\cdot\text{m}^2$  in a temperature range of 240 K to 340 K) that could not be neglected in the temperature dependence of  $m_{T,A}$  for the mixture no. 4. The  $m_{T,A}$  of the mixture varied from  $330 \text{ nA}\cdot\text{m}^2$  to  $260 \text{ nA}\cdot\text{m}^2$  in a temperature range of 240 K to 340 K.

The results of comparison between  $x_{\text{anal}}$  and  $x_{\text{grav}}$  for each sample are summarized in figure 5, which also includes the values of  $x_{\text{grav}}$ ,  $W$ , and  $n$  for each mixture. In the case of mixture no. 1, the relative deviation  $(x_{\text{anal}} - x_{\text{grav}})/x_{\text{grav}}$  and its expanded uncertainty are  $-2.0\%$  and  $5.8\%$ , respectively. Except for sample no. 4, the values of  $x_{\text{anal}}$  and  $x_{\text{grav}}$  were in close agreement. A high-purity  $\text{Gd}_2\text{O}_3$  powder with  $W = 23 \text{ mg}$  was also measured. The temperature dependence of magnetic moment of the high-purity



Gd<sub>2</sub>O<sub>3</sub> powder is similar to a result of magnetic susceptibility in ref.[23]. The difference between  $x_{\text{anal}}$  and  $x_{\text{grav}}$  is -2% and the  $x_{\text{anal}}$  also agrees with its  $x_{\text{grav}}$  within their uncertainties. All values of  $(x_{\text{anal}}-x_{\text{grav}})/x_{\text{grav}}$  except for the sample no.4 are constant within their expanded uncertainties and apparently independent of  $x_{\text{grav}}$ , i.e., the mass fraction of SiO<sub>2</sub> in the samples.

Improving the measurement trueness of this analytical method is one of most significant issues. The Gd<sup>3+</sup> ion has a spin-only magneto-crystalline isotropy with orbital angular momentum of zero value. Then, any influence in the measurements of the magnetic moment is smaller than that of other rare-earth ions. However, the Landé  $g$ -factor values for free Gd<sup>3+</sup> and for the Gd<sup>3+</sup> ion in crystal samples may differ significantly. The discrepancy between  $x_{\text{anal}}$  and  $x_{\text{grav}}$  in this study may be related to the Landé  $g$ -factor in the measurement equation. Measurement of the  $g$ -value obtained with an electronic spin resonance (ESR) spectrometer will be a solution for improving the trueness. An ESR measurement using microwaves with much higher frequency is under investigation.

## Quantification of free radical – purity analysis for stable nitroxyl radicals –

### Samples and conventional method of its purity assessment

As first step to develop an application of the “effective magnetic moment method”, purity analyses of three high-purity organic compounds, each of which had a stable free radical, were tried to be analyzed by this method [24]. The specific compounds tested were 2,2,6,6-tetramethylpiperidine 1-oxyl [TEMPO] (C<sub>9</sub>H<sub>18</sub>NO), 4-hydroxy-2,2,6,6-tetramethyl piperidine 1-oxyl [TEMPOL] (C<sub>9</sub>H<sub>18</sub>NO<sub>2</sub>), and 4-hydroxy-2,2,6,6-tetramethylpiperidine 1-oxyl benzoate [4-hydroxy-TEMPO benzoate, or, 4HTB] (C<sub>16</sub>H<sub>22</sub>NO<sub>3</sub>). The analytical purity as free radical, in the form of the mass fraction, was compared with the purities stated by the manufacturers of the compounds. Such purities of organic free radical chemicals stated by manufacturers have been

conventionally estimated using ‘subtraction method’ [2] or ‘area normalization method’ [1]. In the subtraction method, the purity,  $x_p$ , as a function of  $k$  impurities (for example, with mass fractions)  $x_i$ , is conventionally regarded as  $x_p = 1 - \sum_{i=1}^k x_i$ . Each  $x_i$  is generally measured by a quantitative analytical method with an “empirical measurement equation” [4]. In the area normalization,  $x_p$  is regarded as  $x_p = y_p / (y_p + \sum_{i=1}^k y_i)$ , where the  $y_p$  is peak area due to major component and the  $y_i$  is peak area due to impurity. Common problem on both the subtraction method and the peak normalization method may be that all impurities are not able to be detected and quantified.

### Procedures for analytical method of purity as free radical

ESR measurement using X-band microwave is able to detect single large first derivation peak in a spectrum for high-purity powder of each organic free radical compound, as shown in **figure 6**. This spectrum of high-purity 4HTB powder was taken with an ESR spectrometer (JEOL JES-FA100). **Figure 7** shows a procedure for the purity analysis as free radical by the “effective magnetic moment method”. In such case, the effective magnetic moment of equation 3 becomes as followings;

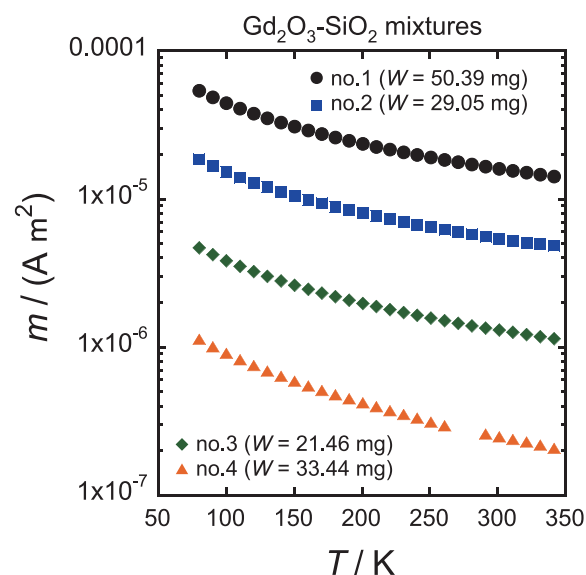
$$\mu_{\text{eff}} = g[S(S+1)]^{1/2} \mu_B, \dots\dots\dots (8)$$

where spin quantum number,  $S$  is 1/2 for free radical. The  $g$  is  $g$ -value obtained from the following fundamental equation of ESR spectroscopy;

$$g = hv / (\mu_B B_0), \dots\dots\dots (9)$$

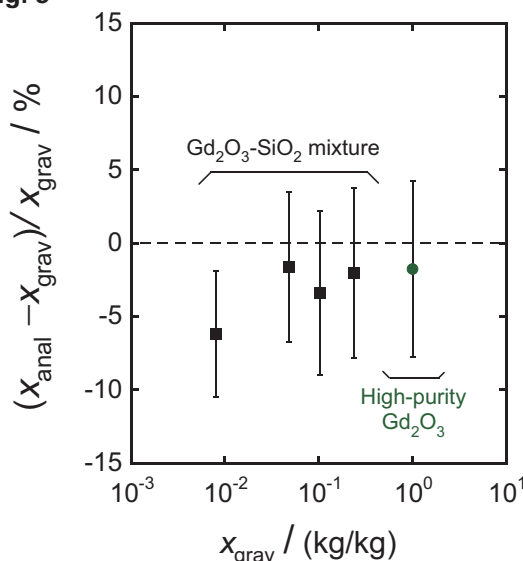
where  $h$  is the Planck’s constant,  $\nu$  is the frequency of the microwaves applied by the spectrometer, and  $B_0$  is the magnetic field intensity obtained from the first derivation peak. This equation accounts for the slight difference between the  $g$ -factor in free space and the actual value in a particular environment.

Fig. 4



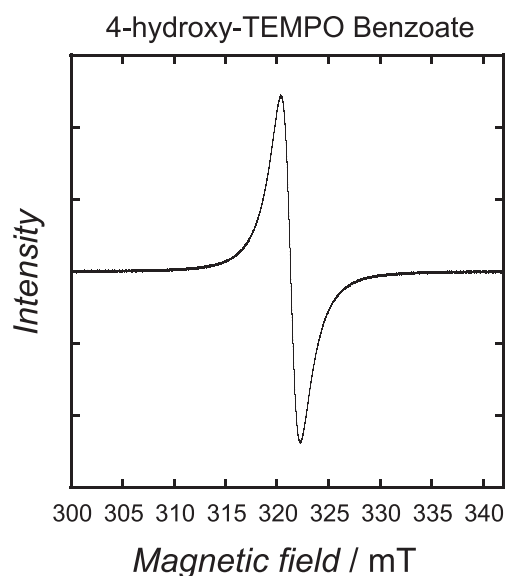
Temperature dependence of the magnetic moment for four Gd<sub>2</sub>O<sub>3</sub>-SiO<sub>2</sub> mixtures under a magnetic field of 796.38 kA·m<sup>-1</sup>(corresponding to 1 tesla).

Fig. 5



Relative deviation of  $x_{\text{anal}}$  from  $x_{\text{grav}}$  for all powder samples of Gd<sub>2</sub>O<sub>3</sub>-SiO<sub>2</sub> mixtures and high-purity Gd<sub>2</sub>O<sub>3</sub>. The  $x_{\text{anal}}$  is analytical concentration of Gd<sub>2</sub>O<sub>3</sub> by the “effective magnetic moment methods. The  $x_{\text{grav}}$  is gravimetric concentration of Gd<sub>2</sub>O<sub>3</sub> by gravimetric blending method. The horizontal axis indicates  $x_{\text{grav}}$ . The error bar for each value represents the corresponding expanded uncertainty, the coverage factor ( $k$ ) of which is 2.

Fig. 6



X-band ESR spectrum of high-purity 4HTB powder.

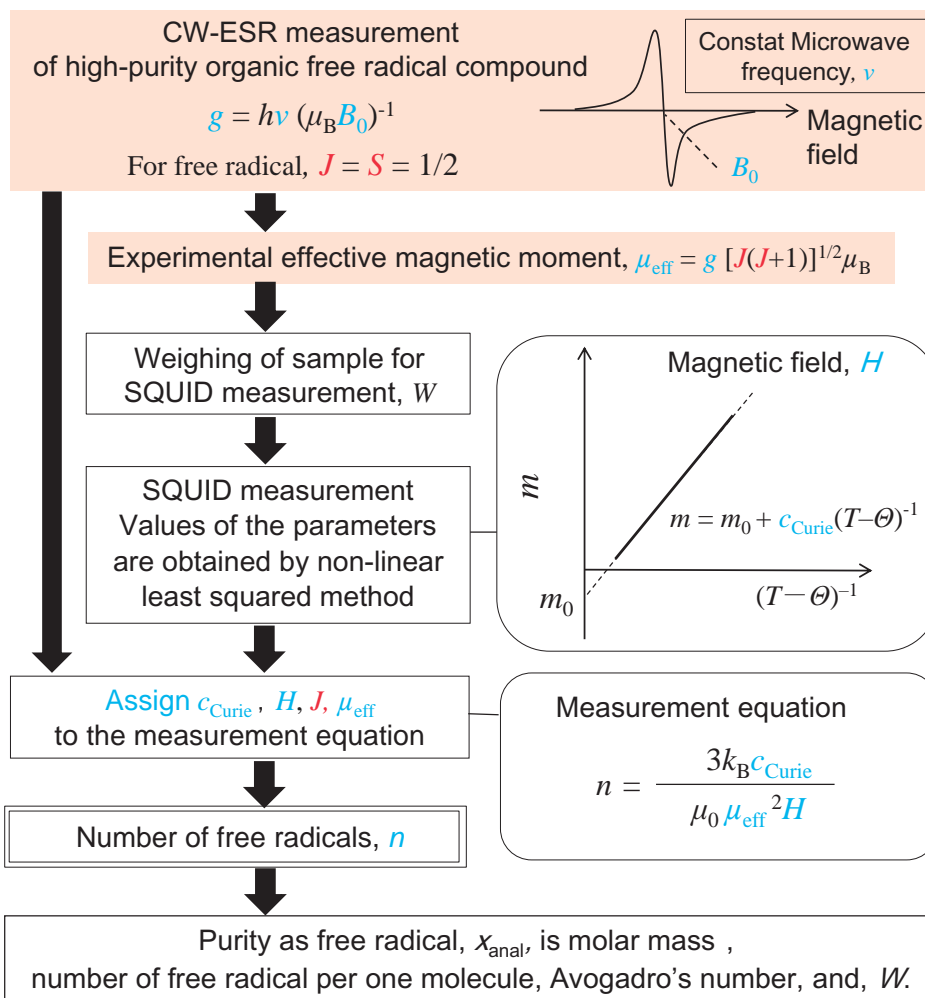
### Experimental results on purity as free radical of high-purity organic compounds

The magnetic moments for the samples were measured under temperatures from 4 K to 300 K as shown in **Figure 8**, when  $H$  was  $796.473 \text{ kA m}^{-1}$  ( $10.000 \text{ kOe}$ ), and when  $W$  for each respective sample was  $12.66 \text{ mg}$  for TEMPOL,  $18.45 \text{ mg}$  for TEMPO, or  $20.93 \text{ mg}$  for 4HTB. The expanded uncertainty of  $W$  was  $0.07 \text{ mg}$ . The temperature dependences of the magnetic moments of TEMPO and 4HTB resemble Curie–Weiss behavior over the whole temperature range. In the case of TEMPOL, the result demonstrates non-Curie–Weiss behavior at temperatures less than  $80 \text{ K}$  and has a broad maximum around  $6 \text{ K}$ . It was suggested by Yamauchi, *et al.* [25] that this behavior of TEMPOL may be due to an antiferromagnetic short-range ordering.

The  $g$ -values of the samples were measured by the ESR spectrometer from near the boiling point of nitrogen to room temperature. The  $g$  of each sample was constant value of  $(2.0072 \pm 0.0002)$  for TEMPO,  $(2.0069 \pm 0.0008)$  for TEMPOL, and  $(2.0071 \pm 0.0004)$  for 4HTB. These values are typical  $g$  values for organic free radicals and are much higher than theoretical  $g$ -factor of free electron,  $g_e$  ( $2.0023$ ).

The values for the analytical purity,  $x_{\text{anal}}$ , and the manufacturer's stated purities for the samples are summarized

Fig. 7



Procedure of purity analysis as free radical for a high-purity organic compound.

in **Table 2**. The values of  $x_{\text{anal}}$  based on the  $g_e$  are also estimated. For each sample, the  $x_{\text{anal}}$  on the  $g$  from the ESR spectrometer is closer to  $1 \text{ kg kg}^{-1}$  than that based on the  $g_e$ . The ESR spectrometer brings effects to improve the accuracy of  $x_{\text{anal}}$ . The temperature range of the regression analyses was from 80 K to 300 K for both TEMPOL and 4HTB. For TEMPO, the temperature range was from 80 K to 260 K. All values of  $x_{\text{anal}}$  are close to  $1 \text{ kg kg}^{-1}$ , and their relative standard uncertainties are 4 to 6%. The  $x_{\text{anal}}$  of TEMPOL is 2% higher than  $1 \text{ kg kg}^{-1}$ . This might be caused by some effect related to the antiferromagnetic ordering [25]. An absolute value of the Weiss temperature,  $\theta$ , of TEMPOL is largest among the three compounds.

As described above, the manufacturers use the results of GC analyses to estimate the purity values that they state. Before a solid sample is injected into a column for separation in the oven in GC, the sample must be sublimated or be vaporized by some method. In general, the sample must be heated in a sample injection chamber prior to being injected into the column. Therefore, there is a possibility of thermal decomposition before the injection of the sample into the column. On the other hand, the measurements by the “effective magnetic moment method” were performed in a temperature region much lower than the melting point. This method has the advantage of being a non-destructive analytical approach, such that the sample is not decomposed by heating of the sample. Conversely, the disadvantage is that this purity analysis method is not applicable if a compound shows a behavior deviated from the Curie-Weiss law with decrease of sample temperature.

ESR method is itself relative quantitative analytical method. Standard solutions for calibrations of the ESR spectrometer are generally prepared using commercial high-purity organic chemicals with radicals and calibration curves are made by using the solutions with different free radical concentrations. A Japanese textbook on bioanalysis using ESR says ‘Purities of commercial nitroxyl radicals are approximately 98%. If you would like to pay attention to accuracy of quantitative analyses, uses of more than two types of high-purity free radical chemicals are recommended’ [26]. This “effective magnetic moment method” has a potential and a possibility to give such analysts reliable high-purity chemicals with free radicals.

The largest uncertainty contribution to uncertainty of the  $x_{\text{anal}}$  is that from  $c_{\text{Curie}}$ . To minimize the uncertainty associated with  $c_{\text{Curie}}$ , both the magnetic moment and the  $g$ -value will have to be measured over a wider temperature range. In addition, the reproducibility of the magnetic moment measured using the

SQUID magnetometer must be improved. Low temperature ESR studies of TEMPO and 4HTB near liquid helium temperature and the analytical purities with relative uncertainties of 1% have been carried out [27].

## Conclusion

In accordance with classification for various analytical methods written in a handbook of ref. 28, this “effective magnetic moment method” is classified as followings;

- semimacro analysis (mass of sample is a range of 10 – 100 mg)
- major constituent determination (concentration is 1 – 100%)
- instrumental analysis and non-destructive analysis
- non-separation analysis

This analytical method is able to determine amount of substance for free radicals or atoms with unpaired electrons, with metrological traceability to the SI. Although current accuracy of this “effective magnetic moment method” is not high under the current experimental condition, the effective magnetic moment has a possibility to develop calibration standards for quantitative analyses using ESR spectrometers or other analytical instruments, in future. I hope that this analytical method will contribute to improve accuracy of free radical analyses, major constituent determination of stoichiometric or non-stoichiometric compounds, etc. If there is a flow of a river such as “SI → potential primary direct methods → potential primary ratio methods → various quantitative instrumental analyses → ...”, I would like to make the river width near upper reaches as wider as possible, by any progress of my research for the effective magnetic moment method.

## Acknowledgments

This work was performed using the SQUID magnetometer in the Nano-Processing Facility (NPF), supported by IBEC Innovation Platform, AIST. Dr. T. Shimosaka of NMIJ/AIST made a program for non-linear least squared method considering uncertainty evaluation. Part of this work was financially supported by JSPS KAKENHI “Grant-in-Aid for Young Scientists (B)” (No. 24750077). I would like to express my gratitude to Dr. T. Kodaira and Dr. K. Mizugaki of AIST for help with the ESR measurement. Staffs in ESR group of the JEOL RESONANCE, and other experts and practitioners of ESR have good communication with me for promotion of use of ESR spectrometers.

This review is based on a Japanese review ‘A quantitative analytical method based on Curie-Weiss law “effective magnetic moment method” ’ published in *Bunseki* **2016** (2) [29], which is a monthly journal for only members of the Japan Society for Analytical Chemistry. This review was partially revised, referring to my original papers of reference 15, 16 and 24. [If you will cite this review, please cite these original papers, too.]

## References

- [ 1 ] D.A. Skoog, D.M. West, F.J. Holler, S R Crouch, Analytical Chemistry : an Introduction, seventh edition, Saunders College Publishing, A Division of Harcourt College Publishers (Orlando, FL, USA) (2000).
- [ 2 ] ISO Guide 35:2006, *Reference materials - General and statistical principles for certification*, Third edition, Switzerland, International Organization for Standardization, (2006), p.31.

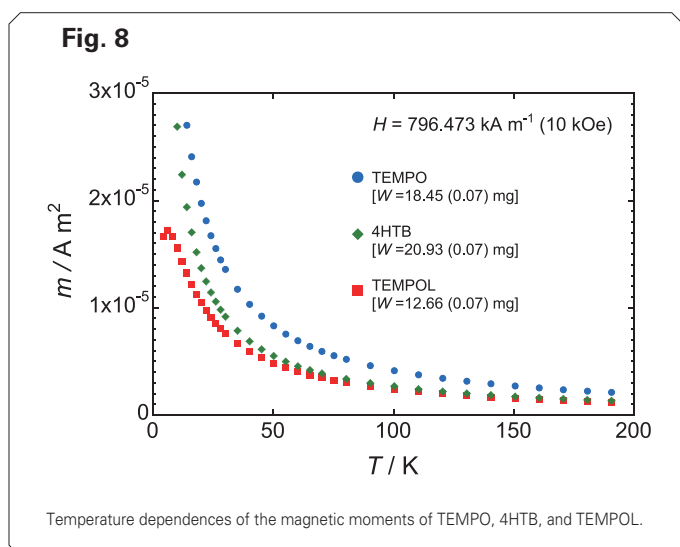
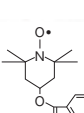


Table 2

High-purity organic compound	Manufacturer's stated purity (measured by GC)	Purity as free radical by "effective magnetic moment method"		Weiss temperature $\theta$ (K)
		$x_{\text{anal}}$ (100 kg kg <sup>-1</sup> )	$x_{\text{anal}}$ (100 kg kg <sup>-1</sup> )	
		$g$ is for free electron, $g_e$	$g$ is experimental value by ESR	
TEMPO 	99.5 wt%	100.3±6.4 ( $g_e = 2.0023$ )	99.8±6.4 ( $g = 2.0072 \pm 0.0002$ )	-2.4±4.8
TEMPOL 	99.5 wt%	102.3±4.0 ( $g_e = 2.0023$ )	101.9±4.0 ( $g = 2.0069 \pm 0.0008$ )	-5.0±2.9
4HTB 	98.5 %	100.6±4.8 ( $g_e = 2.0023$ )	100.1±4.8 ( $g = 2.0071 \pm 0.0004$ )	-0.2±2.9

Analytical purities by the "effective magnetic moment method", manufacturer's purities for powder samples of TEMPO, TEMPOL, and 4HTB. Each value of  $x_{\text{anal}}$  is accompanied by its expanded uncertainty (with a coverage factor of 2).

- [ 3 ] MacGraw-Hill (ed.) *The McGraw-Hill Dictionary of Scientific and Technical Terms, Sixth Edition*, New York, MacGraw-Hill Professional, (2002) p.6.
- [ 4 ] M.J.T. Milton, T.J. Quinn, *Metrologia* **38** 289–296 (2001).
- [ 5 ] H. Ihara, T. Saito N. Sugimoto, *Synthesiology* **2** 13–24 (2009); T. Ihara, T. Saito, *JEOL News*, **51**, 51-60 (2012).
- [ 6 ] T. Miura, *Bunseki*, **2012**, 488 (2012) [in Japanese].
- [ 7 ] T. Atake, Y. Takagi, T. Nakamura, Y. Saito, *Phys. Rev. B*, **37**, 552-554 (1988); T. Atake, H. Kawaji, A. Hamano, Y. Saito, *Report of Research Laboratory for Engineering Materials*, Tokyo Inst. Technol. **15**, 13 (1990).
- [ 8 ] Y. Shimidzu, Y. Ohte, X. Bao. S. Otsuka, Y. Kitamaki, K. Ishikawa, T. Ihara, K. Kato, *Accred. Qual. Assur.* **13**, 389 (2008).
- [ 9 ] N. Matsumoto, H. Honma, Y. Kato, S. Yasuzuka, K. Morie, N. Kijima, S. Ebusu, S. Nagata, Proc. of 9th Int. Symposium on Superconductivity (ISS'96), Sapporo, Japan, Oct.21-24, 1996, *Advances in Superconductivity IX/1*, Eds. Nakajima and Murakami, Vol.1(Springer-Verlag, Tokyo 1997), p.175-178 (ISBN 4-431-70198-2).
- [10] N. Matsumoto, R. Endo, S. Nagata, T. Furubayashi, T. Matsumoto, *Phys. Rev. B* **60**, 5258-5265 (1999).
- [11] N. Matsumoto, K. Taniguchi, R. Endoh, H. Takano, S. Nagata, *J. Low Temp. Phys.* **117**(5/6), 1129-1979 (2000).
- [12] N. Matsumoto, T. Hagino, K. Taniguchi, S. Chikazawa, S. Nagata, *Physica B*, **284-288**, 1978-1979 (2000).
- [13] N. Matsumoto, S. Nagata, *J. Crystal Growth* **210**(4), 772-776 (2000).
- [14] N. Matsumoto, Y. Yamauchi, J. Awaka, S. Kamei, H. Takano, S. Nagata, *Int. J. Inorganic Materials*, **3**, 791-795 (2001).
- [15] N. Matsumoto, K. Kato, *Metrologia* **49**, 530 (2012).
- [16] N. Matsumoto, T. Shimosaka, *Accred. Quality Assur.* **20**, 115-124 (2015).
- [17] C. Kittel, *Introduction to Solid State Physics Seventh Edition*, New York, John Wiley & Sons, Inc, Chapter 14, (1996) .
- [18] S. Blundell, *Magnetism in Condensed Matter*, New York, Oxford University Press Inc. (2001).
- [19] P. Gans, *Data fitting in the chemical sciences by the method of least squares*. Wiley, Chichester, pp. 30–34 (1992).
- [20] W.E. Deming, *Statistical adjustment of data*. Wiley, New York (1943).
- [21] ISO6143:2001, *Gas analysis-Comparison methods for determining and checking the composition of calibration gas mixtures*, Switzerland, International Organization for Standardization, (2001), p.17.
- [22] M. McElfresh, *Fundamentals of Magnetism and Magnetic Measurements Featuring Quantum Design's Magnetic Property Measurement System*, California, Quantum Design, Inc., (1994), <http://qdusa.com/sitedocs/appNotes/mpms/FundPrimer.pdf>.
- [23] S.L. Bud'ko, P.C. Canfield, *J. Mag. Mag. Mater.* **299**, 281–287 (2006).
- [24] N. Matsumoto, T. Shimosaka, *J. Appl. Phys.* **117**, 17E114 (2015).
- [25] J. Yamauchi, T. Fujito, E. Ando, H. Nishiguchi, and Y. Deguchi, *J. Phys. Soc. Jpn.* **25**, 1558 (1968).
- [26] M. Kohno, T. Yoshikawa, T. Ozawa, *Introduction to Electron Spin Resonance for Bio-scientists*, KODANSHA (Tokyo, Japan), (2011) Chapter 2 [in Japanese].
- [27] N. Matsumoto, T. Shimosaka, to be published in *Anal. Sci.*.
- [28] H. Akaishi (ed.), *Handbook of Analytical Chemistry*, 5<sup>th</sup> edition, Maruzen (Tokyo, Japan) (2001) Chapter 1 [in Japanese].
- [29] N. Matsumoto, *Bunseki*, **2016** (2), 63-67 (2016) [in Japanese].

# Introduction of a Next-Generation 200 kV Cryo TEM

Naoki Hosogi EM Business Unit, JEOL Ltd.

In recent years, near-atomic resolution structural information on biological complexes could have been achieved by cryo transmission electron microscopy (TEM). Under this circumstance, JEOL developed a next-generation cryo-TEM aimed at higher efficiency, higher usability and higher resolution. This report introduces this cryo-TEM instrument.

## Introduction

Cryo-TEM provides structural information on a specimen close to its natural state without any disturbance, owing to the specimen preparation process, which excludes chemical reactions and physical stimulations. Recently, cryo-TEM produces very exciting results of structural biology in combination with single particle analysis and electron tomography [1]. This progress of cryo-TEM is realized by the direct electron detector for higher resolution images and by a wealth of automated functions for improved throughput, and by other capabilities. In particular, a remarkable advancement of single particle analysis leads to a number of achievements of near-atomic resolution structural information on biological complexes. Thus, it is expected that these achievements will contribute to drug discovery [2].

JEOL newly developed a cryo-TEM that provides high throughput and high usability for enabling higher-resolution structural analysis. This microscope, nicknamed “CRYO ARM™” was developed based on the JEM-ARM200F (Fig. 1). This microscope is equipped with a 200 kV field emission gun (FEG). In addition, CRYO ARM™ is fitted with a dedicated cryo-stage, a multiple-specimen autoloader, a liquid-nitrogen auto-refill system, automatic image acquisition software, an omega filter and a phase plate. This report introduces the details of those features.

## Electron Gun

First, the author will describe the electron gun. For CRYO ARM™, either of the cold field emission gun (Cold FEG) or the Schottky field emission gun (Schottky FEG) can be selected. Since the energy spread of the emitted electrons from the Cold FEG is about 50% of Schottky FEG (Fig. 2) and the size of the virtual source is less than 10 nm, the electron beam has high coherences. With such a beam, cryo-TEM image has high contrast due to its high spatial coherence and is less affected by chromatic aberration owing to its high temporal coherence. In the low dose density, the signal-to-noise ratio (S/N) of image is

mostly determined by a statistical noise of electrons, since dose density in cryo-TEM is typically several tens of electrons for angstrom square. Namely, the resolution is determined with the competition between the statistical noise and image contrast. It means that Cold FEG has possibility to have higher resolution for cryo-TEM works. In comparison between both Cold FEG and Schottky FEG, platinum iridium was observed with each gun. Images were taken with a high defocus of  $-1000$  nm, as the similar condition of cryo-TEM observation. On that condition, finer lattice image was observed with Cold FEG (Fig. 3). Then, each image was Fourier-transformed to see the Thon rings. Whereas an observed peak was equivalent to 0.19 nm with Schottky FEG, a peak down to 0.14 nm was observed with Cold FEG (Fig. 3).

Fig. 1

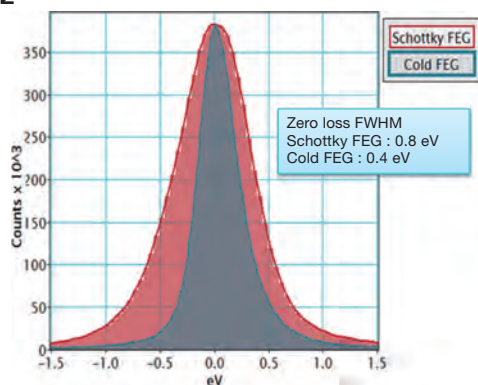


Appearance of a new cryo-TEM, “CRYO ARM™”.

## Cryo Stage and Cryo Polepiece

Since this microscope also has a dedicated cryo stage, cryo-TEM observation can be performed at low temperature < 100 K and with low growth ratio of ice contamination. Either of the high resolution type (HR) cryo-polepiece (CRP) or the high tilt type (HT) CRP can be selected. Guaranteed resolution of each CRP is 0.25 nm (HR-CRP) and 0.30 nm (HT-CRP) at a point resolution of 0.2 nm (HR-CRP) and 0.2 nm (HT-CRP) for lattice resolution, respectively. Tilt angle of each CRP is  $\pm 10^\circ$  (HR-CRP) and  $\pm 70^\circ$  (HT-CRP), respectively. In addition, flip flop function (between  $0^\circ$  and  $90^\circ$ ) is available with HT-CRP, so dual-axis tomography can be done with this polepiece.

Fig. 2

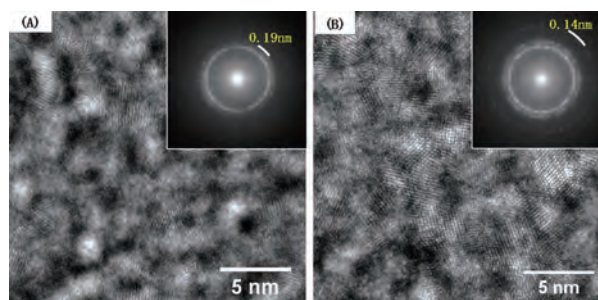


Energy resolutions of each electron gun. Zero-loss spectra acquired with Cold FEG (blue) and Schottky FEG (red) with FWHM (full width at half maximum) being 0.4 eV and 0.8 eV, respectively.

## CryoSPECPORTER™

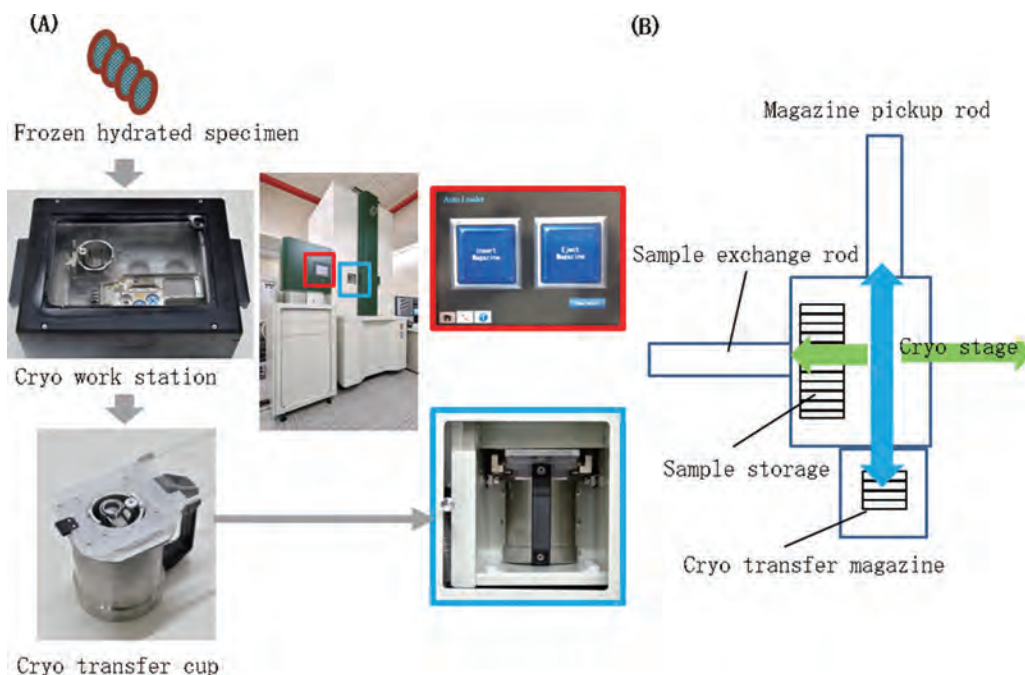
The cryo stage is compatible for multi-specimen auto-loader “CryoSPECPORTER™”, so users can exchange specimens automatically. CryoSPECPORTER™ can accommodate up to 12 of dedicated specimen cartridges for automatically transferring a specific specimen into the cryo-stage (Fig. 4). Loading of the prepared specimen grid into the cartridge is made under a liquid-nitrogen environment using a dedicated cryo work station (Fig. 4A). Up to 4 specimens can be transferred at one time, and loading & unloading of a specific specimen can be made from GUI screen. This capability enables screening of specimens. In addition,

Fig. 3



TEM images of platinum iridium acquired with Cold FEG (A) and Schottky FEG (B). Both images were captured with a defocus of approximately -1  $\mu\text{m}$ . Insets at the upper parts in the both images show Fourier-transformed patterns.

Fig. 4



Transfer of the frozen hydrated specimen into “CRYO ARM™”. (A) In the cryo work station, the specimen is loaded into the cartridge and then, the cartridge is loaded into the magazine at a liquid-nitrogen temperature. The magazine into which the specimen cartridge is loaded is transferred to “CryoSPECPORTER™” with the use of a cryo transfer cup (blue frame). After that, the related operations can be made using a touch panel located at the side of the microscope (red frame). (B) Schematic of “CryoSPECPORTER™”. The magazine transferred by the cryo transfer cup is carried into “CryoSPECPORTER™” through the Magazine pickup rod. The cartridges that accommodate samples are loaded into the Sample storage with the use of the Sample exchange rod. After that, the cartridge specified by the user is transferred into the cryo-stage with the use of the Sample exchange rod.

CryoSPECPORTER™ is cooled by liquid nitrogen, allowing for specimen storing at a temperature of 105 K or below over a long period of time. The microscope column and CryoSPECPORTER™ are evacuated by a turbo-molecular pump, whereas the electron gun chamber is evacuated by a sputter-ion pump. This evacuation system leads to an oil-free, clean vacuum environment.

## Various Automatic Functions

This microscope also incorporates various automation functions that include an automated liquid-nitrogen filling system, auto parallel-beam illumination capability and an automated image acquisition software (JEOL Automated Data Acquisition System: JADAS), thus greatly improving throughput. The automated liquid-nitrogen filling system enables automatic liquid-nitrogen filling, from the liquid-nitrogen tank connected to the outer side of the microscope room, into the cryo-stage and CryoSPECPORTER™ with specific nitrogen residual volume or specific time. The use of a 100 L tank allows for automatic supply of liquid nitrogen for approximately one week.

The newly-developed JADAS is used for single particle analysis. Basic operations are carried out using five buttons on the GUI screen (Fig. 5A), facilitating the operations by novice users. TEM alignment can also be performed using the GUI screen (Fig. 5A). The fundamental process of taking micrograph is as follows. First, a TEM image of the entire surface of a specimen grid is taken in Low Magnification mode for detecting grid meshes. Then, the image acquisition area is moved to each grid mesh and low-magnification images at Magnification mode (search images) are taken to detect holes on the support film. Next, auto focus is conducted onto the supporting film and micrographs of each hole are acquired for single particle analysis. Since several image acquisition techniques are built into this software as recipes, users can acquire data depending on a variety of needs. For example, the Normal recipe performs one-time auto focus for each search image and then, serially acquires the micrographs of all holes (Fig. 5B). On the other

hand, the Careful recipe executes auto focus for the vicinity of all of the detected holes (Fig. 5B). In addition, the Semi-auto recipe conducts auto focus and image acquisition for specific points designated by the user (Fig. 5B).

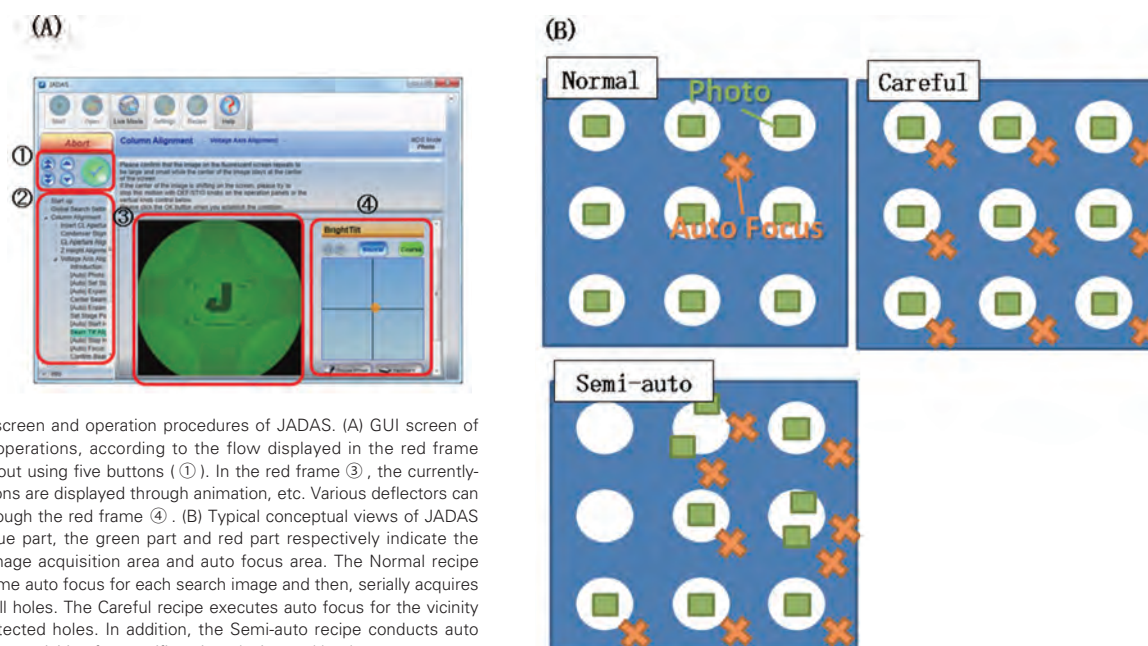
## Omega Filter and Phase Plate

As described above, a specimen observed by cryo-TEM is composed of light elements; thus only the phase contrast is seen. This indicates that the conventional observation techniques provide a very low image contrast. To overcome this limitation, CRYO ARM™ can accommodate two types of phase plates alternately, Zernike-type or Hole-free type. In addition to the omega filter equipped in the microscope, CRYO ARM™ enables high-contrast imaging of biological specimens with the use of a phase plate.

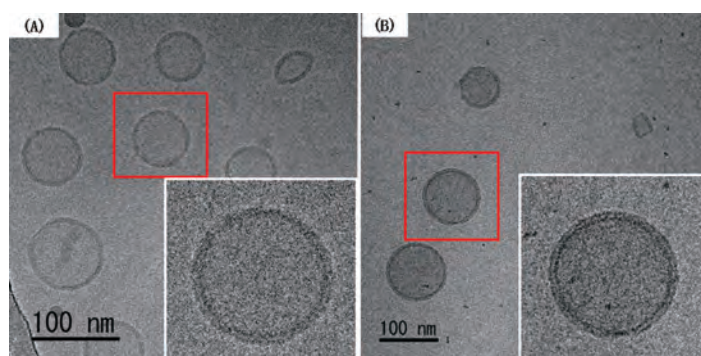
The omega filter is an incolumn-type energy filter, which intercepts energy-loss spectra (electrons) and uses only zero-loss electrons (without energy loss) to form an image. Since this zero-loss image reduces noise, the image provides high contrast (Fig. 6).

On the other hand, the phase plate is located at the back focal plane of the objective lens. This placement converts the phase change of a transmitted wave into the intensity information. Thus, a high-contrast image is obtained even at an exact focus (Fig. 7). Both of the Zernike- and Hole-free phase plates are composed of an amorphous-carbon thin foil and are heated at around 200 °C for imaging. The Zernike phase plate is formed by a thin foil with a center hole of a diameter of 1 μm or less. The use of this phase plate dramatically improves the image contrast, but fringes appear at the periphery of the specimen (Fig. 7B) [3]. In the case of the Hole-free phase plate, the crossover of the electron beam formed on the phase plate causes to generate local charging, for changing the phase of electron waves passing through this site. This can lead to phase contrast comparable to that obtained with the Zernike phase plate [4]. This locally-charged site is much smaller than the hole diameter of the Zernike phase plate; therefore, the fringes mentioned before can be reduced (Fig. 7C).

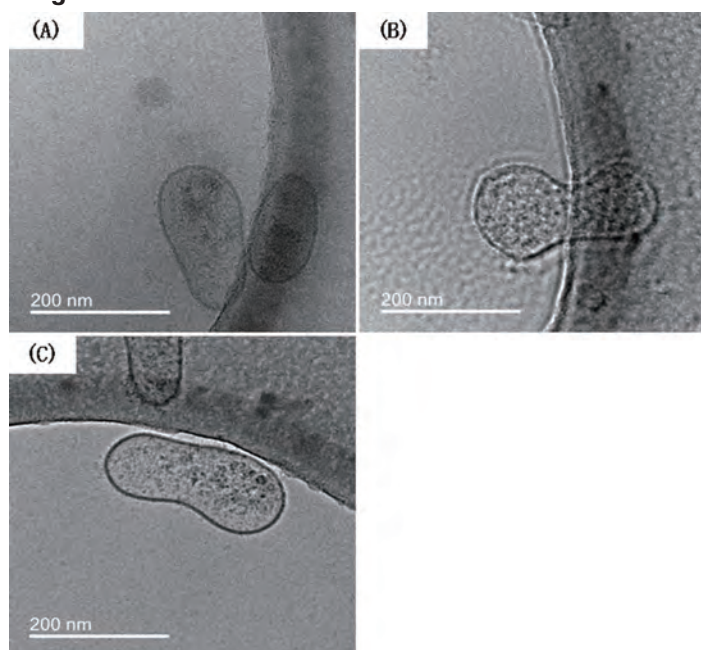
Fig. 5



Outline of the screen and operation procedures of JADAS. (A) GUI screen of JADAS. Basic operations, according to the flow displayed in the red frame ②, are carried out using five buttons (①). In the red frame ③, the currently-needed operations are displayed through animation, etc. Various deflectors can be adjusted through the red frame ④. (B) Typical conceptual views of JADAS recipes. The blue part, the green part and red part respectively indicate the support film, image acquisition area and auto focus area. The Normal recipe performs one-time auto focus for each search image and then, serially acquires the images of all holes. The Careful recipe executes auto focus for the vicinity of all of the detected holes. In addition, the Semi-auto recipe conducts auto focus and image acquisition for specific points designated by the user.

**Fig. 6**

Cryo-TEM images of ice-embedded liposome. Conventional cryo-image (A) and the cryo-image taken with an omega filter (B). Insets at the lower parts in the both images show the enlarged views inside the respective red frames. The microscope used was a JEOL JEM-2200FS. Both images were captured with a defocus of approximately  $-2 \mu\text{m}$ . The slit width was 20 eV and the electron dose was approximately  $20\text{e}/\text{\AA}^2$ .

**Fig. 7**

Phase plate cryo-TEM images of ice-embedded exosomes. Zero-loss image taken with a normal phase plate (A), Zernike phase difference (contrast) image (B) and Hole-free phase difference image (C). The microscope used was a JEOL JEM-2200FS. Zero-loss image (A) was captured with a defocus of approximately  $-2 \mu\text{m}$ . The other images (B and C) were captured at an exact focus. The slit width was 20 eV and the electron dose was approximately  $20\text{e}/\text{\AA}^2$ . Specimen courtesy: Naomi Tominaga at National Cancer Center Research Institute and The University of Tokyo.

## Summary

CRYO ARM™ is now operating at Protonic Nano Machine Group, Graduate School of Frontier Biosciences, Osaka University. CRYO ARM™ is composed of a Schottky FEG, a high-resolution cryo-polepiece, a cryo-stage, CRYOSPECPORTER™, an omega filter and JADAS. Kato *et al.* conducted single particle analysis of  $\beta$ -galactosidase using the microscope and obtained a structural analysis result with a high resolution of  $3.3 \text{\AA}$  [5]. This result demonstrates significantly high-level data acquired with a 200 kV class TEM ([https://www.ebi.ac.uk/pdbe/emdb/statistics\\_volt\\_source.html](https://www.ebi.ac.uk/pdbe/emdb/statistics_volt_source.html)). The data acquisition time was approximately 15 hours and the data analysis time was approximately 3 days (very short time).

Under the circumstance of remarkable development of cryo-TEM, CRYO ARM™ was developed with various advanced features for achieving higher throughput, operability and image resolution. This new cryo-TEM instrument will be expected to contribute to a variety of biological fields including structural biology.

## Acknowledgment

The author would like to acknowledge the support of Takeshi Kaneko, Shuuichi Yuasa, Kimitaka Hiyama, Naoki Fujimoto,

Izuru Chiyo, Akihito Kamoshita, Isamu Ishikawa and Yoshihiro Ohkura who developed this microscope and also the assistance of the project members at JEOL Ltd.

## References

- [ 1 ] Callway, E. The revolution will not be crystallized. *Nature*, **525**, 172-174 (2015).
- [ 2 ] Merk A., Bartesaghi A., Banerjee S., Falconieri V., Rao P., Davis M.I., Pragani R., Boxer M.B., Earl L.A., Milne J.L., Subramaniam S. Breaking Cryo-EM Resolution Barriers to Facilitate Drug Discovery. *Cell*, **165**, 1698-1707 (2016).
- [ 3 ] Hosogi N., Shigematsu H., Terashima H., Homma M., Nagayama K. Zernike phase contrast cryo-electron tomography of sodium-driven flagellar hook-basal bodies from *Vibrio alginolyticus*. *J. Struct. Biol.*, **173**, 67-76 (2011).
- [ 4 ] Malac M., Beleggia M., Kawasaki M., Li P., Egerton R. F., Convenient contrast enhancement by a hole-free phase plate. *Ultramicroscopy*, **118**, 77-89 (2012).
- [ 5 ] Kato T., Hosogi N., Kaneko T., Ishikawa I., Namba K., Performance of State-of-the-art CryoEM, named "Cryo ARM™". *SEIBUTSU BUTSURI*, **56**, S121 (2016).

# Development of Pixelated STEM Detector “4DCanvas”

Ryusuke Sagawa EM Business Unit, JEOL Ltd.

In scanning transmission electron microscopy (STEM), a detector which can record diffraction pattern as a 2-dimensional (2D) image at each electron probe position with high frame rate, is called a pixelated STEM detector. It can be used for various types of researches because the data taken with the pixelated detector contains more information than that is taken with a conventional STEM detector. We have developed the pixelated STEM detector named “4DCanvas” to implement it into an electron microscope. In this paper, the 4DCanvas and its application are reported.

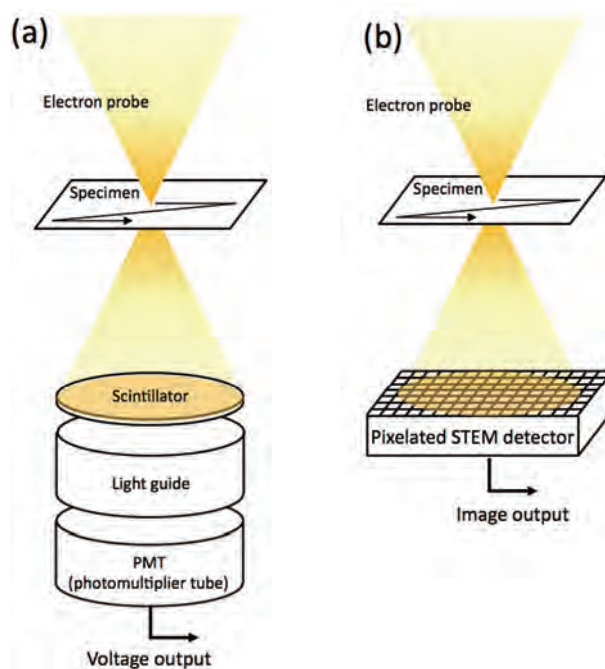
## Introduction

In a conventional STEM detector, a scintillator and a photomultiplier tube (PMT) are used. All or part of the diffraction pattern (convergent beam electron diffraction (CBED) pattern in STEM mode) formed on the detector plane made of scintillation fluorescence is detected by the PMT, creating a STEM image as a probe position brightness signal (Fig. 1(a)). However, electron signal in the diffraction pattern has a structure, representing the specimen information. By changing the shape of the detector, one can obtain various types of images such as annular bright-field (ABF)-STEM image or high angle annular dark-field (HAADF)-STEM image, and these images are useful for characterizing a sample [1]. As the detector has only one channel in these techniques, specimen information is averaged and partly lost. Recently, researches using a multichannel detector (up to 16 channels) are used to obtain a phase contrast image [2]. Further advancing this concept, the pixelated STEM detector uses a CCD or CMOS image sensor for recording a CBED pattern as a 2D image at each STEM probe position (Fig. 1(b)). Thus, information that would be lost with the single channel detector can be utilized. The data taken with the pixelated STEM detector will be 4-dimensional (4D), because it records 2D diffraction pattern images for each position of electron probe that scans over the specimen two-dimensionally. As the image sensor is synchronized to record a 2D diffraction pattern with the electron probe scan step by step, high frame rate is preferable for fast acquisition of the 4D dataset.

## Pixelated STEM detector “4DCanvas”

We have developed the pixelated STEM detector “4DCanvas”. The outer appearance is shown in Fig. 2. The 4DCanvas is integrated into the JEOL electron microscope’s operational environment so one can acquire a 4D dataset with a single click through the operational software as a normal operation. Since the 4DCanvas is installed below the viewing chamber, it is possible

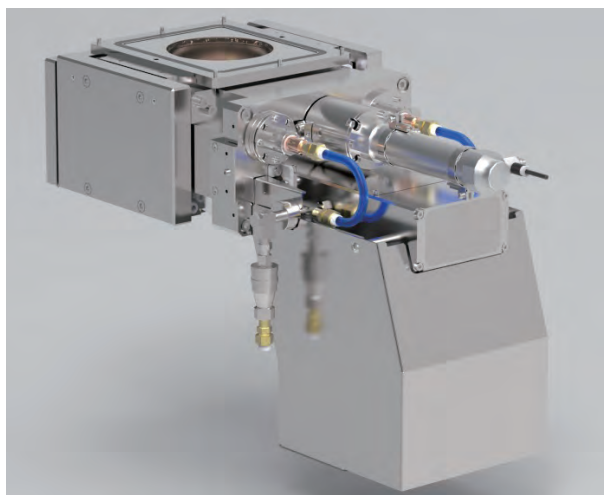
**Fig. 1 Comparison of conventional STEM and pixelated STEM detectors.**



(a) Conventional STEM detector. Electrons that passed through or diffracted by the specimen are converted to light signal by scintillator and detected by PMT. The type of obtained STEM image depends on the shape of the scintillator.  
(b) Pixelated STEM detector. Electrons that passed through or diffracted by the specimen are detected by a 2D image sensor. As the timing of exposure has to be synchronized with the probe scan, high frame rate CCD or CMOS is preferably used.

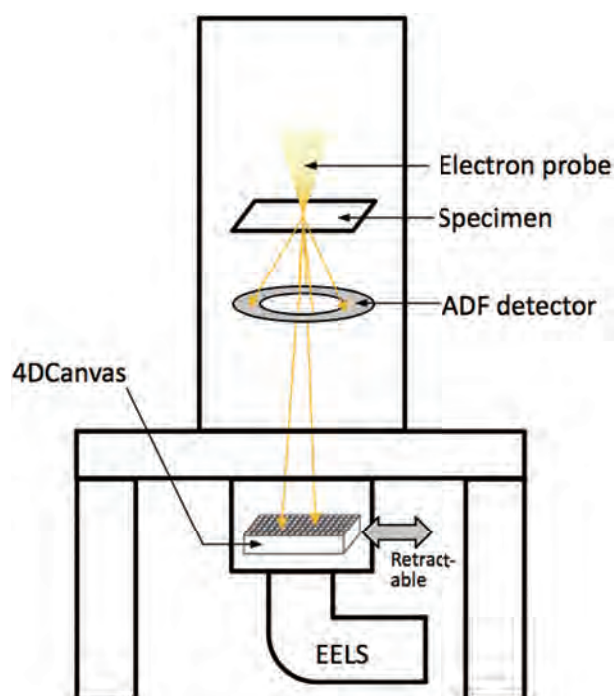
to record images by an annular dark-field (ADF) detector and the 4DCanvas (Fig. 3) simultaneously. In addition, as it

**Fig. 2 Appearance of the pixelated STEM detector "4DCanvas."**



CCD image sensor is contained inside the camera housing, and the camera is retractable by air cylinders. The image sensor is cooled with Peltier device, which is cooled by microscope circulating water.

**Fig. 3 Attachment position of 4DCanvas.**



The 4DCanvas is installed below the ADF detector, enabling a simultaneous recording of 4D dataset and ADF-STEM image. In addition, as it is retractable, a third party camera for TEM image recording and an EELS spectrometer are attachable at the opposite side and on the bottom, respectively.

is retractable from the optical axis, a high resolution camera for TEM image recording at the opposite side and an EELS spectrometer on the column can be installed.

### Direct electron detection image sensor "pnCCD"

An image sensor called pnCCD (PNDetector GmbH) is used in the 4DCanvas. The performances are shown in **Table 1**. The pnCCD is a direct electron detection CCD which does not use a scintillator so the signal generated from one incident electron is very high compared to the readout noise, and the quantum efficiency is almost 100%. Thus, each electron signal is robustly detected and the S/N of the acquired data is high. The number of pixels is  $264 \times 264$ , which is sufficient for a STEM detector. The most advantageous feature of 4DCanvas is that the frame rate is very high. In a full frame readout mode, it is 1,000 fps and with binning, it can be increased to up to 4,000 fps. When the frame rate of 4,000 fps (corresponds to the dwell time of the electron probe of  $250 \mu\text{s}$ ) is used to acquire a STEM image with  $256 \times 256$  pixels, the total acquisition time is expected to be about 16 seconds. The high frame rate is essential for minimizing the effect of specimen drift etc. during the recording. The pnCCD system prepares three readout modes optimal depending on the electron dose. The image sensor has high radiation hardness, thus a replacement of the sensor is not necessary for the use of normal STEM operation.

### Synthetic STEM image created from 4D dataset

In the conventional STEM detector, different shapes of scintillator are used for obtaining a user-preferred type of image. For example, a disk-shaped scintillator is used for a bright-field (BF)-STEM image, and an annular-shaped disk for an ADF-STEM image. In the 4DCanvas, as it records CBED patterns as 2D images, various types of STEM images can be synthesized in real-time or post-process by selecting an integration area on the recorded CBED patterns. **Figure 4** shows STEM images synthesized from a 4D dataset obtained from a monolayer graphene sample at an accelerating voltage of 80 kV. (a) and (b) are BF-STEM and differential phase contrast (DPC)-STEM images, respectively. The integration area for each image is shown in the insets. As the data is taken under the aberration corrected in-focus condition, the image contrast of the BF-STEM image is low. In the DPC-STEM image on the other hand, high anisotropic image contrast in the direction of the integration area is generated. The data was recorded with the frame rate of 2,000 fps and the number of pixels of the STEM image was  $256 \times 256$ , so the total acquisition time was about 30 seconds. In the graphical user interface (GUI) of the 4DCanvas operation system, live image of CBED pattern is displayed in addition to the live synthetic STEM image (**Fig. 5**). These images on the monitor can be saved. The parameters for the integration area can be changed freely.

### Visualization of magnetic field map of Ni thin film

When electron beam passes through a ferromagnetic specimen, it is deflected by a Lorentz force by magnetic field inside the specimen. This deflection will lead to the position shift of the beam in the detector plane. Since the 4DCanvas

records CBED patterns as 2D images, the magnitude and the direction of the beam shift can be directly measured. Thus, magnetic or electric field map that is represented by the vectors of magnetization or polarization can be obtained. **Figure 6** shows a magnetic field map created from 4D dataset obtained from a ferromagnetic Ni thin film. The data was taken with JEM-2800 microscope at an accelerating voltage of 100 kV. Inside the Ni film, magnetic domains, magnetized in in-plane

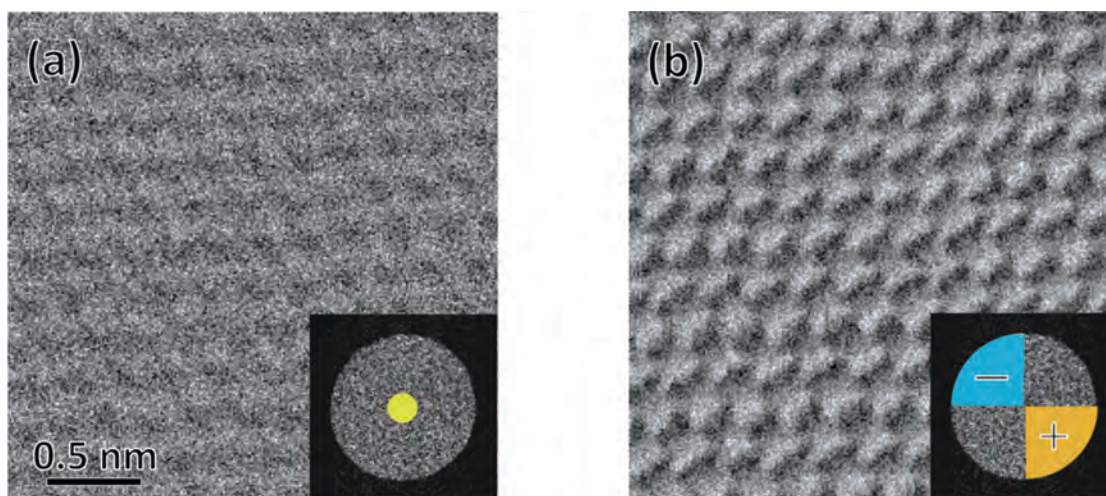
direction, are visible. Figure 6(a) shows a TEM image obtained in a Lorentz mode and domain walls of magnetic field are confirmed near the edge of the film. Figure 6(b) is a magnetic field map created from the 4D dataset obtained from the area indicated by the dashed rectangle in Fig. 6(a) and the magnetic field vectors indicating the magnitude and the direction at each pixel are clearly visualized.

**Table 1 Performance of pnCCD.**

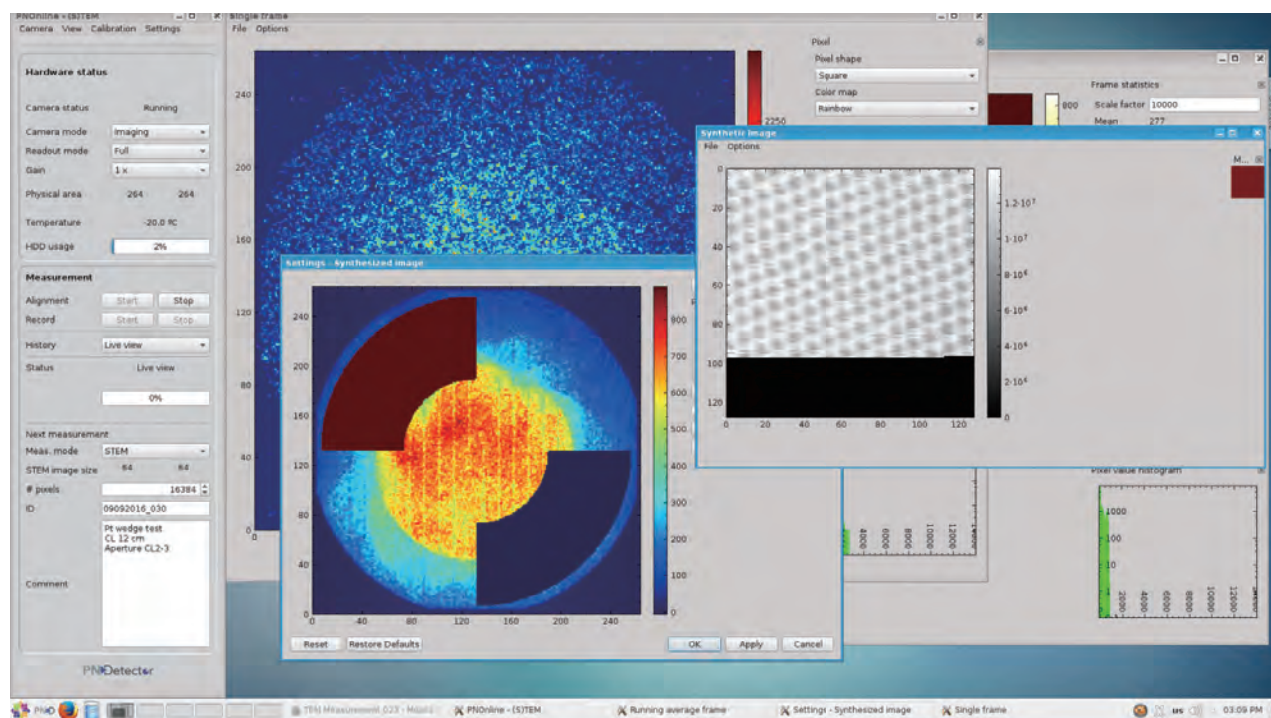
Detector type	Back-illuminated direct electron detection pnCCD
Pixel size	48 × 48 μm <sup>2</sup>
Number of pixels	264 × 264 pixels
Image area	12.7 × 12.7 mm <sup>2</sup>
Frame rate (degree of binning) (number of pixels)	1,000 fps (full frame readout) (264 x 264) 2,000 fps (2-fold binning) (264 x 132) 4,000 fps (4-fold binning) (264 x 66)
SNR	typ. 300:1
Quantum efficiency	typ. > 99% @ 20 kV ~ 300 kV
Operation modes	Single electron mode (best at very low intensities) Imaging mode (standard mode for imaging) Anti-Blooming mode (reduces overflow at high intensities)
Radiation hardness	> 4 × 10 <sup>17</sup> electrons/cm <sup>2</sup> @ 200 kV

The number of pixels of the sensor is 264 x 264. Frame rate is increased to up to 4,000 fps in binning mode. As the readout noise is low and the quantum efficiency is almost 100%, incident electrons are detected without almost any loss. Three types of readout modes: "single electron", "imaging" and "anti-blooming" are prepared depending on the electron dose rate for imaging.

**Fig. 4 Synthetic images of graphene**



(a) BF-STEM image of graphene. The inset shows an example of obtained CBED pattern and the integration area for creating the STEM image which is displayed over the pattern (yellow). The detection semi-angle was 0 - 6.2 mrad.  
(b) DPC-STEM image of graphene. The image is created by subtracting the blue quadrant area and adding the yellow area in the inset. The detection semi-angle was 0 - 31.2 mrad. An anisotropic image contrast is seen in the STEM image, reflecting the direction of the quadrant positions in the inset.

**Fig. 5 Operational GUI of 4DCanvas.**

Live image of CBED pattern is displayed at the center and live image of synthetic STEM (annular DPC image in this case) image is displayed on the right. Settings of the binning, gain and imaging mode are selectable.

## Phase image reconstruction by ptychography

Using a 4D dataset, image processing such as ptychography is possible. Ptychography reconstructs a phase contrast of a specimen with high efficiency and is known as an effective imaging method for a weak phase object such as graphene [3-5]. **Figure 7** shows a phase image of graphene (Fig. 7(b)) reconstructed by ptychography using the same 4D dataset as Fig. 4, and a simultaneously obtained ADF-STEM image (Fig. 7(a)). The S/N and image contrast is higher in the ptychographically reconstructed image. In ptychography, areas that contribute to the phase contrast on CBED patterns (overlapped area between transmitted and diffracted discs) are extracted for corresponding spatial frequencies. This operation removes the area (otherwise becomes noise) which does not contribute to the phase contrast. In addition, since the polarity of phase on each overlapped area can be processed, the phase contrast can be effectively utilized. 4DCanvas is very suitable when this type of operation is required where the shape of the detector needs to be dynamically changed according to the spatial frequency.

## Summary

We have developed the pixelated STEM detector “4DCanvas” which has high sensitivity and high frame rate. Various types of STEM images can be created by processing the obtained 4D dataset. In the future, many functional processes will be developed, since the 4D dataset serves for variety of information.

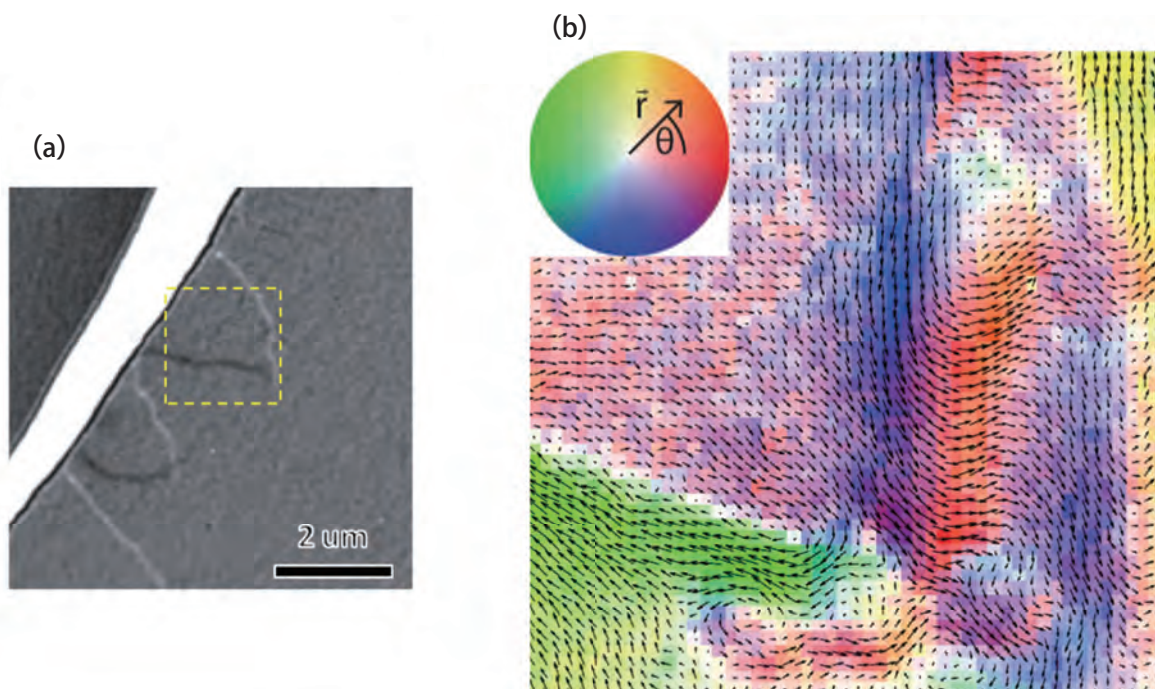
## Acknowledgment

The author would like to acknowledge the support and assistance of Tomohisa Fukuda, Kazunori Somehara, Takamitsu Saito, Hiroyuki Banba, Takanori Kataoka, Yuji Yamazaki, Hidetaka Sawada, Ryo Yamagishi, Kazuya Yamazaki, Shunsuke Yoshida, Isamu Ishikawa, Hideaki Arima, Yukihito Kondo, Yoshihiro Ohkura, Martin Simson, Martin Huth, Henning Ryll, Sebastian Ihle, Robert Ritz, Hao Yang, Lewys Jones, Gerardo Martinez, Heike Soltau, Prof. Peter D. Nellist and the project members at JEOL Ltd.

## References

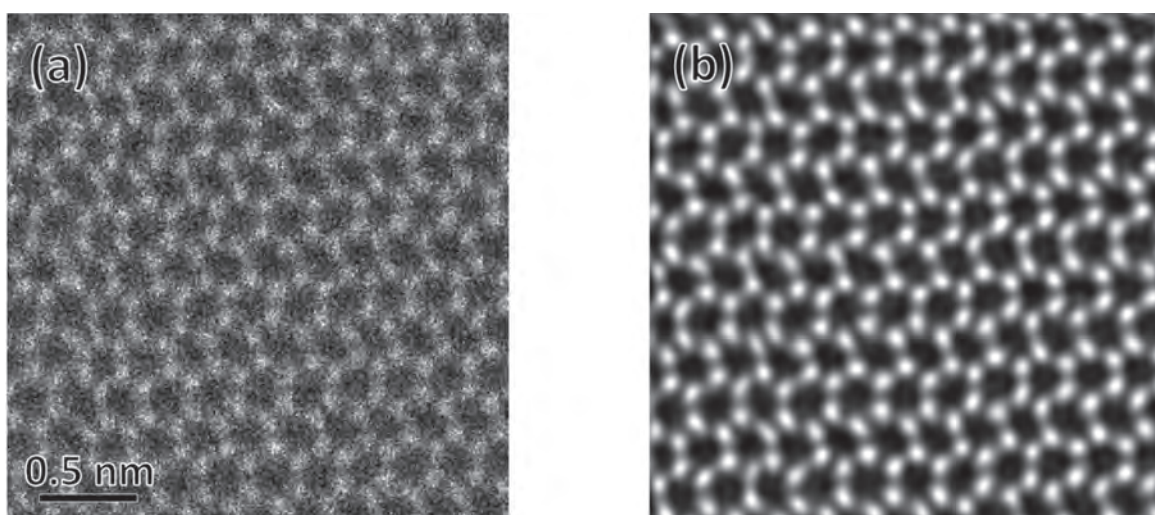
- [ 1 ] E Okunishi et al., *Microsc. Microanal.*, **15** (S2) (2009) 164.
- [ 2 ] N Shibata et al., *J. Electron Microsc.*, **59** (6) (2010) 473.
- [ 3 ] P.D. Nellist et al., *Nature*, **374** (1995) 630.
- [ 4 ] T.J. Pennycook et al., *Ultramicroscopy*, **151** (2015) 160.
- [ 5 ] H. Yang et al., *Nat. Commun.*, **7** (2016) 12532.

**Fig. 6 Magnetic field map from Ni thin film.**



(a) Lorentz TEM image of Ni thin film. A crack in the film is observed and magnetic domain walls are visible near the edge.  
(b) Magnetic field map created by the 4D dataset obtained from the dashed rectangle area in (a). The arrows represent magnetic field vectors calculated from the amount and the direction of the position shift of the transmitted discs at each probe position. The color hue and the saturation in the inset indicate the direction and the magnitude of magnetic field vector, respectively.

**Fig. 7 Phase image of graphene reconstructed by ptychography.**



(a) ADF-STEM image of graphene. The detection semi-angle of ADF detector was 47 - 187 mrad.  
(b) Phase image reconstructed from the 4D dataset obtained simultaneously with (a). The S/N and the image contrast are greatly improved.

# Development of a New Field Emission Electron Probe Microanalyzer JXA-8530FPlus

Satoshi Notoya SA Business Unit, JEOL Ltd.

The JXA-8530FPlus, JEOL's new third-generation Field Emission Electron Probe Microanalyzer (FE-EPMA), comes with enhanced analytical and imaging capabilities. The In-Lens Schottky field emission electron gun combined with new software provides higher throughput while maintaining high stability. In addition, a new multipurpose chamber accommodates a variety of peripheral units for higher expandability for analysis with EPMA. Thus, the JXA-8530FPlus allows for a wider range of EPMA applications to be achieved with higher resolution.

## Introduction

JEOL commercialized the world's first FE-EPMA in 2003. This highly regarded FE-EPMA has long been used in various fields, such as metal research, materials science and geology in both industry and academia. Up until now, approximately 300 units of JEOL FE-EPMAs have been used around the world.

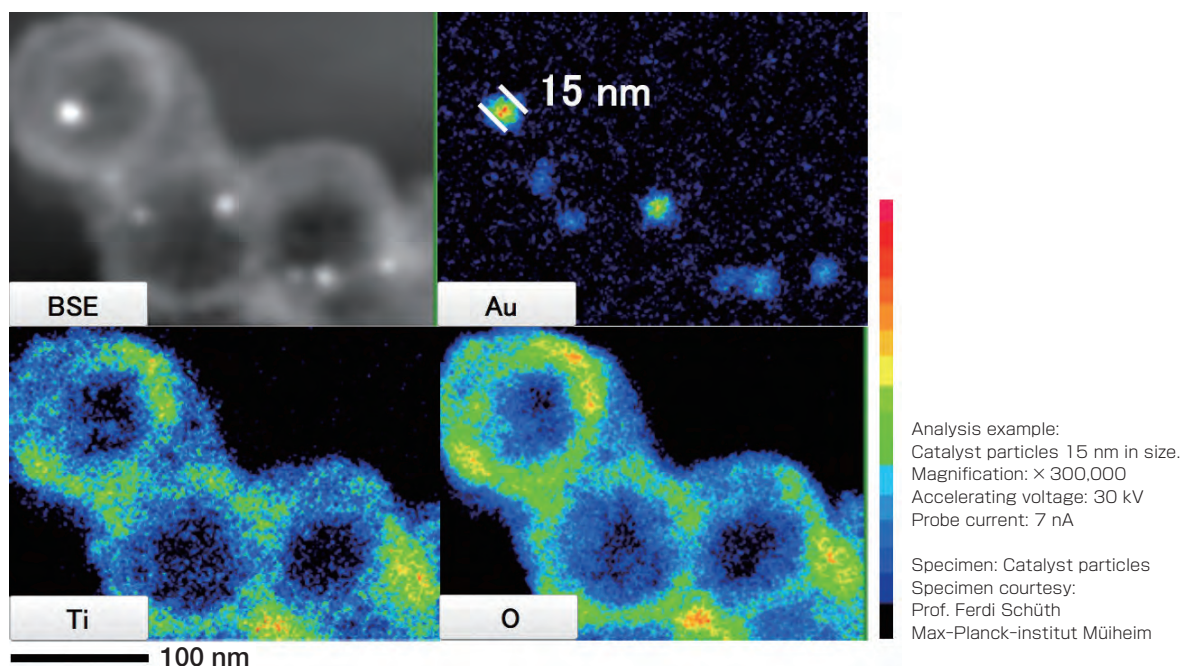
Our new product of the JXA-8530FPlus has more features compared to our conventional FE-EPMA, thus extending EPMA applications to a wider range of fields of elemental analysis.

This report introduces those features.

### 1. In-Lens Schottky Plus FEG EPMA version

The In-Lens Schottky Plus FEG EPMA version, with an optimized angular current density, allows for analysis with a large probe current of 2  $\mu\text{A}$  or more. The resolution of secondary electron image has been improved even under analytical conditions by automatically adjusting for the correct convergence angle. **Figure 1** shows an example of high-magnification elemental mapping with the JXA-8530FPlus.

**Fig. 1 High-magnification elemental mapping with the JXA-8530FPlus.**



## 2. Advanced Software

A wealth of Microsoft Windows-based advanced applications systems are available, including: 1) Trace Element Analysis Program for simpler, optimized analysis of trace elements including adding data collected from up to 5 spectrometers, 2) Phase Map Maker for automatic creation of phase maps based on principal components, 3) Non-Flat Surface Analysis Program for automated WDS analysis of specimens with surface irregularities.

## 3. Flexible WDS configuration

Various X-ray spectrometers (WDSs) can be selected: a Rowland circle radius of 140 mm (140R) or 100 mm (100R), 2 crystal or 4 crystal configurations and a mix of standard or large size crystals.

The XCE (2 xtl) X-ray Spectrometer, the FCS (4 xtl) X-ray spectrometer and the L (large 2 xtl) X-ray Spectrometer for 140R have wide spectrometry range and provide superior wavelength resolution and peak-to-background ratio. The H Type X-ray Spectrometer of 100R provides high X-ray intensity. Users can select from these spectrometers depending on requirements.

## 4. Combined WDS/EDS system

The JXA-8530FPlus comes with JEOL's 30 mm<sup>2</sup> silicon-drift detector (SDD). A high count-rate SDD along with an in-situ variable aperture enables EDS analysis at WDS conditions. EDS spectra, maps and line scans can be acquired simultaneously with WDS data (Fig. 2). For example, when wide-area mapping is conducted with stage-driven specimen movement, the JXA-8530FPlus allows for both elucidation of trace element distribution by WDS and EDS spectral mapping simultaneously. This capability prevents the missing of unexpected elements in an unknown specimen because EDS does not require known elements in advance of the analysis.

## 5. Multipurpose chamber

The JXA-8530FPlus is equipped with a highly-expandable specimen chamber and specimen exchange chamber, enabling you to integrate a variety of optional attachments on the chamber (Fig. 3).

These include:

- Electron Backscatter Diffraction System (EBSD)
- Cathodoluminescence Detectors (panchromatic,

**Fig. 2 Appearance of the silicon drift detector and analysis examples of combined WDS/EDS.**

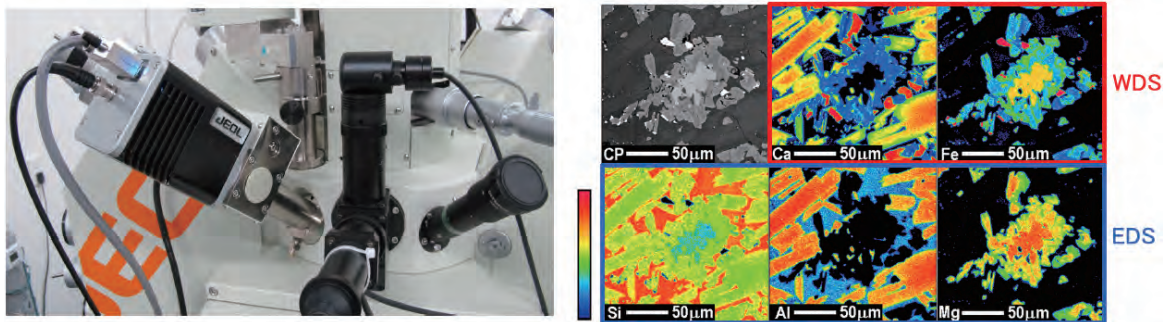
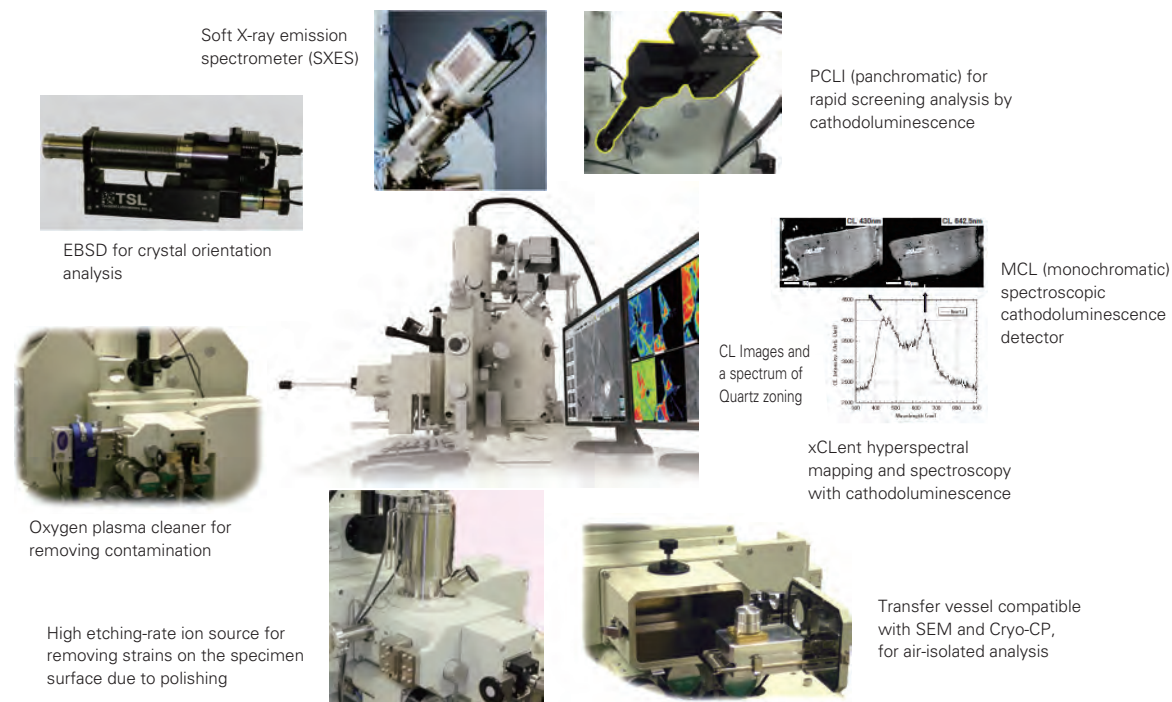


**Fig. 3 Peripheral units to which the JXA-8530FPlus can attach.**



- monochromatic, full color hyperspectral)
- Soft X-ray Emission Spectrometer (SXES)
- Air Isolated Transfer Vessel
- High Etching Rate Ion Source, in-situ cleaner, etc.

### 6. Powerful clean vacuum system

A powerful, clean vacuum system is employed on the JXA-8530FPlus, including two magnetic-levitation turbo molecular pumps. In addition, a two-stage intermediate chamber is provided for the electron optical column, thus maintaining high vacuum in the electron-gun chamber by differential pumping.

The addition of optional Scroll pumps and a liquid nitrogen cold finger create the ultimate oil free vacuum system.

### 7. Soft X-ray Emission Spectrometer (SXES)

An ultra-high energy-resolution Soft X-ray Emission Spectrometer (Fig. 4) was co-developed by the Institute of Multidisciplinary Research for Advanced Materials, Tohoku University (Prof. M. Terauchi) and JEOL Ltd., etc.

The variable-line-spacing (VLS) grating enables simultaneous detection (much like EDS) and allows detection of Li-K and B-K spectra with a high-sensitivity CCD. This spectrometer

achieves superbly high energy-resolution (0.3 eV or better), enabling detailed chemical-bonding state analysis.

### 8. miXcroscopy™ (Correlative microscope)

Multiple coordinate data specified by a Nikon optical microscope can be registered at the same time as the analysis points by EPMA (point logger function) (Fig. 5).

## Main Specifications

The main specifications of the JXA-8530FPlus are shown in Table 1.

## Summary

The JXA-8530FPlus, a new Field Emission Electron Probe Microanalyzer (FE-EPMA), is a successor of JEOL FE-EPMAs that incorporate highly regarded technologies for many years. With enhanced analytical and imaging capabilities and higher expandability, the JXA-8530FPlus will meet diversified needs of customers for new elemental-analysis applications.

**Fig. 4 Appearance of Soft X-ray Emission Spectrometer (SXES).**

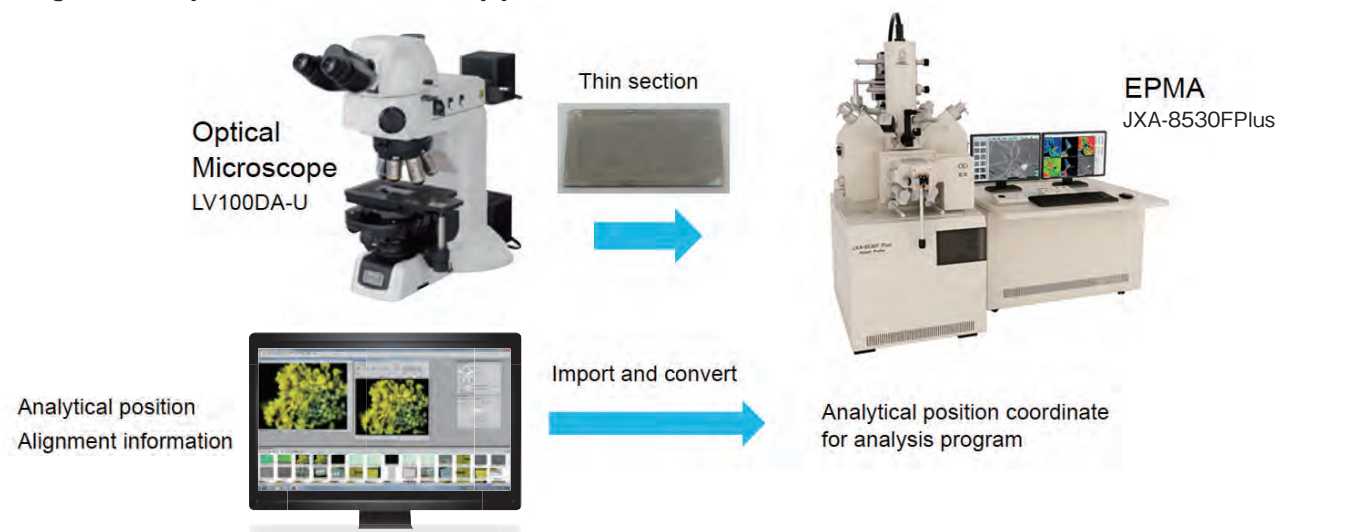


**Table 1 Main specifications of the JXA-8530FPlus.**

Elemental analysis range	WDS: (Be*) B to U, EDS: B to U
X-ray spectrometry range	WDS spectrometry range: 0.087 to 9.3 nm EDS energy range: 20 keV
Number of X-ray spectrometers	WDS: 1 to 5 selectable, EDS: 1
Maximum specimen size	100 mm × 100 mm × 50 mm (H)
Accelerating voltage	1 to 30 kV (0.1 kV step)
Probe current stability	± 0.3%/h
Secondary electron image resolution	3 nm at WD 11 mm, 30 kV
Minimum probe diameter (analytical conditions)	20 nm at 10 kV, 10 nA, WD 11 mm 50 nm at 10 kV, 100 nA, WD 11 mm
Magnification	× 40 to × 300,000 (WD 11 mm)
Scanning image pixel resolution	Up to 5,120 × 3,840

\* When an optional Be analyzing crystal is attached.

**Fig. 5 Analysis with miXcroscopy™.**



# JMS-MT3010HRGA INFITOF, a High Resolution Time-of-Flight Mass Spectrometer (TOF-MS) for Gas Monitoring Analysis

Yukinori Yahata MS Business Unit, JEOL Ltd.

The JMS-MT3010HRGA INFITOF is a compact, high resolution time-of-flight mass spectrometer (TOF-MS). With its latest multi-turn technology, the MS system is especially suitable for gas monitoring analysis, meeting the latest requirements in studies of advanced materials, including hydrogen, ammonia, catalysts, combustion, and battery technologies.

## Introduction

The JMS-MT3010HRGA INFITOF system design was based on the MULTUM series TOF-MS developed by Osaka University.

The system utilizes some of the technologies originally designed for cometary exploration in the ESA's Rosetta mission.

Featuring innovative technologies such as “multi-turn” and “perfect focusing”, the INFITOF accomplishes high mass resolution measurements in an extraordinarily compact unit. This article will describe the features of this unique system, and introduce some of its applications.

## Features

The INFITOF is a “multi-turn TOF-MS for gas analysis” accomplishing high mass resolution in the low mass range. **Figure 1** shows an external view along with its main features.

Typically, TOF-MS mass resolution is too low for the analysis of low molecular weight compounds. However, the INFITOF achieves a mass resolution of 30,000 or more (FWHM) at  $m/z$  28. The system is also capable of detecting hydrogen atoms, which is extremely difficult for conventional TOF-MS systems.

**Figure 2** shows the measurement example for typical low molecular weight compounds in the low mass range.

High mass resolution is needed for most of the materials

**Fig. 1 External view and major features of the JMS-MT3010HRGA INFITOF.**

### ○ Compact unit

- ⇒ Small footprint (equal to desktop PC)
- ⇒ Easily transportable (40 kg)

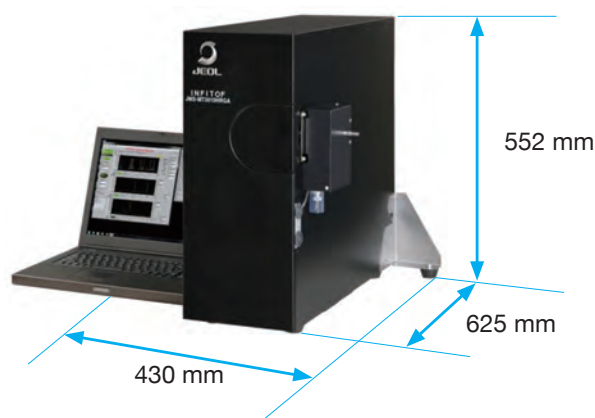
### ○ High resolution

- ⇒ Maximum resolution: 30,000 or more ( $m/z$  28)
- ⇒ HR-SIM (real time monitoring)

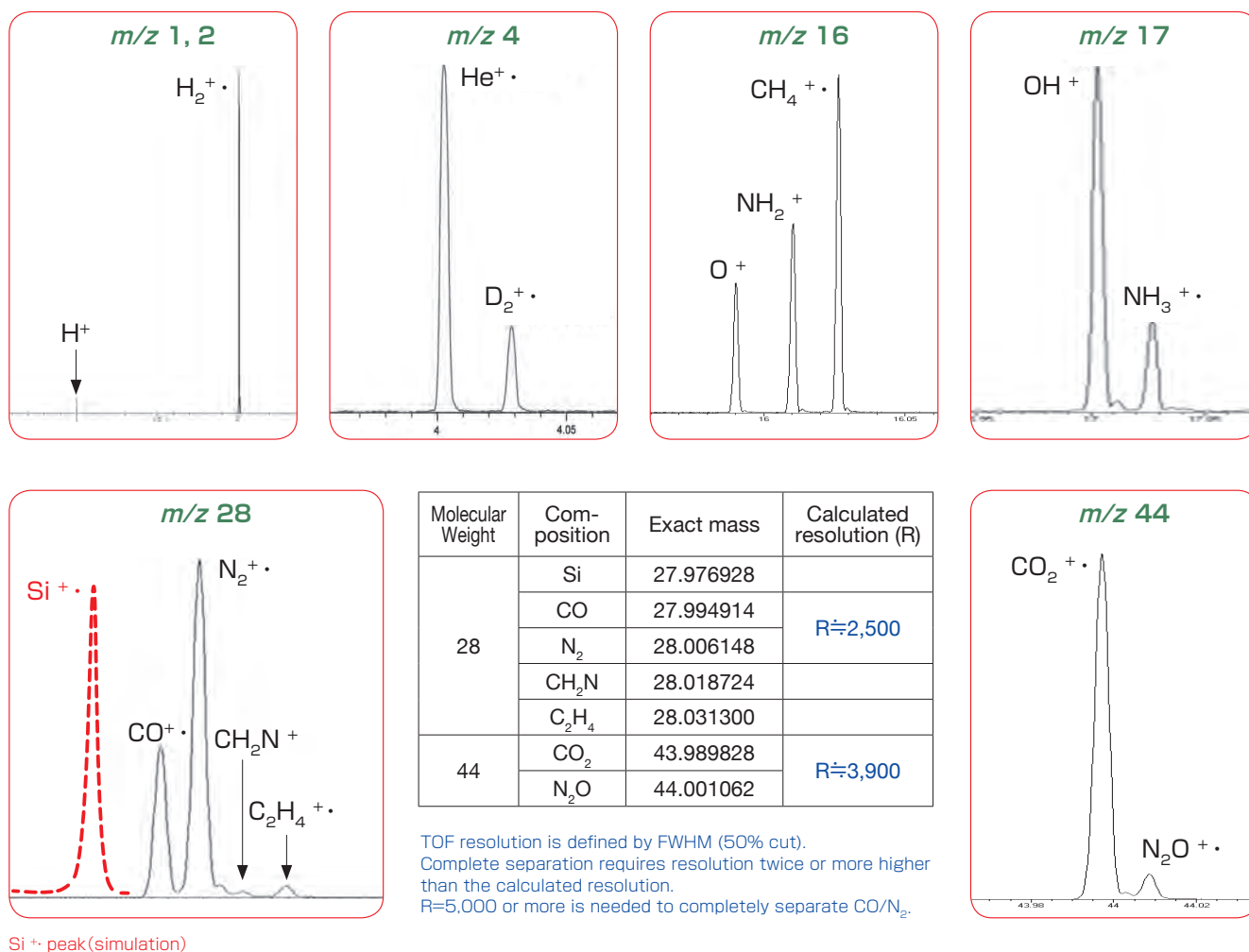
### ○ Hydrogen detection

- ⇒ Detects hydrogen peak ( $m/z$  1)

Performance    Mass range:  $m/z$  1 to 1,000  
                      Mass resolution: > 30,000 (FWHM) ( $m/z$  28)  
                      Sensitivity: Atmosphere:  $^{39}\text{Ar}$  S/N  $\geq$  10



**【JMS-MT3010HRGA INFITOF】**

**Fig. 2 Mass separation of gases that are frequently examined by our clients.**

in Fig. 2 ( $H/H_2$ ,  $D_2$ ,  $CH_4$ ,  $NH_3$ ,  $CO$ ,  $N_2O$ ). The results shown demonstrate that the INFITOF can successfully separate the masses for these materials.

**Figure 3** is a 24-hour continuous analysis of standard gases (10 ppm each). The stability of resolution was confirmed before and after the analysis using  $CO/N_2$ . These results demonstrate that the system is capable of stable continuous analysis of gases at low concentrations (10 ppm), which is effective for monitoring gases generated in rechargeable batteries and chemical reaction furnaces.

**Figure 4** is an analysis of combustion gases in a flame. The gases were generated by a methanol lamp and directly drawn into the instrument through a capillary tube for analysis. Combustion compounds such as  $H_2$ ,  $H_2O$ ,  $CH_4$ ,  $CO$ ,  $N_2$ ,  $CO_2$ ,  $NO$ ,  $N_2H$ , and  $NO_2$  were detected, while  $O_2$  was minimally detected. The high resolution capability of the INFITOF makes it a powerful tool for the analysis of combustion reactions and heat generated gases (TG-MS, TPD-MS) in the field of advanced materials research.

**Figure 5** is a simple observation of isotope exchange reaction when heavy water ( $D_2O$ ) was combined with light water ( $H_2O$ ). Vaporized  $D_2O$  and  $H_2O$  were mixed in an oven, and the mixture was analyzed using the INFITOF. These results demonstrate that HDO ( $m/z$  19) was formed through H/D isotopic exchange reactions. The INFITOF had no problem separating masses at  $m/z$

19 ( $HDO/H_3O$ ) and  $m/z$  20 ( $D_2O/H_2DO$ ).

The high resolution INFITOF system is a powerful tool for a variety of applications, including absolute composition analysis and behavior observations for water, nuclear safety research, catalytic reactions, and functional analysis of battery technologies.

## Conclusion (Summary)

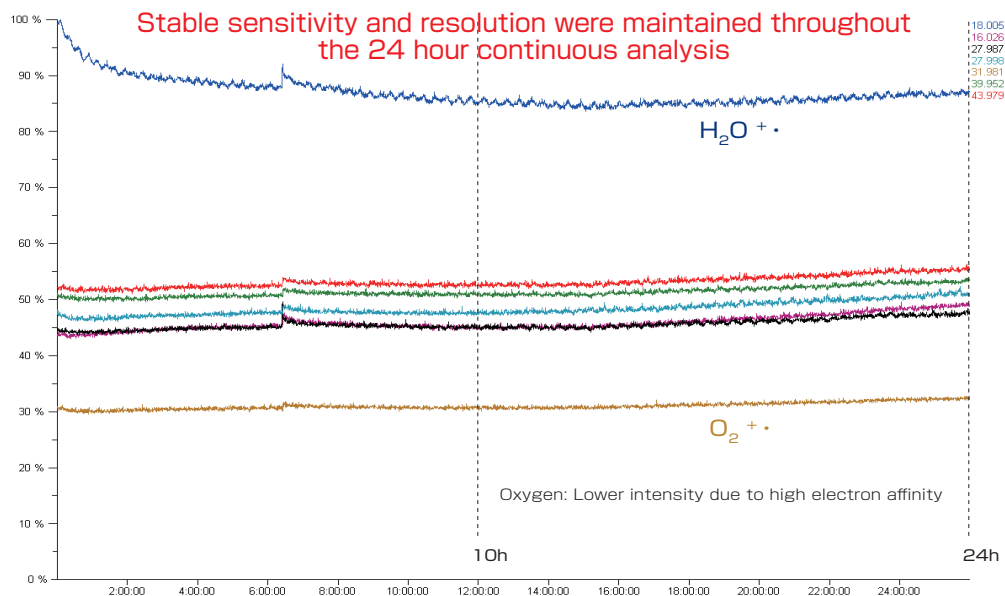
The JMS-MT3010HRGA INFITOF is a compact TOF-MS for gas monitoring analysis that is capable of high resolution measurements in the low molecular weight range. This system is suitable for a wide range of applications from monitoring and analysis of gases generated from materials to behavioral observations of hydrogen. Because it is a powerful tool for the analysis of hydrogen, ammonia, catalysts, combustion products, and gases generated from battery technologies, the INFITOF meets the most advanced research requirements in the field of renewable energy development.

## Acknowledgment

The author would like to thank Koji Okuda, JEOL USA, Inc., for acquiring the data showing H/D isotopic exchange reactions between light water and heavy water.

**Fig.3 Stability in standard gas analysis.**

Stability:  $R=6,000$  (24 hours)



Sample gases	Color
18.01057 (H <sub>2</sub> O)	Vacuum residue
16.03130 (CH <sub>4</sub> )	10 ppm
27.99492 (CO)	10 ppm
28.00615 (N <sub>2</sub> )	10 ppm
31.98983 (O <sub>2</sub> )	10 ppm
39.96238 (Ar)	10 ppm
43.98983 (CO <sub>2</sub> )	10 ppm

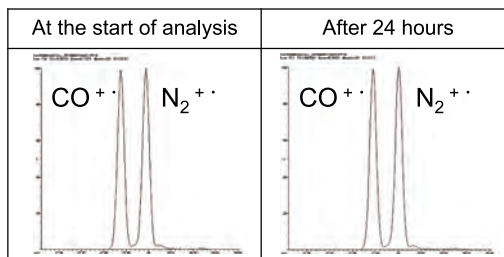
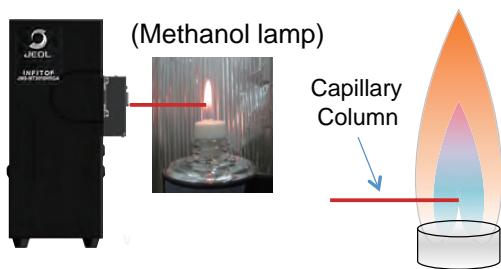


**Fig.4 Analysis of combustion gases in flame.**



**Ionization : EI ,**  
**Resolution  $\approx 5000(m/z)$**

- Excerpts from composition calculation
- Composition formula on MS spectrum is estimated from composition calculation result

Measured Mass	Formula	Calculated Mass	Error (mmu)
2.013960	H <sub>2</sub>	2.015650	-1.7
14.002768	N	14.003070	-0.3
15.024254	CH <sub>3</sub>	15.023475	0.8
15.995558	O	15.994920	0.6
16.031929	CH <sub>4</sub>	16.031300	0.6
17.003216	HO	17.002745	0.5
18.010739	H <sub>2</sub> O	18.010570	0.2
27.994779	CO	27.994920	-0.1
28.004476	N <sub>2</sub>	28.006150	-1.7
29.003286	CHO	29.002745	0.5
29.016814	HN <sub>2</sub>	29.013975	2.8
30.001639	NO	29.997990	3.6
30.013364	CH <sub>2</sub> O	30.010570	2.8
31.020285	CH <sub>3</sub> O	31.018395	1.9
31.989066	O <sub>2</sub>	31.989830	-0.8
32.027544	CH <sub>4</sub> O	32.026220	1.3
43.989236	CO <sub>2</sub>	43.989830	-0.6

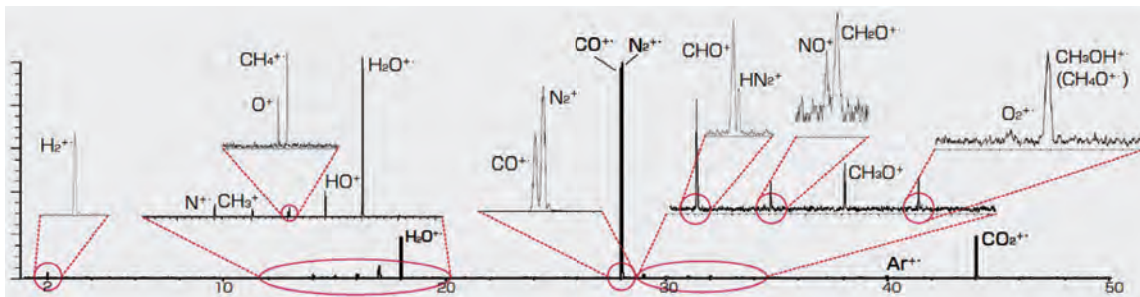
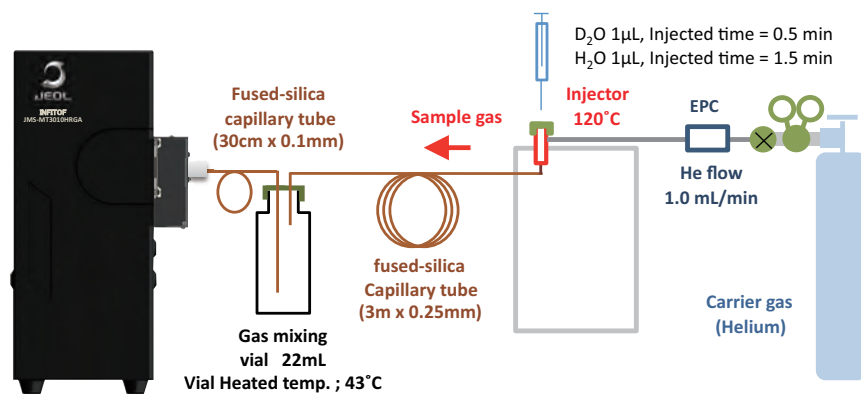


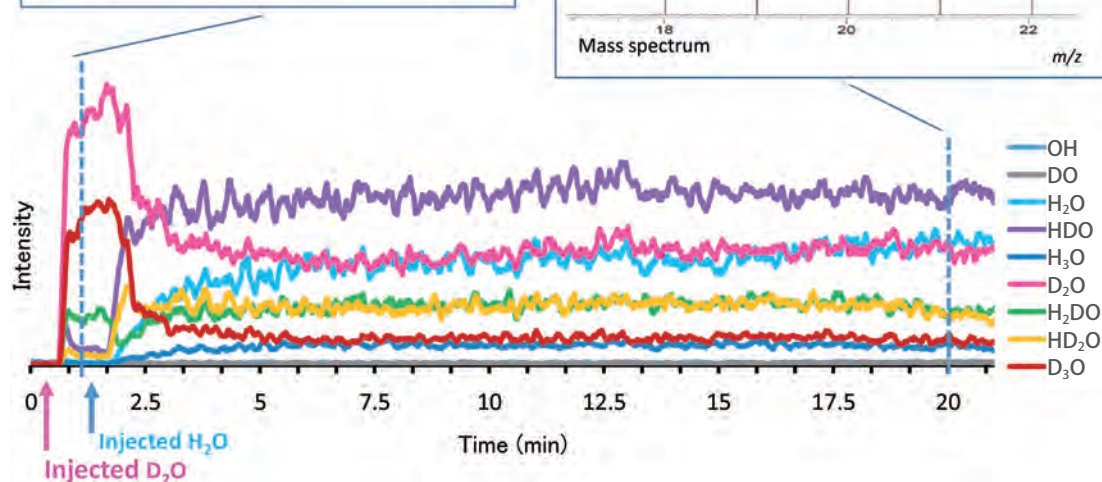
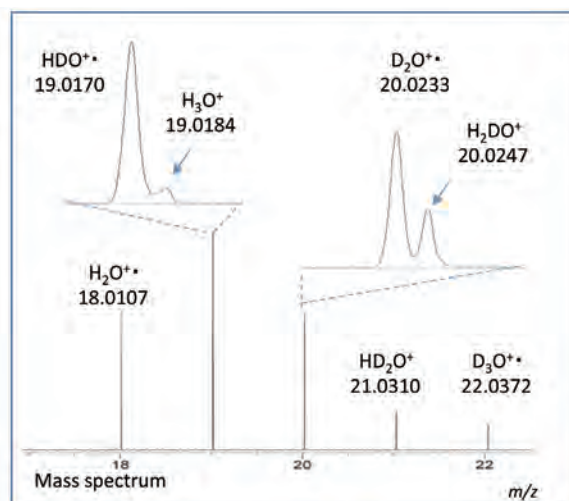
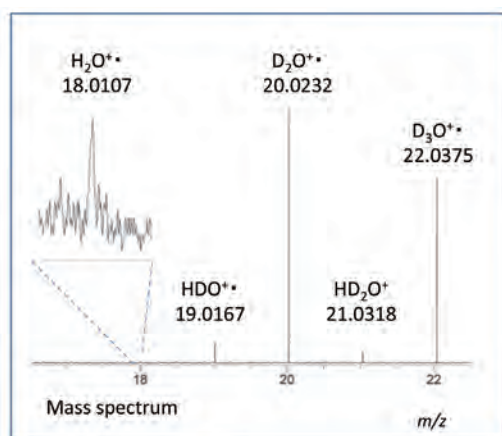
**Fig. 5 Real time monitoring for H/D exchange reaction of water.**



( Schematic drawing of experimental equipment )

Measurement condition	
Measurement mode	Extended mode
Turn	150
Resolution	Resolution = 30,000 ( $m/z$ 18 )
Ionization energy	15eV
Detector voltage	2700V
Scan speed	1sec/spectrum
Expand mass spectrum	10sec averaged

Formula	Measure range( $m/z$ )
HO	17.00274 ± 0.0005
DO	18.00901 ± 0.0005
H <sub>2</sub> O	18.01056 ± 0.0005
HDO	19.01685 ± 0.0005
H <sub>3</sub> O	19.01839 ± 0.0005
D <sub>2</sub> O	20.02312 ± 0.0005
H <sub>2</sub> DO	20.02466 ± 0.0005
HD <sub>2</sub> O	21.03094 ± 0.0005
D <sub>3</sub> O	22.03722 ± 0.0005



# The Development of the ROYAL HFX Probe

A. Zens,<sup>1</sup> T. Miyamoto<sup>2</sup>, R. Crouch<sup>1</sup>, T. Bergeron<sup>1</sup>,  
M. Frey<sup>1</sup>, A. Nomura<sup>2</sup>, Y. Horino<sup>2</sup>, T. Nishida<sup>2</sup>

<sup>1</sup> JEOL USA Inc.

<sup>2</sup> JEOL RESONANCE Inc.

We report in this article the development of a  $^1\text{H}, ^{19}\text{F}$ , X NMR probe. Here we use circuitry that uses magnetic coupling to do on demand experiments where one of the three nuclei is observed and the other two are decoupled. The implementation of this circuitry in a routine NMR probe was found to be superior to capacitive coupling methods. The full broadband capability of this probe allows for the structure elucidation of nearly all types of chemical species that contain  $^1\text{H}$  and  $^{19}\text{F}$  nuclei and hence is a truly versatile and routine NMR probe.

## Introduction

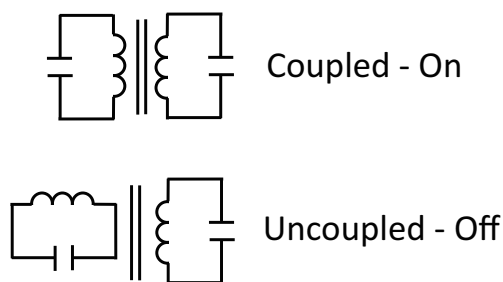
The advantages of using magnetic coupling to do  $^1\text{H}^{19}\text{F}^{13}\text{C}$  experiment are described by Zens et. al. [1]. In this paper we describe how this circuitry was extended to include  $^1\text{H}^{19}\text{F}$  experiments in the development of the first  $^1\text{H}, ^{19}\text{F}$ , X broadband probe.

## General Concepts and Theory

As described in reference 1, the basic concept is to use inductive coupling to split the high frequency sample coil resonance into two modes corresponding to the observe frequency for  $^1\text{H}$  and  $^{19}\text{F}$ . Inductive coupling was found to be superior to a circuit similar to the Haase circuit because the minimum capacitance of the variables in this circuit results in unacceptable losses when the circuit is in the uncoupled mode. [2]. The inductive and capacitive circuits are essentially equivalent in the coupled mode.

The inductive circuit used here can be described pictorially as shown in **Fig. 1**, the two distinct modes, coupled and uncoupled,

**Fig. 1 Pictorial view of the two orthogonal modes of the magnetically coupled H/F circuit.**



are shown as being orthogonal to each other. To implement this circuit we have constructed two coils. The first coil is similar to an Alderman – Grant coil [3]. It serves as the sample observe coil and detects the resonance of the spins, i.e.  $^1\text{H}$  and  $^{19}\text{F}$ . The second coil is what we call the idler coil. This coil is used solely to couple to the sample coil and split the fundamental resonance into two modes. To accomplish this idler coil is resonated half way between the  $^{19}\text{F}$  and  $^1\text{H}$  resonances. In the coupled mode the magnetic axis of the idler coil overlaps with the magnetic axis of the sample coil creating two modes. The degree of separation of the two peaks depends on the degree of rotation of the idler coil which can increase or decrease the k value, the amount of coupling between the two coils. **Figure 2** shows this interaction. **Figure 3** shows the sample coil and idler in close proximity to each other. The red arrow shows that we can rotate the idler coil in a manner that couples and decouples the interaction between the two coils.

## Practical Aspects of Observing and $^1\text{H}$ and $^{19}\text{F}$

**Figure 4** illustrates the relationship between the idler frequency and the circuit fill factor (CFF) [4]. The circuit fill factor is a measure of the circuit efficiency and is independent of the Q and sample fill factor for a given mode in the probe. Here one can adjust the efficiency of the coupled mode to favor one mode or nuclei over the other. **Table 1** shows the PW(90) values and powers for the HFX probe in both the decoupled and coupled modes. The data here clearly indicates that the idler frequency of the circuit was set to favor  $^{19}\text{F}$  performance over  $^1\text{H}$  performance. For the coupled mode we wanted to keep the PW(90) values shorter for  $^{19}\text{F}$  so as to be able to efficiently observe the larger chemical shift region of  $^{19}\text{F}$ .

In order for the idler frequency to be set such that PW(90) values can be adjusted for optimal usage a mechanism to measure the idler frequency in the probe had to be devised. The idler frequency in the probe is different than when it is outside the probe

**Fig. 2 Idler coil interaction with the sample coil.**

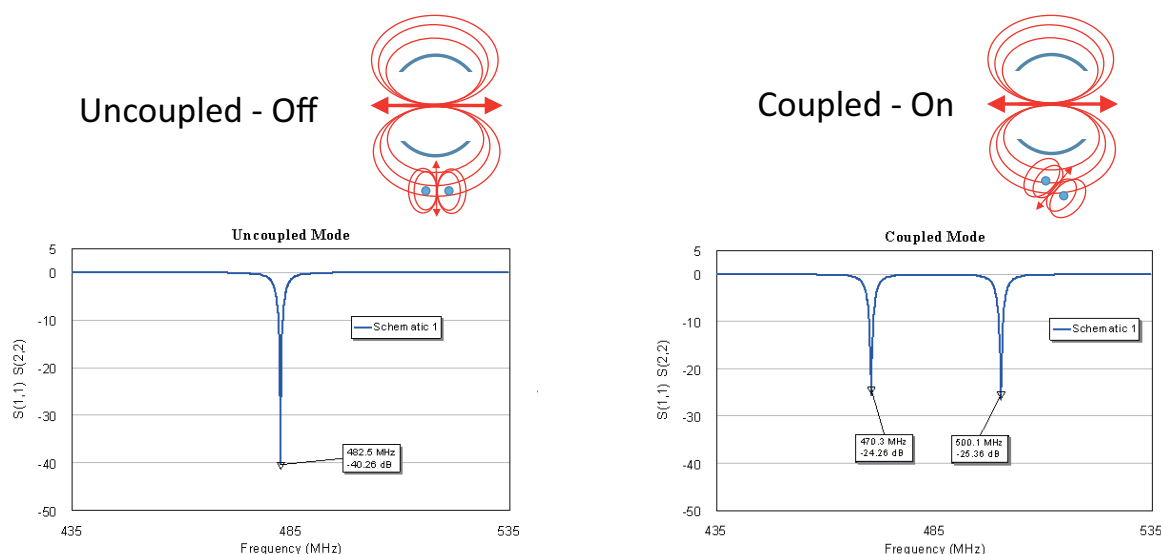


**Fig. 3 Sample Coil and Idler coil in close proximity.**

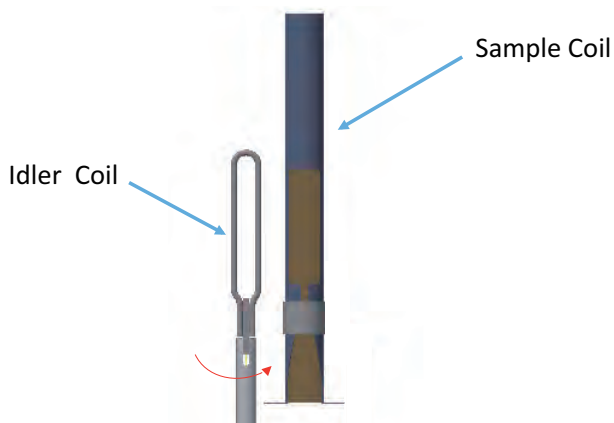
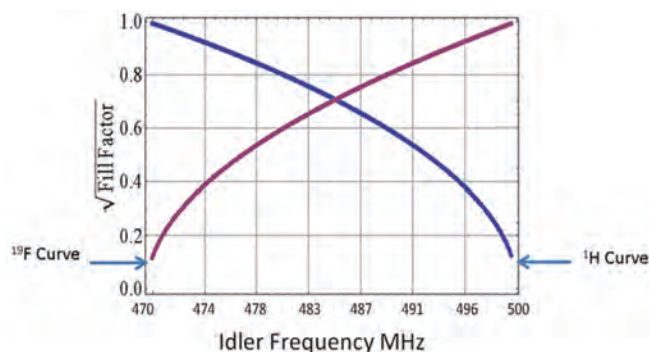


**Fig. 4 SQRT of Circuit Fill Factor vs Frequency**



The square root of the circuit fill factor versus the idler frequency. Note that the fill factor improves for a particular nucleus the further the idler frequency is away from its observe frequency.

**Table 1 Power and PW(90) data for ROYAL HFX Probe**

Power	32.5 W	32.5 W
Observe	<sup>1</sup> H	<sup>19</sup> F
Measurement	PW(90)	PW(90)
Uncoupled	7.01 us	8.67 us
Coupled	11.17 us	9.84 us

due to the presence of metallic objects like the Faraday screen etc. We have also noted that the idler frequency is dependent on its orientation the sample region for the same reason.

Figure 5 shows the S11 plot of the high frequency channel when the probe is in the coupled mode (5a). Note here that when the sample coil resonance is tuned to a higher frequency the amplitude of the lower resonance decrease and also moves towards the center of the plot. Tuning the sample coil to yet a higher frequency results in a similar action with the lower resonance moving further towards the center of the plot and the amplitude moving lower, figures 5b and 5c. Here when the

amplitude goes to zero this is the idler frequency because the idler is no longer interacting with the sample coil [5]. Using this measurement method we can determine the frequency that the idler coil needs to be set at on the bench in order for it to have the correct frequency when it is in the probe. As stated earlier we usually set this frequency slightly higher so as to optimize the <sup>19</sup>F PW(90) over that of the <sup>1</sup>H PW(90) in the coupled mode.

Figure 6 shows the components used in the construction of the idler coil. Here the idler coil is constructed from a single copper loop that is not compensated in terms of susceptibility. The non-spin line-shape of the probe was found not to be impacted by the presence of this coil. The sapphire chip capacitor [6] shape was modified by the use of a rotary grinding tool so that it could fit in the available space in the probe between the sample coil and the Faraday shield. Note here that the modified chip is soldered to the chip using an alignment fixture (not shown).

### Testing and Performance

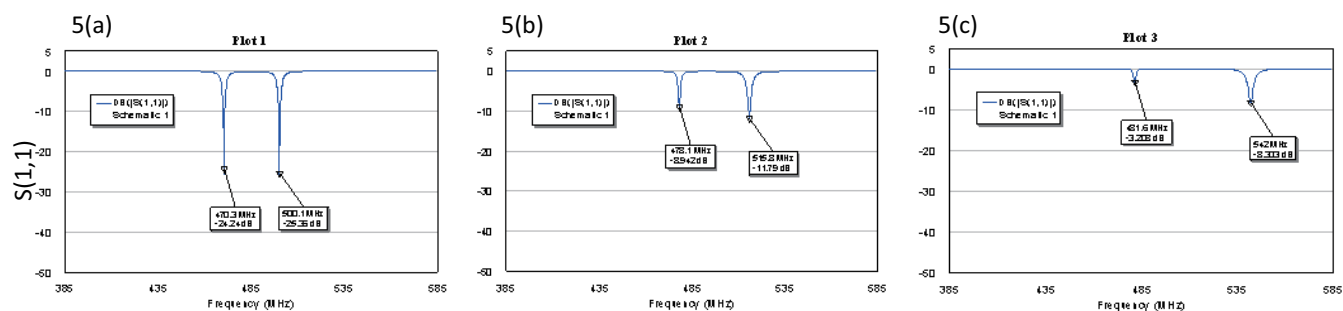
From the outset the goal of this HFX development project was to produce a routine NMR that had the same performance at the JEOL ROYAL Probe but with the additional capability of simultaneous <sup>1</sup>H and <sup>19</sup>F decoupling. Table 2 shows the data

accumulated for this probe. What is remarkable here is that none of the routine performance numbers have been impacted by the addition of the idler coil. The only additional test required for the probe are those related to the coupled mode of operation. For  $^1\text{H}/^{19}\text{F}$  decoupling, test with the diplexer combiner are needed to insure that noise from the decoupling in either  $^1\text{H}$  or  $^{19}\text{F}$  doesn't leak into the other channel. See Fig. 7. Figure 8 shows the non-spin line-shape for the probe on 1%  $\text{CHCl}_3$ . This is important to emphasize for the routine 2D experiments that this probe enables.

## Applications Data

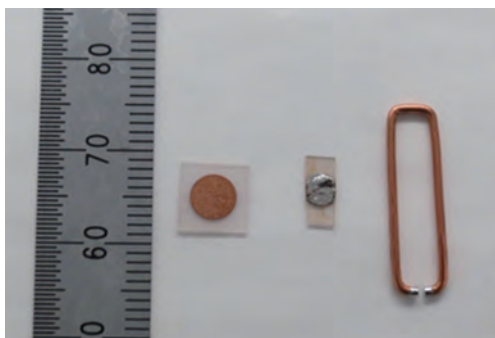
Figure 9 clearly shows the decoupling capability of the ROYAL HFX probe. The 64 kHz of decoupling bandwidth indicated using adiabatic decoupling is sufficient to decouple all the  $^{19}\text{F}$  nuclei in this challenging molecule. Additional band width can be achieved by using the JNM-ECZ500R console sequencer. In Fig. 10 we show that the noise floor for  $^{31}\text{P}$  and  $^{13}\text{C}$  observe nuclei is not increased as we turn on the decoupler channels of the

**Fig. 5**



Plots of coupled mode S11 amplitude versus sample coil tune frequency. Note here that the amplitude is decreasing for the left resonance in the plots as the sample coil frequency is moved to a higher frequency. When the left most resonance goes to zero amplitude it will be at the idler frequency. This plot allows us to determine the idler frequency in the coupled mode.

**Fig. 6**



Components used for idler coil construction. Note here that the sapphire chip is modified with a grinding tool to a smaller width. This chip (right of center) is then soldered to the single turn coil using an alignment fixture.

**Table 2 ROYAL HFX Probe Performance Data**

ROYAL HFX Probe Performance		
Observe Mode	PW(90)	S/N
$^1\text{H}$ Uncoupled	6.6 $\mu\text{s}$	893.00
$^1\text{H}$ Coupled	9.8 $\mu\text{s}$	552.00
$^{19}\text{F}$ Uncoupled	7.7 $\mu\text{s}$	845.00
$^{19}\text{F}$ Coupled	9.4 $\mu\text{s}$	666.00
$^{31}\text{P}$ TPP	15 $\mu\text{s}$	156.00
$^{13}\text{C}$ ASTM	12 $\mu\text{s}$	291.00
$^{15}\text{N}$ Formamide	24 $\mu\text{s}$	43.00

**Fig. 7**



Diplexer combiner with 90dB of isolation between the  $^{19}\text{F}$  and  $^1\text{H}$  channels.

**Fig. 8 Non-spin line-shape spectrum for ROYAL HFX probe.**

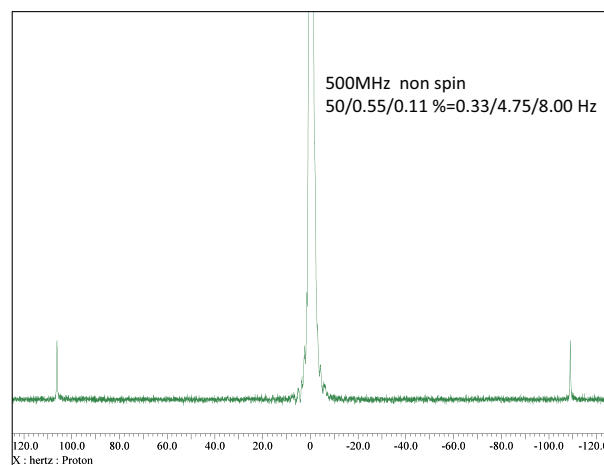
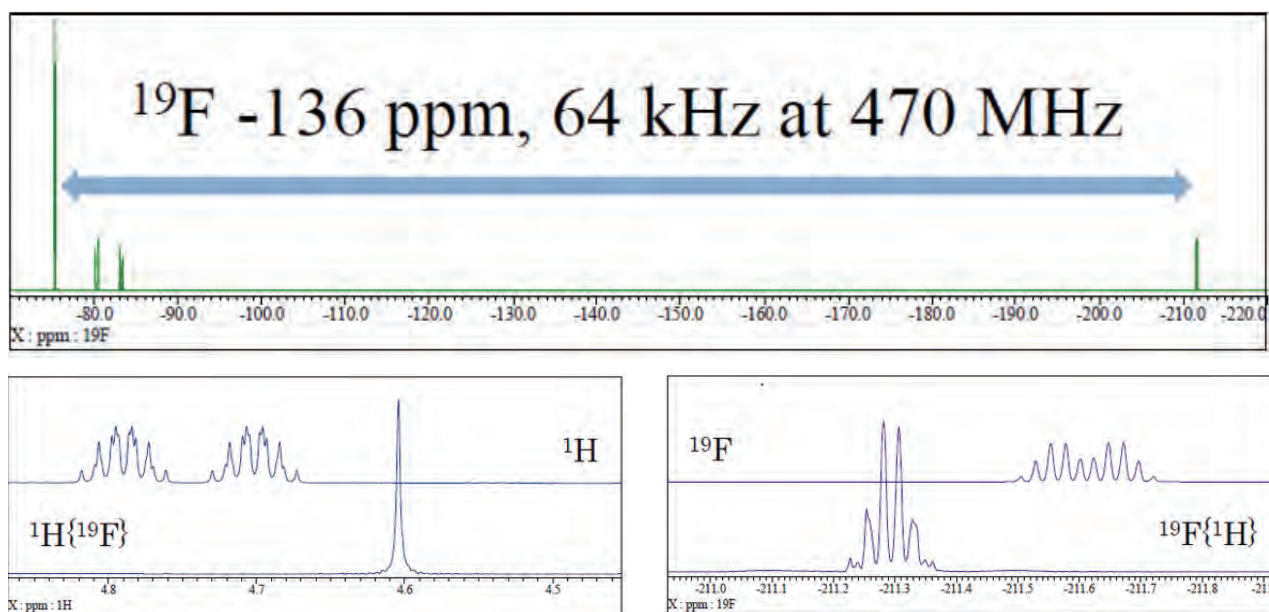
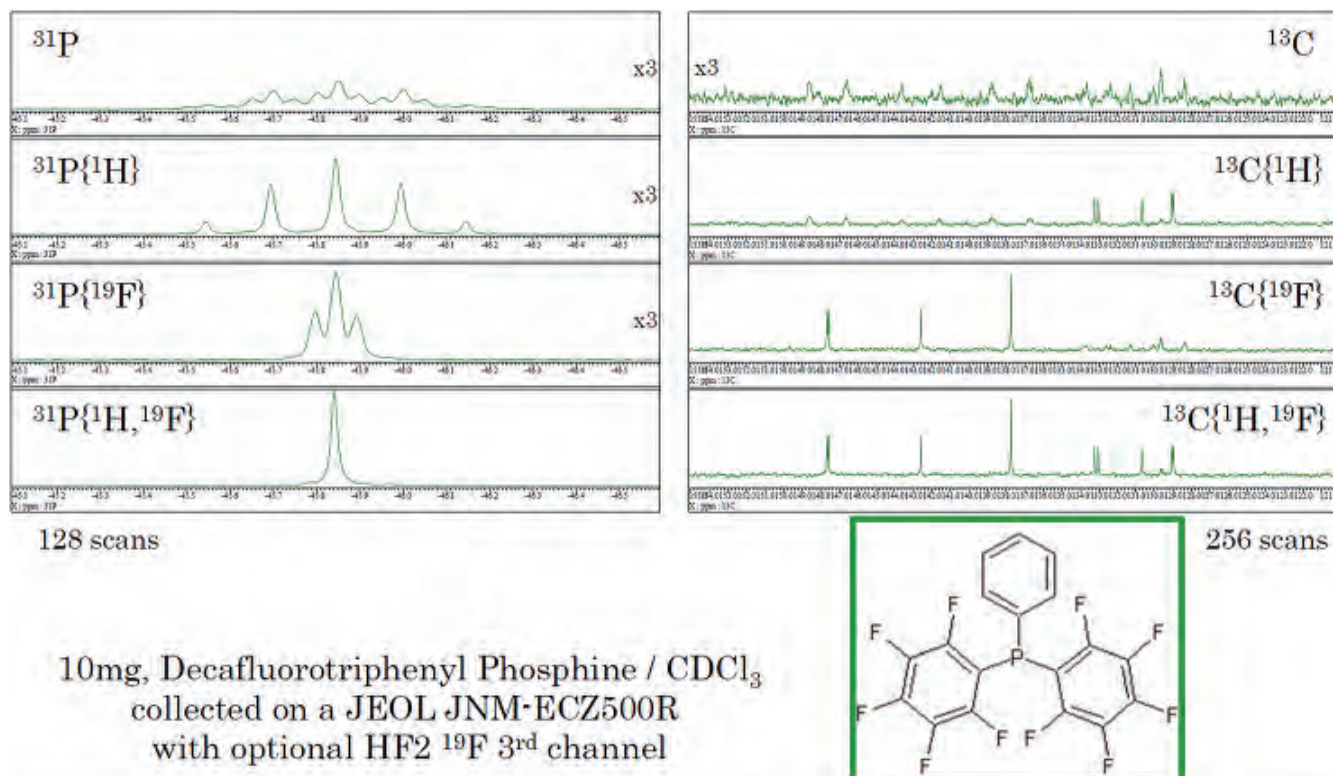


Fig. 9



Here we are emphasizing the decoupling capability of the new ROYAL HFX Probe. The 1,1,2,2,3,3-Hexafluoropropyl ethyl ether molecule offers a decoupling challenge for  $^{19}\text{F}$ . Here we use a conventional decoupling adiabatic sequence to decouple  $^{19}\text{F}$  from  $^1\text{H}$ . However, if needed we can extend this decoupling range by using the sequencer capabilities of the JEOL JNM-ECZ500R console.

Fig. 10



One of the important things to watch for in doing H/F experiments is the noise level in the spectra while decoupling. In these  $^{31}\text{P}$  and  $^{13}\text{C}$  observe spectra you can see that the noise floor remains constant while going from no decoupling (noise floor X3) to full decoupling with  $^1\text{H}$  and  $^{19}\text{F}$  simultaneously.

spectrometer. **Figure 11** shows the aromatic region  $^{13}\text{C}$  observe spectra of Voriconazole. With simultaneous  $^1\text{H}/^{19}\text{F}$  decoupling the spectrum is clearly simplified allowing for structure verification. In **Fig. 12** we demonstrate the ability to acquire HMBC with and without  $^{19}\text{F}$  decoupling while observing  $^{15}\text{N}$ .

## Conclusion

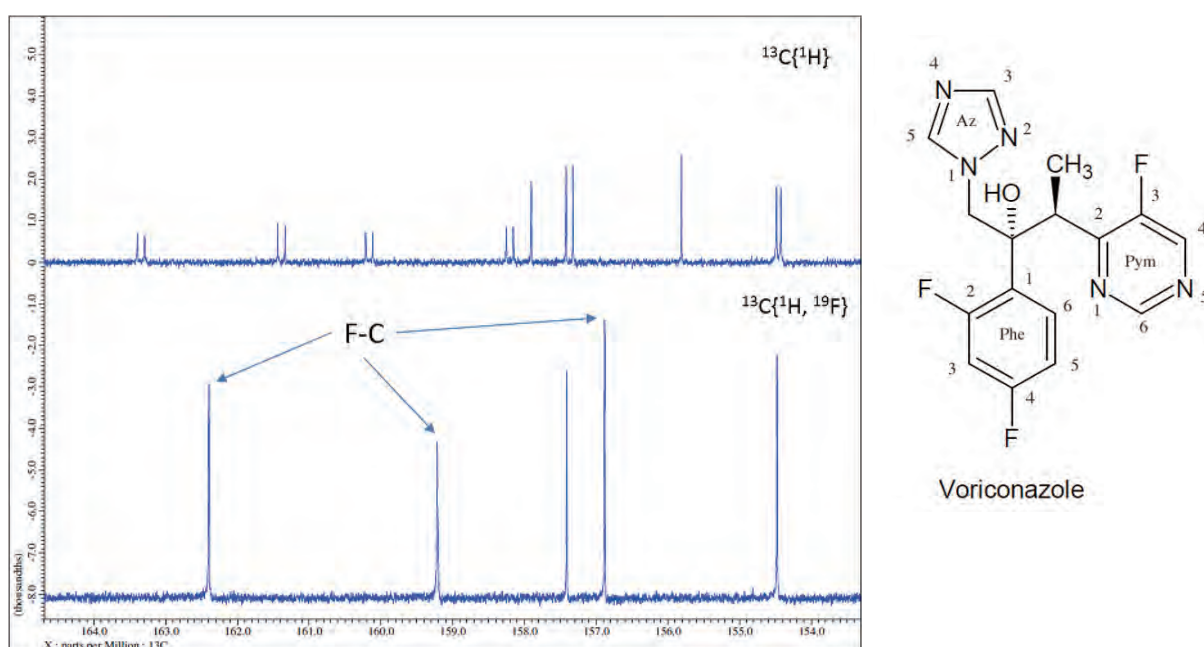
The new ROYAL HFX Probe provides on demand capability which is a first in NMR. Never before have so many experiments been available in one NMR probe. The ease of use and sensitivity of the probe will allow chemist greater structure elucidation capabilities in a convenient and easy to use format. The use of magnetic coupling to achieve this capability was a breakthrough. For more than 30 years probe builders have struggled to build a probe that has this on demand capability.

Now with this new capability chemist can quickly determine the structure of a much wider list of molecules that extends from  $^{31}\text{P}$  to  $^{15}\text{N}$  observe nuclei.

## References

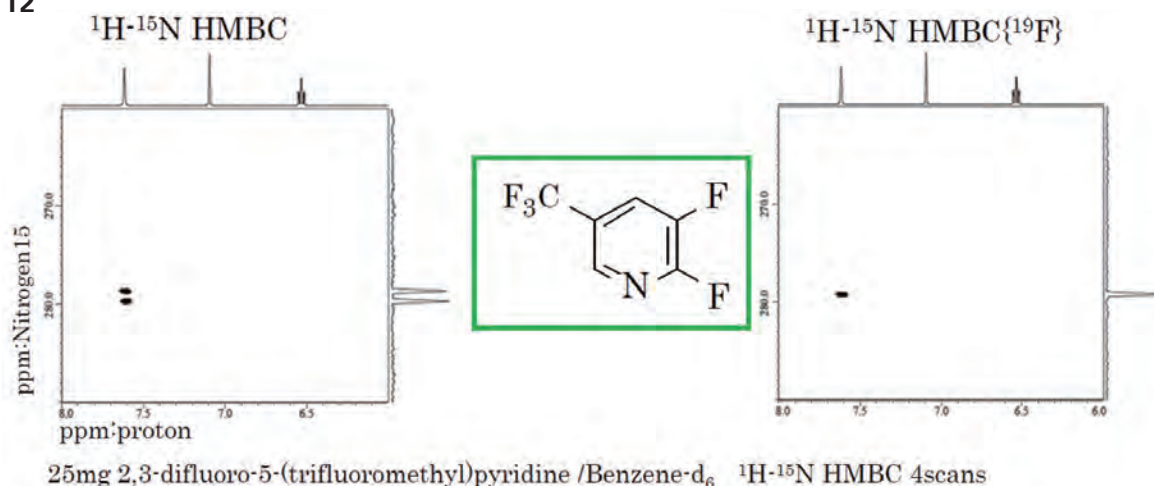
- [ 1 ] P. Bowyer, J. Finnigan, B. Marsden, B. Taber, A. Zens, *J. Magn. Reson.* **261** (2015) 190-198.
- [ 2 ] J. Haase, N.J. Curro, C.P. Slichter, *J. Magn. Reson.* **135** (1998) 273-279.
- [ 3 ] D. W. Alderman and D. M. Grant, *J. Magn. Reson.* **36** (1989) 477.
- [ 4 ] B. Taber and A. P. Zens, *J. Magn. Reson.* **159** (2015) 114-120.
- [ 5 ] B. Marsden, B. Taber, and A. Zens, *J. Magn. Reson.* **268** (2016) 25-35.

**Fig. 11**



The ability to simultaneously decouple both  $^1\text{H}$  and  $^{19}\text{F}$  as a structure elucidation tool is exemplified by these spectra of Voriconazole.

**Fig. 12**



The ROYAL HFX probe has the ability to do unusual complex experiments on demand.

Here we show the HMBC plots for  $^1\text{H}$ - $^{15}\text{N}$  HMBC and  $^1\text{H}$ - $^{15}\text{N}$  HMBC( $^{19}\text{F}$ ) further illustrating the structural elucidation capability of the ROYAL HFX Probe.

# Latest Technologies of Electron-Beam Vacuum Deposition Used for Film Formation

Masanori Kamioka, Akira Taniguchi, Toru Takashima IE Business Unit, JEOL Ltd.

Electron-beam deposition technique is one of thin-film formation technologies, which is widely used for film formation for metal electrodes on electronic devices, various optical coatings for camera components, anti-reflection coatings for glass lenses, etc.

Since 1960, JEOL has been developing and marketing a variety of electron-beam deposition equipment and deflection-type electron beam sources for electron-beam vacuum deposition (hereinafter, called deflection-type electron beam source), focused mainly on the optical coating industry.

In recent years, the performance and quality demanded for electronic devices and optical components have become increasingly higher and conventional technologies of electron-beam deposition do not satisfy the market needs. Thus, new functions and improved performance are required for the deflection-type electron beam source. To respond to high-level requirements for product quality, JEOL has marketed new electron beam sources and electron beam source power supplies, achieving the development of an unprecedented process and improved yield. We have also newly developed an electron-beam induced indirect heating deposition source, focused on the organic device market. Applications of this new deposition source have started to the coating of metals, fluorides, etc.

## Introduction

The starting point of prevailing the electron-beam deposition technology in Japan corresponds to an epoch-making event of color-TV broadcasting in Tokyo Olympic. That is, this new technology has gradually extend its use for the formation of multi-layer anti-reflection coatings made from high-melting-point dielectric materials, which could not be made using the conventional resistance heating technique. Today, diversified evaporant materials are available for electron-beam deposition. Under this circumstance, the new electron-beam deposition technology plays a significant role as a coating technique of electrode films for various electronic devices and optical coatings (mainly, smart phones) by efficiently heating and vaporizing a variety of materials ranging from sublimable materials to high-melting-point materials. Since the dawn period of this beam deposition technology, JEOL began the development of the deflection-type electron beam source and continued to develop new products, with the aim of meeting the rapidly-expanding demands for electron-beam deposition equipment. Nowadays, owing to the establishment of good electron-beam shape and additional functions such as electron-beam sweep, a number of JEOL equipments are operating in the manufacturing sites worldwide.

The principle of the electron-beam deposition is regarded as simple in principle and well-established technique. But, in order to respond to the demands of increasingly-higher class coating specifications and more reduced costs, the requirements for the supplier makers of the deflection-type electron beam source are changing day by day. We present one specific example. Along with higher pixel resolution of camera (single-lens reflex camera, smart phone camera, etc.), requirements for the appearance quality of optical coatings have been becoming increasingly higher. The quality of the appearance is determined by the size of defects including particles and pinholes, and the number of defects revealed by the observation of the coating appearance and therefore, there are various required specifications. Currently, a very high-level specification of the defect size of 5  $\mu\text{m}$  or less is requested. However in the future, it is presumed that the defect size of sub-micrometers would be requested. To meet such severe requirements, the performance of the deflection-type electron beam source is important, which plays a core role in the coating process.

In addition, there are another cases where a substrate to be coated do not have resistance against the irradiation of a high-energy charged particle beam, or an evaporant material is not suited to be irradiated with a high-energy electron beam. Thus,

only an improvement of the deflection-type electron beam source, based on conventional technologies, cannot satisfy the needs of users. The conventional deflection-type electron beam source is constructed in such a way that, the electron beam is deflected 180° or 270° and directly irradiated onto the evaporant material. But aiming to break through the limitations of the conventional beam source, JEOL has newly developed a bombardment deposition source in which a vessel filled with an evaporant material is directly irradiated with an electron beam and the evaporant material is indirectly heated (electron-beam induced indirect heating).

This report introduces the latest technologies of the deflection-type electron beam source and the new bombardment deposition source which is first marketed into an industrial use.

## High Functionality Electron Beam Source Power Supply ICE Series

An infrared cut filter, located at the front of an image sensor of a digital camera, uses optical multi-layer coatings, on which high-refractive material (TiO<sub>2</sub>, etc.) and low-refractive material (SiO<sub>2</sub>) are deposited alternately. Along with increased pixels, the image sensor also produces higher pixel resolution and therefore, demands for optical components are becoming increasingly higher. The coating of the infrared cut filter is deposited by electron-beam deposition. Recently, defects in a coating with the size of micrometer-order cause a problem, thus improvement of

the appearance quality becomes a challenge. The coating defect arises from various causes. The main causes originated from the deflection-type electron beam source in the deposition process are as follows.

- ① Bumping of the evaporant material originally filled in the crucible or materials dropped from the peripheral of the crucible.
- ② Vaporization of particles adhered to the peripheral of the crucible, due to the irradiation of backscattered electrons.
- ③ Incorporation of particles into the film resulting from the vaporization of the particles adhered to the peripheral of the crucible, which occurs due to arcing.

We present the countermeasures for the above phenomena. For ① and ②, an appropriate choice of an evaporant material or reduction of the volume of the excessive films around the crucible by re-designing of the structure of a deposition instrument can improve the problem to some extent. For ③, a rapid arc recovery function implemented in a new lineup of electron beam source power supply BS-720xxICE series (**Fig. 1**) provides effective performance. This capability can reduce the electron-beam irradiation outside the crucible down to a negligible level at the occurrence of arcing, thus suppressing the ejection of particles (**Fig. 2, Fig. 3, and Fig. 4**). In addition, local melting of the evaporant material or residual un-melted materials can cause the ejection of particles. Thus, to improve the yield, stabilizing the surface shape of melted material and simplified deposition-

**Fig. 1 Electron beam power supply. BS-72020ICE/BS-72050ICE (left), BS-72010ICE (right)**



BS-72020ICE / BS-72050ICE

BS-72010ICE

**Fig. 2 Accelerating-voltage fast recovery performance at the generation of arcing.**

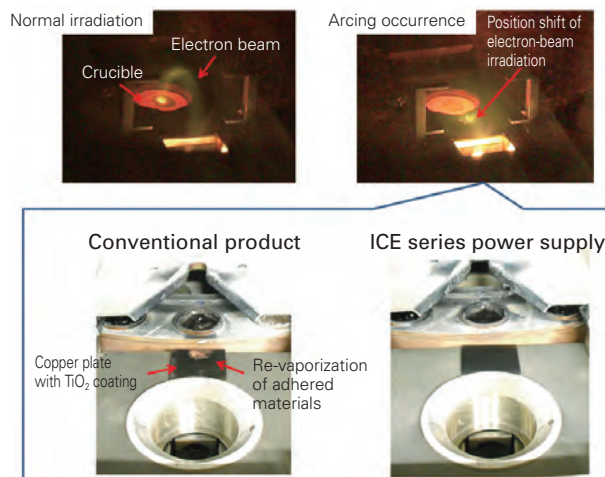


**Fig. 3 Fast arc recovery performance of BS-720xxICE series power supply.**

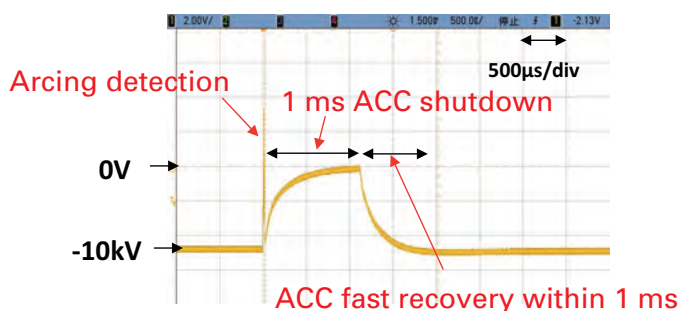
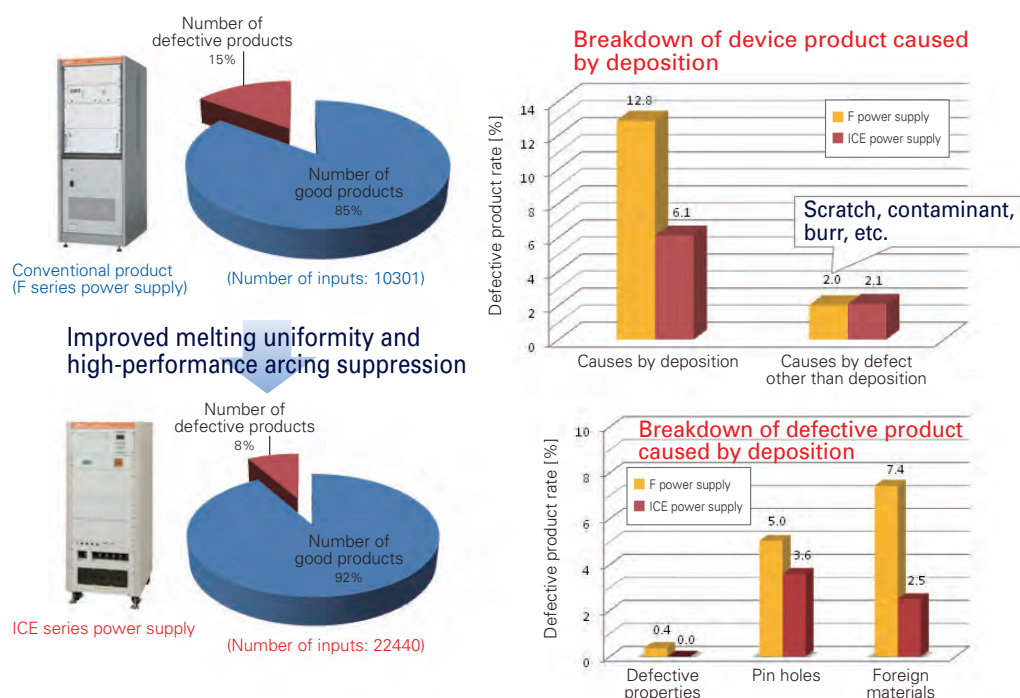


**Fig. 4 Example of yield improvement with BS-720xxICE series power supply.**



parameter adjustment are very crucial. The BS-720xxICE series electron beam source power supply comes with three types of electron-beam sweep modes. The surface shape of the melted material is stabilized by choice of a mode appropriate for a corresponding evaporant material and fine adjustment of the sweep parameters (Fig. 5).

### High-Performance Deflection-type Electron Beam Source

Recent optical components require significantly high performance, high quality and also greatly reduced costs. To respond to this reduced-cost challenge, the deflection-type electron beam source requires the reduction of consumables and the increase of the filament lifetime (in terms of the maintenance cycle). The deflection-type electron beam source BS-600xx series (Fig. 6) achieves a longer lifetime by adopting a U-shaped filament that suffers no influence from ion bombardment. This feature leads to high productivity (Fig. 7).

The deflection-type electron beam source is often installed into a batch-type deposition instrument, which vents the chamber at the completion of processes for inserting or retracting the processed products, thus this electron beam source is exposed to the air for a longer time. In the successive deposition process under a vacuum, a heated filament acts as the thermal source. As a result, gases adsorbed inside the electron beam source are emitted, leading to the arcing with frequent occurrence due to an instantaneous pressure rise between a high-voltage applied material and a ground potential material. Since the arcing gives rise to large fluctuations of the electron-beam accelerating voltage, the orbital radius is changed at the moment of the discharge, greatly changing the electron-beam irradiation position. This phenomenon causes an unstable deposition rate or particle generation due to spitting particles, resulting in a deteriorated production yield.

In addition to higher performance of the accelerating voltage power supply offered by the ICE series electron beam

source power supply, both of the deflection-type electron beam source BS-60060DEBS and BS-60070DEBS have a sufficient spatial distance between the high-voltage applied material and the ground potential material, so as to suppress the arcing. Furthermore, both models are specially designed so that the peripheral of the filament assembly is spatially opened to a vacuum chamber in order for the emitted gases to be smoothly exhausted. Figure 8 shows the discharge suppression performance of the new deflection-type electron beam source in graphs which compares the conventional and new beam sources, in terms of the frequency of arcing occurring when the pressure near the filament of the deflection-type electron beam source is increased up to a normal working pressure or higher. In the

**Fig. 5 Application example of the circle scan mode in BS-720xxICE series.**

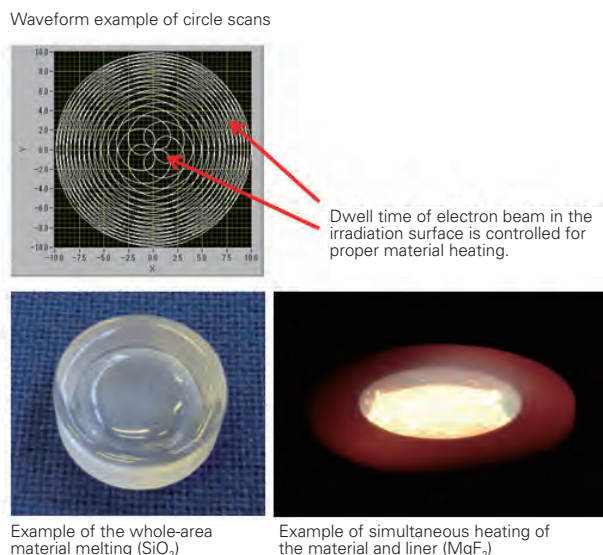
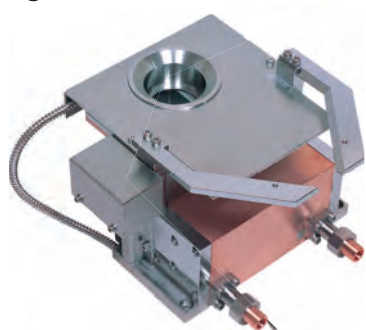


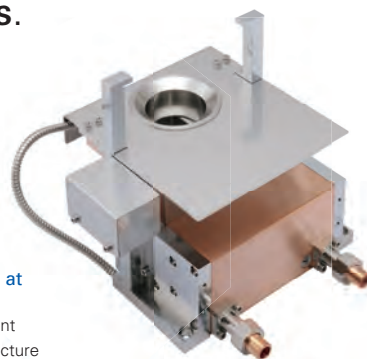
**Fig. 6 Electron beam sources: BS-60060DEBS/ BS-60070DEBS.**



**BS-60060DEBS**

**Damage suppression due to backscattered electrons**

- Use of a long-life filament
- Arcing suppression structure
- Compatible with the dimension of 102-type electron beam source



**BS-60070DEBS**

**Without pole-pieces at the crucible side**

- Use of a long-life filament
- Arcing suppression structure
- Compatible with the dimension of 102-type electron beam source

**Fig. 7 Comparison of the performance between long-life filaments.**

φ0.8 U-type (for 60060 and 70)



Japanese patent No.3814114

φ0.55 spiral type (for 102)



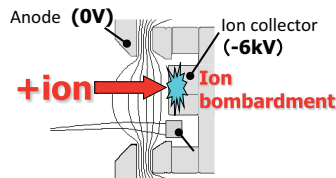
φ0.55 U-type (for 60030, 40 and 50)



Japanese patent No.3814114

**Conditions for filament lifetime test**

- ◆Test equipment: Vacuum coater, 1300 mm dia.
- ◆Deposition pressure: Pressure is constantly controlled at  $3.0 \times 10^{-2}$  Pa by APC (O<sub>2</sub>)
- ◆Output from electron beam source: 6 kV 0.6 A
- ◆Deposition material: Tungsten
- ◆Notes: O<sub>2</sub> gas is introduced close to the crucible of the electron beam source.



**Filament lifetime (time up to wire breakage)**

φ0.55 spiral type **AVE.3.5 h (1 time)**

φ0.55 U-type **AVE.32 h (9 times)**

φ0.8 U-type **AVE.54 h (15.4 times)**

φ0.55 spiral type φ0.55 U-type φ0.8 U-type



○ Wire breakage sites

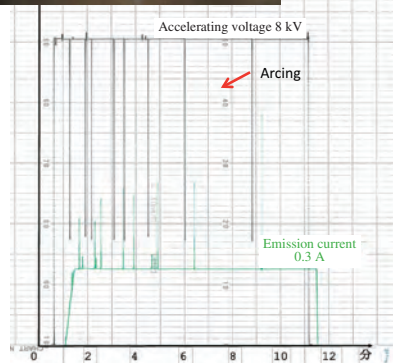
**Fig. 8 Arcing suppression performance of the new deflection-type electron beam source.**

BS-60040VDGN

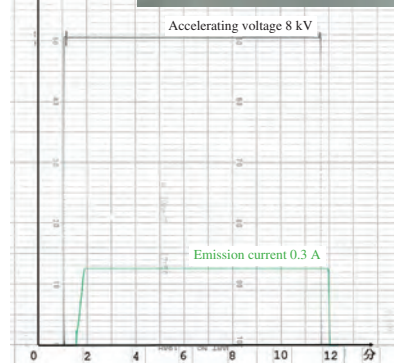
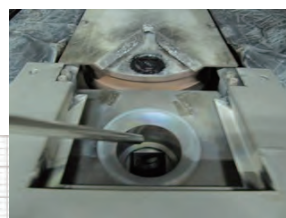


**Test conditions**

- Equipment: Vacuum coater, 1300 dia.
- Output: 8 kV, 0.3 A, 10 min
- Pressure: 0.15 Pa, Ar 400 ml/min
- Material: Ta<sub>2</sub>O<sub>5</sub>(OA-100)



BS-60060DEBS



conventional electron beam source, arcing frequently occurred, making it impossible to stably operate. But in the new electron beam source equipped with an arcing suppression structure, no arcing occurred. This result demonstrates the effectiveness of the new beam source.

### Metal-Deposition Deflection-type Electron Beam Source, Suitable for Film Formation at Low Temperature

Sputtering or electron-beam deposition technique is utilized to form electrode thin films for electronic devices. Recently, the lift-off process has frequently used in the LED manufacturing process because it can achieve both high throughput and cost reduction. This trend remarkably increases the adoption of the deflection-type electron beam source as a deposition source. In the lift-off process, resist coating is applied prior to exposure and developing and then, successive electron-beam deposition is carried out for

metal film formation, and finally the resist is removed and device patterns are formed. This method has a merit to omit the ion etching process in the conventional etching method. However to the contrary, the lift-off method definitely requires film formation at a low substrate temperature that is sufficiently lower than the heat-resistance temperature of the resist.

Electrode film formation for the LED is generally performed without heating the substrate. But, there are some cases where resist deformation arises at a temperature exceeding the heat-resistance temperature of the resist coated onto the substrate, due to the radiation heat from a heated evaporant material, direct heating of the substrate by backscattered electrons, or the secondary radiation heat from inner walls of the deposition instrument. To solve this problem, we marketed the metal-deposition deflection-type electron beam source BS-60210DEM that enables the suppression of direct or indirect thermal influence of backscattered electrons on the substrate by effectively utilizing magnetic fields. This unique electron beam

**Fig. 9 Backscattered-electron trap mechanism of the deflection-type electron beam source for metal-deposition.**

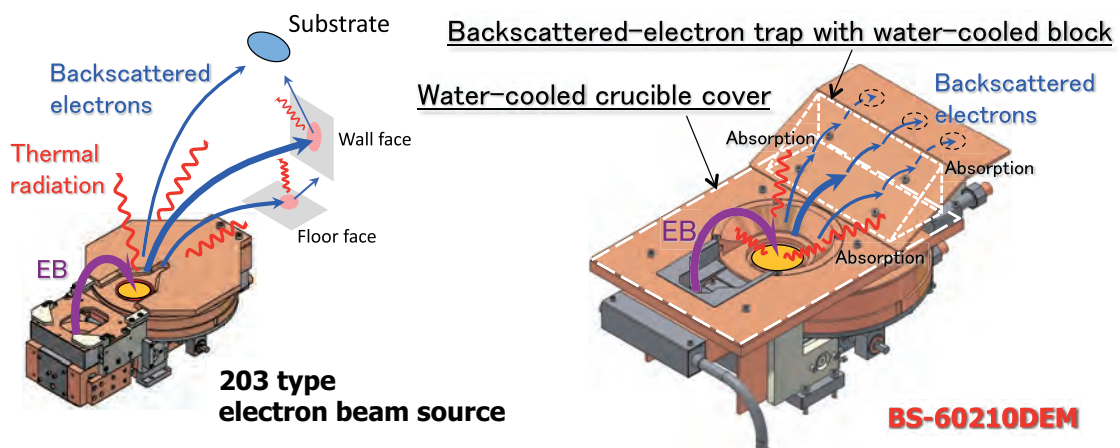
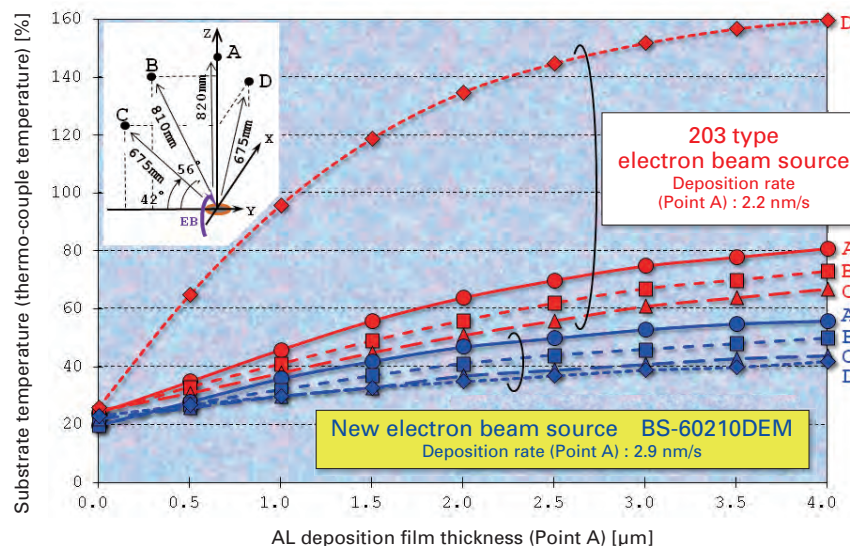


**Fig. 10 Low-temperature deposition of aluminum with the deflection-type electron beam source for metal-deposition.**



source has been used as the volume manufacturing basis.

The main feature of this electron beam source is a built-in backscattered electron trap at the back of the crucible. The BS-60210DEM forms a magnetic field in the upward and back space of the crucible (Fig. 9), which deflects the backscattered electrons to give them directivity to low angles. The magnetic field formed by the backscattered electron trap has an adverse influence on the beam deflection angle of the deflection-type electron beam source and the convergence of the beam. Thus, in order to extract proper performance of both electron beam and backscattered electron trapping of the electron beam source, optimal adjustment is implemented. Figure 10 shows the effect of suppressing the rise of substrate temperature during aluminum deposition. It is revealed that the new electron beam source suppresses the temperature increase of the substrate after film formation, compared with that using the conventional electron beam source.

### Bombardment Deposition Source with Indirect Heating

The deflection-type electron beam source is sometimes used for film formation of electrodes of organic EL devices because of the advantages of this beam source in terms of high deposition rate and film formation at low temperature. But from the operation viewpoint of this electron beam source, there arises a problem where the irradiation of a high-energy electron beam onto an evaporant material generates X-rays and backscattered electrons, and a desired luminescence performance cannot be obtained due to damage to organic films if the X-rays and backscattered electrons enter the organic layers of the organic EL device.

To prevent this problem, we respond to users by providing a deflection-type electron beam source that adds countermeasure techniques to organic EL devices. To be precise, we use a technique that lowers the electron-beam accelerating voltage to 3 kV or less, so as to reduce the X-ray influence, and a technique that deflects backscattered electrons by a magnetic field produced near the substrate in advance of the electron beam entering into the substrate.

However, the measure to lower the accelerating voltage reduces the power for the evaporant material and the relationship between power and deposition rate becomes trade-off. The magnetic-field generator, which is used for the countermeasure to backscattered electrons, gives rise to a complex instrument configuration when this is applied to a wide-area substrate, thus causing a problem of increased costs in the instrument. In order to overcome those problems, we developed the bombardment deposition source BS-60310BDS (Fig. 11), which does not require countermeasures for X-rays and backscattered electrons while maintaining the advantage of proper deposition-rate control and low-temperature film formation.

The main features of the bombardment deposition source are as follows. A vessel (called "liner") in a vacuum is heated by an electron beam from downward of the liner. Then, the heat from the liner is transferred to an evaporant material by thermal conductivity and thermal radiation, and the evaporant material is melted and vaporized. This construction isolates the electron-beam generation source from the vapor generation region. Thus, electrons and X-rays generated from the electron beam source is completely, physically isolated from the substrate owing to a cover, etc., and do not reach the substrate. Furthermore by heating the liner having a small thermal capacity with an electron beam with high thermal control, the deposition rate is easily controlled. Since the instrument construction separates the electron beam source from the liner, the liner configuration is allowed to be the Revolver type. This is also an advantage because the Revolver type liner achieves that a single deposition source is applicable to formation of multi-layer coatings consisting of various materials, film formation of thick monolayer coatings and other applications.

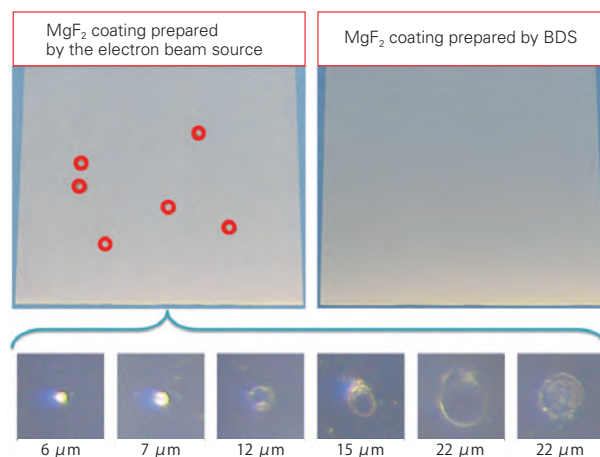
Owing to these features, the bombardment deposition source is successfully used to deposit materials for organic EL devices while suppressing damage to organic films, and also provides distinguishing effects for deposition of low-defective optical coatings and coating formation of fluoride materials. The followings are representative results.

Figure 12 shows photos that compare the appearance of MgF<sub>2</sub> coating deposited with the deflection-type electron beam source and the bombardment deposition source. MgF<sub>2</sub> coating

Fig. 11 Bombardment deposition source BS-60310BDS



Fig. 12 Deposition of low-defective MgF<sub>2</sub> film with the bombardment deposition source.



deposited with the deflection-type electron beam source causes point defects due to the bumping from the evaporant material. The size of defects ranged from 6 to 22  $\mu\text{m}$ . The image sensors for the digital camera, which essentially need an optical coating filter, have been reducing an area per pixel owing to the cost reduction. In recent years, the point defect of the order of a few  $\mu\text{m}$  is judged to be not acceptable and therefore, the generation of such point defects indicates the yield deterioration. It is of prime importance to reduce the defect size to 0 (zero) as small as possible. On the other hand, the substrate deposited with the BS-60310BDS does not generate a problematic point defect, achieving a greatly improved quality of appearance.

**Figure 13** shows spectral data that compares the optical properties of  $\text{YF}_3$  used for optical coating, which were deposited onto a quartz substrate in our experiment. Fluoride materials are mainly used for optical coatings over the range of ultraviolet and infrared region, and the formation of the film requires small optical loss (absorption and scattering). From this spectral data, a film sample deposited with the deflection-type electron beam source deteriorates its optical properties over the range of 600 nm or less. This result confirms that, as the wavelength is shorter, the loss increases more. But a film sample deposited with the BS-60310BDS keeps its optical properties over the range down to 300 nm, indicating suppression of the optical loss to a low level.

**Figure 14** shows the comparison of the melted residues of  $\text{YF}_3$  deposited using the bombardment deposition source BS-60310BDS and the deflection-type electron beam source. When the deflection-type electron beam source is used, ionization of the material is seen during the deposition and as a result, the melted residue after the deposition changed to black. This adverse phenomenon is due to the fact that  $\text{YF}_3$  was dissociated caused by the electron-beam energy and a lack of fluorine gives rise to a significant increase of absorption. On the other hand, when  $\text{YF}_3$  was deposited with the BS-60310BDS, no ionization was seen and also, the melted residue after the deposition kept its color to be white. From this result, it is concluded that, the

difference in coating absorption rate is determined by whether or not the high energy electrons pass through a vapor cloud, and that the use of the BS-60310BDS suppresses the dissociation of fluorine and enables the formation of optical coatings with small optical loss.

## Summary

The electron-beam deposition technology, which was based on expert skills at its first stage, has been developing to be used as mass production tools without requiring skills over a long period of history. But on the other hand, the specifications demanded for the coating product have become increasingly higher, which include a variety of superior techniques for electron beam source and its control. JEOL is providing not only equipment, but also sophisticated solutions suitable for various needs, based on many years of knowhow. Recently, the lineup of the BS-720xxICE series achieves higher performance of electron-beam control power supply. In addition, the marketing of the new bombardment deposition source BS-60310BDS achieves deposition capable of reducing damage to the substrate and of decreasing absorption to films. Thus, this new product is further extending its applications to a wide range of deposition. We of JEOL will determined to make strenuous efforts to continually acquire cutting-edge technology of electron beam deposition source for the purpose of supporting the optical coating industry. This is our core mission as a leading company of the electron beam deposition source.

## Acknowledgments

The authors would like to acknowledge the support of an optical coating processing manufacturer which kindly provided data of yield improvement at the mass production level about improved quality of appearance in the ICE series power supplies.

**Fig. 13** Deposition of low-absorption  $\text{YF}_3$  film with the bombardment deposition source.

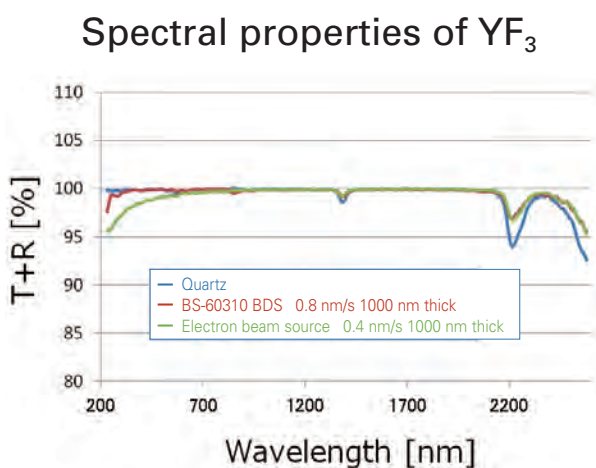
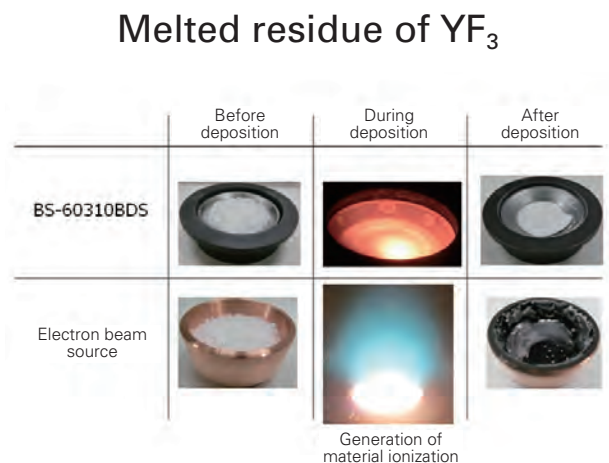


**Fig. 14** Comparison of the melting state of  $\text{YF}_3$  deposited with the bombardment deposition source and deflection-type electron beam source.



# New-Generation Analyzer BioMajesty™ Zero Series, JCA-ZS050, and Its Contribution to Clinical Analysis

Kazushige Kojima    Medical Equipment Engineering Division, JEOL Ltd.

BioMajesty™ is the brand of our high-throughput clinical chemistry analyzers that are developed to pursue “faster, accurate and more economic chemistry measurements” with micro-volume sampling.

JEOL now offers a new next-generation analyzer BioMajesty™ Zero series, as the latest challenges to the “ultimate zero” (refining the essence of basic technologies to the finest) in addition to the legacy of more than 7,000 analyzers that have been distributed in Japan and worldwide.

## Introduction

BioMajesty™ (BM) series has realized “faster”, “accurate” and “micro-volume sampling” for clinical chemistry analysis that measures various components of blood and urine, such as protein, enzyme, sugar level and electrolytes. It has expanded its share in many clinical laboratories.

As the needs are emerging for pre-diagnosis examination for doctors to consult to patients with the test results on hand, clinical laboratories are accelerating the automation in laboratory workflow as the connection to Laboratory Automation System (LAS) and Laboratory Information System (LIS) to streamline the everyday workflow.

Maintaining various types of analyzers and controlling the quality of data have become one of the main tasks for laboratory technicians today to ensure the quality of measured data.

Needs are growing for “simple maintenance” as wide range of analyzers have to be maintained by very limited number of laboratory technicians. Needs are also increasing for the features in analyzer to assist laboratory technicians in “monitoring entire flow of measurement” for correct data, “avoiding sample-to-sample carryover” among different analyzers on LAS and “locating non-specific reaction” deriving from patient samples.

As the challenge to the “ultimate zero”, our new brand of BioMajesty™ Zero series has been developed under totally renovated concept for software and hardware with focus on the following 4 keywords. It offers various long-wanted features that are completely new from the legacy BM series. We are proud to present JCA-ZS050 (ZS0505), the first offspring as BM Zero series.

## 4 Keywords in BM Zero Series Development

### 1. Carryover Avoidance

#### Avoiding sample-to-sample carryover

- New wash mechanism to avoid sample-to-sample carryover
- Enhanced settings and more sophisticated check logics for carryover avoidance

### 2. Micro-Volume Technology

#### Achieving micro-volume measurement with the minimum 40 µL reaction volume

- Micro-volume measurement mode for small sample volume
- Micro-volume measurement with the minimum 40 µL reaction volume

### 3. Innovative Operation

#### Offering innovative features and pleasant usability

- Simple and intuitive operation panel
- Active Trace function to offer reliable test data

### 4. Simple Maintenance

#### Realizing easy customer maintenance based on ergonomic design

- Daily maintenance area of within 40 cm of reach from an operator
- Tool-less easy maintenance

## Specifications

JCA-Z-050 boasts throughput of the maximum 1,800 tests/hour with the clinical chemistry tests 1,200 tests/hour and ISE tests 600 tests/hour (Table 1). Inheriting a distinctive feature of pre-dilution mechanism from the legacy BM series, ZS050 realizes the micro-volume measurement with the minimum 40 µL reaction volume. The clear coated hairline finish appearance distinguishes ZS050 as the brand of new breed (Fig. 1).

### 1. Carryover Avoidance Avoiding sample-to-sample carryover

Wash in alkaline and acid detergents is available on ZS050 for the wash between different types of samples such as serum and urine. With the wash port placed on the trajectory of each probe as the legacy BM series, ZS050 accommodates new detergent supply ports inside the wash port for alkaline and acid detergents, which are used to perform wash for each probe, cuvettes and the mixing rod for carryover avoidance (Fig. 2).

With sample pre-dilution mechanism (Fig. 3) on board, ZS050 has 2 separate probes; a dilution probe unit (DPU) for

preparing diluted samples and a sample probe unit (SPU) for sampling the diluted samples to reaction cuvettes. Throughput is never lost on ZS050 as SPU continues to aspirate diluted samples and dispense them into the reaction cuvettes without interruption while DPU is being washed in alkaline or acid detergent supplied from its own wash port after sampling from ST is completed (Fig. 4).

This capability achieves sample-to-sample carryover avoidance wash without affecting the entire throughput of ZS050 while loss in throughput is more or less expected with conventional chemistry analyzers in proportion to the number of wash performed. The feature should offer great advantage in connection with LAS at clinical laboratories. Wash in alkaline detergent should work effectively for sample-to-sample carryover avoidance especially for infectious tests. Wash settings between different sample types will ensure the accuracy of data for tests such as protein, albumin and CRE of which measurement concentration ranges largely differ between serum and urine. The check logic is more sophisticated to effectively flag data with high risk of sample-to-sample carryover.

**Table 1 JCA-ZS050 Specifications**

	JCA-ZS050
Throughput	Chemistry test 1200Tests/Hour
	ISE test 600Tests/Hour
	Total 1800Tests/Hour
Reaction cuvette	Plastic Cuvette with light path length of 4 mm
Reaction volume	40 to 120 µL
Positions on RTT1/2	RTT1 : 70 ml × 60
	RTT2 : 70 ml × 15 + 40 ml × 45
Max. number of data storage	Up to 100 data
Max. number of registerable controls	100 types
Required pure water volume	22 L/hour(maximum during normal use)
Dimensions	1470 mm(W) × 914 mm(D) × 1449 mm(H)
Power source	200 V
Distinctive features	Sample pre-dilution unit
	Dilution Sample Tray(DST) rerun/Sample Tray(ST) rerun selectable
	Sample-to-sample carryover avoidance
	Active Trace function

**Fig. 1 JCA-ZS050 Analyzer Appearance**



**Fig. 2 Enhanced Wash mechanism**

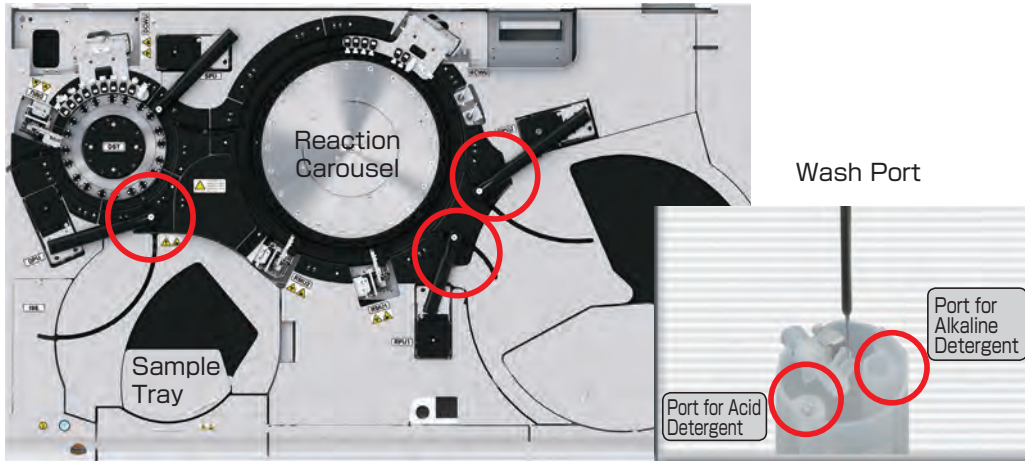


**Fig. 3 Limitation of sampling volume**

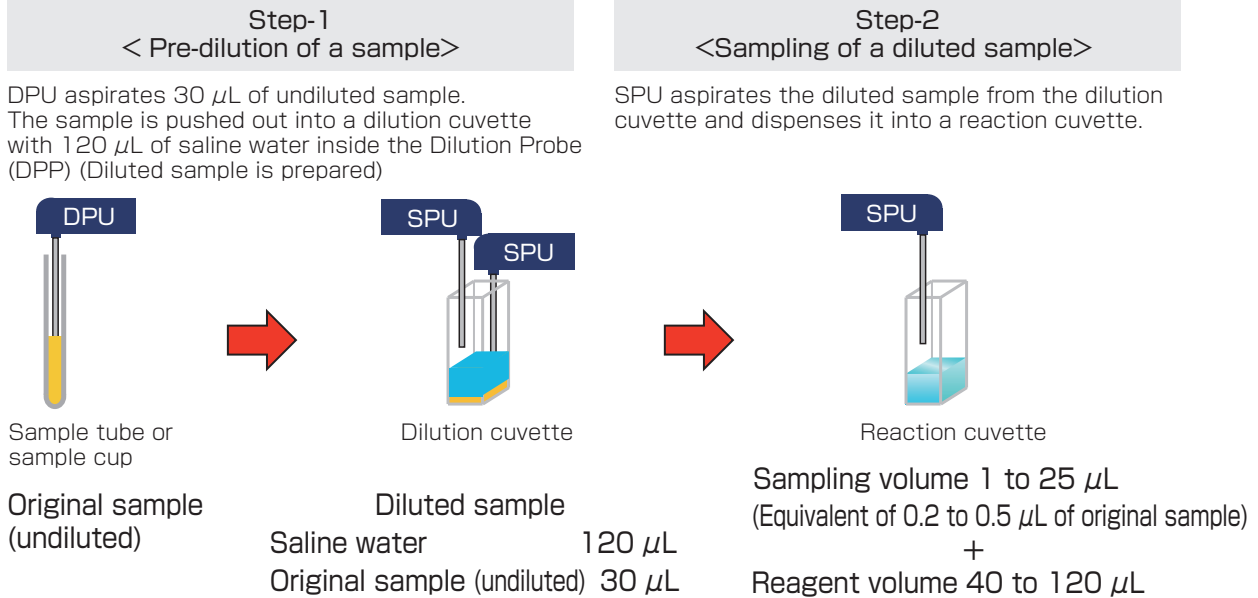
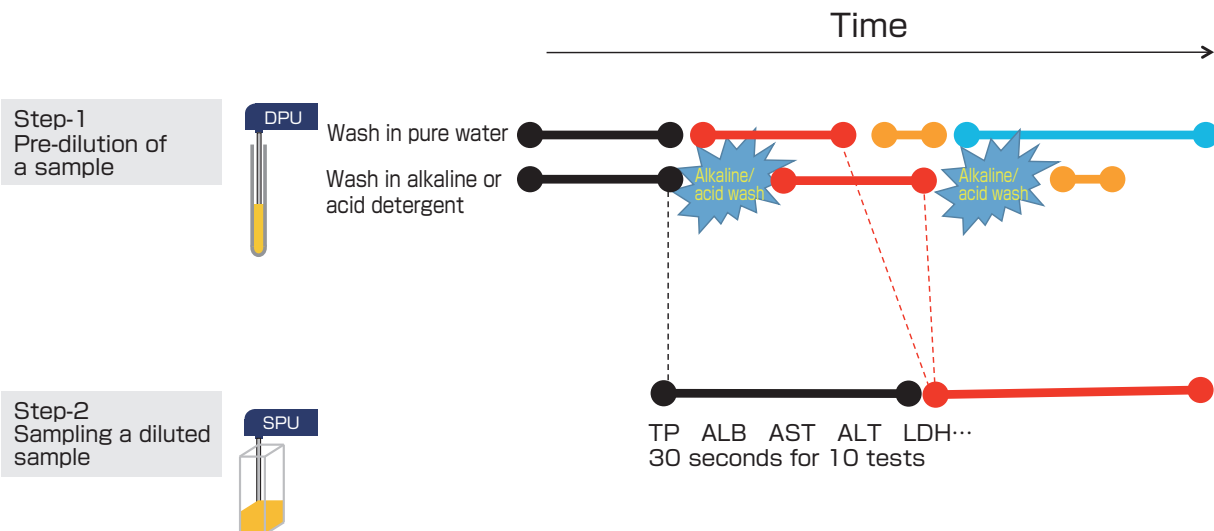


**Fig. 4 Efficient Wash process taking advantage of the sample pre-dilution mechanism**



## 2. Micro-Volume Technology Achieving micro-volume measurement with the minimum 40 µL reaction volume

<Inheritance of the legacy sample pre-dilution mechanism>

The legacy BM series features the sample pre-dilution method in which a diluted sample is prepared in the dilution cuvette prior to reaction in each reaction cuvette. This pre-dilution method has achieved micro-volume measurement with even smaller volume of sample and reagent for tests for which such measurement was thought to be difficult due to the limitation of minimum sampling volume. New reaction cuvette allows measurement with minimum reaction volume of 40 µL with more flexible analytical conditions. **Figure 5** shows the within-run reproducibility gained from the reaction setting of 40 uL of reagent 1.

<Introduction of micro-volume measurement mode>

Micro-volume measurement mode is effective especially when the volume of sample is limited from an infant or a child. Following features are available in the micro-volume measurement mode:

- 1) Pre-defining order of measurement different from standard-volume samples
- 2) Checking required total sample volume on screen for ordered tests. Orders can be edited or deleted on the screen.
- 3) Required original sample volume is automatically adjusted from 30 µL to 10 µL in accordance with types and numbers of the tests
- 4) Sample is aspirated from close to the bottom of a small volume cup when liquid level sensor detects lower remaining sample volume than specified, reducing the dead volume in the cup.

Customer can simply set the samples on pre-defined positions on the sample tray (ST) to perform the measurement in micro-volume mode as the micro-volume measurement setting can be readily assigned to positions on the ST.

## 3. Innovative Operation Offering innovative features and pleasant usability

ZS050 offers a “HOME” window as an effective tool to lead users through variety of information from the analyzer (**Fig. 6**). This single window serves as a portal and gives users easy access to information such as system status, maintenance schedule, reagent information (remaining volume and expiration date), detergent replacement and measurement progress simply by touching or clicking relevant location on the window.

<Settings for calibrator and control sample combination>

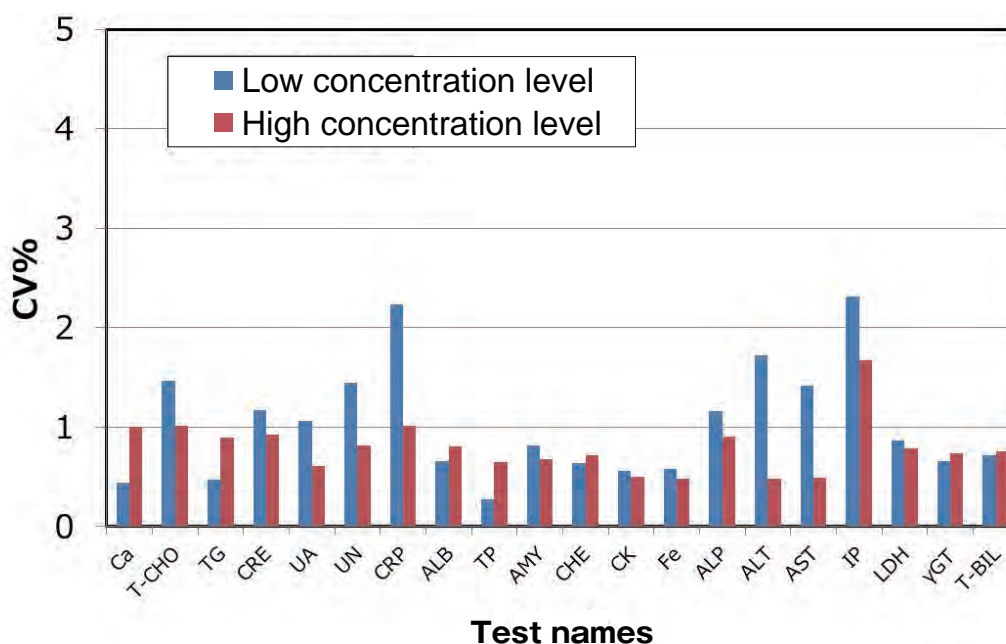
Maximum 15 sets of combination can be pre-registered for calibrators and control samples in accordance with the QC plan in a day and by days of weeks. New setting in Auto Startup/Shutdown function offers reagent blank measurement using system water. These new settings will help laboratory technicians to more streamline the everyday workflow.

<Active Trace function>

Active Trace function boosts the accuracy in measured data. It lets users to immediately and directly access monitoring windows linked to each measurement data. Such windows include information crucial to the analysis of measure data such as calibration curve, reaction time-course, clotting detection, liquid level sensing and sample logs. The function serves as a very effective tool to quickly identify the cause of unexpected erroneous data.

Window for reaction-time course now includes a feature to register customer-defined time-course, allowing the comparison between registered and measured time-courses. Newly implemented reaction process check function locates deviation in 8 pre-defined or customer-defined ranges in the time-course by calculating the average, slope and variance in each range, leading to accurate identification of a range in the reaction time-course where the abnormality occurred. Flexibility and variation

**Fig. 5 Within-run reproducibility**



are also expanded in the detection of abnormality in reaction time-course by utilizing the calculated values to compare the ratio and difference between ranges. Active Trace function should work as a novel quality control tool to assure the quality of test data.

#### 4. Simple Maintenance Realizing easy customer maintenance based on ergonomic design

With the concept of simple maintenance based on ergonomics design, ZS050 features “Daily Maintenance Area 40” and “Periodical Maintenance Area 60” along with wide range of on-screen guidance to support an operator. Maintenance areas are defined as within 40 cm of reach for daily maintenance such as reagent management and replenishment of consumables, and within 60 cm of reach for other periodical maintenance. Probes and mixing rods can be simply replaced without tools.

Detergents and consumables packed in pouches are

automatically diluted for specified dilution ratio and replenished to reservoir bottles inside the analyzer once the remaining volumes reach below specified. (Fig. 7) LED lights navigate in blue for the replacement of the pouches when they are empty, facilitating promptness of maintenance at all hours without interrupting the measurement.

#### Summary

As the resolution to ever-growing needs from customers, ZS050 incorporates a variety of new features. It realizes not only simple/intuitive operation and ease of maintenance, but also the capability to proactively hedge unpredictable risks. Among all, features like Carryover Avoidance and Active Trace should become the standard for future clinical chemistry analyzers.

ZS050, developed as the latest challenges to the “ultimate zero”, should be the powerful and reliable partner to clinical laboratories.

Fig. 6 ZS050 “HOME” window



Fig. 7 Automatic detergent/consumables replenishment system



Navigation by LED light

# Introduction of New Products

Atomic Resolution Analytical Electron Microscope

## NEOARM JEM-ARM200F

POWERED BY Neo Engine

### Improved resolution by "Neo Engine"

- C-FEG with NEO ASCOR -

ASCOR (Advanced STEM Cs corrector) can suppress the six-fold astigmatism aberration which limits resolution after Cs correction.

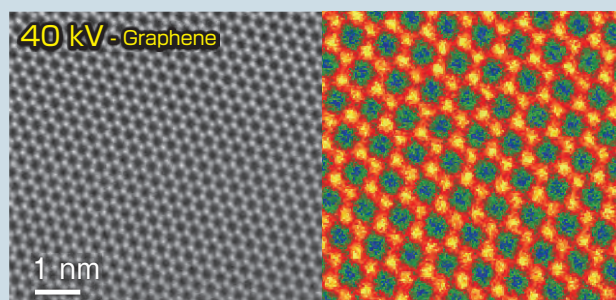
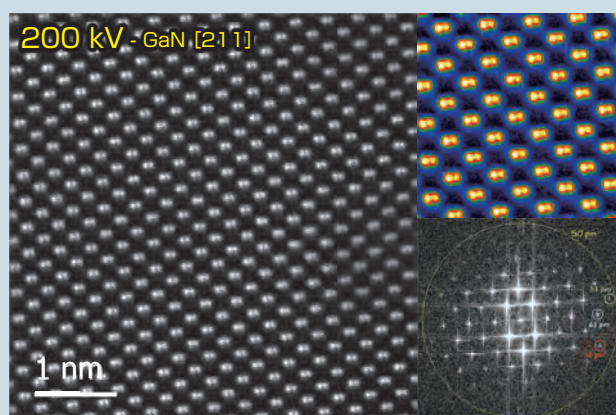
The combination of Cold FEG and ASCOR gives low chromatic aberration and expands the diffraction limit, achieving higher resolution than ever.

### Easy and quick automated aberration correction

- Integrated JEOL COSMO™ auto tune -

JEOL COSMO™, the aberration correction software, enables quick high resolution observation by a "NEO algorithm". Now, no special sample is required for corrector tuning.

Challenge to 60 pm



### Enhanced contrast of light elements by "e-ABF"

- Dedicated ABF detector -

An e-ABF (enhanced ABF) image is easily obtained with a newly designed detector.

The e-ABF is observable as a "live image" with real-time signal processing showing enhanced contrast of light atoms.

### High signal STEM images over all accelerating voltages

- Perfect sight NEO detector -

The new "perfect sight" detector, which acquires high STEM signals over all accelerating voltages, is integrated into the NEO detector. The detector, which uses hybrid scintillators, enhances the STEM signal 2.0 times at 60 kV and 1.5 times at 200 kV over the previous YAP detector.

### Observation under field free condition

- Lorentz lens setting integrated -

No excitation of the objective lens allows one to observe magnetic domain boundaries in a ferromagnetic specimen. This Lorentz mode comes as standard on the NEOARM.

### Observation of microscope in a bright room

- Integrated Viewing Camera system -

A camera for the viewing chamber is equipped as standard.

Sample search, microscope alignment and all other functions are doable just by looking at a PC monitor.

Certain products in this brochure are controlled under the "Foreign Exchange and Foreign Trade Law" of Japan in compliance with international security export control, JEOL Ltd. must provide the Japanese Government with "End-user's Statement of Assurance" and "End-user Certificate" in order to obtain the export license needed for export from Japan. If the product to be exported is in this category, the end user will be asked to fill in these certificate forms.

**ARGENTINA**  
COASIN S.A.C.I.yF.  
Virrey del Pato 4071,  
C1430CAM-Buenos Aires  
Argentina  
Tel. 54-11-4552-3185  
Fax. 54-11-4555-3321

**AUSTRALIA & NEW ZEALAND**  
JEOL(AUSTRALASIA) Pty.Ltd.  
Suite 1, L2 18 Aquatic Drive  
- Frenchs Forest NSW 2086  
Australia  
Tel. 61-2-9451-3855  
Fax. 61-2-9451-3822

**AUSTRIA**  
JEOL (GERMANY) GmbH  
Gute Aenger 30  
85356 Freising, Germany  
Tel. 49-8161-9845-0  
Fax. 49-8161-9845-100

**BANGLADESH**  
A.O. CHOWDHURY SCIENCE & SYNERGY PVT. LTD.  
87, Suhrawardy Avenue, Floor 2  
Banjara, Dhaka1212  
Bangladesh  
Tel. 8802-9882272, 8953450, 8953501  
Fax. 8802-9854428

**BELGIUM**  
JEOL (EUROPE) B.V.  
Planet II, Gebouw B  
Louvainssesteenweg 542,  
B-1930 Zaventem  
Belgium  
Tel. 32-2-720-0560  
Fax. 32-2-720-6134

**BRAZIL**  
JEOL Brasil Instrumentos Cientificos Ltda.  
Av. Jabaguará, 2958 5° andar conjunto 52  
C/OM-600, Sao Paulo, SP  
Brazil  
Tel. 55-11-5070 4000  
Fax. 55-11-5070 4110

**CANADA**  
JEOL CANADA, INC.  
3275 Tere Rue, Local #8  
St-Hubert, QC, J5Y-8Y6, Canada  
Tel. 1-450-676-8776  
Fax. 1-450-676-6994

**CHILE**  
ARQUIMED INNOVATION  
Arturo Prat 828,  
Santiago, Chile  
Tel. 56-2-634-6266  
Fax. 56-2-634-4633

**CHINA**  
JEOL(BEIJING) CO., LTD.  
Zhongkeziyuan Building South Tower 2F,  
Zhongguancun Nanshanje Street No. 6,  
Haidian District, Beijing, P.R.China  
Tel. 86-10-6804-6321  
Fax. 86-10-6804-6324

**JEOL (BEIJING) CO., LTD., SHANGHAI BRANCH**  
Room 1505/1506, Nol 300Xi Kang Road,  
Jing an Dist., Shanghai, 200040, China  
Tel. 86-21-6248-4838/4874/4537/4404  
Fax. 86-21-6248-4075

**JEOL (BEIJING) CO., LTD., GUANGZHOU BRANCH**  
M1601, World Trade Center Building,  
#371-375, Huan Shi Road East, Guangzhou,  
Guangdong Prov., 510095, P.R.China  
Tel. 86-20-8778-7848  
Fax. 86-20-8778-4268

**JEOL (BEIJING) CO., LTD., WUHAN BRANCH**  
Room A2118, Zhongshang Plaza Office Bldg.,  
No. 7 Zhongnan Road, Wuhan,  
Hubei, 430071, P.R.China  
Tel. 86-27-8713-2567  
Fax. 86-27-8713-2567

**JEOL LTD. (BEIJING) CO., LTD., CHENGDU BRANCH**  
1807A Zongfu Building,  
NO. 35 Zongfu Road, Chengdu, Sichuan, 610016  
P.R. China  
Tel. 86-28-86622554  
Fax. 86-28-86622564

**EGYPT**  
JEOL SERVICE BUREAU  
3rd Fl. Nile Center Bldg., Nawal Street,  
Dokki, (Cairo), Egypt  
Tel. 20-2-3335-7220  
Fax. 20-2-3338-4168

**FRANCE**  
JEOL (EUROPE) SAS  
Espace Claude Monet, 1 Allée de Giverny  
78290, Croissy-sur-Seine, France  
Tel. 33-1-3015-3737  
Fax. 33-1-3015-3747

**GERMANY**  
JEOL (GERMANY) GmbH  
Gute Aenger 30  
85356 Freising, Germany  
Tel. 49-8161-9845-0  
Fax. 49-8161-9845-100

**GREAT BRITAIN & IRELAND**  
JEOL (U.K.) LTD.  
JEOL House, Silver Court, Watchmead,  
Welwyn Garden City, Herts AL7 1LT, U.K.  
Tel. 44-1707-377117  
Fax. 44-1707-373254

**GREECE**  
N. ASTERIOUDIS S.A.  
58-58 S. Tirkoupi Str. P.O. Box 26140  
GR-10022, Athens, Greece  
Tel. 30-1-823-8383  
Fax. 30-1-823-9567

**HONG KONG**  
FARMING LTD.  
Unit No. 1009, 10/F., Prosperity  
603 King's Road, North Point, Hong Kong  
Tel. 852-2815-7250  
Fax. 852-2581-4635

**INDIA**  
JEOL INDIA Pvt. Ltd.  
Unit No. 305, 3rd Floor,  
ABW Elegance Tower,  
Jasola District Centre,  
New Delhi 110 028, India  
Tel. 91-11-6472-2578  
Fax. 91-11-4060-1235

**JEOL India Pvt. Ltd., Mumbai Branch**  
Regus Mumbai  
Levels Ground & 1, Trade Centre Bandra Kuria Complex 1108,  
Bandra (E) Mumbai, 400051, India  
Tel. : +91-22-40700700

**INDONESIA**  
PT. TEKNO LABINDO Perita Perkasa  
Komplek Gedung Bukit Indah Blok I/11  
Jl. Bukit Gasing Raya Kelapa Gading Permai,  
Jakarta 14240, Indonesia  
Tel. 62-21-46847057/58  
Fax. 62-21-45642729

**ITALY**  
JEOL (ITALIA) S.p.A.  
Palazzo Pagnotti - Milano 3 City,  
Via Ludovico il Moro, 6/A  
20080 Basiglio(MI) Italy  
Tel. 39-02-9041431  
Fax. 39-02-90414343

**KOREA**  
JEOL KOREA LTD.  
Dongwo Bldg 7F, 1443, Yangjae Daero,  
Gangdong-Gu, Seoul, 05355, Korea  
Tel. 82-2-511-9501  
Fax. 82-2-511-2635

**KUWAIT**  
Ashraf & CO. Ltd.  
P.O.Box 3555 Safat 13036, Kuwait  
Tel. 965-1805151  
Fax. 965-24335373

**MALAYSIA**  
JEOL(MALAYSIA) SDN.BHD.  
508, Block A, Level 5,  
Kelana Business Center,  
97, Jalan SS 7/2, Kelana Jaya,  
47301 Petaling Jaya, Selangor, Malaysia  
Tel. 60-3-7492-7722  
Fax. 60-3-7492-7723

**MEXICO**  
JEOL DE MEXICO S.A. DE C.V.  
Arkansas 11 Piso 2  
Colonia Napolos  
Delegación Benito Juárez, C.P. 03810  
Mexico D.F., Mexico  
Tel. 52-5-55-211-4511  
Fax. 52-5-55-211-0720

**Middle East**  
JEOL GULF FZE  
P.O. Box No. 371107  
Dubai Airport Free Trade Zone East Wing 5EA No. 404,  
Dubai, UAE  
Tel. 971-4-609-1497  
Fax. 971-4-609-1498

**PAKISTAN (Karachi)**  
ANALYTICAL MEASURING SYSTEM (PVT) LTD.(AMS LTD.)  
14-C Main Sehar Commercial Avenue Lane 4,  
Khayaban-e-Sehar,  
D.H.A.VII, Karachi-75500, Pakistan  
Tel. 92-21-35345581/35340747  
Fax. 92-21-35345582

**PANAMA**  
PROMED S.A.  
Parque Industrial Costa del Este  
Urbanización Costa del Este  
Apartado 0818-01755, Panama, Panama  
Tel. 507-303-3100  
Fax. 507-303-3115

**PHILIPPINES**  
PHILAB INDUSTRIES INC.  
7487 Bagtikan Street, SAV Makati,  
1203 Metro, Manila Philippines  
Tel. 63-2-826-8269  
Fax. 63-2-897-7732

**PORTUGAL**  
Izasa Portugal Lda.  
R. do Proletariado, 1  
2790-138 CARINAXIDE, Portugal  
Tel. 351-21-424-73-00  
Fax. 351-21-419-60-20

**RUSSIA**  
JEOL (RUS) LLC.  
Krasnoprolétaireskaya Street. 16,  
Bld. 2, 127478, Moscow,  
Russian Federation  
Tel. 7-495-748-7791/7792  
Fax. 7-495-748-7793

**SAUDI ARABIA**  
ABDULREHMAN ALGOSAIBI G.T.C. (Riyadh)  
Algosabi Building-Old Airport Road  
P.O. Box 215, Riyadh 11411, Saudi Arabia  
Tel. 966-1-477-7932

**SCANDINAVIA**  
SWEDEN  
JEOL (Nordic) AB  
Hammarbacken 6A, Box 716, 191 27 Sollentuna  
Sweden  
Tel. 46-8-28-2800  
Fax. 46-8-29-1647

**SINGAPORE**  
JEOL ASIA PTE.LTD.  
2 Corporation Road  
#01-12 Corporation Place  
Singapore 618494  
Tel. 65-6565-9880  
Fax. 65-6565-7552

**SOUTH AFRICA**  
ADI Scientific (Pty) Ltd.  
370 Angus Crescent,  
Northlands Business Park, 29 Newmarket Road  
Northridge, Randburg, Republic of South Africa  
Tel. 27-11-482-1983  
Fax. 27-11-482-1466

**SPAIN**  
ZASA Scientific SLU.  
Argoneses, 18, 28108 Alcobendas,  
Madrid, Spain  
Tel. 34 902 20 30 80  
Fax. 34 902 20 30 81

**SWITZERLAND**  
JEOL (GERMANY) GmbH  
Gute Aenger 30  
85356 Freising, Germany  
Tel. 49-8165-77346  
Fax. 49-8165-77512

**TAIWAN**  
JIE DONG CO., LTD.  
7F, 112, Chung Hsiao East Road,  
Section 1, Taipei, Taiwan 10020 (R.O.C.)  
Tel. 886-2-2395-2978  
Fax. 886-2-2322-4655

For NMR & Mass Spectrometer Products  
Widetrion Technologies Corp.  
No.8-2, No.77, Sec.2, Zhonghua E Rd.,  
East Dist., Tainan City 701, Taiwan (R.O.C.)  
Tel. 886-6-289-1943  
Fax. 886-6-289-1743

(For Mass Spectrometer Products)  
Tech Max Technical Co., Ltd.  
5F, No.11, Wuqun 2nd Rd., Wuqu Dist.,  
New Taipei City 248, Taiwan (R.O.C.)  
Tel. 886-2-8990-1779  
Fax. 886-2-8990-2559

For Semiconductor Products:  
JEOL TAIWAN SEMICONDUCTORS LTD.  
2F-2, No.192, Dongguang Rd.  
East Dist., Hsinchu City 30059,  
Taiwan (R.O.C.)  
Tel. 886-3-571-5656  
Fax. 886-3-571-5151

**THAILAND**  
BECTHAI BANGKOK EQUIPMENT & CHEMICAL CO., Ltd.  
300 Phrayothin Rd. Phrayathai, Bangkok 10400,  
Thailand  
Tel. 66-2-615-2929  
Fax. 66-2-615-2350/2351

JEOL ASEAN TECHNICAL CENTER (JATC)  
MTEC building room 533  
114 Moo9, Thailand Science Park  
Pachayothin Rd., Klong 1, Klong Luang,  
Pathumthani 12120  
THAILAND  
Tel. 66-2-564-7738  
Fax. 66-2-564-7739

**THE NETHERLANDS**  
JEOL (EUROPE) B.V.  
Lirweg 4, NL-2153 PH Nieuw-Vennep,  
The Netherlands  
Tel. 31-252-623500  
Fax. 31-252-623501

**TURKEY**  
Tekser A.S.  
Kartal Cad. No: 55/3 Inonu Wah.,  
Atasehr 34755, Istanbul, Turkey  
Tel. 90-216-5736470  
Fax. 90-216-5736475

**USA**  
JEOL USA, INC.  
11 Deaton Road, Peabody, MA 01960, U.S.A.  
Tel. 1-978-535-5900  
Fax. 1-978-536-2205/2206

JEOL USA, INC. WEST OFFICE  
5658 Stoneridge Drive Suite #110  
Pleasanton, CA 94588, U.S.A.  
Tel. 1-925-737-1740  
Fax. 1-925-737-1749

**VENEZUELA**  
GOMSA Service and Supply C.A.  
Urbanización Montalbán III  
- Residencias Don Andres - Piso 7 - Apartamento 74  
Avenida 3, entre calles 7 y 6  
Montalbán, Caracas, Venezuela  
Tel. 58-212-443-4342  
Fax. 58-212-443-4342

**VIETNAM**  
TECHNICAL MATERIALS AND RESOURCES  
IMPORT-EXPORT JOINT STOCK COMPANY(REXCO)  
Hanoi Branch  
SALES & SERVICE  
155-157 Lang Ha Street, Dong Da District, Hanoi, Vietnam  
Tel. +84 (43) 562 0516  
Fax. +84 (43) 853 2511